Design and Development Towards a Novel Prosthesis for Total Shoulder Arthroplasty to Reduce Aseptic Glenoid Loosening

Submitted by

Roopam Dey

for the degree of

Doctor of Philosophy

in the

Department of Human Biology

University of Cape Town

September 2018

The financial assistance of the National Research Foundation (NRF) towards this research is hereby acknowledged. Opinions expressed, and conclusions arrived at, are those of the author and are not necessarily to be attributed to the NRF.

Dedicated to my parents

Pradipta and Krishna

Abstract

Total shoulder arthroplasty (TSA) is the most common surgical solution, that helps in restoring the structural and functional integrity of a diseased glenohumeral (GH) joint with intact rotator-cuff. A 300% increase in the usage of TSA has been observed since 2007, along with 2.5% increase in revision rate. Aseptic glenoid loosening accounts for 37% of post-surgical failures in TSA. Eccentric loading of the prosthetic glenoid cup, leading to the *"rocking horse"* effect, is one of the prevalent causes of aseptic glenoid loosening. Current anatomical total shoulder prosthesis (ATSP) geometry does not consider all the GH morphometric features, for example the elliptical shape of the humeral head. Moreover, the morphometric studies leading to the initial ATSP design did not consider the GH morphology of any sub-Saharan population. Hence, there exists a gap in understanding of the implications of certain morphometric features on the functionality of a post-TSA GH joint.

This thesis had two primary aims to address this gap in knowledge. Firstly, to study the GH morphometric variations between cohorts representing native European (Swiss) and native sub-Saharan (South African) populations. Secondly, to develop anatomically inspired ATSP design concepts and test them using biomechanical and finite element (FE) models, *in-silico*, under standardised testing protocols.

The morphometric analysis suggested that an average Swiss humeral head radius of curvature was larger ($P<0.05$) than the average South African humeral head. By comparing the biological head sizes, across both the populations, with the dimensions of the commercially available humeral heads, it can be inferred that suitable humeral prostheses are currently not available for individuals with head sizes >28mm or <19mm. Considering both the populations, the inherent shape of an average humeral head was found to be elliptical. The thickest region of the head was found to lie in the posterior region and not at the geometric center. Hertzian contact theory was applied to calculate the GH stresses produced by

symmetric and asymmetric elliptical heads. Higher concentric stresses (P<0.001), within the acceptable limit for polyethylene, were observed to be imparted by the asymmetric heads.

Population-specific musculoskeletal models were developed to study the post-TSA kinematic variation. When an identical range of motion (RoM) was performed by these models, population-specific variation in muscle moment arms was observed. The novel glenoid designs were not found to alter the post-surgical kinematics. FE models of the bi-radial, compartmental and pear-shaped glenoid implant designs were subjected to compressive and shear loading according to the American Society for Testing and Materials (ASTM). Using the bi-radial the glenoid cup, with thickened posterior-superior surface, anatomically relevant force distribution patterns could be replicated. Compartmentalising the glenoid prosthesis into concentric and eccentric regions with the gaps, proved to be highly beneficial. When compared to a commercially available glenoid prosthesis, the compartmental prosthesis was able to contain the GH forces to the concentric region for longer, delaying the eccentric loading and therefore potentially reducing the *"rocking horse"* effect.

In the light of the above observations, two conclusions can be drawn from this thesis. Firstly, it would be beneficial if population-specific ATSP were made available for natives of certain geographic locations. Secondly, glenoid prosthesis designs could be compartmentalised to contain the GH joint forces within the concentric regions of the cup which might aid in the reduction of post-TSA complications.

Table of Contents

Motivation

Beautiful things come to you,

from the most unexpected sources,

especially when you are not looking for them.

- *unknown*

Human beings are moulded by evolution and staying curious is in our nature. For ages, the humanity has pursued knowledge to better understand gigantic cosmic and microscopic biologic phenomena. The foundation for the modern fields of astronomy and medicine were laid during the Greco-Roman, Egyptian and Vedic periods.

Earliest contributions to these fields by Ptolemy, Copernicus, Aryabhatta, Ibn Yunus, Galileo Galilei, Aristotle, Charaka, Peseshet and many other pioneers paved the way for recent ground-breaking observations by Newton, Einstein, Dirac, Darwin, Robert Hooke, Watson and Crick, Louis Pasteur and others. The common factor, binding all these great pioneers together was their quest for the beautiful world of knowledge.

Evident use of prosthetic joint replacements in modern surgical practice was reported by Dr. Themistocles Gluck in the late 19th century. Since then, contributions by Dr. Jules Emil Pean, Sir John Charnley, Dr. Charles S. Neer and Dr. Paul Grammont have revolutionized the field of articular joint replacement.

Deriving inspiration from the stalwarts and keeping an open mind as the ancient philosophers, I undertook research on possibly improving the design of shoulder replacement prostheses. This thesis is my earnest effort to contribute to the existing field of knowledge regarding the glenohumeral joint and its anatomically shaped prosthesis.

Acknowledgements

I would like to begin by acknowledging my supervisors, Dr Sudesh Sivarasu and Dr Stephen Roche, for their constant support and guidance. Apart from providing me with adequate research freedom, Dr Sivarasu, has also helped me find my way out of numerous rabbit holes. Dr Roche's surgical perspectives have been essential in making this study clinically relevant. The University of Cape Town (UCT) and the Division of Biomedical Engineering have been really kind to me throughout my doctoral research. I would like to thank the management for the conducive research environment and the infrastructure provided.

The members of orthopedic biomechanics and medical devices labs at UCT have been an absolute pleasure to work with. I would like to thank Jonathan, Leanne, Dr Giovanni, Saadiq, Yasheen, Megan, Sam and Rosslee for being supportive. It is always challenging to settle in a different country. I must thank Gokul, Giancarlo, Ziana, Rick, Calvin, Bhawani and Arun who have made me feel at home in Cape Town, sometimes going out their ways to help me and treating me like family. Triroopa, thanks for being supportive, understanding and patient. I would also like to acknowledge Dr Bhushan Borotikar, Dr Thomas Franz, Dr Tinashe Mutsvangwa, Dr Theo Rosch, Charles Harris, Stefan Steiner, Dr Nathanael Narra, Dr Johan Charilaou and many others, who have been always available for technical and non-technical advice throughout my doctoral degree. It was a pleasure to collaborate and work as co-authors with many of them. A special thanks to Dr Kylie de Jager and Dr Tamer Abdalrahman. While long supportive e-mails from the former kept me going during thesis write-up, the later helped me with his invaluable research experience.

My parents' support has been invaluable. I wouldn't have been the person I am today, without their love and sacrifices. I dedicate the thesis to them. Finally, I thank the Almighty for taking care of me and blessing me with the *will* to push through the last three years.

Declaration

I, Roopam Dey, hereby declare that the work on which this thesis is based on my original work (except where acknowledgements indicate otherwise) and that neither the whole work nor any part of it has been, is being, or is to be submitted for another degree in this or any other university.

I empower the university to reproduce for the purpose of research either the whole or any portion of the contents in any manner whatsoever.

I confirm that I have been granted permission by the University of Cape Town's Doctoral Degrees Board to include the following publication in my PhD thesis, and where co-authorships are involved, my co-authors have agreed that I may include the publication(s):

a. **Dey, R., Roche, S., Rosch, T., Mutsvangwa, T., Charilaou, J., & Sivarasu, S. (March 2018).** ***Anatomic variations in glenohumeral joint: an interpopulation study.*** **Journal of Shoulder and Elbow Surgery OA, 2(1), 1-7. https://doi.org/10.1016/j.jses.2017.11.007.**

Signature:

Date: **14th September 2019.**

Student Name: **Roopam Dey.**

Student Number: **DYXROO001.**

List of Abbreviations

3D	Three Dimensional.
AA	Angulus Acromialis.
AC	Acromioclavicular joint.
ADL	Activities of Daily Living.
AI	Angulus Inferior.
AP	Anterior-Posterior.
API	Application Programming Interface.
AP_w	humeral head base Width in the Anterior-Posterior direction.
ASTM	American Society for Testing and Materials
ATSP	Anatomic Total Shoulder Prosthesis.
C7	7^{th} vertebra of Cervical spine.
CH	referring to the Swiss dataset and musculoskeletal model.
CHI	referring to the Chinese musculoskeletal model.
CI	Conformity Index.
CoR	Center of Rotation.
C_r	theoretical Contact Radius
CT	Computerised Tomography.
DGL	Dynamic Glenoid Loosening.
EL	Lateral Epicondyle of humerus.
EM	Medial Epicondyle of humerus.
EMG	Electromyography.
FE	Finite Element.
FEAP	Finite Element Analysis Pipeline.
FEP	Feature Extracting Pipeline.
GH	Glenohumeral joint.

GHOA	Glenohumeral Osteoarthritis.
GC	Glenoid Center.
G_{rad}	Radius of the glenoid.
HA	Hemiarthroplasty.
h_{cntr}	Central height of the humeral head.
h_{peak}	Peak Height of the humeral head.
H_{rad}	Radius of the humeral head.
HSS	Hospital for Special Surgery.
IJ	Incisura Jugularis.
ISB	International Society of Biomechanics.
ISG	International Shoulder Group.
MTP	Motion Testing Pipeline.
NMA	non-Manifold Assembly.
NSM	Newcastle Shoulder Model.
OA	Osteoarthritis.
PHF	Proximal Humeral Fractures.
PMMA	Polymethyl Methacrylate.
PS	Posterior-Superior.
PP	Peak Point of the humeral head.
PX	Processus Xiphoideus.
RHE	Rocking Horse Effect.
RoC	Radius of Curvature.
RoM	Range of Motion.
RS	Radial Styloid.
RTSA	Reverse Total Shoulder Arthroplasty.
SA	referring to the South African dataset and musculoskeletal model.
SC	Sternoclavicular joint.
SHR	Scapulo-Humeral Rhythm.

SI	Superior-Inferior.
SI_w	humeral head base Width in the Superior-Inferior direction.
ST	Scapulothoracic joint.
TSA	Total Shoulder Arthroplasty.
TSP	Total Shoulder Prosthesis.
TSS	Trigonum Spinae Scapulae.
T8	8^{th} vertebra of Thoracic spine.
UHMWPE	Ultra-High Molecular Weight Polyethylene.
US	Ulnar Styloid.

List of Tables

List of Figures

List of Equations

CHAPTER 1

Introduction

1.1 The Shoulder

The shoulder joint (Fig. 1.1) is formed by the articulation of the scapula, humerus, clavicle and thoracic cavity. The complete shoulder range of motion (ROM) is achieved by the complex coordinated interactions among the Acromio-Clavicular (AC), Gleno-Humeral (GH), Scapulo-Thoracic (ST) and Sterno-Clavicular (SC) joints.

The GH joint is the most mobile joint in a human body where the humeral head (ball) translates and rolls on the glenoid fossa (socket). The structural (bony) conformity of the joint is mechanically insufficient to keep the GH surfaces together. The surrounding soft tissues play a major in stabilizing the GH joint. The articulating surfaces are cocooned by 3 layers of the joint capsule and further supported by the rotator-cuff muscles, the deltoid and the long head of the bicep muscle (Lippitt & Matsen, 1993).

The osteokinematics of the GH bones does not allow the joint to achieve its full extent of natural RoM. To achieve the entire GH RoM the arthrokinematics of the whole shoulder girdle plays an important part. The hinged rolling motion of the SC joint, the upward gliding motion of the ST joint and the translating-rolling motion of the GH joint synergize together to derive functional activities. This teamwork of the shoulder joints could be best observed during its elevation in the frontal plane. The SC joint and the GH joint shares the elevating motion in a ratio of 2.34:1 (Scibek & Carcia, 2012).

Apart from partially stabilizing the GH joint, the muscles in the shoulder girdle allow movements such as abduction, forward flexion, elevation, adduction, internal and external rotation. The major muscle groups which perform the motions are the rotator cuff and the deltoid muscles. Even though there are several muscles such as the teres major, levator scapulae, rhomboids, triceps and trapezius among others, which support the shoulder function (Rockwood, 2009), the success of the Total Shoulder Arthroplasty (TSA) majorly

depends on the post-surgical functionality of the deltoid & rotator cuff muscles and their tendons. Hence, the current thesis will be focused on studying the post-surgical functionality of these two sets of muscles, using *in-silico* musculoskeletal models.

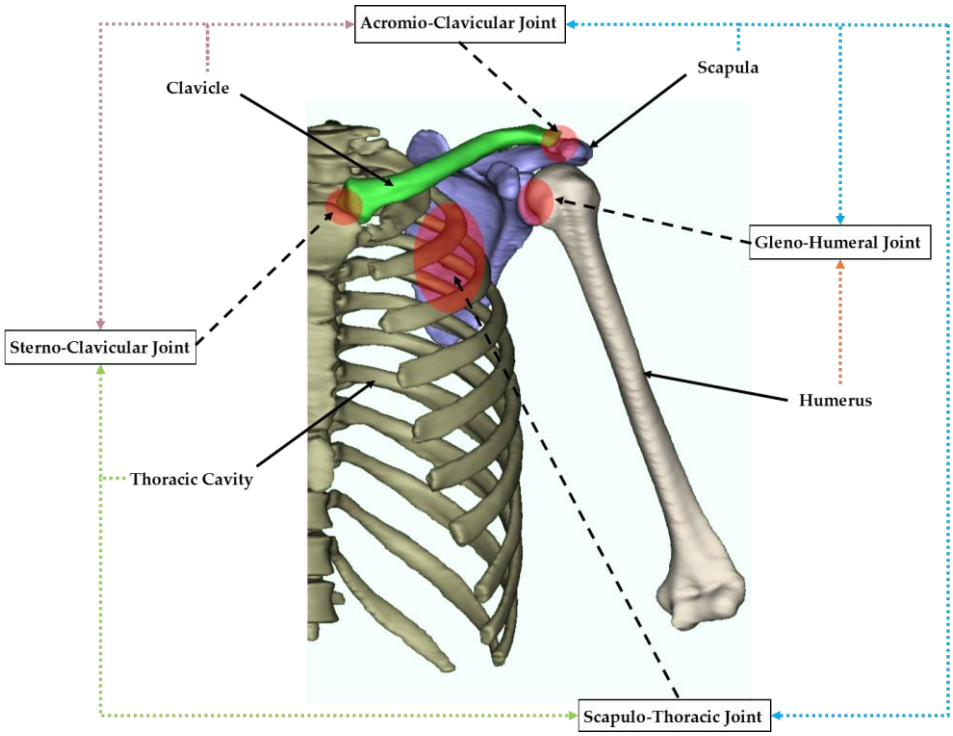

Figure 1.1 Schematic representation of the various articulations of the shoulder girdle essential for GH RoM.

1.2 Glenohumeral Arthritis

GH arthritis is one of the conditions that is treated using TSA. There are two major types of arthritis affecting the human body, Osteoarthritis (OA) and Rheumatoid Arthritis (RA). Both of these categories of bone diseases have been reported to affect the synovial joints (National Collaborating Centre for Chronic Conditions, 2009; Sinusas, 2012). Age, bone loss, gender, past joint injuries and lifestyle could be one of the root causes of OA. OA is characterized by the loss of cartilage on the joint surfaces leading to trabecular bone friction giving rise to intense joint pain (Creamer, 2000; Sinusas, 2012). RA is an autoimmune disease characterized by inflamed synovial joint membranes due to the release of protein-degrading enzymes.

Worldwide OA is listed as one of the top 5 disabilities. It has been predicted that 130 million human beings would be affected with OA by 2050. Apart from the health-related side

effects of OA, like depression, obesity, and heart disease, it also imposes a huge economic burden on the individual and national level. In the year 2012, the United States of America has lost $100 billion as OA affected individuals had to terminate their jobs (Arthritis Foundation, 2018).

Osteoarthritis (OA) of the GH joint, though not as prevalent as hip and knee, affects 32.8% of individuals whose age is 60 years and above (Chillemi & Franceschini, 2013). This decreases the available ROM of the joint and induces pain. Degradation of the GH joint has been observed in 15% of the Rheumatoid Arthritis (RA) patients in sub-Sahara Africa (Mue et al., 2013). Akinpelu et al., 2010, had reported that 7.3% of the Nigerian population, suffering from degenerative diseases, were detected with GHOA. Above the age of 65 years, 55.1% of the city dwellers and up to 82.7% of the rural population of South Africa are at risk of OA (Usenbo et al., 2015). Parker & Jelsma, 2010, found the prevalence of GHOA and GHRA in 7% of the underprivileged population of Cape Town, South Africa. An aging population is always more susceptible to arthritis (Arthritis Foundation, 2018). In South Africa, 4.6 million people fall under the category of being elderly, with an age of >60 years (STATS SA, 2017). This puts these individuals at greater risk of OA. Along with this, the South African medical device industry has been reporting an average annual loss of $770 million, since 2015, (Fig. 1.2) as most of its medical devices including shoulder implants are being imported (The International Trade Administration, 2017).

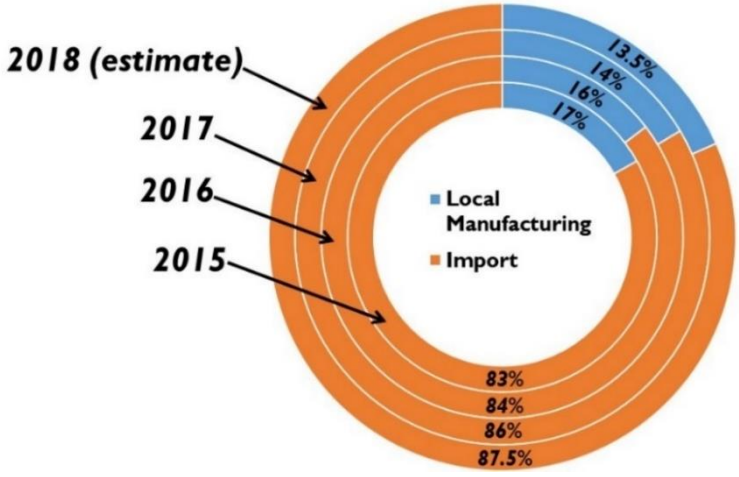

Figure 1.2 Large proportion of South Africa's medical devices are imported from more developed nations.

1.3 Introduction to Total Shoulder Arthroplasty

Proximal humeral fractures (PHF) are the third most common fractures in the world (Mauro, 2011) and the most common fracture of the humerus (Kim et al., 2012). PHF directly affects the functionality of the GH joint and if not detected in the initial stages, could lead to GHOA. Though the actual statistics are unknown, PHF is common in South Africa due to the prevalence of contact sports like rugby and high rate of trauma caused due to violence. PHF and GH arthritis are the main indications for TSA.

In the early 1970s, TSA was introduced as a surgical technique to replace dysfunctional GH joint surfaces. The prosthetic humeral head was metallic, and the glenoid cup implant was made from polyethylene. Initially, the prosthetic GH joint surfaces were highly conformed and constrained. This design approach mimicked a perfect ball and socket joint but led to severe glenoid cup damage leading to polyethylene fractures and implant failures (Wirth & Rockwood, 1996). Current prosthesis designs are a modification of the initial unconstrained, Neer Mark II prosthesis, introduced by Dr Charles S. Neer (Deore et al., 2018; Frich et al., 1988; Neer II et al., 1982). The loading surface of the prosthetic humeral head is manufactured of cobalt-chromium (Co-Cr) alloy and the load bearing surface of the glenoid implant is manufactured using ultra high molecular weight polyethylene (UHMWPE). A brief historical timeline of the Anatomical Total Shoulder Prosthesis (ATSP) is presented in Figure 1.3. A surgical technique called the *deltopectoral approach,* used to implant the prosthetic components have remained almost identical since its initiation (Neer II, 1955).

Current TSA prosthesis designs could be, broadly, categorized as the third generation GH prostheses. While the first and the second generation ATSPs were focused on functional restoration of the GH joints, the current prostheses designs were the first of its kinds to cater for the best representation of the proximal humeral geometry along with restoring GH functionality (Boileau & Walch, 1997; Robertson et al., 2000). This has increased (Day et al., 2010) their usage (Fig. 1.4), along with RTSA, even in the younger patients (Padegimas et al., 2015). Recent follow-up studies have reported higher post-operative patient satisfaction (Styron et al., 2015) and reduction in many of the post-surgical complications.

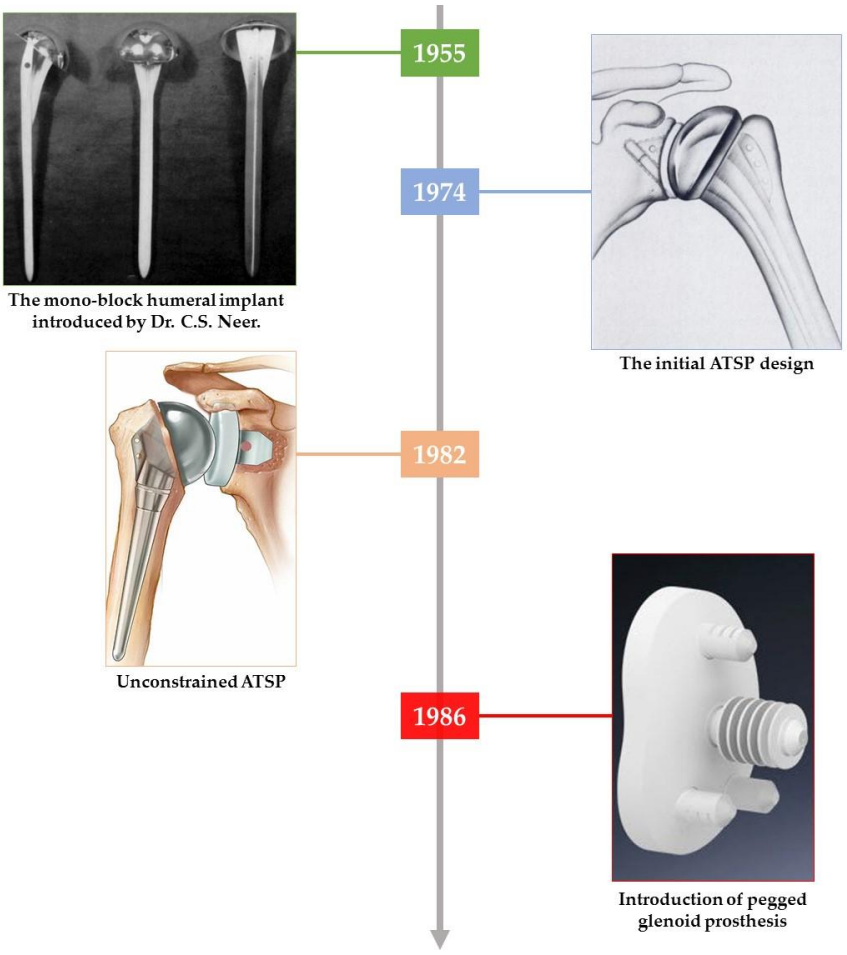

Figure 1.3 Important evolutionary landmarks of the Anatomical Total Shoulder Prosthesis since its inception. *sourced from* (Deore et al., 2018; Lazarus et al., 2002; Neer II, 1955, 1974; Neer II et al., 1982).

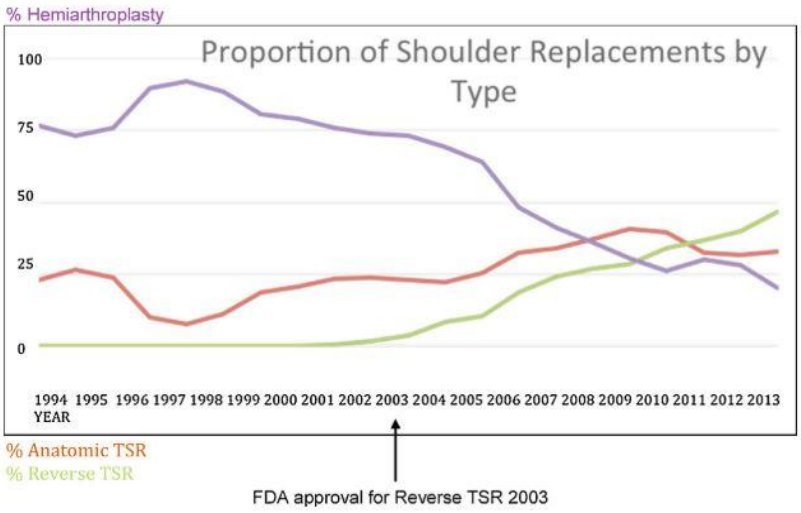

Figure 1.4 Increase in the use of TSA occurred around the same time as the unreliability of hemiarthroplasty (HA) was recognized. The reduction in the use of the HA occurred as the arthritis was observed to spread into the glenoid surface from the humerus. This led to future revision surgeries. *sourced from* (Deore et al., 2018).

1.4 Post-Surgical Complications

Although the complication rates were reduced, with the third-generation ATSP designs, they have not been eradicated. Initial glenoid failure mechanism was observed due to *"stress shielding"* in metal-backed prostheses (Bohsali et al., 2006; Boileau et al., 2015; Bonnevialle et al., 2013; Papadonikolakis & Matsen, 2014). In an all-polyethylene glenoid cup implant instability leading to its aseptic loosening is the major cause for failure (Eichinger & Galvin, 2015). This kind of failure has been attributed to the *"rocking horse"* effect (Fig. 1.5 a-b). The complication rates due to glenoid loosening are varied and has been reported to depend on the ease and efficiency of the cementing technique (Lazarus et al., 2002; Matsen III et al., 2008), rotator cuff deficiency (Franklin et al., 1988) and the amount of GH prosthetic mismatch (Walch et al., 2002).

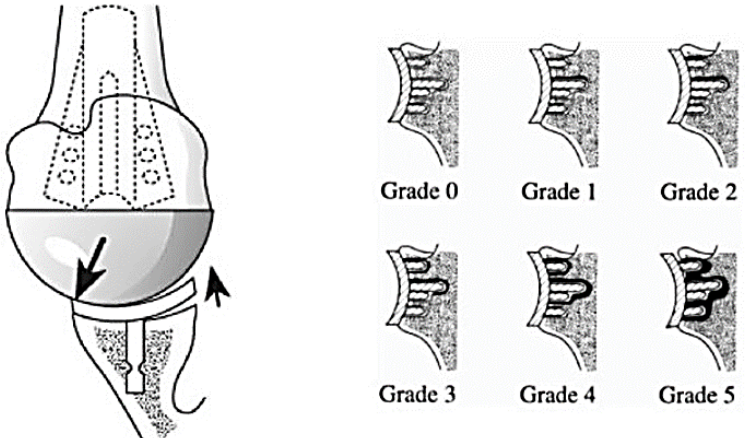

(a) (b)

Figure 1.5 The eccentric loading of the glenoid component shown in (a) is the main cause of the glenoid loosening at the bone cement interface. *sourced from* (Matsen III et al., 2008). (b) The grades of loosening for the pegged glenoid component were introduced by Lazarus et al., 2002, based on the amount of radiolucency observed in post-TSA radiographs. Grade 0 signifying no loosening and Grade 5 signifying complete loosening of the glenoid cup.

At five-year follow-up of 1673 TSA surgeries Somerson et al., 2018, reported 20.4% (highest) failure due to glenoid component. The glenoid loosening related failure rates increase with time, post-TSA. Bonnevialle et al., 2013, investigated the cause of 42 TSA revision surgeries, between 1991 and 2006, and reported 46% of them were due to glenoid component loosening. On the other hand, a two-year follow-up of 77 TSA observed 13.3%

glenoids with radiographic proof of loosening (Kiet et al., 2015). The progressive loosening of the glenoid cup, reduces the longevity of TSA (Matsen III et al., 2008). Even though there has been an advancement in the ATSP design, TSA techniques, and post-operative rehabilitation, there is an acute need for the development of a stable GH prosthesis for TSA to reduce the eccentric loading of the glenoid.

1.5 Thesis Scope, Goals and Organization

ATSP design modifications could be one of the strategies that could be implemented to reduce the post-TSA glenoid failures. The scope of this thesis was, firstly, to study GH morphometry of the native South African population. Secondly, the scope also included conceptualising and testing novel ATSP designs. Adequate care was taken to develop prostheses which did not alter the current surgical approach and the tests were performed within the current standards. The thesis is divided into three sets of goals which the chapters help to achieve. A schematic representation of the thesis organization is provided in Fig. 1.6, this would make it easier for the reader to understand the flow of the document. Brief explanations of the goals are provided ahead.

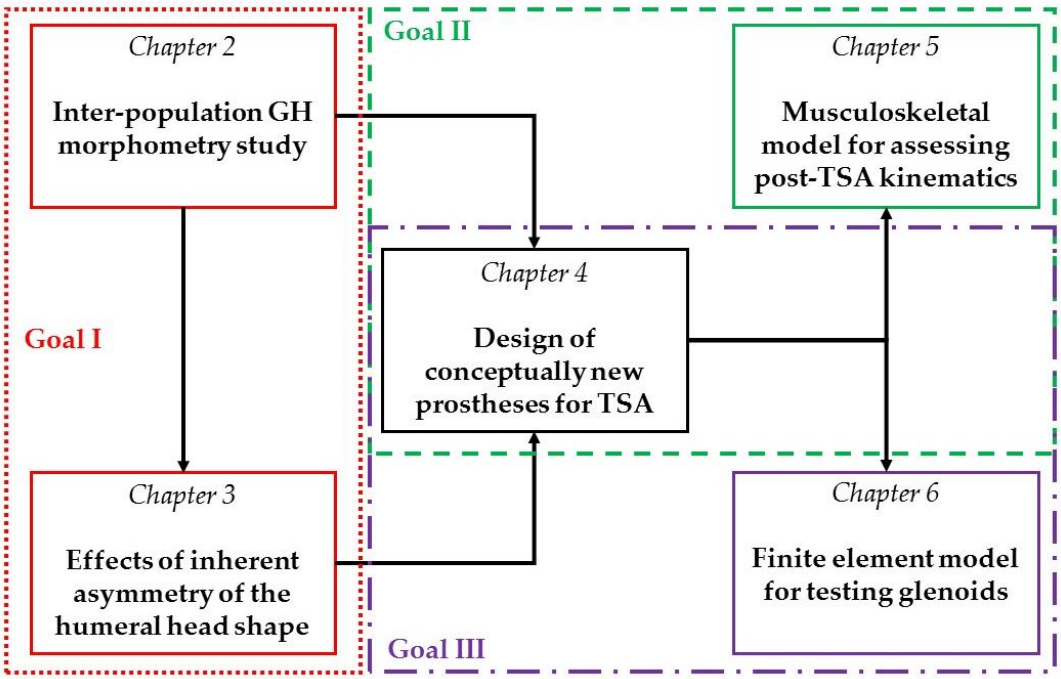

Figure 1.6 Thesis organization and layout of the chapters according to the pre-determined goals.

1.5.1 Goal I

The morphometric studies which led to the initial development of ATSP were conducted on GH joints obtained from American (Robertson et al., 2000) and European (Boileau & Walch, 1997) Caucasian populations. There is no existing study which suggests that the commercially available ATSPs cater for the native population of South Africa.

Therefore, the first goal of this thesis is to study and compare the GH articulating surfaces of a South African cohort and compare them with a European GH data set. This study is spread over Chapter 2 and 3. Chapter 2 is focused on explaining the method implemented in studying the morphometry and describes the inter-population differences. Chapter 3 studies the theoretical effect of the altering the humeral head shape from a perfect sphere to an eccentric ellipse.

1.5.2 Goal II

The second goal of the thesis was to investigate the post-TSA kinematics of the novel conceptual designs of TSA prosthesis. These designs were developed by incorporating the morphometric observations from Chapter 1 & 2 in order to combat the current modes of failure. Chapter 4 describes the design process involved in the creation of these prostheses and Chapter 5 details the development of a post-TSA musculoskeletal model and the kinematic changes introduced by the new prosthesis designs.

1.5.3 Goal III

The final goal of this dissertation is to analyze the performance of the prostheses designs under loading conditions standardized by ASTM. Chapter 6 describes in detail the Finite Element (FE) model and the observations from the subluxation tests performed on the glenoid models. Even though, novel humeral and glenoid components designs were created in Chapter 4, to adhere to the strict timeline of the research only new glenoid designs were tested using the FE model.

The final chapter synthesizes the conclusions from the previous chapters and provides recommendations and possible directions for future work.

CHAPTER 2

Part of this chapter has been peer-reviewed and published as:

Dey, R., Roche, S., Rosch, T., Mutsvangwa, T., Charilaou, J., & Sivarasu, S. (March 2018). *Anatomic variations in glenohumeral joint: an interpopulation study.* Journal of Shoulder and Elbow Surgery OA, 2(1), 1-7. https://doi.org/10.1016/j.jses.2017.11.007.

Part of this chapter has been presented (podium) as:

Dey, R., Roche, S., Mutsvangwa, T., and Sivarasu, S. *An inter-population study between African and European glenohumeral articulating surfaces.* 8th World Congress of Biomechanics (WCB), Dublin, Ireland. (July 2018)

Dey, R., Roche, S., Rosch, T., Mutsvangwa, T, Charilaou, J. and Sivarasu, S. Are South African shoulders different? An unique inter-population morphometric investigation. 63rd Congress of the South African Orthopaedic Association (SAOA), Port Elizabeth, South Africa. (Sept 2017)

Morphometry of the GH Joint and its Population Specific Variations

2.1 Introduction

Total Shoulder Arthroplasty (TSA) surgically replaces the arthritic articulating surfaces of the GH joint (Mue et al., 2013), in the presence of intact rotator cuffs, with an ATSP (Bishop & Flatow, 2005; Green & Norris, 2001; Kaback et al., 2012; Lehmann et al., 2010; Sanchez-Sotelo, 2011). Although, the current design of the ATSP has been successful is alleviating shoulder joint pain and restoring the functionality of the joint, underlying complications such as glenoid component loosening and humeral head subluxation reduces the success of this surgical intervention (Bohsali et al., 2006; Gregory et al., 2009; Hasan et al., 2002; Hill & Norris, 2001; Kaback et al., 2012; Matsen et al., 2008; Nagels et al., 2002; Postacchini et al., 2012; Raphael et al., 2010; Wirth & Rockwood, 1996).

The initial design of the ATSP, as proposed by Neer, was aimed towards mimicking the GH joint function (Brand, 2011). Since then, modifications have been made to accommodate for the head inclination angle, retroversion angle and implants have also become more modular to accommodate for reverse shoulder prosthesis (Boileau et al., 2006; Hertel & Ballmer, 2003; Mackay et al., 2001; Parker & Jelsma, 2010).

The current trend followed by various ATSP manufacturers (e.g. DePuy Global Shoulder System, and Tornier Aequalis prosthesis) is to provide surgeons with options of a particular humeral head size with different heights and version angles (Wang et al., 2005). Keeping in mind, the evolution of the shoulder prosthesis design (Chapter 1.3), it could be predicted that the future prosthesis designs would most likely be patient specific as seen in hips and knees (Coigny et al., 2016). This would be an advantageous strategy to pursue considering the subject-specific variations. Studying towards developing population-specific

ATSP design could be argued to be an intermediate step forward and this would partly be the focus of this chapter.

In sub-Saharan Africa, shoulder arthritis is a common joint disease (Akinpelu et al., 2010; Owaydhah et al., 2017). Orthopedic related disorders feature in the top ten Burden-of-diseases in South Africa (De Beer & Bhatia, 2009; Health Metrics and Evaluation, 2010). Approximately 1000 ATSPs are annually implanted in South Africa, and most of the prostheses used are imported creating a financial burden on the country (Samed, 2014). The glenohumeral morphometry of the native South African population has been rarely studied. Along with this, considering the financial burden and the country's geographic location, there is a need to carve a niche for medical implant industry in the country. The aim of this chapter is to describe the process implemented to retrieve and compare the GH joint morphometry of two cohorts belonging to two geographically independent regions. One of the subsets, representing sub-Saharan Africa, was sourced from the South Africa and the other subset, representing Europe was sourced from Switzerland.

Worldwide, 21% to 32% of the TSAs have to be revised due to post-surgical complications like glenoid loosening (Bohsali et al., 2006; Bonnevialle et al., 2013; Hill & Norris, 2001; Junaid et al., 2010). As explained in Chapter 1.4, the *"rocking horse"* effect has been identified as one of the main causes for glenoid loosening (Matsen III et al., 2008; Wirth et al., 2012). Improper understanding of the shoulder anatomy, which varies with the geographical location of the population (Cabezas et al., 2016; Matsumura et al., 2016; Zhang et al., 2016), might result in ATSP designs which do not replicate the optimum GH morphometry. This could reduce the efficacy of the surgery and its long-term success (Bonnevialle et al., 2013; Hertel & Ballmer, 2003; Merolla et al., 2013). The morphometric studies referred to, for the earliest designs of unconstrained ATSP did not consider the GH morphometry of African population. In the light of the above reasons, it could be considered essential to study the native population of this country and incorporate any distinguishing features to create an ATSP design.

2.2 Anatomy of the Glenohumeral Joint

The GH joint articulation (Fig. 2.1) could be geometrically represented as a ball and socket joint made up of the humeral head and the glenoid fossa. Unlike the hip joint where the acetabulum almost engulfs the femoral head, the glenoid fossa on the lateral edge of the scapula is an open structure and provides limited conformance to the head of the humerus. The high range of motion is partly due to the fact that the glenoid fossa, does not resist the translation and rolling of the humeral head (Halder et al., 2000).

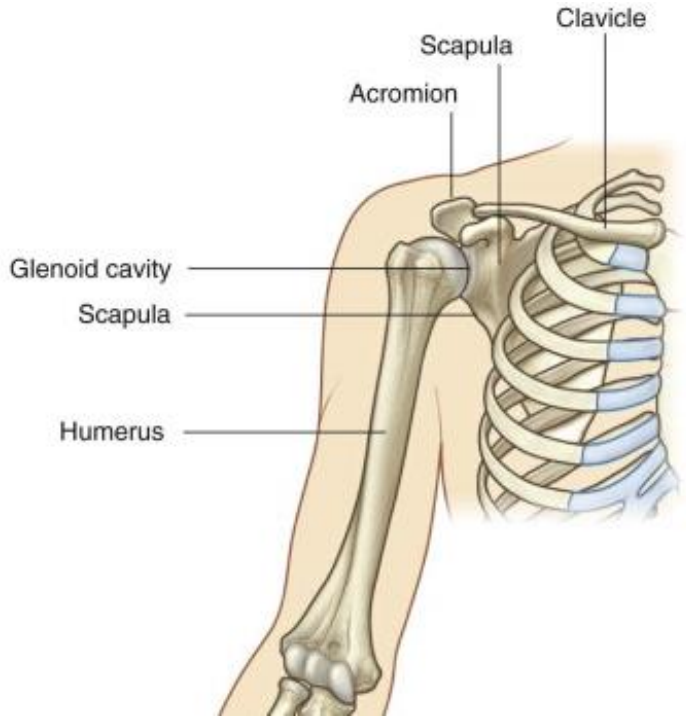

Figure 2.1 The Glenohumeral (GH) joint formed by the glenoid fossa and the humeral head articular surfaces. *Sourced from* (Drake et al., 2015).

The stability of the joint is by the virtue of the surrounding soft tissues like the rotator cuff muscles, the glenoid labrum, the joint capsule and the reinforcing ligaments. These structures support the glenoid and the humeral head articulation and prevent subluxation under loading (Fig. 2.2 a-b). As explained earlier, the complete RoM of the shoulder is due to the complex coordinated interactions of the GH, the SC, the AC and the ST joints (Brand, 2011; Skirven, 2011). In a healthy shoulder, the initiation of the loading or movement is from the

GH joint and it contributes to around 65% of the total RoM (Brand, 2011). Therefore, it becomes the most important load-bearing articulation in the entire shoulder girdle.

The glenoid cavity (Fig. 2.3 a-b) is concave in shape and has a 7.4° of retroversion and is tilted by 10° in the superior direction(Halder et al., 2000). The superior tilt is altered by GH arthritis (Daggett et al., 2015). The glenoid fossa has a deeper concavity in the superior-inferior (SI) axis and has a shallower surface when viewed from the anterior-posterior (AP) axis. The horizontal distances between the AP margins increase as one comes down from the supra-glenoid tubercle towards the infra-glenoid tubercle. Therefore, anatomically, the glenoid is thicker and broader inferiorly (Iannotti et al., 1992; Mamatha et al., 2011). This makes the glenoid a pear-shaped structure. Various other glenoid shapes, like the oval and the inverted comma, have been reported in the literature but the pear-shaped glenoid are more common (Mamatha et al., 2011).

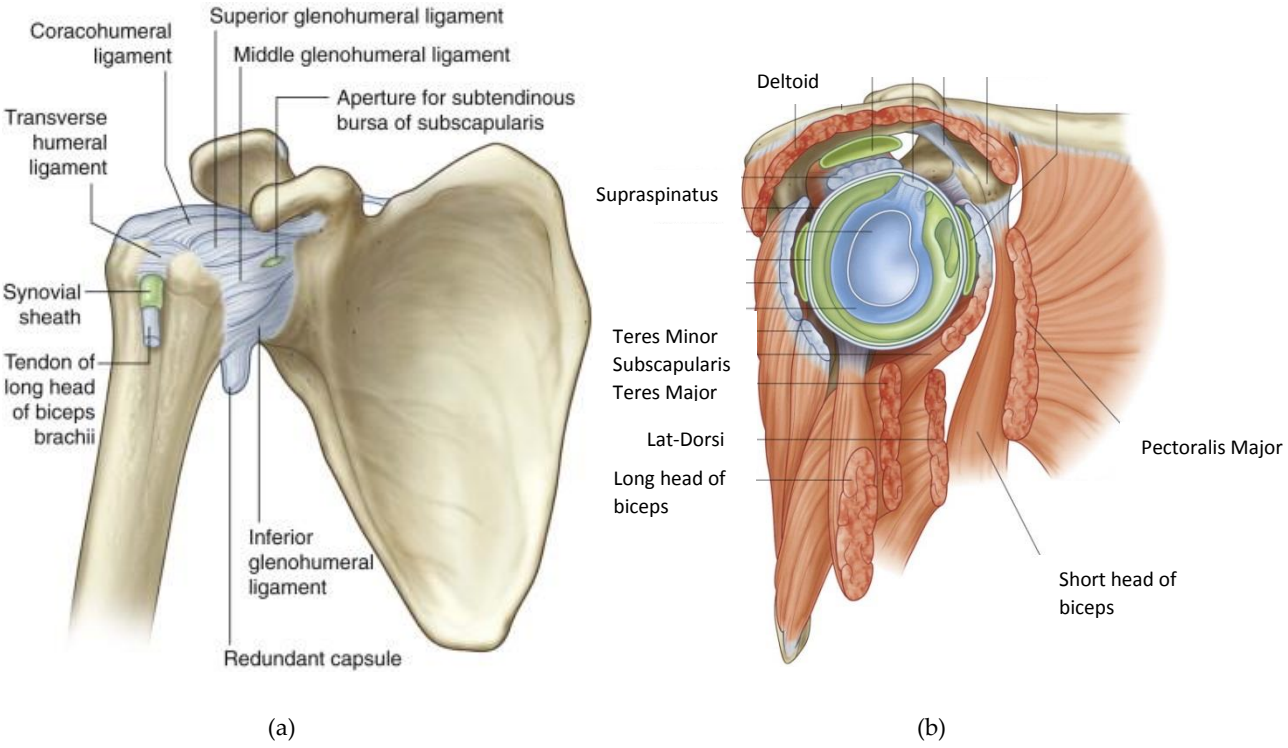

Figure 2.2 The soft tissues around the glenohumeral articulation stabilizing the joint. (a) Joint capsule and ligaments; (b) Surrounding muscles. *Sourced from* (Drake et al., 2015).

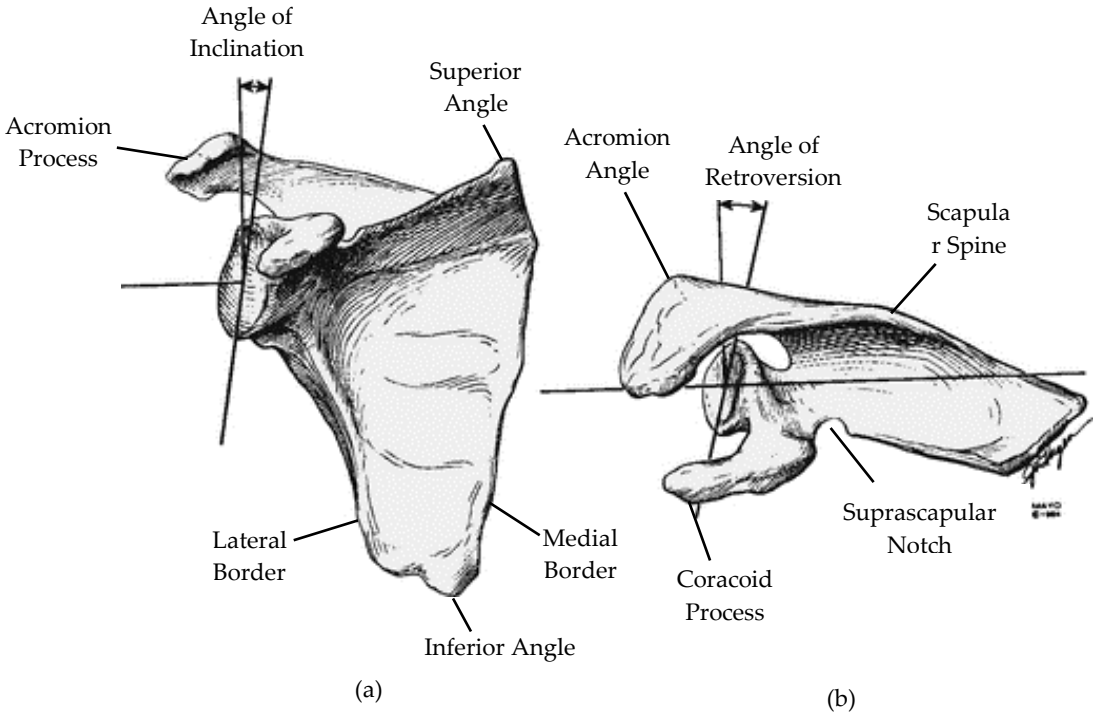

Figure 2.3 Schematic representation of various bony landmarks of the scapula and the (a) superior and (b) medial tilt of the glenoid fossa with respect to the straight line passing through the center of the glenoid. *Modified from* (Halder et al., 2000).

The surface area of the glenoid fossa is 30% to 40% less than that of the humeral head. The glenoid labrum around it increases its depth, adding stability to the joint (Halder et al., 2000; Skirven, 2011). A study (Zumstein et al., 2014) showed that the cartilage around the glenoid was the thickest in the superior region and very thin in the inferior region. On an average, the RoC of the glenoid cavity was found to be 60% larger than the humeral head RoC.

The humeral head (Fig. 2.4) projects, medially and superiorly, out of the humeral shaft and translates on the surface of the glenoid. It is ovoid in shape, has 30° to 40° of retroversion with a superior tilt of 45° (Fig. 2.5 a-b). The anterior-posterior concavity of the humeral head is greater than the superior-inferior concavity (McPherson et al., 1997). It has more than half of its surface area covered with articular cartilage. The articular cartilage is the thickest in the central region and thinnest in the periphery (Zumstein et al., 2014). This opposite cartilage thickness properties of the GH articular surfaces allow for a greater conformity between them and reduces the probabilities of dislocations. The neck joining the shaft and the head is very small, therefore the lack of bony conformity around the head is advantageous for the GH joint

and allows it to help extend the arm in multiple planes (Halder et al., 2000; Peltz et al., 2015). The center of the proximal humeral head sphere has a medial and posterior offset of an average of 6.9mm and 2.6mm respectively (Fig. 2.6), with respect to the humeral shaft axis (Boileau & Walch, 1997). The rotational movement of the humeral head on glenoid is permitted by conformance of the structures in the SI aspect.

Figure 2.4 The anatomy of the proximal humeral head. *Sourced from* (Drake et al., 2015).

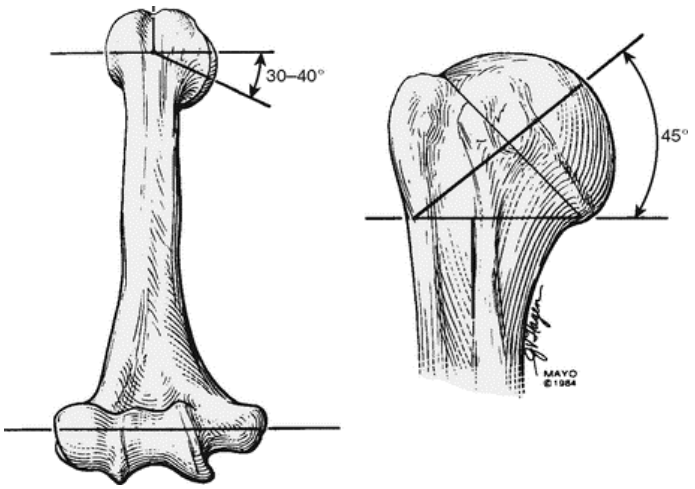

(a) (b)

Figure 2.5 The morphometric features of (a) humeral head retroversion and (b) humeral head inclination. *Sourced from* (Halder et al., 2000).

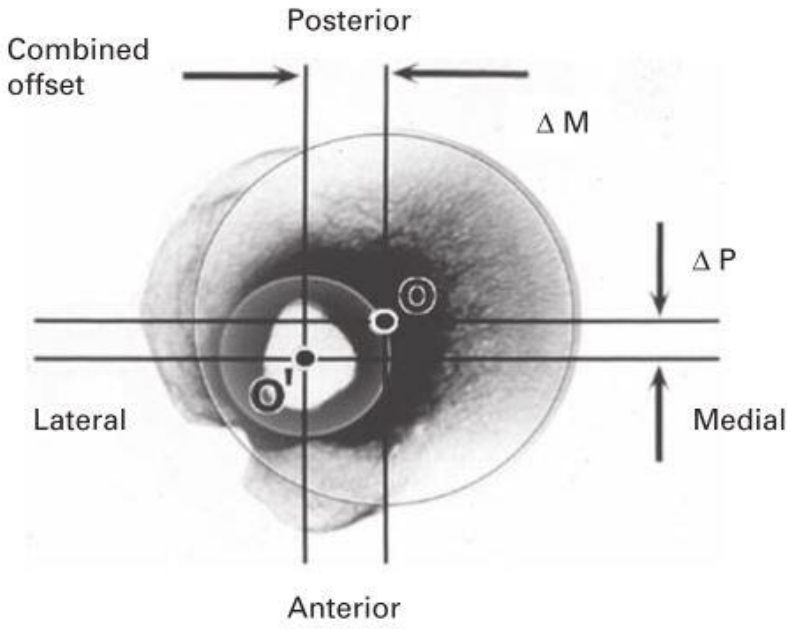

Figure 2.6 The humeral head offset. The medial and the posterior offsets are calculated as the distance between the humeral head center 'O' and the humeral shaft center 'O' in their respective axes. *Sourced from* (Boileau et al., 2006).

2.3 Need for Understanding Inter-Population Morphometric Variations

Every individual human being is different. Some of these differences are easily identified by their appearance, their habits and their way of living. Based on these differences it could be safe to group many individuals into populations arising from a geographical location. Some studies have gone deeper into investigating these populations' skeletal morphometry and have concluded that there is more inter-population variation than it meets the eye (Ousley et al., 2009; Ubelaker & DeGaglia, 2017).

Inter-population variance has been established in several skeletal structures, such as, in facial structure (Vioarsdottie et al., 2002), shape of the cranium (Donlon, 2000), humerus (İşcan et al., 1998), pelvis (Kurki, 2013), femoral head diameter (Ubelaker & DeGaglia, 2017), mandible (Loth & Henneberg, 1996), etc. Hence, it could be expected that the humeral head and glenoid cavity might also have inter-population differences. Only two studies were found to investigate the humerus (Steyn & Işcan, 1999) and the scapula (Churchill et al., 2001) of

African population and compare them to their non-African counterparts, belonging to the same country. Few limitations could be identified from the above-mentioned studies, firstly, these studies did not make use of more precise automatic morphometry measuring techniques and secondly, the accuracy of the inter-population differences observed might have been reduced since the entire cohort belonged to the same geographical location.

As we steadily progress towards TSA design modification to achieve better post-operative performances, it might be justifiable to expect that the shoulder implant might follow the same evolution path adopted by hip (Coigny et al., 2016; Jun & Choi, 2010) and knee (Slamin & Parsley, 2012) implants, in becoming subject specific. With that in mind, it might be beneficial to initially investigate and develop shoulder implants addressing the population-specific variations. Population-specific prostheses might prove to be a cheaper alternative to a personalised prosthesis in a developing country.

GH sexual dimorphism has been repeatedly reported in the literature (Churchill et al., 2001; İşcan et al., 1998; Kranioti & Michalodimitrakis, 2009; Mckenna, 2017; Merrill et al., 2009; Papaioannou et al., 2012; Steyn & Işcan, 1999). As far as the glenoid is concerned, most of these studies are focused on the height and the width of glenoid fossa (Churchill et al., 2001; Mamatha et al., 2011; Mckenna, 2017; Papaioannou et al., 2012). The current study would focus on RoC of the glenoid and its relationship with the humeral head.

The variation of the glenoid fossa and proximal humeral head morphometric features crucial for ATSP design. These parameters have been rarely studied to determine morphological differences among populations. There are limited anthropometric data available regarding sub-Sahara African GH joints. This could lead to an inaccurate sizing of the implant, giving rise to post-surgical complications. Considering these factors, the current chapter is focused on comparing the GH joint morphology of two geographically distinct populations using an automatic method of morphometric feature extraction.

2.4 Feature Extracting Pipeline (FEP) for measuring the shoulder articular surfaces

2.4.1 Population under study

To detect distinguished morphometric features of Sub Sahara African GH joints it was important to select two geographically distinct population groups for comparison. A Caucasian and a non-Caucasian group of cadavers were selected from Switzerland and South Africa respectively.

A database of 90 GH joints (average age 50.9 ± 17.9 years) was created from upper body (hip and above) Computerised Tomographic (CT) scans of embalmed cadavers. The Swiss scans were digitally sourced from the SICAS Virtual Skeleton Database (VSD) (Kistler et al., 2013) and the South African scans were performed at the Division of Radiology, University of Cape Town (UCT) on the cadavers sourced from the Department of Anatomy, UCT.

Among the 90 shoulders, 45 belonged to the Swiss dataset (CH) and the remaining 45 belonged to the South African dataset (SA). The CT scans were inspected, and any scan that was found to have a deformed GH articular surface due to the formation of a bone spur and/or fracture was excluded. Out of the 90 scans, 2 scans from each data set were excluded due to such findings. This reduced the number of shoulders to 88, on which this morphometric study was performed. The demographic details of the two data sets are provided below in Table 2.1.

Table 2.1 Information of the CT scans used for this study

	Swiss Data Set	**South African Data Set**
Racial Distribution	Caucasian	Non-Caucasian
Acquired from	The SICAS Medical Image Repository	University of Cape Town Cadaver Lab
Age in years	53 years (19 to 90)	49 years (20 to 82)
Male : Female	20:25	26:19

2.4.2 Three-dimensional (3D) GH joint reconstruction

The entire data set of the CT scans were individually exported to Materialise Mimics® (Materialise, Leuven, Belgium) in a process previously implemented by Bryce et al., 2008. Mimics® is an image processing software platform which allows auto-segmentation of human bones according to a pre-set greyscale value (Fig. 2.7). This technique was applied to segment out the bony structures such as the thoracic cavity, the clavicle, the humerus and the scapula. The region of interest (RoI) for this study was the bones forming the GH joint (Fig. 2.8 a), i.e. the humerus and the scapula. These two bones were separated from the rest of the scan area by using the crop mask feature. This feature enables to detach the RoI from the segmented 3D model of the thorax. Post detaching the scapula and the humerus, the common pixels that form a layer of attachment between the two entities (Fig. 2.8 b) were carefully removed and the bones were separated as two individual entities.

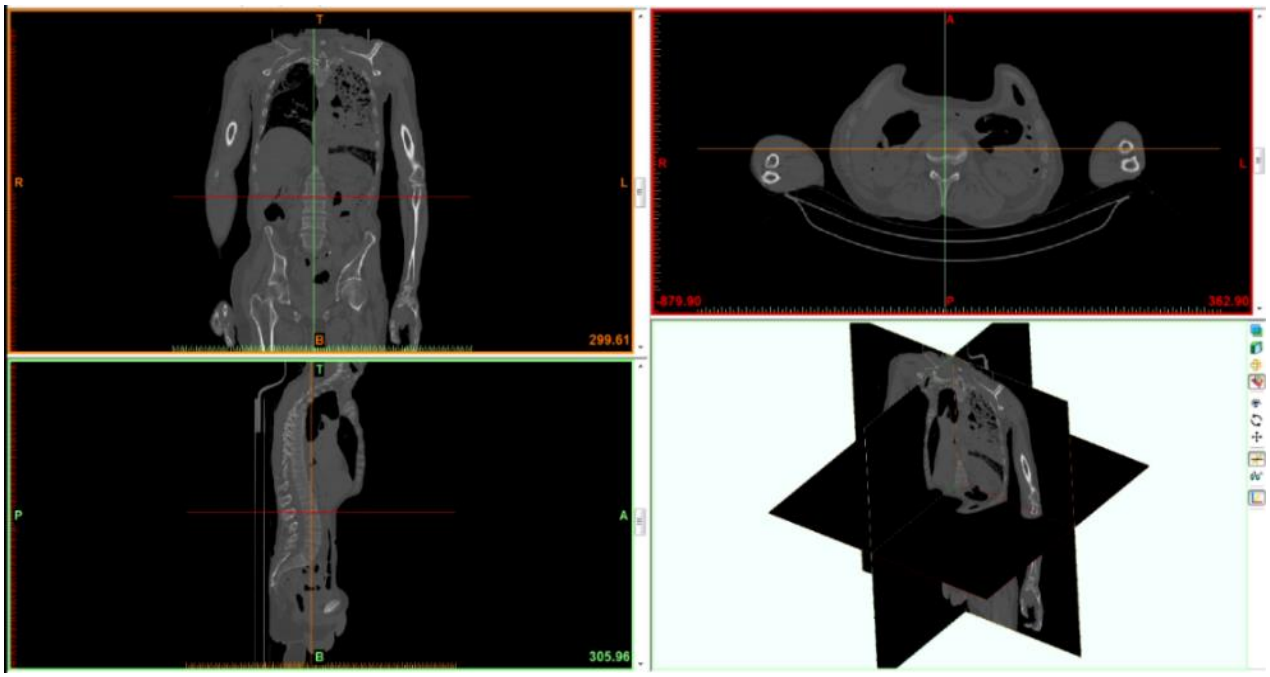

Figure 2.7 The platform of Materialise Mimics® which was used to convert the stacks of the two-dimensional (2D) Computerised Tomographic (CT) images of the bones into three-dimensional (3D) objects which were later used in this study to measure its morphometry.

The humerus and the scapula were exported from the Mimics® platform as binary steriolithographic (.stl) models (Fig. 2.9). These models represent the 3D reconstructed object

with point clouds with their x, y and z coordinates. In order to make the 3D humerus compatible to the computer-aided design (CAD) platform of SolidWorks (Dassault Systems, Velizy-Villacoublay, France), the number of triangles for each bone was reduced to below 20000 in an open source mesh processing software, MeshLab (Cignoni et al., 2008). Post reducing the triangles the humerus was imported back to SolidWorks where the *in-silico* TSA was performed.

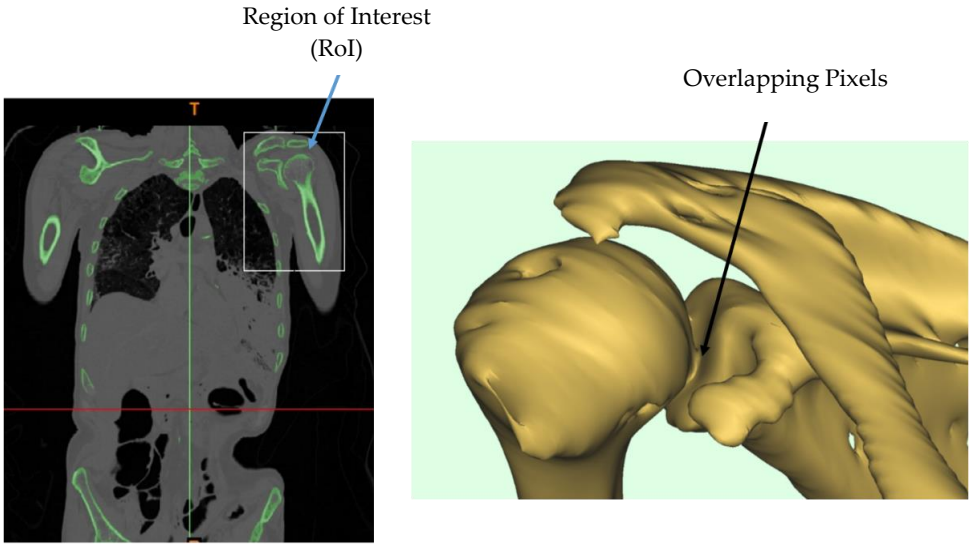

Figure 2.8 The region of interest (RoI), marked by the white rectangle, covered the lateral aspect of the scapula which included the glenoid fossa and the whole of the humerus; (b) The 3D reconstructed bones with highlighting the overlapping pixels between the articulating surfaces which were later removed.

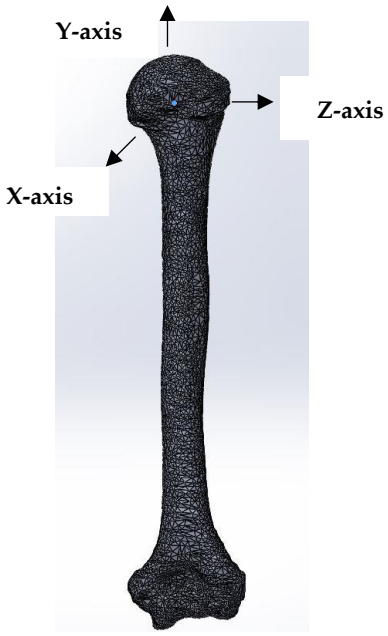

Figure 2.9 The humerus bone represented by clouds of triangles forming the 3D mesh. The coordinate system of the bone defined in accordance to the International Society of Biomechanics.

In Mimics® the inherent coordinate system is pre-defined. To perform the *in-silico* TSA, it was important to make a common coordinate system for every humerus. To achieve this the guidelines provided by the International Society of Biomechanics (ISB) was followed (Wu et al., 2005). The center of the humeral was selected as the origin; the perpendicular line joining the center of the straight line connecting the inferior condyles of the humerus was assigned as the y-axis; the x and the z-axes were assigned to the perpendicular lines propagating towards the anterior and medial aspects respectively (Fig. 2.9).

The Global AP® (Johnson and Johnson, DePuy) prosthesis was the product of choice of our clinical partner. Hence, the guidelines provided by the same manufacturers were applied to perform the TSA in SolidWorks under the guidance of an experienced shoulder surgeon. To mark the lateral and medial boundaries of the articular surface the point of bulge out and bulge in were marked (Fig. 2.10 a). A straight line was drawn joining these points underneath the articular surface. A common plane was formed between the inherent top-view plane of the platform the line joining boundary points. This plane was (Fig. 2.10 b) was called the cutting plane. This plane was used to create a rectangular section to recover only the articular surface. This process produced repeatable results which were comparable to the literature (Schaaf & Bell, 2008).

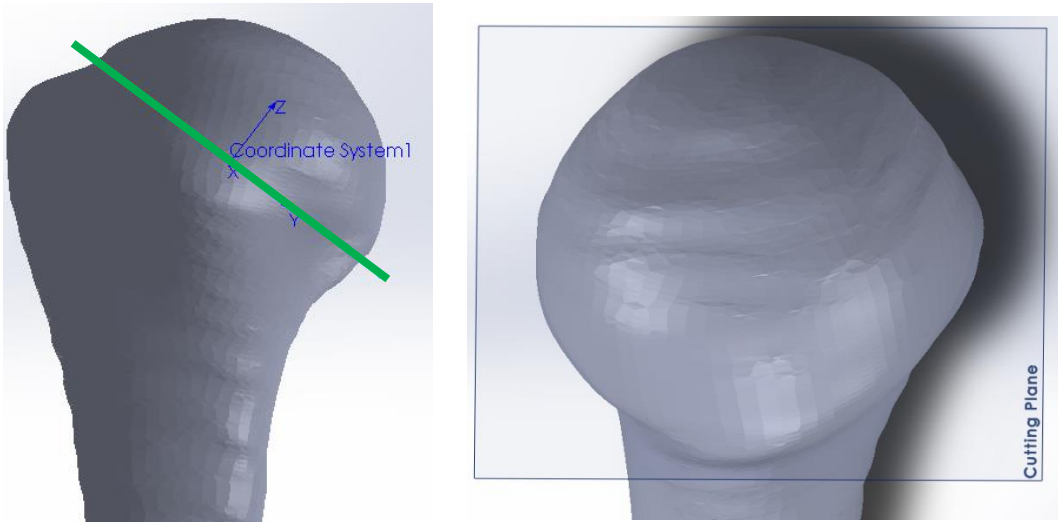

(a) (b)

Figure 2.10 (a) The surgical line which was drawn according to the specifications of the implant manufacturer; (b) The cutting plane was created using the surgical line, under the humeral head articular surface.

A separate coordinate system was assigned to the humeral head articular surface (Fig. 2.11). The center of the articular surface was selected as the origin; the z-axis was assigned to the central perpendicular line propagating towards the articular surface to the origin; The y-axis was assigned to the perpendicular line propagating towards the inferior (medial) aspect of the surface; the x-axis was assigned to the line propagating from the origin towards the anterior aspect (right humerus) and towards the posterior aspect (left humerus).The scapula was not modified in any manner as most feature extractions for the glenoid were performed within the Mimics platform.

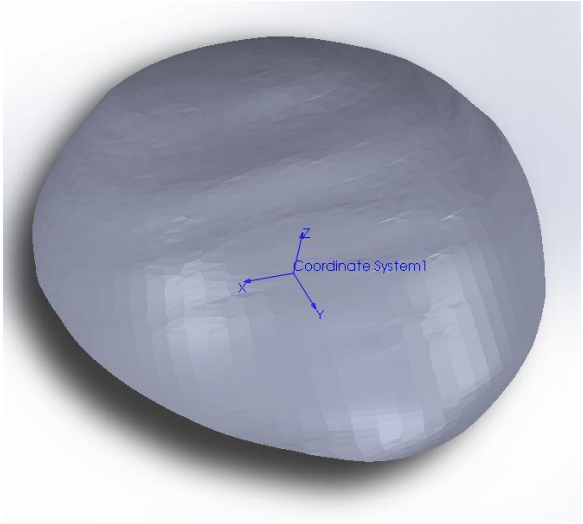

Figure 2.11 The humeral head coordinate system used to measure the morphometry of the humeral head.

2.4.3 The morphometric feature extracting technique

The Feature Extracting Pipeline (FEP) was built in MATLAB (MathWorks, Natick, MA, USA) and the features (Fig. 2.12 a-d) that were extracted are listed below along with their extraction techniques:

i. Humeral head circular diameter – To fit the best circle around the head the maximum diameter in the SI and the AP direction and the head thickness were calculated. Finally, the RoC was calculated using the formula (Eq. 2.1) given below. To access the maximum diameter in the AP and SI directions, a script was generated (Appendix A) which calculated the maximum distance from the

center of the head in the X and Y directions (Fig. 2.12 a). The best fit of the circle was ensured by the fact that the circle encompassed both the center of the head and the point of maximum diameter both in the SI and AP directions.

$$Humeral\ Diameter = 2 \times [(Height \div 2) + ((Base\ Width^2)/(8 \times Height))] \quad (2.1)$$

ii. Humeral head spherical RoC – An interactive script was generated using MATLAB to fit the sphere on the surface of the humeral head (Fig. 2.12 b). It was designed to be compatible with Materialise Mimics®. The script read the locus of minimum 15 points created to form a spline on the humeral head surface. These splines were created to cover the articulating surface of the head.

iii. Glenoid spherical RoC – A spline was created inside the glenoid cavity of the 3D segmented scapula in Materialise Mimics® (Fig. 2.12 c). The spline was segmented using a minimum of 15 points. The spline was drawn on the surface on the glenoid taking into account the inherent shape (pear, semi-colon or oval (Mamatha et al., 2011)) of the cavity.

iv. GH mismatch and conformity index – The RoC mismatch of the humeral head glenoid articular surfaces was calculated using the formula (Eq. 2.2). The conformity index (CI) was measured as the dimensionless ratio (Eq. 2.3) (Walch et al., 2002).

$$Glenohumeral\ Mismatch = Glenoid\ RoC\ - Humeral\ Head\ RoC \quad (2.2)$$

$$Conformity\ Index\ = Humeral\ Head\ RoC\ \div Glenoid\ RoC \quad (2.3)$$

v. Humeral height – To automatically extract the humerus height, the 3D model of the humerus was set-up such that the straight line joining the two condyles was assigned as the x-axis and the line perpendicular to the line joining the condyles and the highest superior locus of the bone was assigned as the z-axis. A custom code was generated to connect the most inferior and superior loci in the z-axis with a line passing through the geometric center of the line joining the inferior condyles of the humerus (Fig. 2.12 d).

vi. Humeral head thickness – The humeral height was calculated using a perpendicular line from the center of the humeral head to the humeral head articular surface, as shown in (Fig. 2.12 a).

vii. Humeral head peak points – This is a novel morphometric which is elaborated in the Chapter 3.

2.5 Statistical Tests Employed

The open source statistical software *R* was used to perform the statistical analysis. The observed data were separated, into various sub-datasets, according to their country of its origin (Swiss and South African), position in the body (Left and Right) and gender (Male and Female).

Shapiro-Wilk tests were performed to analyze the distribution of the observations for each of the parameters in each dataset. Along with the tests for normality, Quantile-Quantile (QQ) plots were generated to support the tests. To determine whether the observed differences, between the data sets, were significant, T-tests were performed for the normally distributed parameters and Wilcoxon Signed-Rank Tests on the rest. The level of significance was set at 0.05. A two-tailed post-hoc power analysis was performed for the two population and gender groups using G* Power v3.1 (Erdfelder et al., 1996; Faul et al., 2007, 2009). The α value for this analysis was set as 0.05.

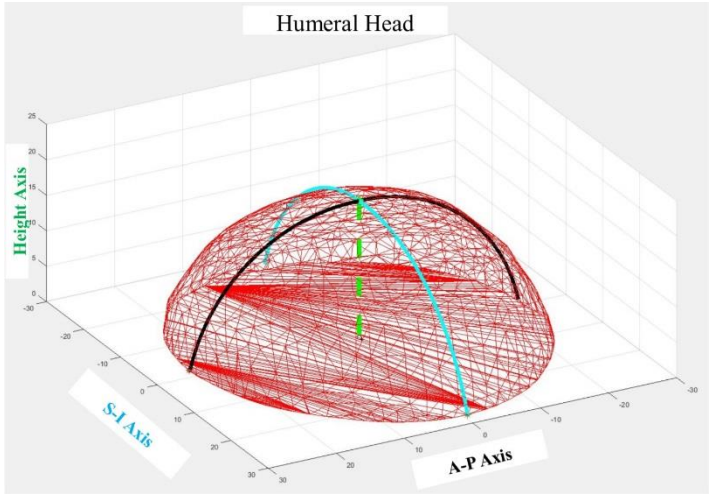

(a)

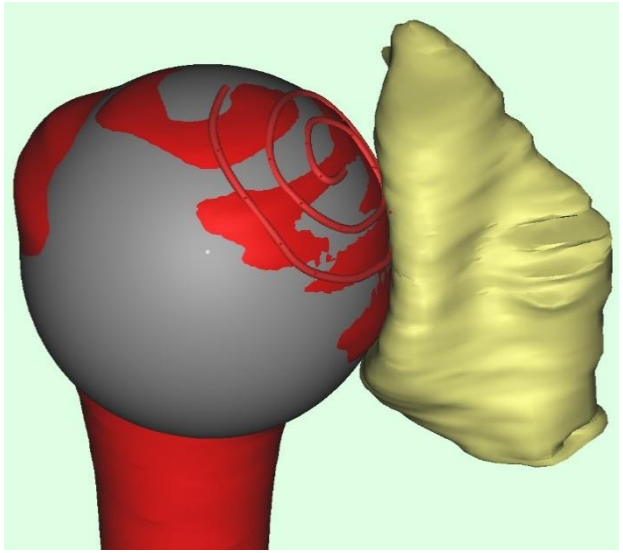

(b)

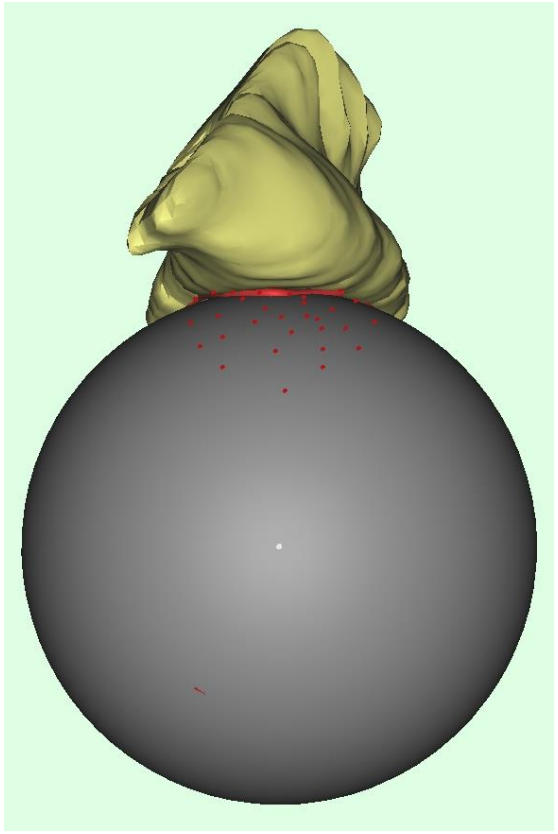

(c)

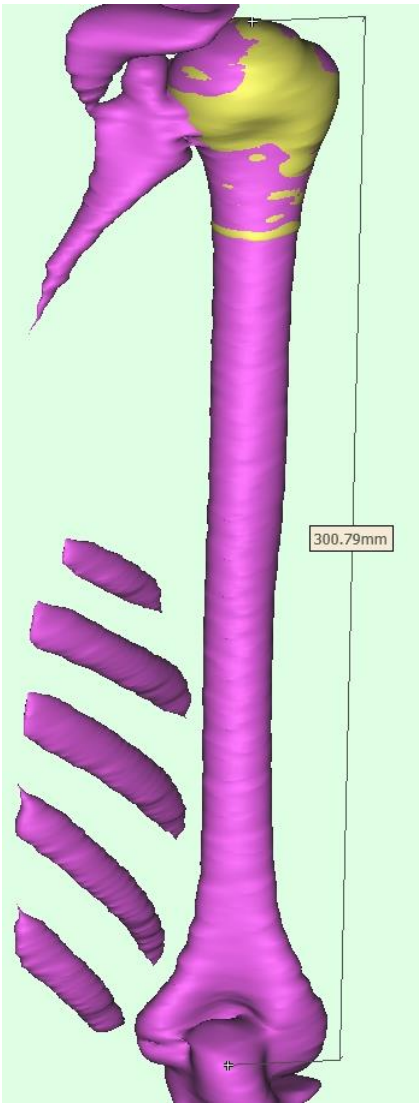

(d)

Figure 2.12 The measured morphometries of the humerus and glenoid. (a) The AP (black) and SI (blue) circular diameter and the thickness (green) of the humeral head articular surface; (b) Humeral head spherical RoC; (c) Glenoid fossa spherical RoC; and (d) Humeral height.

2.6 Observed Morphometric Variations

The results of the tests for normality are presented as QQ plots (Appendix B) for each of the measured parameters for every sub-data sets created. Most of the observed values were found to be distributed normally throughout the sub-datasets. The non-normal distributions were observed in Glenoid RoC for the SA, CH and Left sub-data sets. The CI and the humeral head thickness were observed to have non-normal distributions in the Right and Male sub-datasets respectively. The Female sub-cohort was found to have the most non-normally distributed parameters, listed as, SI circular diameter, Humeral height, Humeral RoC, Glenoid RoC, CI and GH mismatch. In this section, the results of the morphometric extraction process are elaborated into three different sub-sections.

These sub-sections, which were segregated according to the sub-datasets created earlier, discusses the morphometric variations in each of the parameters mentioned above. The observed average morphometric dimensions along with their average standard deviations are represented in Fig. 2.13 a-h. The sub-datasets which were observed to be significantly different are marked with an arrow and asterisk (*). The highest standard deviation was observed for the GH mismatch.

2.6.1 Inter-population variations

The average circular diameter in the AP and SI axis for the South African (SA) & the Swiss (CH) population were found to be 44.6 ± 4.1mm and 49.7 ± 4.5mm & 46.6 ± 3.5mm and 51.6 ± 4.6mm respectively. The observed difference in the AP direction was found to be significant ($P < 0.05$) but the difference in the SI direction was not significant ($P>0.05$). For the SA dataset, the 10^{th} and the 90^{th} percentile were found to be 39.2mm and 51.0mm, in the AP axis, and 43.7mm and 56.3mm, in the SI direction. Similarly, for the CH dataset, the 10^{th} and 90^{th} percentile in the two axes were found to be 41.9mm and 51.4mm & 45.0mm and 58.3mm respectively.

The average CH population was found to have larger spherical RoC (24.4 ± 2.5mm) for the humeral head but their glenoid RoC (30.3 ± 5.1mm) was smaller than that of the SA

population whose average humeral head RoC and glenoid RoC was measured to be 23.2 ± 2.6mm and 31.1 ± 3.9mm respectively. The difference in the humeral RoC was found to be significant (P<0.05) but the difference in glenoid RoC was not significant (P>0.05). The 10th and the 90th percentile for the humeral head RoC for the SA & CH populations were found to be 19.8mm and 26.4mm & 20.7mm and 27.6mm respectively. The 10th and 90th percentiles for the glenoid RoC for the SA & CH populations 26.2mm and 37.1mm & 24.3mm and 37.7mm respectively.

The average humeral height of the SA cohort was 323.4 ± 21.9mm. The 10th and the 90th percentiles were 292.2mm and 355.8mm. For the CH cohort, the 10th and the 90th percentiles of humeral height were 287.8mm and 344.2mm. The average CH humeral height was found to be smaller by 8.4mm with the average dimension being 315.0 ± 21.1mm. This morphometric difference was not statistically significant.

The average CH humeral head (19.5 ± 1.9mm) was found to be thicker than the average SA humeral head (18.9 ± 2.2mm) by 0.5mm. This observed difference was not found to be statistically significant (P>0.05). The 10th and the 90th percentile for the humeral head thickness were found to be 16.5mm and 22.2mm respectively, for the SA cohort, and 16.6mm and 22.3mm respectively, for the CH cohort.

SA GH joint had higher average RoC mismatch (7.9 ± 3.1mm) when compared to their CH (5.7 ± 3.9mm) counterparts. The average difference was about 2.2mm and this difference was found to be significant (P<0.05). The observed conformity index for both the populations was < 1, suggesting that the humeral head RoC was smaller than the glenoid RoC. The average conformity index for the CH population (0.8 ± 0.1) was higher than the SA population (0.75 ± 0.07) by a value of 0.06 and this difference was found to be significant (P<0.001).

2.6.2 Bilateral variations

The average circular diameter in the AP and SI axis for the left humeral heads were found to be 45.5 ± 3.9mm and 50.4 ± 4.6mm & 45.6 ± 3.9mm and 50.8 ± 4.7mm respectively. The average right humeral RoC was measured to be 23.7 ± 2.5mm and the average left humeral RoC was

measured to be 23.8 ± 2.8mm. The difference in the spherical RoC for the humeral head and the glenoid were < 1mm. The right humerus height (319.7 ± 22.5mm) and the humeral head thickness (19.4 ± 1.9mm) were found to be greater than the left humerus height and thickness (318.1 ± 21.3mm and 19.0 ± 2.3mm respectively) by 1.5mm and 0.3mm respectively. The glenohumeral mismatch and the conformity index were found to have similar values for the average right (7.0 ± 3.5mm and 0.7 ± 0.1) and the left (6.7 ± 3.9 and 0.8 ± 0.1) humerus. All the observed differences for the bilateral humerus were not statistically significant.

2.6.3 Gender variations

The average circular diameter in the AP and SI axis for the male and the female humeral heads were found to be 47.1 ± 3.1mm and 52.9 ± 3.5mm & 44.1 ± 4.1mm and 48.2 ± 4.5mm respectively. The differences in the SI (4.7mm) and the AP (3.0mm) were found to be statistically significant (for both the cases $P<0.001$). The average spherical RoC of the humeral head and the glenoid cavity were found to be greater for the male (24.9 ± 1.9mm and 32 ± 4.04mm) compared to females (22.6 ± 2.7mm and 29.4 ± 4.7mm) by 2.3mm and 2.7mm respectively. These differences were found to be significant ($P<0.001$ for humeral head RoC and $P=0.02$ for glenoid RoC). The humeral height and the humeral head thickness were larger for the males (327.9 ± 17.6mm and 19.7 ± 1.6mm) than the females (309.2 ± 21.8mm and 18.7 ± 2.4mm) and the observed differences were 18.7mm and 0.98mm respectively. The noted differences were significant ($P<0.001$ for humeral height and $P<0.05$ for humeral head height). The inter-gender difference between the glenohumeral mismatch, 6.8 ± 3.6mm for males and 6.6 ± 3.8mm for females, and the conformity index, 0.8 ± 0.1 for males and 0.8 ± 0.9 were found to be not statistically significant.

The observations suggesting no bilateral variation and distinct inter-gender variations in the GH morphometry match with previously reported studies (Churchill et al., 2001). A human body has symmetric bone geometry and hence the absence of bilateral GH morphometric variations might suggest that there are no significant computing errors present in the morphometric analysis detailed in this chapter and further validating the methods.

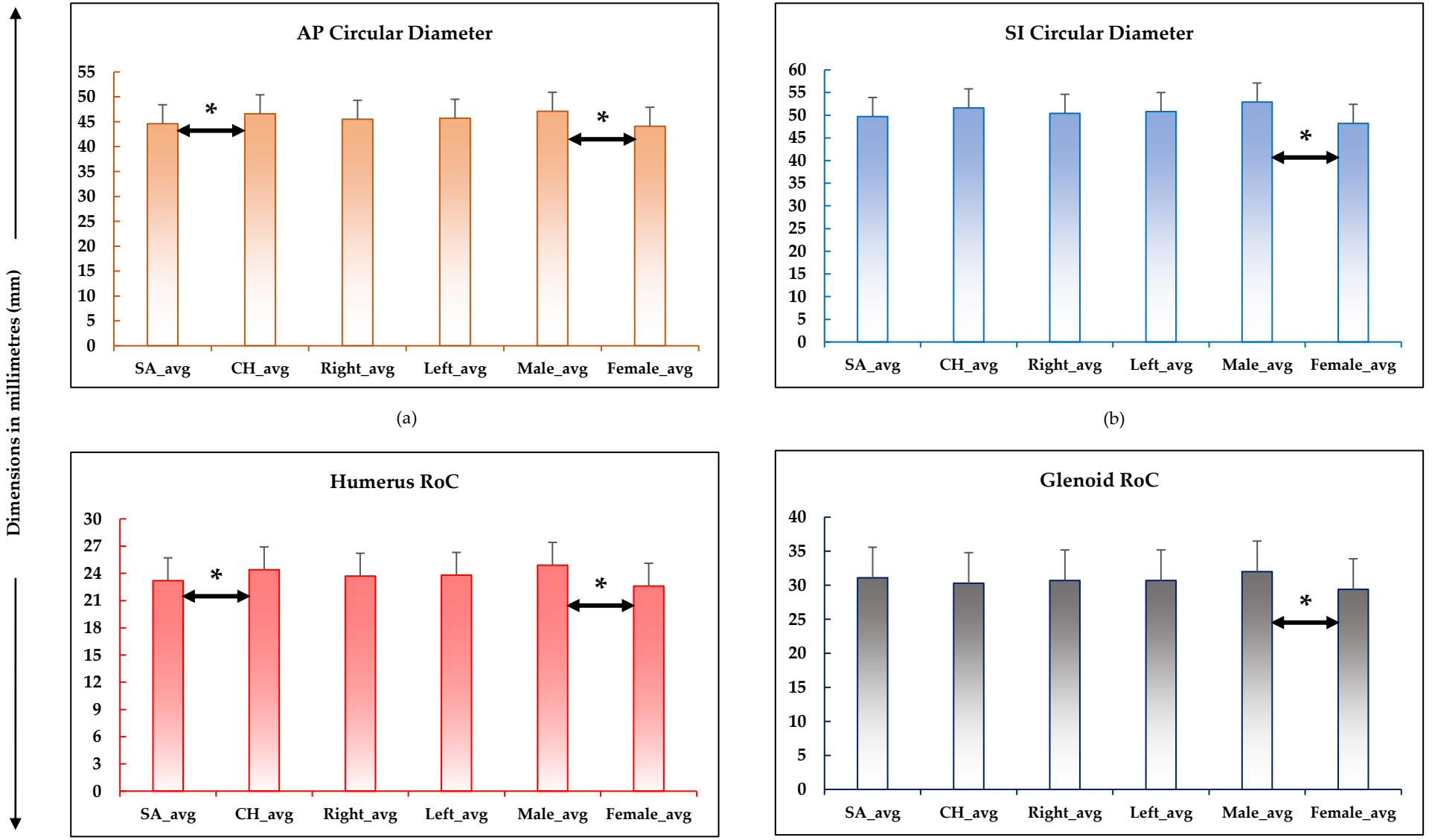

Figure 2.13 Observed average values and standard deviations of each morphometric parameter for every sub-dataset. The asterisk (*) refers to statistically significant differences between the groups on either end of the double-headed arrow. (a & b) AP and SI circular diameter respectively; (c & d) Humeral and Glenoid RoC respectively. (*continued in next page*)

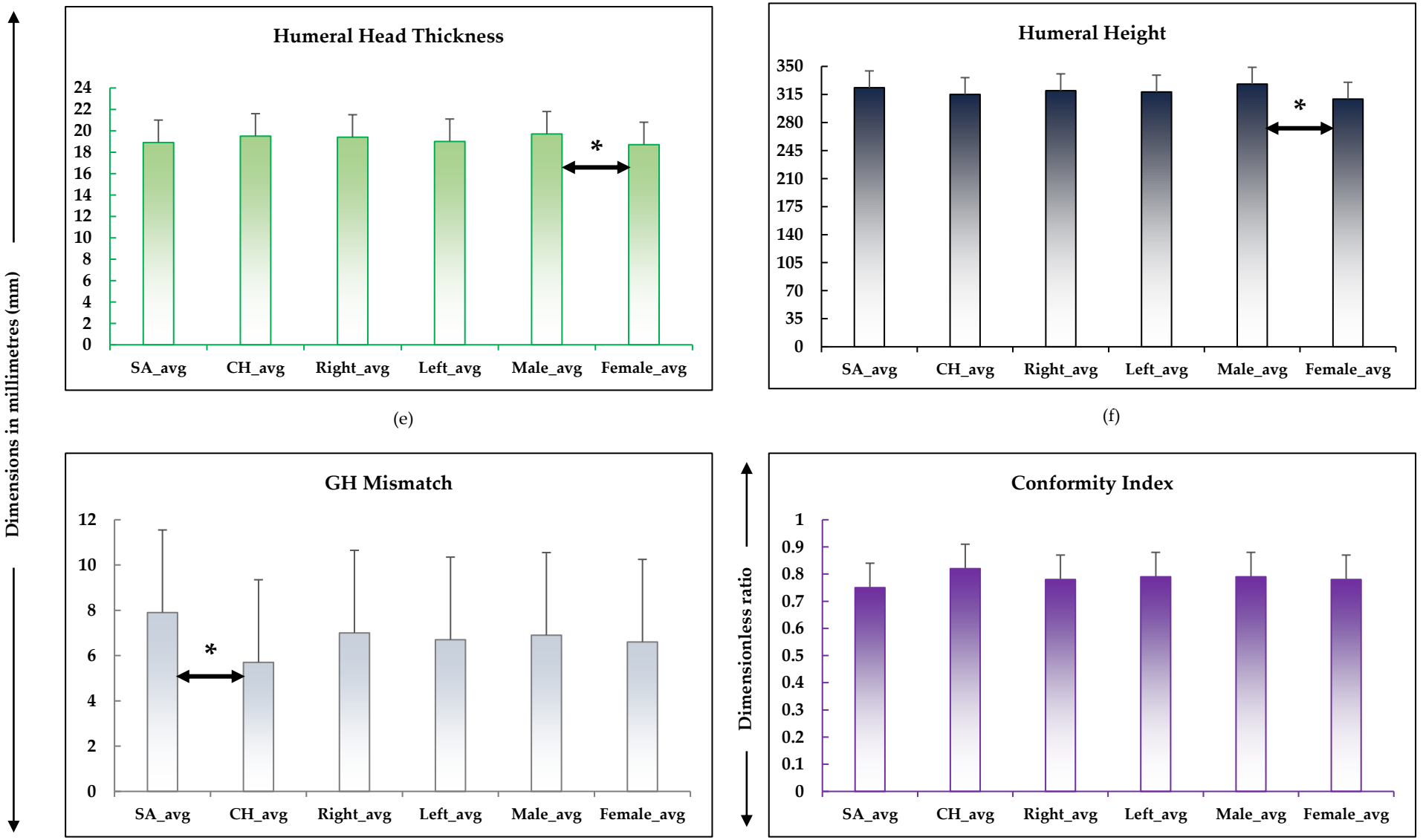

Figure 2.14 Observed average values and standard deviations of each morphometric parameter for every sub-dataset. The asterisk (*) refers to statistically significant differences between the groups on either end of the double-headed arrow. (e) Humeral head thickness; (f) Humeral height; (g) GH mismatch and (h) Conformity Index.

2.7 Discussion

Various authors (Boileau & Walch, 1997; Boileau et al., 2001; Bryce et al., 2008; Churchill et al., 2001; Green & Norris, 2001; Matsumura et al., 2016; Milner & Boldsen, 2012) have studied the underlying anatomy and the morphometric differences of normal and diseased (Humphrey et al., 2016; Knowles et al., 2016) GH joints. In the light of the current literature, it could be assumed that the morphometric variances between healthy GH joint of two different populations with an aim to develop a population-specific shoulder implant, in a process suggested by Aitchison et al., 2009, has not been extensively studied.

This chapter provides a detailed description of the morphometric evaluation of two geographically distinct populations, leading to findings of significant differences in the GH joint articulating surfaces between the populations under study. The post-hoc power analysis performed on the two population sets showed that the calculated differences had an effect size of 0.52 and the power to detect this effect size was 0.7. The analysis gave an estimate of the sample size (N ~ 58) per population set required to achieve a statistical power of 0.8 (Cohen, 1992). The inadequate sample size of the two data sets was a limitation of this study. For the gender groups, the calculated effect size for $\alpha = 0.05$ was 0.81, which can be considered a large effect (Cohen, 1992) and the power for this study to detect the effect was found to be 0.97. The observations from the CT scan data were not compared with corresponding radiographs and this could be considered as the second limitation of this study.

According to the literature humeral head has a dual curvature spherical geometry and its circular diameter vary in the SI and the AP axes (Humphrey et al., 2016; Knowles et al., 2016; Matsumura et al., 2016; Michael L Pearl & Kurutz, 1999). Similar variation in circular diameter of the head was observed in the current study. This validates the method applied in this study. Circular diameter of the humeral head provides a 2D measurement of the otherwise spherical surface. A recent study found that measuring the circular dimensions of the humeral head gives a better understanding of its morphometry (McPherson et al., 1997). Boileau & Walch, 1997, studied a group of 65 French humeri and found the average humeral

head diameter in the AP axis to be 46.2mm. In this study, it was found the average diameter in the same axis for the CH population to be 46.6mm (Fig. 2.14). This suggests that the European humeral articulating surfaces are of similar size. The average SA circular diameter and Humeral RoC was found to be significantly smaller than the CH group (Fig. 2.14).

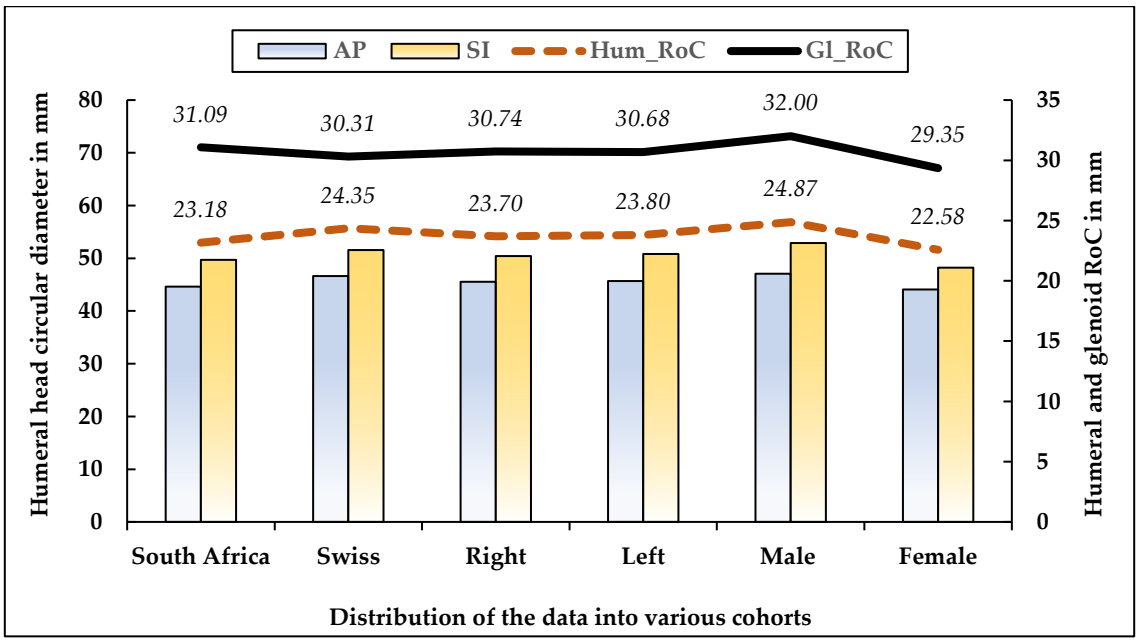

Figure 2.15 Overall distribution of humeral head circular diameters in AP and SI axes and the RoC of humeral head articulating surfaces and the glenoid fossa for the various cohorts studied.

One of the forensic studies had reported that individuals belonging to the South African population of European Descent (SAED) group have larger humeral heads than the rest of the population (Steyn & Işcan, 1999). The average humeral articular surface diameter of a set of Chinese humerus was reported to be 42.9 ± 3.6 mm (Zhang et al., 2016) which is very similar to the Japanese population (Matsumura et al., 2016) but lower than the average SA and CH articular surface diameter. This suggests that there exists a distinct variation in humeral head sizes among populations originating from different geographic locations. Extensive studies have not been performed on studying the GH surface geometry of the Sub-Saharan population, hence it could be assumed that the current design of the ATSP is based on the European and American samples. The current study might be able to fill the existing knowledge gap.

It is advantageous to compare the correlation of morphometric parameters. This could aid in determining the consequences of altering any prosthetic design feature on a related morphometric parameter. It is evident from the literature that the humeral RoC has a strong correlation with the glenoid RoC (Iannotti et al., 1992) and a similar trend could be observed from Fig. 2.14. In this study, the humeral head thickness was compared to the AP & SI circular diameter of the humeral articular surface, the humeral RoC and the height of the humerus. This comparison was performed for SA, CH, male and female sub-groups. The bilateral groups were not considered in this comparison as no significant differences, in the studied morphometries, were observed in between the groups. The best-fit regression lines comparison for the populations and genders are shown in Fig. 2.15 and Fig. 2.16 respectively.

Positive correlation, of various strengths, was observed for all the plotted data suggesting that the increase in humeral thickness resulted in an increase in the other morphometric parameters for all the cohorts. Humeral head thickness was found to vary significantly in between genders but variance observed between the populations studied were not statistically significant (Fig. 2.13 e). The calculated correlation coefficient (R) values for the regression lines were observed to be highly varied between the genders but not so much between the populations, justifying the earlier observations.

The humeral height was observed to not have a strong correlation with the head thickness with the coefficient of correlation (R) values of 0.054 (male), 0.44 (female), 0.44(CH) and 0.39 (SA). Among the studied cohort, males were observed to have the weakest correlation coefficient values 0.42 (Thickness vs RoC), 0.36 (Thickness vs SI diameter), 0.44 (Thickness vs AP diameter) and 0.054 (Thickness vs Height). Moderate (R>0.5) to strong (R>0.7) correlation was observed for the rest of the regression plots. Knowles et al., 2016, observed a significant decrease in the correlation, from strong to very weak, between the SI and the AP circular head diameter when healthy and osteoarthritic subjects. were compared. The observed value of R between SI and AP circular diameter for humeral heads was strong for both the gender groups, R=0.83 of males and R=0.84 for females (Fig. 2.17) confirming that the studied humeral heads were obtained from only healthy GH joints.

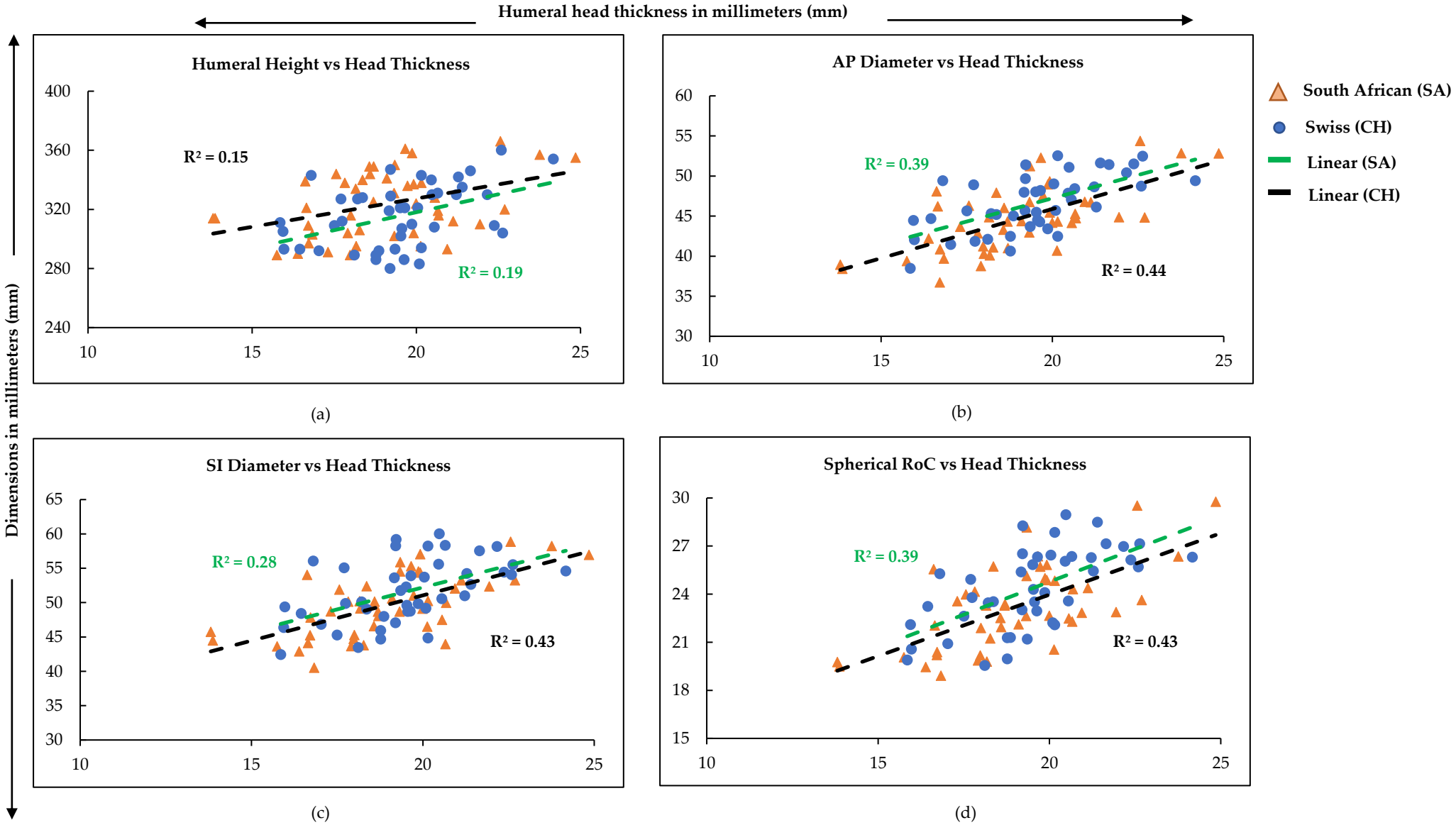

Figure 2.16 Scatterplots describing the relationship between the humeral head thickness and (a) humeral height; (b) AP diameter; (c) SI diameter; and (d) Spherical RoC comparing the South African and the Swiss populations.

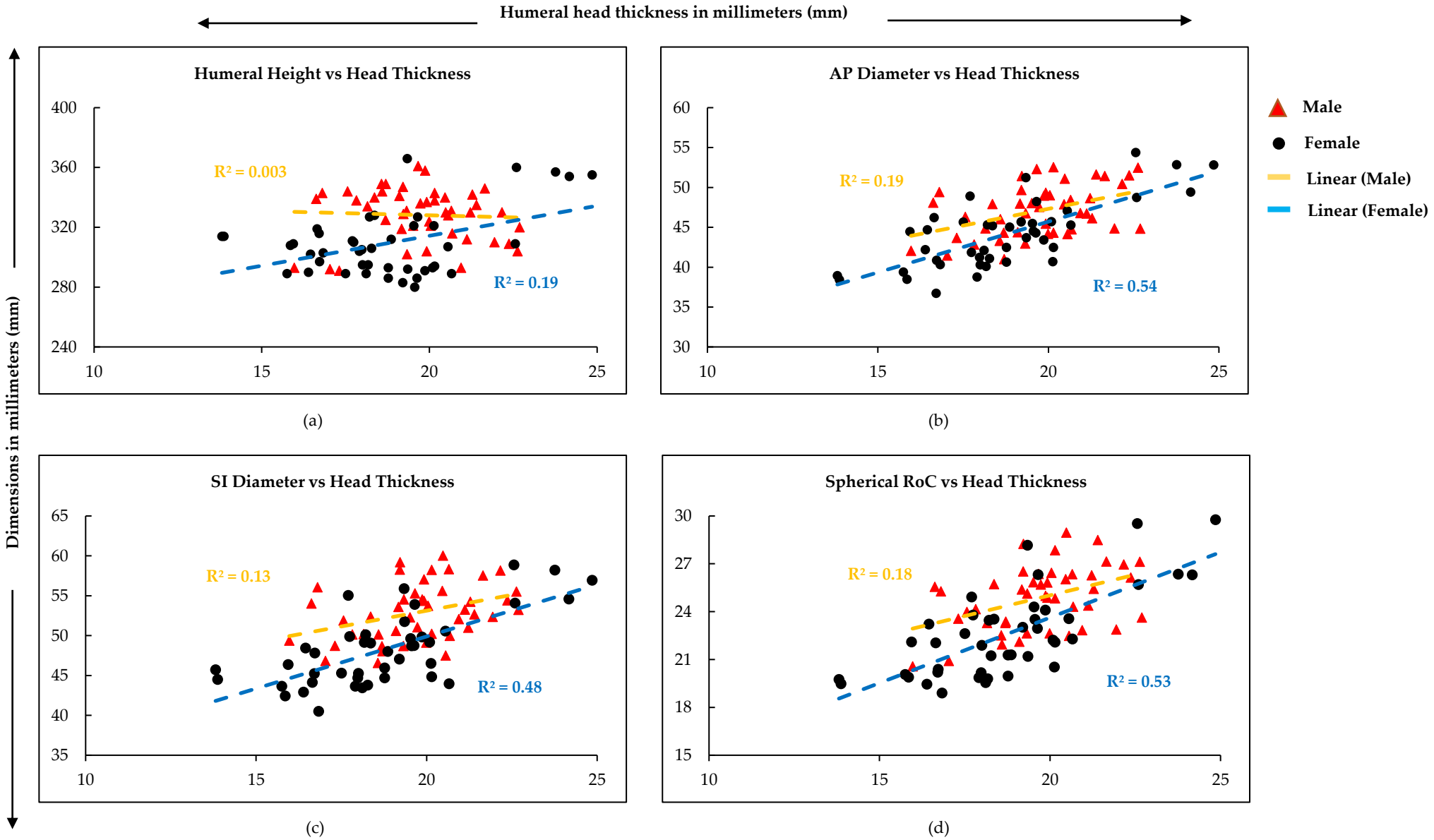

Figure 2.17 Scatterplots describing the relationship between the humeral head thickness and (a) humeral height; (b) AP diameter; (c) SI diameter; and (d) Spherical RoC comparing the male cohort and female cohort.

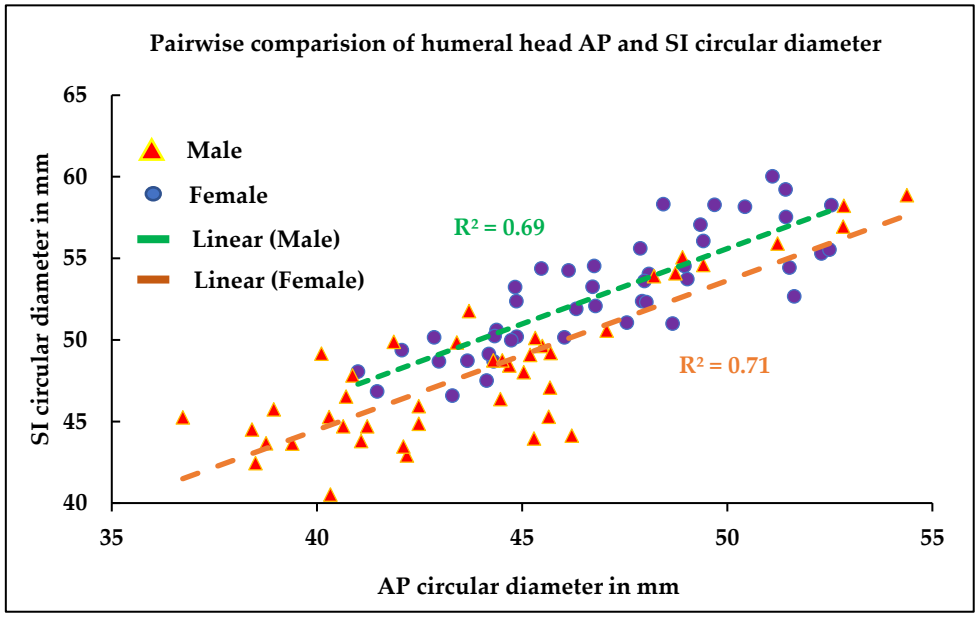

Figure 2.18 Scatter plot describing the relationship of the AP and SI circular diameter of the humeral head articular surfaces belonging to the females and males.

The commercially available humeral head prostheses are designed with various options of RoC and thickness as plotted in Fig. 2.18. Along with the commercially available prostheses, the regression lines, that best represent the relationship between the head RoC and head thickness, for the SA and CH cohorts were also plotted. The population-specific regression lines were compared to prosthetic humeral head sizes sourced[1] by Global AP® (De Puy, 2013); Vectis (Elite Surgicals, 2017); UNIC (Evolutis, 2016); Equinoxe® (Exactech, 2017); Arrow® Prime (FH Ortho, 2017); Cofield 2 (Smith and Nephew, n.d.); Reunion® (Stryker, 2017); Aqualis Ascend TM (Wright Medical Group Inc., 2016); Biomet® (Zimmer, 2009).

In the current study cohort, 8 out of the 88 humeral heads were discovered for which no commercially available humeral head prosthesis exists. The sizes of the head that are most commonly available range between 20mm & 28mm, in terms of RoC, and 15mm & 21mm, in terms of thickness. There exists only 3 implant manufactures who provide prosthetics humeral heads with <20mm RoC and there are no manufacturers which cater to the required dimensions for individuals having humeral heads >28mm RoC. Though the Cofield II prosthesis provides one prosthesis with RoC of 29mm, its thickness renders it not to be a

[1] This study was not funded by any of these shoulder prostheses manufacturers.

proper fit for the available joint space. It is evident from Fig. 2.19 that the average thickness of the articulating surface does not drastically change as the manufacturers may assume. The prostheses Global AP®, Aqualis Ascend™ and Reunion® were found to have a better potential to fit the joint space of the population studied. The Fig. 2.18 also suggest that the currently available ATSPs might be able to cater for both the average SA and CH populations but not for the possible outliers.

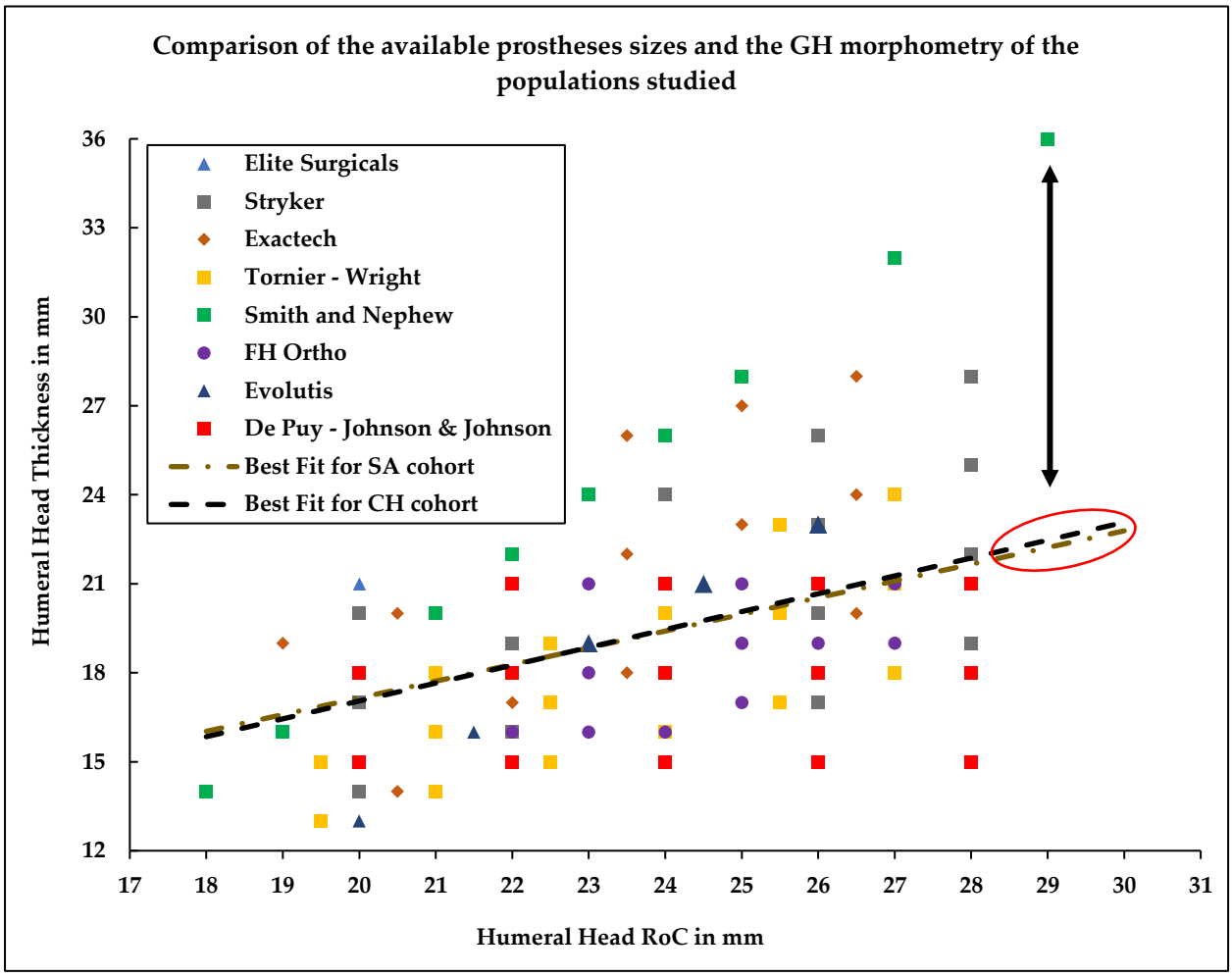

Figure 2.19 Graphical representation of the commercially available sizes of humeral heads from different manufacturers and their comparison of the best-fit regression line between the humeral head articular surface RoC and humeral head thickness calculated for both the populations under study. The best fit regression line for both the population cohorts under study were very similar. This might suggest that the current ATSP designs might cater for both the populations. The red circle highlights the range of humeral head sizes for which there are a limited amount of adequately sized prostheses available commercially. The black double-headed arrow represents the mismatch in size between the biological humeral head and its closest available humeral head prosthesis, in cases, the humeral RoC is >28mm.

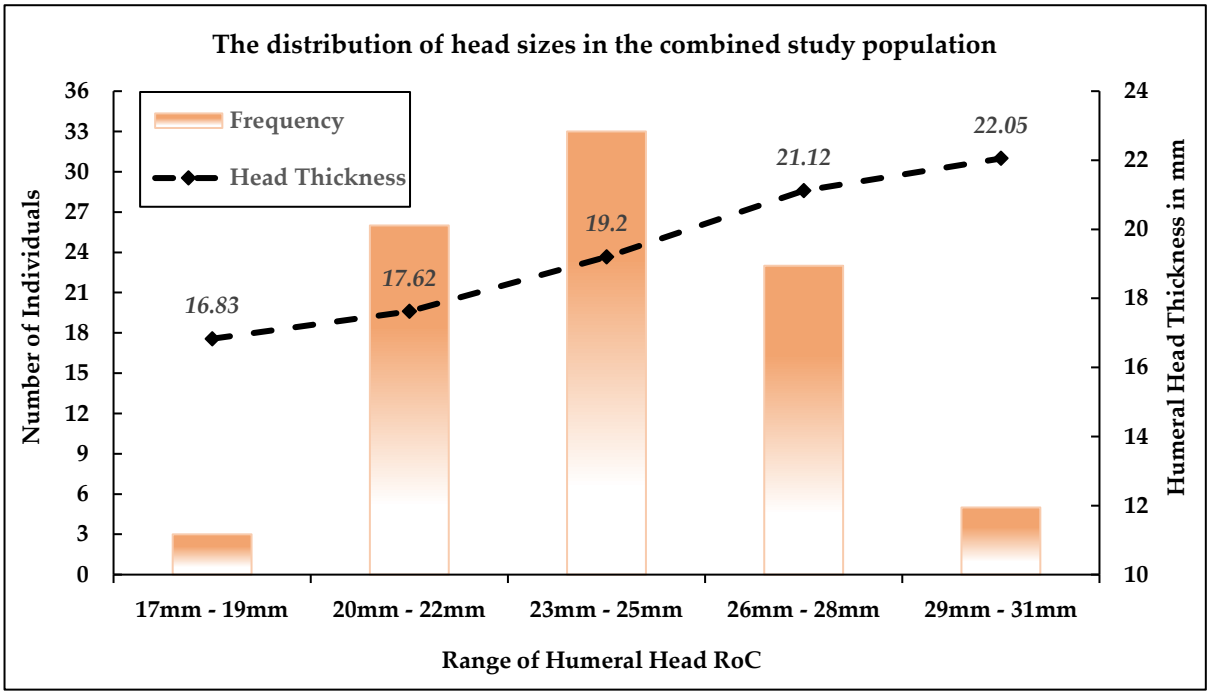

Figure 2.20 The histograms represent the number of subjects falling in the pre-set range of humeral head sizes and the variation of average humeral head thickness in the whole study cohort.

The average ratio of the SI and AP base widths (SI_w and AP_w) of the humeral head was found to be 1.09 for the whole data set and the geographic location of the shoulder did not have any effect on this. The ratio increased with the increase in the AP and SI circular diameter as reported in Humphrey et al., 2016. The average difference in the SI_w and AP_w was 4.07 ± 1.9mm, this average mismatch increased to 5.23mm when the SI_w was >52mm. Majority of the humeral head prostheses are designed with an identical AP and SI base width. The observations from this study suggest that the AP_w and SI_w are unequal and when the size of the humeral head is >48mm the base width ratio is >4. This is a design criterion that might have been overlooked until now. The possible effect of this elliptical nature of the humeral head base will be presented in the next chapter.

Variation in humeral head size is a better discriminating parameter between males and females, compared to femoral heads (Mckenna, 2017; Milner & Boldsen, 2012; Papaioannou et al., 2012). This study found that the average male humeral head circular diameter and the spherical RoC of both the head and the glenoid were significantly larger than their female counterparts. This is in-line with the past studies (Humphrey et al., 2016; Owaydhah et al.,

2017; Ray et al., 2015; Steyn & Işcan, 1999). In the current study, significant differences were observed between the SA male and CH male cohorts in terms of humeral head circular diameter, in both the SI and AP directions and the spherical RoC. The current study failed to establish similar significance for the female cohort which could be attributed to the fact that there was a higher difference in the number of female subjects in the SA and CH population under study.

No significant differences were found in any of the above-mentioned groups of morphometric parameters for the bilateral humerus in either of the populations suggesting that the left and right shoulders in healthy individuals are similar in anatomy. Previous studies have shown that there is no geometrical difference in the dominant and non-dominant shoulders of an individual in both healthy and diseased population (Michael L Pearl & Kurutz, 1999). This study did not find any significant differences in the glenoid spherical RoC, humerus height and the humeral head height between the CH and the SA population. Churchill et al., 2001, studied 172 scapulas and were unable to report any significant differences between the American and non-American glenoid articulating surface. These findings indicate that glenoid articulating surfaces do not vary as extensively as the humeral head surfaces. The study by Steyn & Işcan, 1999 suggested that the SAED population had longer humerus than the native population. This study found that the average SA humerus to be longer than the average CH humerus. Another limitation of the current study was that the height and weight of the subjects were unknown and hence the findings of this study could not be correlated with these factors to generate a conclusive inference.

Humeral head thickness gives an indication of the correct sizing of the prosthesis to prevent over- or under-stuffing of the joint. Boileau & Walch, 1997, calculated the average thickness of the humeral articular surface to be 15.2mm. The values observed in our study, for both the CH (19.48mm) and SA (18.97mm) populations, were higher to the ones reported in the literature. The reason for this difference could be attributed to the fact that the authors of the previous study focused on measuring the morphology of the proximal humerus and not the whole humeral articulating surface. The *'hinge point'* selected by Boileau & Walch, 1997,

was different from the current surgical procedure, specified in DePuy, 2013; Zimmer, 2009, and the humeral articular cutting plane suggested in De Wilde et al., 2012. The average humeral head height observed by Ray et al., 2015, was 9.2mm, which was much lower than the values observed in the literature (Boileau & Walch, 1997; Hertel et al., 2002; Knowles et al., 2016) or the average value observed in our study. One possible reason for this might be that the study (Ray et al., 2015) was performed on Indian subjects, who might have different anatomical features than the European or African populations. Japanese humeral head height measured in (Matsumura et al., 2016) was considerably smaller than the observed humeral head height in this study. These populations might be in need of population-specific ATSP prostheses owing to their smaller articular surface size, and hence future studies should be focused on this aspect. Male humeral height, humeral head height, and glenoid spherical RoC were significantly greater than the female which was in line with the previously conducted studies (Churchill et al., 2001; Steyn & Işcan, 1999; Zhang et al., 2016). Intra-population gender variations were not studied, and this could be a topic for future research.

2.8 Conclusion

In conclusion, this GH morphometric study was not only able to derive meaningful inter-population differences but also highlighted the implant sizes that are not catered for, by the commercial implant manufacturers. Future shoulder morphology studies would be able to implement a similar study protocol, presented in this chapter, to examine healthy and osteoarthritic GH surfaces. Strong evidence of GH morphometric variations between the gender groups was observed in this study. The average humeral head size of a Swiss cohort was found to be bigger than an average South African humeral head. This study might aid future ATSP designs that could cater to populations of different ethnic origin and add to previous GH morphometric studies of ethnically varied population groups (Matsumura et al., 2016; Zhang et al., 2016). The biomechanical effect of population-specific modelling of the ATSP is detailed in Chapter 5, using *in-silico* musculoskeletal studies. The following chapter discusses the effect of the *"peak point"* PP on the GH forces, post-TSA.

CHAPTER 3

Part of this chapter has been presented (podium) as:

Dey, R., Inyang, W, Mutsvangwa, T., Charilaou, J., Roche, S. and Sivarasu, S. *A comparative shoulder morphometry study towards a novel metric - Peak Points.* 24th Annual Meeting of the European Orthopaedic Research Society (EORS), Bologna, Italy. (Sept 2016).

Dey, R., Roche, S. and Sivarasu, S. *Recent findings in glenohumeral joint contact mechanics.* 3rd South African Biomedical Engineering Conference (SABEC), Stellenbosch, South Africa. (Apr 2018).

Humeral Head Articular Surface 'Peak Points' and its significance

3.1 Introduction

Post-TSA contact kinetics between the ATSP components have been studied *in-silico* (Terrier et al., 2012, 2006) and *in-vivo* (Massimini et al., 2010; Bergmann et al., 2007, 2011). Most of these studies have approximated the humeral head and glenoid contact as a symmetric sphere-in-sphere (Iannotti et al., 1992). Few of these studies also have also assumed that the point of GH contact and force transfer occurs through the centrally thickest region of the head. The morphometric study detailed in the previous chapter indicates that the geometric center of the head might not be its thickest region. This feature might influence the GH force transfer.

The indications for TSA and their reasons for failure have been previously discussed. One of the established causes of the *"rocking horse"* effect could be improper force transfer between the implants. Current humeral head prostheses are designed as a part of a spheroid, truncated at various distances in its 3rd principal axis, representing the height or thickness. For example, if a dimension of a humeral prosthesis is described as 40mm x 15mm it would suggest that its RoC is 20mm and its height at the center (h_{cntr}) is 15mm. Commercially available humeral components are designed with circular bases, which attaches to the modular stem component (DePuy Synthes, 2013; Zimmer, 2009). These circular bases define the geometry of the articular surface as symmetric spherical structure.

Findings from Chapter 2.6 suggest that the biological humeral head bases might be elliptical in nature. Similar findings have been reported by Humphrey et al., 2016. The base widths of the head in SI and AP directions were unequal and SI_w was higher than AP_w. In a recent rigorous study of 76 humeral heads, it was observed that elliptically modeled humeral heads fit on to the resected humeral surfaces better and thereby possibly reduces overhang (Humphrey & Gale, 2018). These studies of elliptical heads did not take into consideration the

effects of geometrical asymmetry caused due to the unequal RoC and base widths in the SI and AP directions, post-TSA.

Current prosthesis designs are spherical in nature, with its thickest region at the center. It can be argued that due to the elliptical shape of the biological humeral head its point of maximum thickness will be at an offset from the geometric center. The purpose of this chapter is, firstly quantify the asymmetry of the biological humeral head and secondly, to compare GH forces generated by symmetric and asymmetric elliptical models of humeral head prostheses, using Hertzian contact model (Hertz, 1896).

3.2 Materials and Methods

This study employs an identical FEP and algorithm that has been explained in Chapter 2.4, to extract the humeral head from the reconstructed model of the humerus (Fig. 3.1). The automatic feature extracting script in MATLAB (Appendix A) was implemented to calculate the locus and the vertical distance to the *"peak point"* (PP) of the humeral articular surface from its base and this distance was defined as the head's peak height (h_{peak}) (Fig. 3.2 a-c). The PP for all the humeral heads were calculated and inter-population, inter-gender, and bilateral variances were investigated.

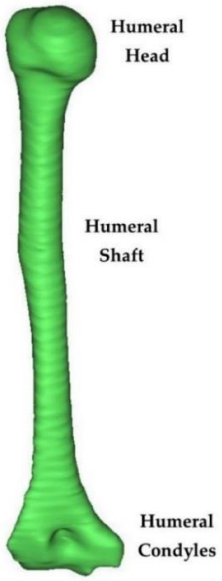

Figure 3.1 Reconstructed right humerus.

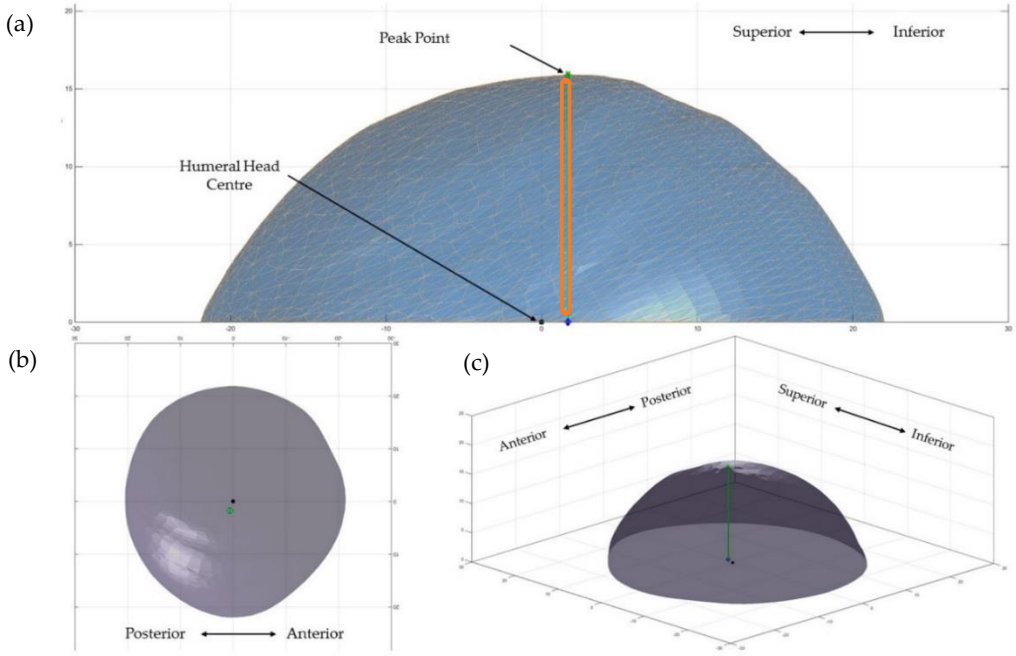

Figure 3.2 (a) Schematic representation of a biological humeral head articular surface generated by the FEP. The black dot represents the humeral head center and the blue cross represents the base of the thickest region on the head leading to the PP. The peak height of the head is represented by the orange line. The top and the isometric views of the humeral head representing the position of the PP, at an offset from the center are represented in (b) and (c) respectively.

To study the effect of the PP and peak height on the GH contact area two sets of humeral heads were created (Fig. 3.3 a-b). One of the sets was modelled using the h_{peak} and the second set of humeral heads were modeled using the h_{cntr}. The h_{cntr} for all the eighty-eight humeral heads were calculated using the relationship between the SI humeral base width (SI_w) and h_{cntr} by Humphrey et al., 2016. The SI_w values, used for this step were sourced from our earlier morphometric study. Humeral head circle fit radius (H_{rad}) changes with the height. Therefore, to model the elliptical heads using h_{peak} and h_{cntr}, Eq. 2.1 (Dey et al., 2018) was modified into Eq. 3.1. The circle-fit radius was calculated in AP and SI axes. The base of the humeral head was assumed to be elliptical. The major axis of the ellipse was SI_w and the minor axis was assumed to be the width of the base in AP axis (AP_w). The values of the minor and major axes were kept constant for all the heads and their values were sourced as the observed average SI_w (49mm) and AP_w (45mm) from Dey et al. 2018.

$$H_{rad} = Humeral\ Diameter \div 2 \quad (3.1)$$

The radius (C_r) of the contact circle formed between the articular surfaces was calculated using Eq. 3.2 (Puttock & Thwaite, 1969). The effective radius (R') was calculated using Eq. 3.3 (Puttock & Thwaite, 1969). To calculate R', the glenoid radius (G_{rad}) of curvature was kept constant 30mm. This value was selected to keep the GH mismatch average value above 5.5 mm. A prosthetic mismatch of >5.5 mm was found to significantly reduce the post-TSA complications (Walch et al., 2002). The C_r for the whole data set was calculated under the static compressive loading (F_a) condition of 750N (ASTM International, 2012), applied from the humeral head towards the glenoid.

The load was modelled to be applied along the maximum thickness of the head (Fig 3.3 a). This was performed to mimic the standardized test set-up of ASTM. To achieve this the elliptical heads were separated along the major (SI_w) and the minor (AP_w) axes. This separation took place at the center of the h_{cntr} heads and the PPs for the h_{peak} head group. This provided two spherical cross-sections of the elliptical head on which Hertzian (Hertz, 1896) contact principles were applied. A function of the prosthesis' material property, the equivalent modulus is represented by E', which had a constant value of 8.5 x 10^8 MPa, calculated using Eq. 3.4 (Hertz, 1896; Puttock & Thwaite, 1969). The values of Poisson's ratio (σ) and Young's modulus (E) for Co-Cr and UHMWPE, used to calculate E', are provided in Table 3.1.

Table 3.1 Material properties used in the Hertzian contact model.

	Young's Modulus (MPa)	**Poisson's Ratio**
Humerus (Co-Cr)	2.2 x 10^5 (ASM International®, 2009) (E_1)	0.29 (ASM International®, 2009) (σ_1)
Glenoid (UHMWPE)	763 (Croop & Lobo, 2010) (E_2)	0.32 (Croop & Lobo, 2010) (σ_2)

$$C_r = \sqrt[3]{\frac{3 \times R' \times P}{4 \times E'}} \quad (3.2)$$

$$R' = \frac{GH\ mismatch}{G_{rad} \times H_{rad}} \quad (3.3)$$

$$\frac{1}{E'} = \frac{1-\sigma_1^2}{E_1} + \frac{1-\sigma_2^2}{E_2} \tag{3.4}$$

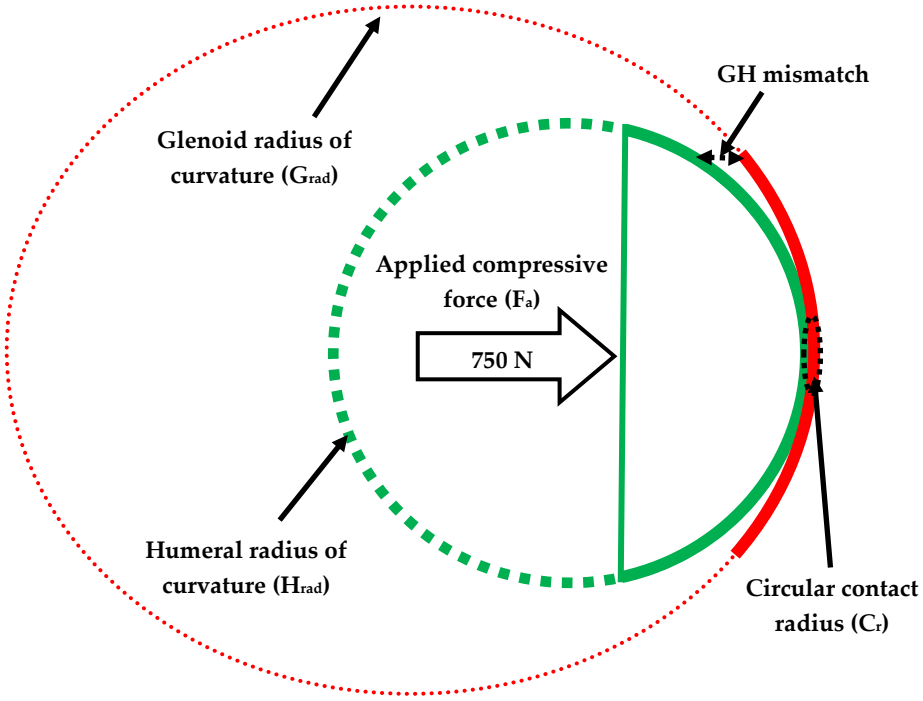

(a)

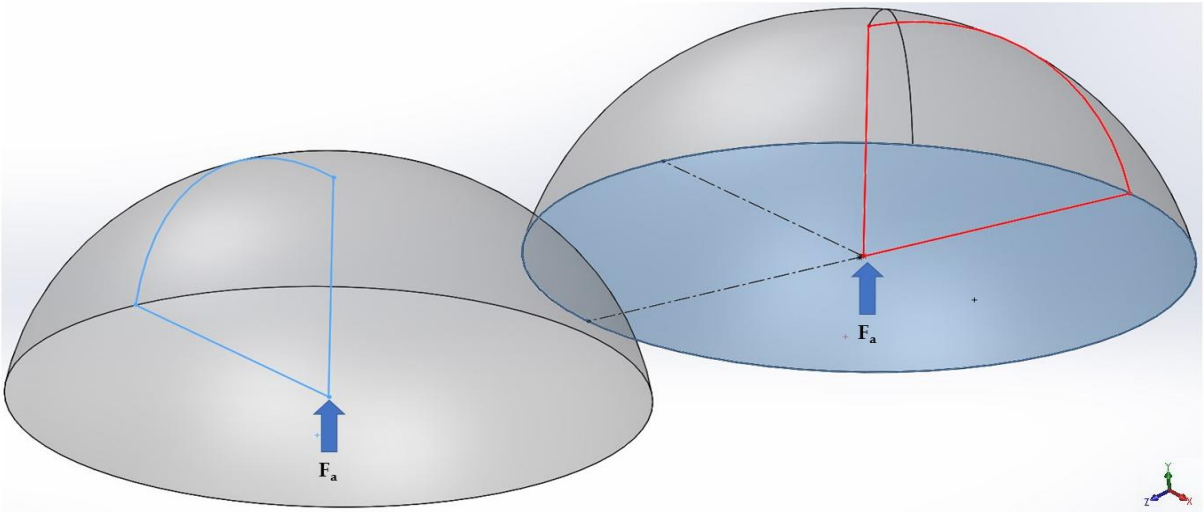

(b)

Figure 3.3 Schematic cross-sectional representations of the (a) glenohumeral articulation set-up under a load of 750N, to calculate the C_r; The applied force (Fa) was directed towards the (b) center of the humeral head modelled with hcntr and in line with the PP for the heads modelled with h_{peak} (red line).

3.3 Statistical Tests Employed

Statistical Package for Social Sciences (SPSS) software, version 25 (IBM Corp, Armonk, NY, USA) was used to statistically analyze the observations. The PP values were separated into three sets. Each set had two subsets, created according to the country of origin of the humerus (SA and CH), its position in the body (right and left) and the gender of the cadaver (female and male).

Two sets of H_{rad} and C_r were calculated using SI_w and AP_w. Each set was further separated into two subsets according to the height used to calculate these parameters (h_{peak} and h_{cntr}). All the four subsets, mentioned above, were analysed for normality using Shapiro-Wilk tests. Mann Whitney (non-parametric) and two-tailed t-tests (parametric) were implemented to analyze the statistical significance between the paired subsets. The significance was set as $P<0.05$. Post-hoc power analysis (two-tailed) was performed in G* Power (Erdfelder et al., 1996) with $\alpha=0.05$.

3.4 The Distribution of Peak Points and its effect on the GH contact

The resected humeral head articulating surfaces were processed using the FEP and the values of the abscissa and the ordinate of the PP were recorded. The coordinates of the PP were represented on a 2D planar graph, as shown in Fig. 3.4. Fig. 3.6 and Fig. 3.7. The 2D surface of the graph is divided into four quadrants, anterior-superior (AS), posterior-superior (PS), Posterior-Inferior (PI) and anterior-inferior (AI). In the anterior-posterior (AP) axis the peaks ranged from +3.03mm to -3.33mm from the center of the head as the origin. In the superior-inferior (SI) axis the peaks ranged from +3.71mm to -4.34mm on either side of the origin. The average PP for all the 88 heads under study was found to lie in the PI quadrant. Further analysis of this novel morphometric parameter is explained in the sections below.

3.4.1 Interpopulation variations

The South African average PP lies in the AI quadrant of the humeral head, as could be seen from the Fig. 3.3. The Swiss average peak point lies in the PS quadrant. The AP distance

between these two average PP is 0.5mm and the SI distance between them is 0.4mm. The difference is statistically significant in the SI direction (P<0.05), whereas in the AP direction no significance could be derived (P=0.05). The highest concentration of the PP in the SA data set (33.3%) was observed to be in the AI quadrant followed by the PI, AS, and the PS quadrants (Fig 3.4). For the CH data, 41.9% of the PP were observed to lie in the PS quadrant, followed by the AI, PI, and the AS quadrants. This positional difference was found to be statistically significant (P<0.05) suggesting that the head thickness and its position changes with head size.

3.4.2 Bilateral variations

The observed differences between the average peak point of a right humerus, when compared to that of a left humerus was found to be small and not statistically significant (P> 0.05) in both SI and the AP axes. As illustrated in Fig 3.5, the average peak points almost overlap each other.

3.4.3 Gender variations

The average peak point for the male subjects was in the PS quadrant and the average peak point for the female subjects was in the PI quadrant (Fig 3.6). These averages were separated by 0.2mm in the AP axis and 0.4mm in the SI axis. These differences were not statistically significant (P>0.05). The distribution of the peak points across the various quadrants of the humeral head is shown in Fig. 3.7. The PPs were equally distributed (29.5%) in the PS and the AI quadrants. The AS quadrant had the least amount (14.8%) of PP and the remaining PPs (26.1%) were found to in the PI quadrant. The average peak height was the highest in the PS quadrant and lowest in the AS quadrant. These differences were not found to be statistically significant (P>0.05).

3.4.4 Contact Radius and Area

The average C_r values for the SI and the AP axes calculated for the prosthetic heads modeled using the peak and the central heights are presented in Table 3.2. The difference in contact radius was statistically significant (P<0.001) in both the axis. Compared to the AP direction, the circular area under contact, was observed to be significantly (P<0.001) higher in the SI direction for both the subsets.

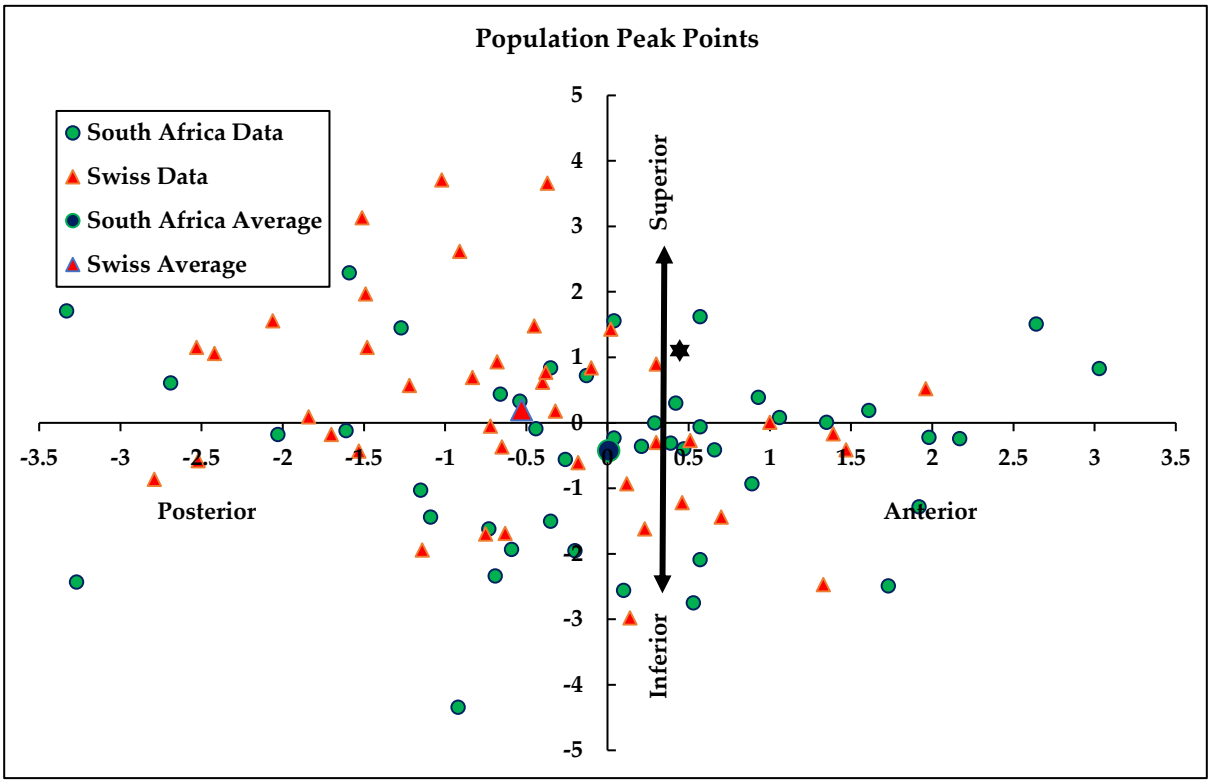

Figure 3.4 The spread of population-specific peak points. The CH peak average peak point lies in the superior-posterior quadrant and the SW average peak point lie in the anterior-inferior quadrant. A Significant difference was observed in the SI axis. (* Statistically significant).

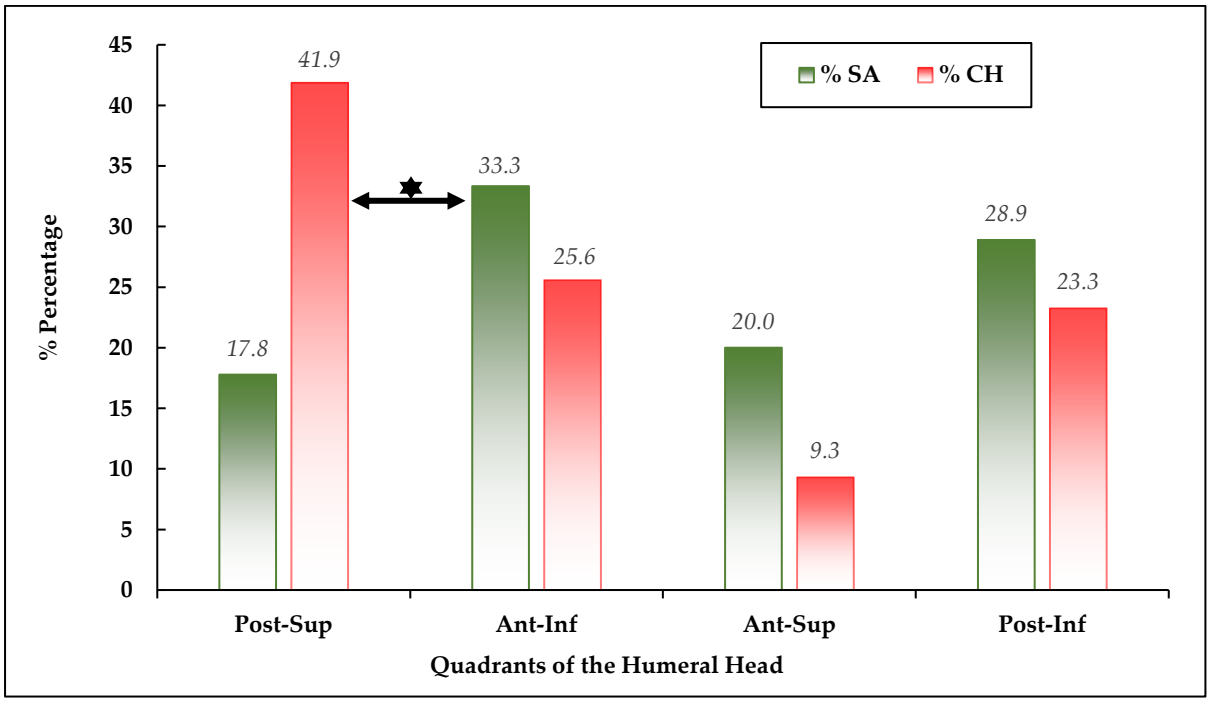

Figure 3.5 The percentage distribution of the peak points across various quadrants of the humeral head articular surface for the SA and CH population. (*Statistically significant).

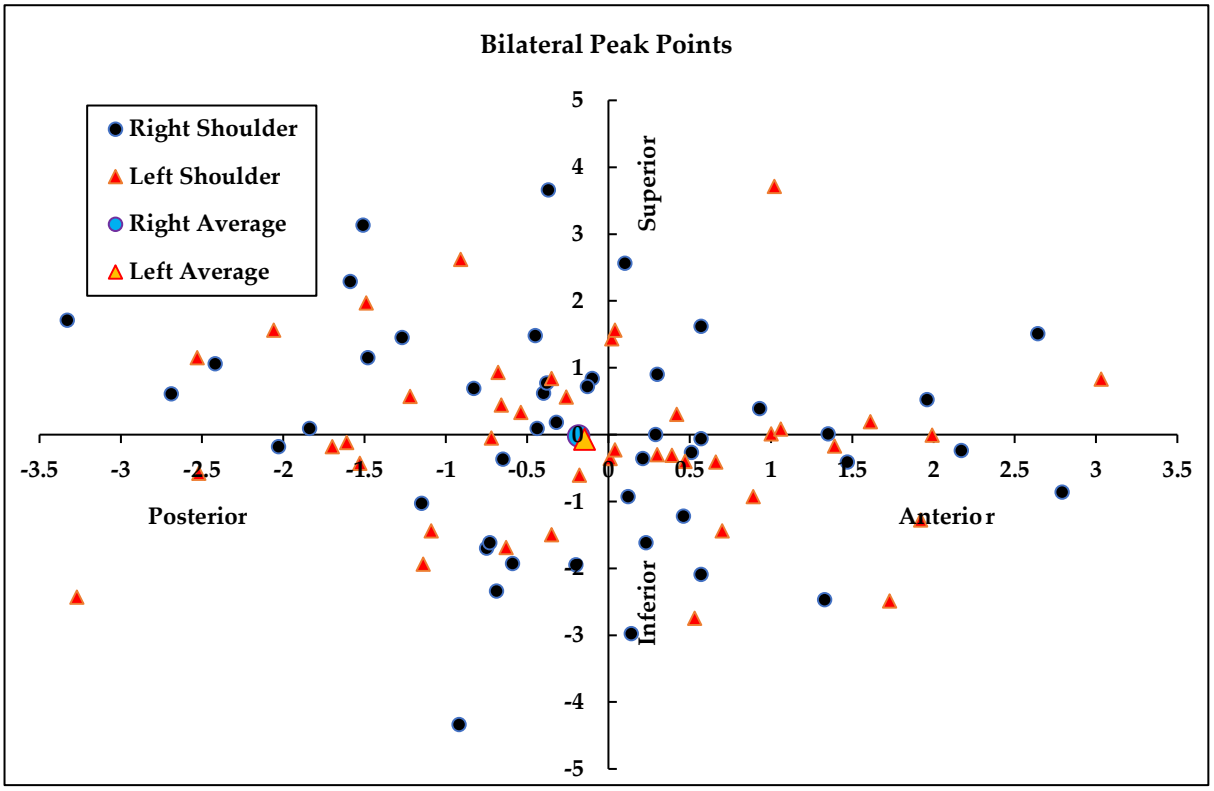

Figure 3.6 The spread of the bilateral peak points. The average peak points for the left and right peak points were found to lie almost on top of each other.

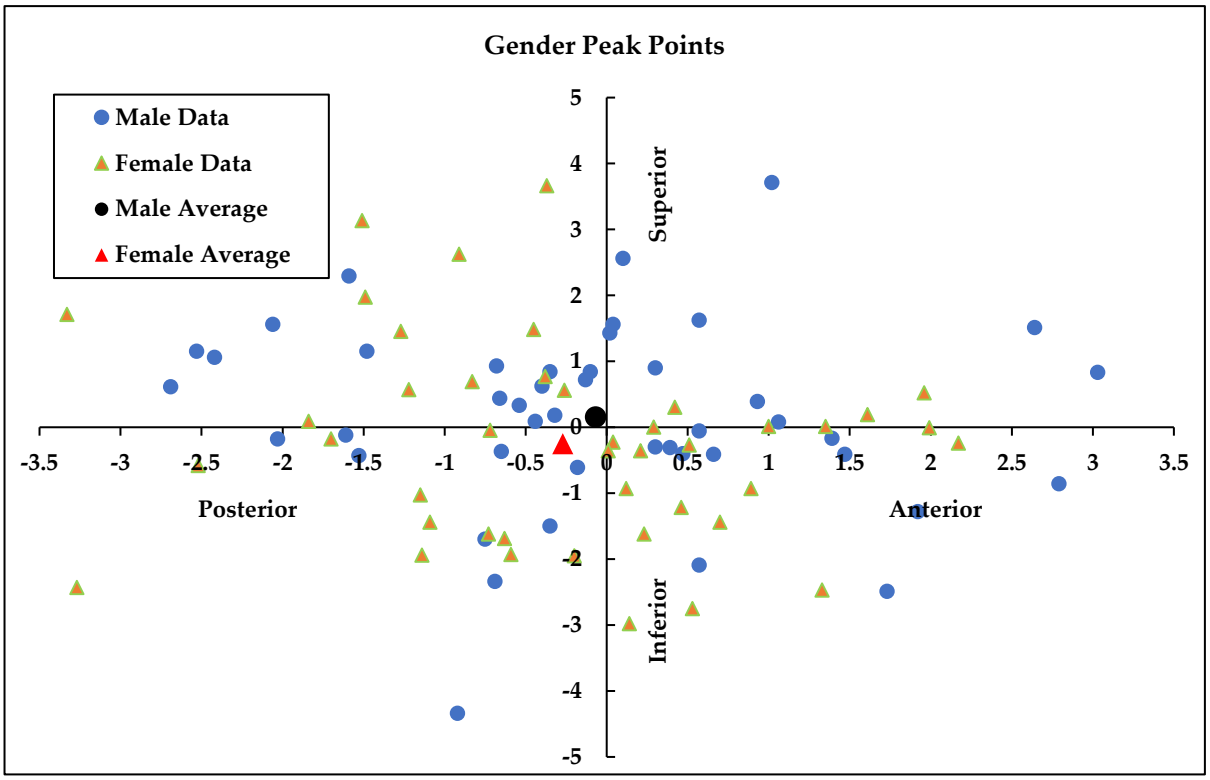

Figure 3.7 The spread of the PPs for the male and the female datasets. The average PPs for both the data set were observed to lie in two different quadrants but not significantly separated.

Table 3.2 The measured (average ± std. dev.) radius and the circular area under contact for the subsets in the SI and AP axes.

Humeral Head Base Width (mm)	Average GH Contact Radius (C_r) (mm)		Average Contact Area$^{\Psi}$ ($\pi * C_r^2$) (mm^2)	
	h_{peak}	h_{cntr}	h_{peak}	h_{cntr}
SI_w = 49	4.84 ± 0.47	4.98 ± 0.29	73.56 ± 17.1	77.87 ± 9.4
AP_w = 45	4.01 ± 0.14	4.06 ± 0.1	50.49 ± 3.7	51.76 ± 2.7

$^{\Psi}$ *the value of π was approximated as 3.14*

3.5 Clinical Significance of the Peak Points

Unconstrained anatomical shoulder prostheses have been extensively used to replace arthritic GH joints using TSA (Boileau et al., 2006). Its predicted usage is going to rise in the coming years (Padegimas et al., 2015). Glenoid component loosening has been a widely accepted reason for post-TSA complications and failures (Bonnevialle et al., 2013; Junaid et al., 2010; Matsen III et al., 2008). Post-surgical load transfer between the GH bones has been demonstrated to be non-anatomical (Patel et al., 2014). The spherical shape (DePuy Synthes, 2013) of the prevalent humeral head prosthesis fails to take into account the eccentric nature of the head (Dey et al., 2018; Hertel et al., 2002; Humphrey et al., 2016). The current study could demonstrate the effect of the asymmetric elliptical shape on the GH forces.

The average offset of the PP from the geometric center of the humeral base was observed to be < 1mm. Even though this difference was small in magnitude it had a significant effect on the thickness of the humeral head surface. The height (thickness) of the humeral head prosthesis could be a determining factor for the curvature of the articulating surface. Morphometric studies have reported a high correlation between the head thickness and RoC (Dey et al., 2018; Zhang et al., 2016). This study found that a healthy head might not be the thickest at the center. The average PP, for all the humeral heads under study, was observed to lie at an average distance of 0.25mm (AP) and 0.12mm (SI) from the center of the head. This further altered the maximum height (h_{peak}) of the humeral head which had a significant effect on the GH forces and contact area under compressive loading (Table 3.2).

A previous morphometric study by Knowles et al., 2016, on healthy and individuals with shoulder OA, observed the head thickness to be at an offset from the head center for both the cohorts. In the current study, the average h_{peak} was found to be 1.32mm higher than the h_{cntr}. This variation was found to be significant (P<0.05) with an effect size of 0.75 and the probability of Type II error being less than 1%. A mathematical relationship, with high coefficient of correlation (R=0.74), was established between the h_{peak} and the SI_w (Fig. 3.8) which was different from the reported (Humphrey et al., 2016) relationship between h_{cntr} and SI_w.

Humeral head size (H_{rad}) was found to alter the PP position. For larger heads, i.e. humeral heads having Hrad >24mm, the PPs were majorly located in the anterior quadrants of the head and the opposite was observed for smaller (H_{rad} <24mm) heads. Welch's t-test (Kohr & Games, 1974) was performed to compare the differences in h_{peak} between the large and the small head size groups. The observed mean difference of 2.23mm was found to be significant (P<0.05). This further corroborates the fact that the humeral head size may determine the position and value of its maximum thickness.

Increase in the h_{peak} and anterior migration of the PPs, in larger heads, could have a functional related to it. One of the probable functional advantage of the above observation is described below. These structural differences between smaller and larger heads might enable the later to generate sufficient torque during axial rotation. Given the neutral position of GH articulation, as described by Omori et al., 2014, it could be expected that the anterior aspect of the head produces most of the torque produced for axial rotation. In the case of a larger head, the torque required for this rotation increases as it is deep-seated inside a larger glenoid. Therefore, the observation that the mean position of the PPs being in the anterior aspect of larger heads might increase the lever arm aiding the heads to produce the torques required for the rotational motion. The extent to which the PPs affect the torque produced by the humeral head is an investigation which is out of the current thesis' scope.

Populations belonging to different geographical regions have been reported to demonstrate variation in humeral head geometry (Dey et al., 2018; Zhang et al., 2016). This study demonstrated significant variation (P<0.05) in PPs location, in SI axis, between a

European population subset and an African population subset. The effect size of this difference was observed to be medium, with the value of 0.42 (McDonald, 2014), and the power of statistics was 0.5. Significantly different (P<0.05) distribution of the PPs were also observed in between the population subsets studied. A majority (41.9%) of the CH heads had their PPs located in the PS quadrant whereas, a majority (33.3%) of the SA heads had their PPs located in the AI quadrant of the head. Knowles et al., 2016 observed the humeral head to be the thickest in the PS quadrant, which matches with the average PP location for the CH cohort. The current study was not able to establish any significant differences between the gender and bilateral subsets. Bilateral humeral heads were expected to demonstrate minimum variation in their morphometric geometry as the bones were sourced from healthy cadavers

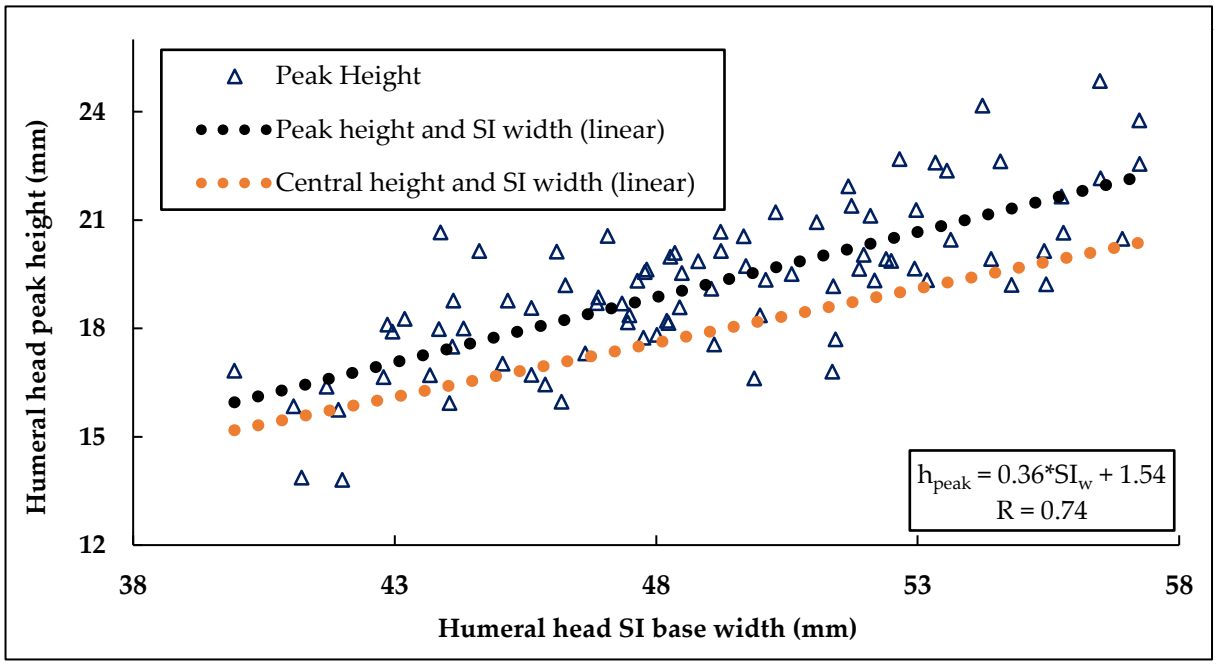

Figure 3.8 Representation of the linear relationship between the SI base width of the humeral head and its peak height (h_{peak}).

The *"rocking"* of the glenoid prosthesis due to an imbalance of humeral forces, on the polyethylene surface, has been observed by various authors. The separation of the glenoid prosthesis from the reamed glenoid face occur at the bone cement interface (Matsen III et al., 2008). This separation could be possibly reduced by improving the oseteo-integration of the

cancellous bone of the scapula and gaps/fins (DePuy Synthes, 2013) present in the polyethylene glenoid component. The overall change in the thickness of the humeral head was expected to affect the curvature of the articular surface and hence the GH area under contact. This study observed that the average GH circular area under contact for prosthetic heads modelled using h_{peak} was lower than the heads modelled using h_{cntr} by 5.23mm^2 and 2.16 mm^2 in SI and AP axes respectively. The observed average differences, for the complete dataset comprising of 176 humeral head, was found to be significant (P<0.05) in both the axes. The mean observed power and effect size, for both the axes combined, was 0.63 and 0.35 respectively. The SI_w and AP_w were assumed to be constant to ensure that the observed changes were only due to the change in the prosthesis height which further altered the RoC.

Gupta et al., 2004 had observed, under a similar theoretical setting, the glenoid area under contact to be 17.114mm^2. This value was lower than the current observation. One possible reason for this variance in observation could be the different loading force employed by the two studies. While the current study applied 750N, standardized by ASTM, the study from the literature applied a physiological load of 393N (Gupta et al., 2004). As the current study used a group of symmetric and asymmetric, elliptically shaped heads with constant values of mismatching base widths, the increase in area under contact could only be due to the change in the RoC of the humeral surface. This change in RoC was introduced by changing the thickest region of the head from the center (h_{cntr}) to the location of the peak point (h_{peak}).

Using a load of 393N, the current study observed a combined (both for h_{cntr} and h_{peak}) mean decrease of 34.7% and 34.9% in the SI and AP GH contact areas respectively. Under physiological loading conditions in a healthy cadaveric shoulder, Warner et al., 1998, reported a contact area of 58mm^2 and 83mm^2, an increase of 30.1%, when the joint was loaded with 222N and 444N respectively. Although, the current study was not able to match the calculated values of the GH contact area from the literature,(Gupta et al., 2004) as the contact area could have varied due to the size of the prosthesis and respective material properties, it was successful in demonstrating reduction in the contact area with the reduction of the applied force (F_a). Jobe & Iannotti, 1995, reported that the available arc of articulation on a biological

glenoid fossa is 14% more in the SI axis. The RoC of the humeral head prostheses modeled in this study was, on an average, 9.96% greater in the coronal plane. The influence of these two factors, stated above, might have been the cause behind the 33.5% (for heads modelled with h_{cntr}) and 31.4% (for heads modelled with h_{peak}) increase in the coronal plane contact area compared to the transverse plane. Therefore, the theoretical two-dimensional GH area under contact is a blend of the ellipses formed by the combination of the AP and the SI contact areas in the coronal and the transverse axes (Fig. 3.8).

For the loading condition used in this study, i.e. normal (compressive) loading of the glenoid using 750N (ASTM International, 2012), the calculated pressure on the glenoid component, corresponding to the humeral head modelled with h_{peak}, was higher. The mean pressure applied by a humeral head, modelled with h_{cntr}, was found to be lower by 5.88% and 2.49% in the SI and AP axes respectively. Average contact pressures observed in this study, in SI axis 9.6MPa (h_{cntr}) and 10.2MPa (h_{peak}) & in AP axis 14.48MPa (h_{cntr}) and 14.85MPa (h_{peak}), were within the range of the von Mises stresses and contact pressures, on the glenoid implant surface, reported by previous finite element analysis investigations (Terrier et al., 2012, 2006; Zhang et al., 2013). This indicates that no uncharacteristic or polyethylene damaging pressures were produced by altering the humeral head design.

Localising the force on the glenoid might reduce eccentric loading and rocking horse effect. It could be argued that, in the case of an all-polyethylene glenoid component, increasing surface pressure might increase the stress at the bone cement interface, in-turn, increasing the strain on the cancellous scapular bone (Pascal Boileau et al., 2015; Papadonikolakis & Matsen, 2014; Terrier et al., 2018). This might be beneficial for stronger post-surgical bone growth under higher mechanical load (Tanck et al., 2006), according to Wolff's Law (Frost, 1994). Incorporating PPs in the current designs of the humeral head prosthesis might also result in increase in pressure on the glenoid, within the limits of UHMWPE material properties. There are several factors which affect the contact GH area and the implant-to-bone pressure transfer. It is important to keep in mind that the observations reported in this study were only due to

changing the shape of the humeral head. Future computation analysis on the loading characteristics of an asymmetric elliptical heads would be beneficial.

3.6 Conclusion

This study showed that the center of the humeral articular surface base does not coincide with the highest point on its articulating surface, the *"peak point"* (PP). The position of the PP was observed to lie at an offset from the centre with the highest observed occurrence in the posterior region of the head. The distribution of the PP concentration was also observed to be population specific.

The distance between the humeral head base and the PP, i.e. peak height, was significantly higher than the central thickness of the humeral head. Incorporating the elliptical nature of the humeral head into creating theoretical models, this chapter presented a study comparing the GH forces generated by symmetric (h_{cntr}) and asymmetric (h_{peak}) prostheses. From this study, it could be concluded that heads modelled with PP transferred higher concentric pressures into the glenoid cup and these pressure values were found to be within the stress limits of UHMWPE. This might result in reduced edge loading of the glenoid cup and higher load transfer towards the glenoid vault.

Although, symmetrically shaped spherical prosthetic humeral heads could be aesthetic in perception and easier to manufacture, asymmetric elliptical prostheses could be functionally beneficial. Limited studies exist on the investigation of usefulness of a non-spherical and an elliptical humeral head (Humphrey & Gale, 2018; Jun et al., 2013). Hence, further investigations are recommended to research the effect of shape and PP on post-TSA GH kinematics and kinetics.

In Chapter 2 and in the current chapter few morphometric features were identified which are not incorporated in the currently available prostheses design. Among the features, the average population-specific humeral head size variance and its PP will be taken forward into the next chapter to design novel humeral heads. The reason for not incorporating the elliptical shape as one of the prosthetic head design features, was the difficulty related to

suitable validation of the observed results. The next chapter will also detail novel glenoid cup design concepts which would aim at reducing the eccentric loading of the polyethylene cup.

CHAPTER 4

Morphometry Informed Design of Total Shoulder Prosthesis

4.1 Introduction

Unconstrained design of ATSP, e.g. Neer Mark II became the gold standard since its inception by Charles Neer II in the early 1970s (Wirth & Rockwood, 1996). Even though short-term follow up studies have reported improved post-operative GH functionality (Brand & Bigliani, 2011; Frich et al., 1988), multiple variations in the design of the humeral and the glenoid components have been made since. A brief timeline of important modifications of ATSP is provided in Chapter 1.3 along with the description of changes. These design changes could be broadly classified into two categories. Functional design changes improved post-surgical range of motion and reduced instability while structural design changes improved implant-to-bone load transfer and reduced glenoid deformation due to wear (Matsen III et al., 2008).

Moving away from a fully conformed GH prosthesis towards non-conformed prosthesis required the humeral head RoC to be smaller than the glenoid. This gave rise to the GH implant mismatching system which provided more mobility room for the head and an overall increase in post-surgical RoM (Karduna et al., 1997). A further functional advantage was introduced by increasing the surface area of the glenoid implant by making it oval in shape (Williams & Abboud, 2005). Though this feature was not perfectly anatomical, it resembled the shape of the glenoid fossa affected with OA and had the same effect on the GH RoM as increasing the component mismatch. An oval shaped glenoid cup is designed with the assumption that all the OA glenoids have the same amount of deformation, which might not be the case.

Several morphometric studies, including the study described in Chapter 2, have observed that humeral head is elliptically shaped (Boileau & Walch, 1997; Dey et al., 2018; Hertel et al., 2002; Humphrey et al., 2016; Iannotti et al., 1992). The recent drive in shoulder

implant design is to shape the humeral head prosthesis as an ellipsoid. Modeling the humeral head implant non-spherically increases post-surgical RoM in axial rotation and reduces implant overhang along with localising the load on a smaller area on the glenoid surface (Chapter 3.5, Humphrey & Gale, 2018; Jun et al., 2013, 2016).

Few of the implant design features, inducing favorable post-surgical functionality, as mentioned above, affect the kinetic interactions of the implant components. Increasing the component mismatch by 15mm increased the GH contact pressure and the bone-cement stresses by 300% and 200% respectively (Terrier et al., 2006). These increases could be considered large enough to damage the polyethylene surface of the glenoid component. Terrier et al., 2006, also reported that a GH mismatch of less than 10mm increased the contact pressure within the limits polyethylene yield strength but the risk of component wear remained. Post-operative radiolucent lines behind the glenoid component are a common indicator of implant loosening. Increasing the mismatch between 5.5mm and 10mm was found to reduce the radiolucent lines significantly (Walch et al., 2002). Although there exists no constant value of prosthesis mismatch, this factor is generally dependent on the size of the implant. The current process of fixing the CI for the ATSP designs by the manufactures is unknown and the value of the commercial prosthetic mismatch are not available.

Metal-backed glenoid components were introduced with the advantage of being implanted as a press-fit without bone cement (Cofield, 1994). Although initial tissue in-growth was observed, these implants were not immune to post-operative complications. The polyethylene articulating surface wear and tear was reported to be higher with metal-backed prostheses compared to all-polyethylene glenoids (Boileau et al., 2002, 2015, 2006; Wallace et al., 1999). Stress shielding caused by the metallic component of the implant was one of the major reasons for the high polyethylene wear rate. The higher load bearing metal back component concentrated a large amount of force on the implant, while transferring only a smaller portion of the humeral load into the glenoid. This eventually caused delamination of the polyethylene surface press-fit onto the metal back. The all-polyethylene glenoid implants used for TSA currently are designed with sufficient thickness making it structurally stable.

Initially, Vitallium was used to manufacture the humeral head prosthesis (C. S. Neer II, 1955). Co-Cr alloys became the material of choice for manufacturing the loading surface of the shoulder implant because it was highly corrosion resistant and ductile (Saini et al., 2015). UHMWPE became the gold standard for manufacturing the load bearing surfaces of the shoulder implant since the late 1960s. UHMWPE was found to be more biocompatible than its predecessors and improved wear properties due to crosslinking (Kurtz et al., 1999; Musib, 2012; Wirth et al., 2009). A recent study on ceramic humeral head indicated that the polyethylene wear was significantly reduced. Long-term implications of ceramic implant might be crucial before adapting the material for TSA (Mueller et al., 2017).

The third-generation shoulder prostheses have included many anatomical design features in the humeral and glenoid components. Options of positioning the humeral component at different inclination and retroversion angles were introduced along with multiple peg design at the back of the glenoid (Pearl & Kurutz, 1999; Razmjou et al., 2013). Recent studies have reported the development and testing of a hybrid glenoid prosthesis (Wang, et al., 2005; Zhang et al., 2013) and an inset glenoid implant (Gunther & Lynch, 2012; Gunther et al., 2012). The hybrid glenoid cup was designed with a conforming central region and a non-conforming periphery. It was reported to have no significant effect on the post-surgical kinematics and kinetics when compared to a single radius glenoid implant. It could be expected that the hybrid glenoid would provide resistance to humeral translation at the edge of the conforming region. The uncharacteristic forces generated due to this resistance could potentially harm the polyethylene surface, due to wear and tear, in the long run.

An inset glenoid design partially replaces the damaged glenoid surface. As the inset glenoid is implanted to cover majority of the central glenoid surface, there is a lower risk of eccentric loading on the prosthesis. A mid-term follow-up of the inset glenoid indicated improved RoM and reduced occurrence of radiolucent lines. Although the preliminary results of using this patient-specific glenoid implant are encouraging, the surgical procedure implemented might result in a higher bone loss. While the fixation of a commercially available pegged glenoid implant requires, on an average, 4 holes on the glenoid surface, the inset

glenoid fixation requires multiple (>4 as observed) holes to be drilled on the surface. Apart from this, there is no matching humeral head available for this smaller implant. If the inset glenoid prostheses are used without making necessary design changes to the pairing humeral heads, the later might lead translate towards the exposed bone giving rise to metal-bone contact leading to pain and possible dislocation. Anchoring the inset prosthesis to the bone with a central keel-styled fixation, instead of multiple pegs, might result in aseptic loosening as reported in the literature (Junaid et al., 2010; Strauss et al., 2009; Williams & Abboud, 2005).

Most of the third generation TSA implants lack long-term follow-up studies and hence their role in reducing post-surgical complications. Persistence of aseptic loosening of the glenoid due to *"rocking horse"* effect is the underlying complication reducing the longevity of the TSA prosthesis. This chapter introduces new designs of humeral and glenoid prosthetic components. The humeral components were designed using population-specific morphology and the glenoid components were designed with the aim to reduce eccentric loading.

4.2 Governing Design Parameters

The existing TSA prosthesis, available commercially, provide a varying range of humeral and glenoid components which could be principally differentiated based on RoC and height. For the glenoid prosthesis, the height and the width are also varied to fit the glenoid vault, created while reaming the surface. Hence it was decided to investigate the effect of these parameters on the performances of the muscles around the GH joint and the contact forces of the joint. All the prosthesis designs were done in Dassault Systems SolidWorks® and these designs were exported in stereolithographic (.stl) format, which made them compatible with Materialise Mimics® and OpenSim.

4.2.1 Humeral head component

The major geometric parameters governing the thickness of the humeral head component were the humeral head thickness and the size of the head, determined by the RoC. The skeletal design of the humeral head (Fig. 4.1 a) was based on two geometric foundations, the articulating sphere, and the base circle. The height of the part was defined by the distance

between the center of the base circle and the articulating sphere forming the h_{cntr}. This provided a platform where the RoC of the sphere and the height of the articulating surface could be customized according to the need to create a set of the humeral head prostheses. An example of which is presented in (Fig 4.1 b).

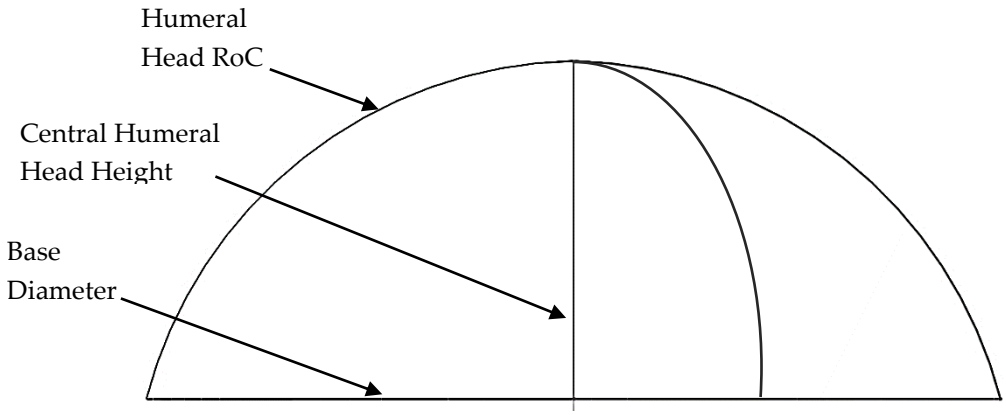

(a)

(b)

Figure 4.1 (a) The skeleton design of the humeral head that was used to design most of the (b) final prostheses shaped as a symmetric spherical section.

4.2.2 Glenoid component

The glenoid cup design was governed by a concentric spherical section joined by a spline enabling customization of the cavity RoC. The skeleton of the design (Fig 4.2 a-b) was made such that the thickness between the concentric spheres was kept constant at 3mm. A thickness

of 3mm was closer to the ideal thickness, recommended by (Terrier et al., 2012), of 4mm and it can be argued that reducing or increasing the thickness might have induced high concentrated stresses on the polyethylene surface. The height and the width of the prosthesis (Fig. 4.2 c) were modeled according to the design parameters of the Global AP for a specific RoC represented by the spherical edge dimensions.

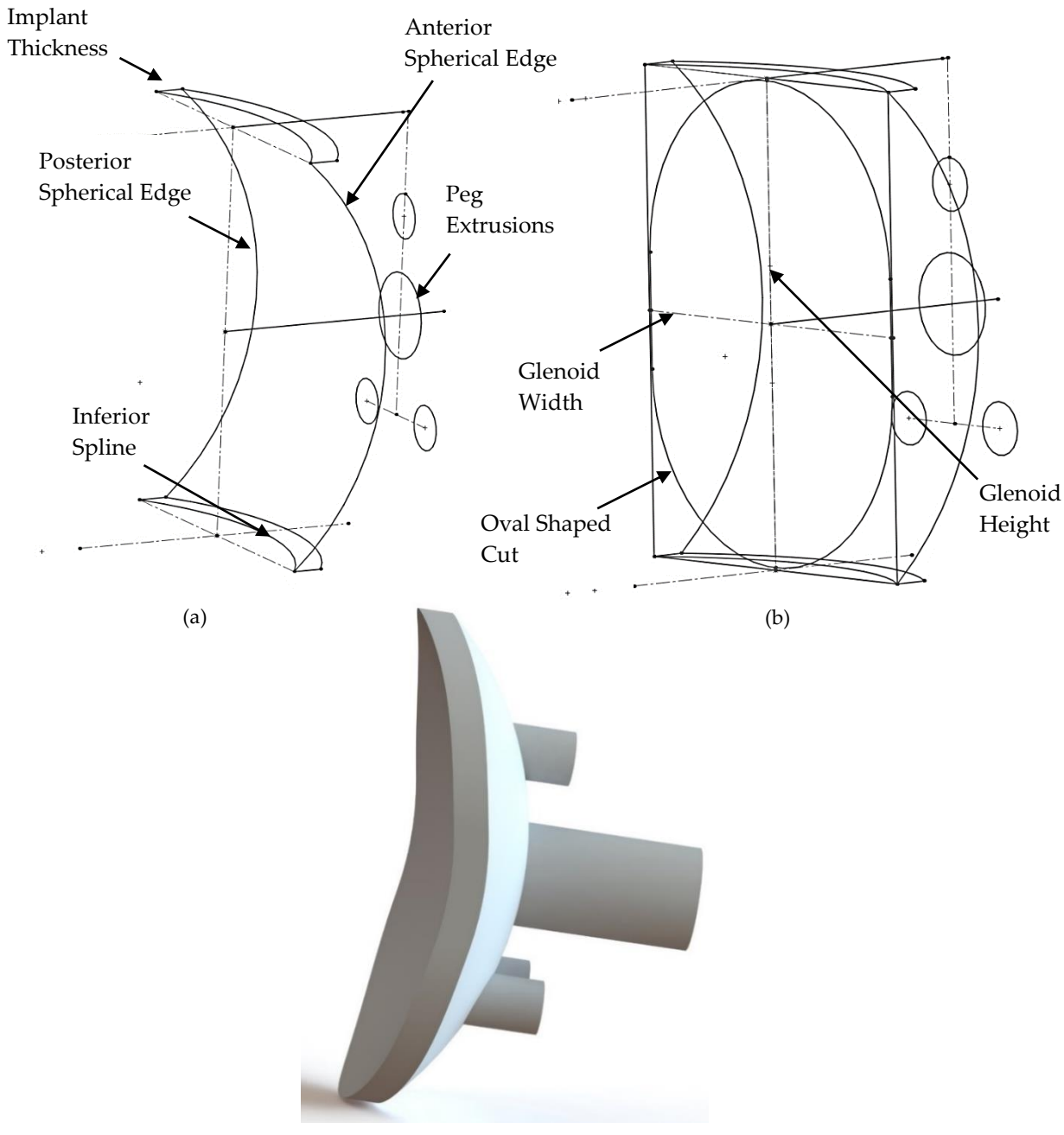

Figure 4.2 (a) The skeletal design of the glenoid prosthesis, moulded into the cup shape using the (b) ellipsoid shaped cut to accommodate for the prosthesis height and width to extrude the (c) final design.

4.3 The Design Process and Outcomes

The prosthesis designs could be divided into control models, populations specific humeral head prostheses and novel glenoid designs. All the prostheses groups are described below;

4.3.1 Control models

The designed prosthesis will be tested for post-surgical kinematic and kinetic performances. The need for this testing is two folded. Firstly, to investigate if there was any variation in the GH musculoskeletal performance after introducing a population-specific implant and secondly to test the effect of the prostheses design changes on reducing eccentric loading. The musculoskeletal and finite element observations using the control models serve as a benchmark, to which the performance of the novel prostheses will be compared to. This will aid in identifying the effect of introducing the design parameters, that were used to generate the novel ATSP designs.

4.3.1.1 Humeral head control models

The humeral control models were sized according to the available prosthetic dimensions. The RoC ranged from 20mm to 28mm, with an increment of 2mm, and the height was ranged for each of the humeral heads were selected as 15mm, 18mm, and 21mm. This combination was followed for all the head sizes except for smallest and the largest heads with RoC 20mm and 28mm. The complete list of the sizes created as, a possible, control model is given in Table 4.1.

Table 4.1 The parameters used to create the humeral control models

Model Name	Head Size (mm)	Head Height (mm)		
		15	18	21
Head Control Size 1	20	✓	✓	
Head Control Size 2	22	✓	✓	✓
Head Control Size 3	24	✓	✓	✓
Head Control Size 5	26	✓	✓	✓
Head Control Size 6	28		✓	✓

4.3.1.2 Glenoid cup control models

The glenoid prosthesis was reverse engineered from the Global AP (De Puy, 2013). Even though, commercially, the glenoids only vary in their RoC to create an accurate model of the available glenoids the measure of their height and width were essential. The complete list of glenoid models with their dimensions is listed in Table 4.2.

Table 4.2 The design parameters used to create the glenoid control models.

Model Name	Glenoid Size (mm)	Cup Height (mm)	Cup Width (mm)
Cup Control Size 1	22.75	31	23
Cup Control Size 2	24.75	33	25
Cup Control Size 3	26.75	35	26
Cup Control Size 5	28.75	38	29
Cup Control Size 6	30.75	41	31

4.3.2 Population specific humeral head components

From the morphometric study, detailed in Chapter 2, it was found that the South African and the Swiss population had differently sized heads. In the same chapter it was also concluded that the currently available prostheses will be able to cater for the average size of both the populations. However, other studies performed on Asian populations have reported humeral head sizes for which finding adequate prosthesis still remains a challenge (Zhang et al., 2016). No study has investigated the post-TSA effects of this variation in humeral head size across different populations.

To investigate the effect of this population-specific difference on the GH kinematics average humeral heads were designed for each of the populations. Apart from these two populations, the Chinese average humeral head size (Zhang et al., 2016) was modeled and also its kinematic performance was compared with the previous populations. For the SA and

CH populations there were no observed significant differences in the glenoid morphometric parameters. Therefore, its effect on the GH kinematics and forces were not studied.

4.3.2.1 Humeral components with average dimensions

The design of the population-specific humeral head used the same skeletal frame as previously shown in (Fig. 4.1). The base diameter of all the prostheses was fixed at 50mm. The dimensions for the humeral heads are provided in Table 4.3.

Table 4.3 Dimensions of the population-specific humeral head prosthesis designs.

Prosthesis	Head Size (mm)	Head Height (mm)
South African Average Head	23.2	18.9
Swiss Average Head	24.4	19.5
Chinese Average Head	22	16.9

4.3.2.2 Humeral components with varying peak points

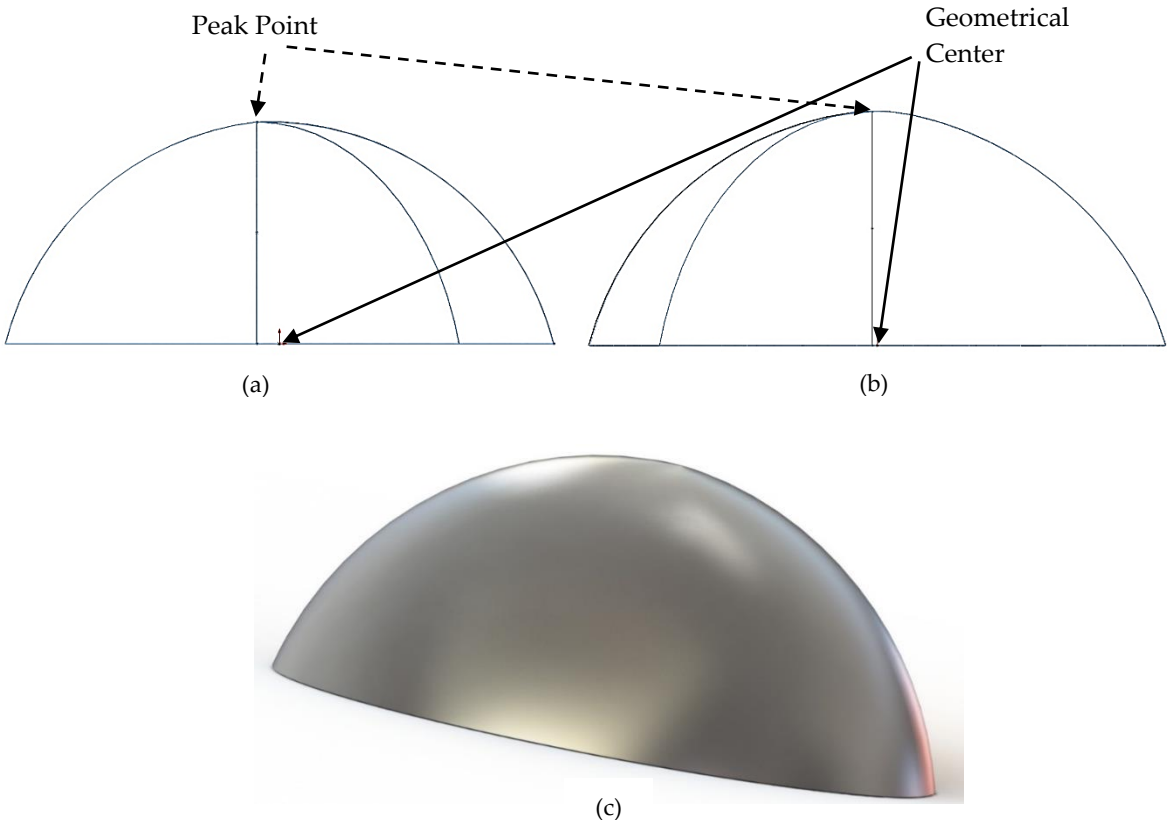

Figure 4.3 The (a & b) skeleton of the humeral head designed with an off-center peak point creating (c) the final humeral head prosthesis incorporating the PP and the asymmetric nature of the biological humeral head.

To design the humeral heads with off-centered peak points a new design skeleton was created (Fig. 4.3 a-b). The offset and the h_{peak} selected for the humeral head were based on the observations from the SA and CH inter-population study. The RoC and the base diameter were kept constant at 56mm and 50mm respectively. The spherical head (Fig. 4.3 c) was created using radially segmented quadrants joined together using the base circular profile. As the PP information of an average Chinese humeral head was not available, no specific prosthesis was designed representing this population.

4.3.3 Novel glenoid component designs

The purpose to develop the new glenoid cup designs was to increase concentric loading of the prosthesis within the stress limits, in order to reduce chances of *"rocking"* of the implant (Farng et al., 2011; Gregory et al., 2009; Raphael et al., 2010). These designs were aimed at transferring majority of the GH joint reaction force into the scapula. Proper loading of the scapula could be expected to promote better bone growth and osteointegration of the prosthesis.

The glenoid cup designs described below were based on the control models of the glenoid, designed earlier. The modifications were only made to the articular surfaces and care was taken not to alter the design features of the prosthesis essential for surgical implantation. The designs described below were their initial iterations and recommendations will be made on the designs based on their performances in tests performed in Chapter 5 and 6.

4.3.3.1 The Bi-radial design

The structural properties of glenoid cavity bone vary across its surface area. The depth of the bone is the highest in the center and shallowest along the anterior and posterior aspects. The strength and Young's modulus of the posterior region of the cavity are higher than the anterior aspect, especially the posterior-superior quadrant (Anglin et al., 1999; Matsuki et al., 2018). Moreover, the strength of the glenoid cancellous bone decreases significantly with the depth (Anglin et al., 1999). During the glenoid component implantation, the cavity is reamed and this could result in loss of bone strength (De Puy, 2013).

To provide a better anatomical GH articular surface to the prosthesis, the posterior-superior quadrant of the implant was thickened (Fig. 4.4). The implant thickening was done by increasing the RoC of the region by 3mm. This increase was in the same order as the thickness of the prosthesis (3 mm), which is a constant for all the sizes, and hence the possible bone loss. The bone loss takes place during the reaming process, though the extent of glenoid reaming is surgeon specific, the reaming depth considered here was within the accepted limits (Yongpravat et al., 2013a).

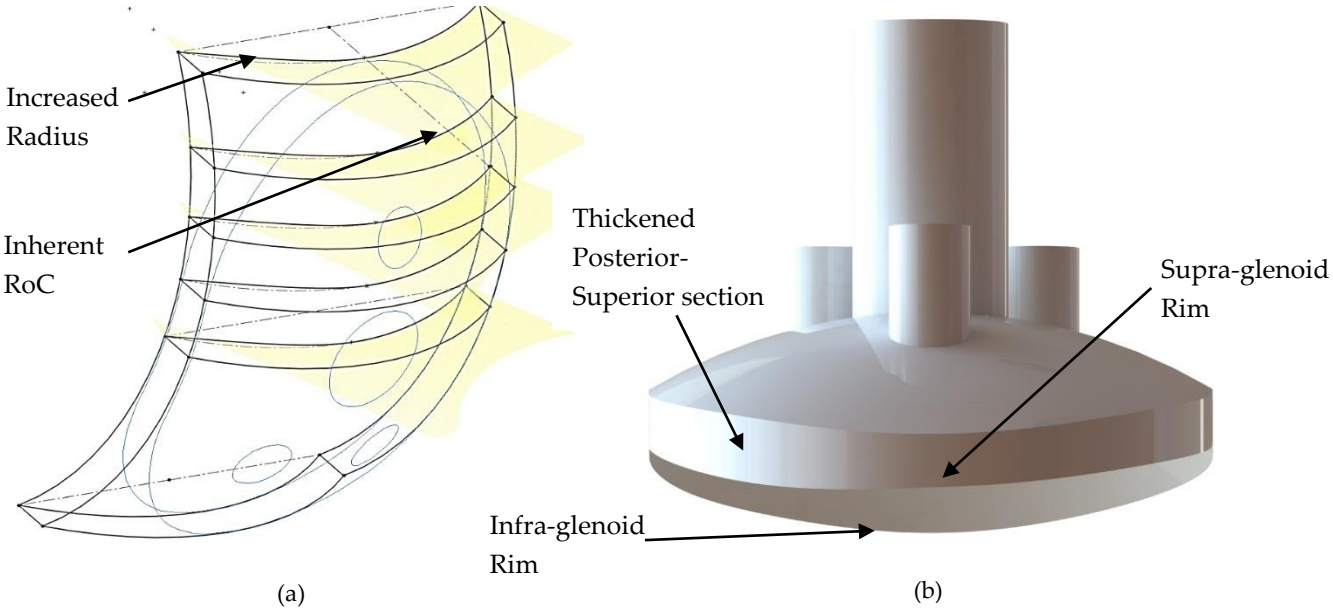

Figure 4.4 The bi-radial glenoid. (a) The skeleton of the design showing the guide curves to control the curvature. (b) The final model.

4.3.3.2 The Pear-shaped design

The conformity index of the GH articulation ranges between 0.63 and 0.78 (Dey et al., 2018; McPherson et al., 1997). The margins posterior pegs on the glenoid prosthesis (control models) were found to be 23.5 mm apart. The average ratio between the overall height of the glenoid prosthesis and the peg margins were found to be 0.67. Hence, from the above observations, it could be inferred from this that to achieve concentric loading the contact centroid of the GH articulation should lie within the 70% area of the glenoid prosthesis surface, to maintain stability and transfer a majority of the load into the bone through the pegs.

To investigate the point of contact on the glenoid prosthesis during different RoM, the surface of the glenoid control prostheses was divided into a concentric and an eccentric region of contact as shown in (Fig. 4.5). The contact centroids for the motions studied in Massimini et al., 2010 were plotted on the surface of the prostheses. Massimini et al., 2010, used the Anatomical Shoulder System (Zimmer, Warsaw, Poland) which closely resembles the geometry of the Global AP prosthesis (Zimmer, 2009).

60% of the plotted GH contact points were found to lie within the limits of the concentric area and the remaining 40% of the contact centroids were found to be lying in the eccentric loading region (Fig. 4.6 a). This distribution of contact centroids changes when the force shift, due to friction, is considered. The GH articulation is achieved by a combination of rolling and translative motion creating moment and friction respectively. The point of force transfer between the GH surfaces was shifted from the contact centroid by a distance equal to the ratio of the moment and the frictional force (Bergmann et al., 2007).

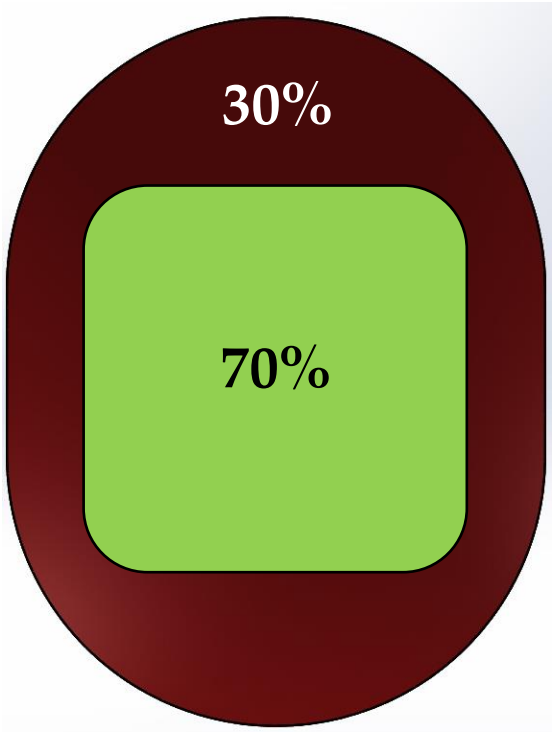

Figure 4.5 Schematic representation of the concentric (green) and the eccentric (red) regions of a glenoid prosthesis.

On an average, this shifting occurred by 3mm. To plot the point of force transfer between the surfaces, the contact centroids were shifted by the average value and it was found that 74% of the RoM produced eccentric loading while the rest were still within the concentric loading region (Fig. 4.6 b). Hence a need was realized to develop a prosthesis with the potential to reduce the eccentric loading, especially in the superior region. The most probable anatomical glenoid prosthetic design that could achieve this functionality could be pear-shaped. This kind of designs has been previously reported in the literature (Hopkins, 2004; Schrumpf et al., 2011) and hence could not be considered an original design concept. Modifications to this design would be made, on the AP axis, and testing this glenoid design would also aid in validating the study explained in Chapter 6.

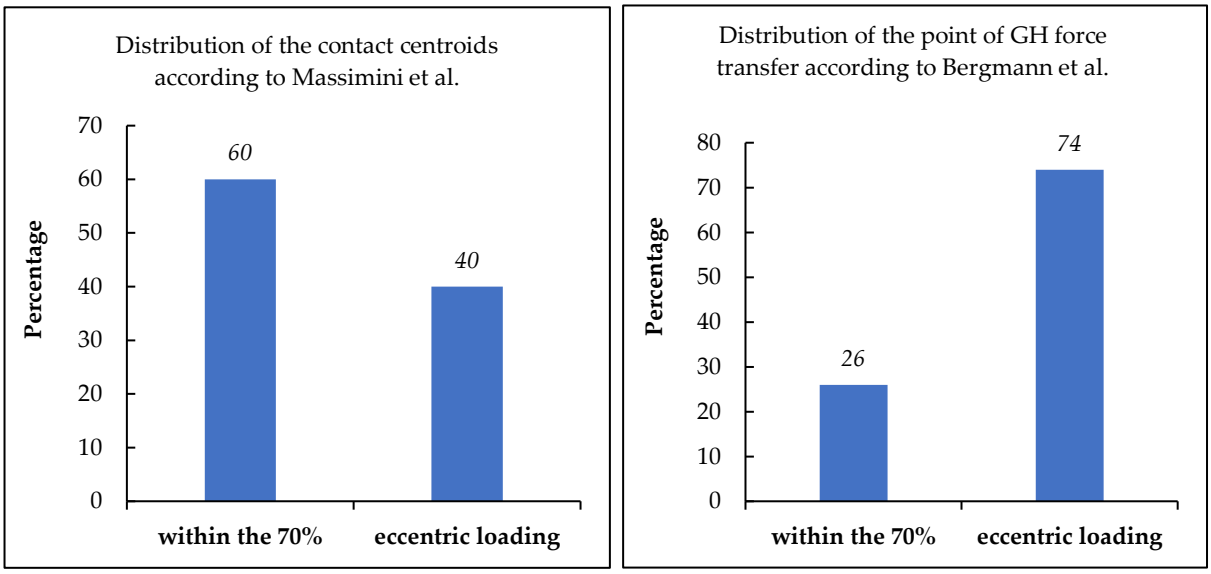

(a) (b)

Figure 4.6 (a) The position of the contact centroid on the glenoid cup during RoM (b) The positions of the contact centroid when the force was taken into account, for every RoM.

In order to reduce the surface area through which the eccentric load may get transferred and to reduce the overhang of the prosthesis around the glenoid it was essential to truncate the edges of the glenoid component. Truncation of the prosthesis created a pear-shaped structure which resembled the anatomical shape better than the existing prostheses (Fig. 4.7 a-b). The average anatomical difference between the superior and inferior AP margins was found to be 7.1mm and the ratio between the same was observed to be 1.44 (Mamatha et al.,

2011). To provide higher AP stability, the difference between the AP margins was increased to 11mm and the ratio was increased to 1.55. These dimensions are subject to vary in the future according to the observations made during the future tests.

Reduction in the available translation region on the superior aspect glenoid might be a concern for this implant. This feature has been linked with reduction of GH RoM (Williams & Abboud, 2005). The aim of this implant was to reduce eccentric loading. By providing adequate thickness to the implant this aim could be achieved. It would be interesting to observe any signs of reduction in RoM during the musculoskeletal study. If any reduction was observed necessary design changes would be made both to the GH mismatch in order to provide more room for the humeral head prosthesis to translate on the glenoid.

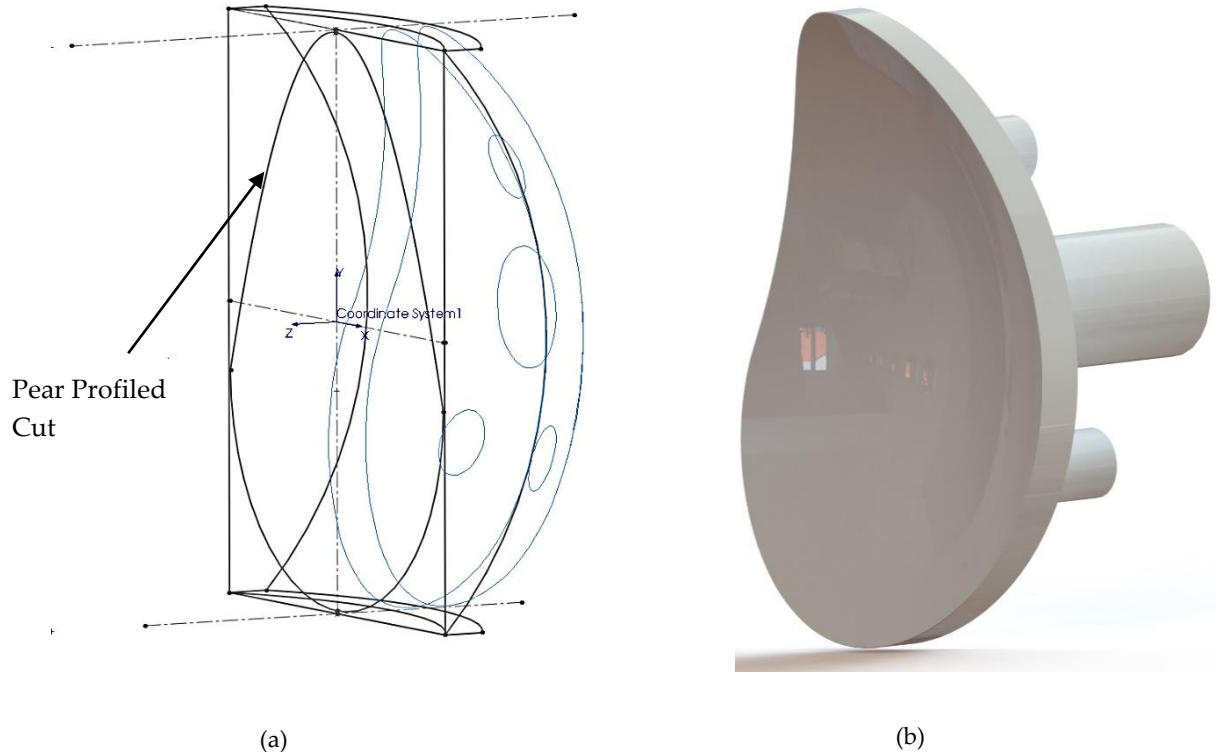

(a) (b)

Figure 4.7 The cutting profile used to convert the spherical shape of the glenoid was modified into the (a) pear shape to create the (b) final model.

4.3.3.3 The Compartmental design

The GH forces transverse radially outwards, from the point of contact, on the surface of the glenoid component (Buchler et al., 2002; Wang et al., 2005; Zhang et al., 2013). Hence, the prosthesis periphery is subjected to eccentric loading caused by a component of the GH joint force. To reduce this eccentric load transfer sections of the glenoid cup were removed to create a glenoid component best representing both the healthy (pear shaped) and the OA glenoid fossa (oval shaped)

Compartmentalising the prosthesis separated the surface into pear-shaped concentric and oval-shaped eccentric articular regions. The designed gap between these two regions was kept at 1mm, subjected to change based on further tests. The device was continuous in the anterior, posterior and the inferior aspect, while the eccentric transfer was restricted in the superior and the PI and the AI regions (Fig. 4.8 a-b).

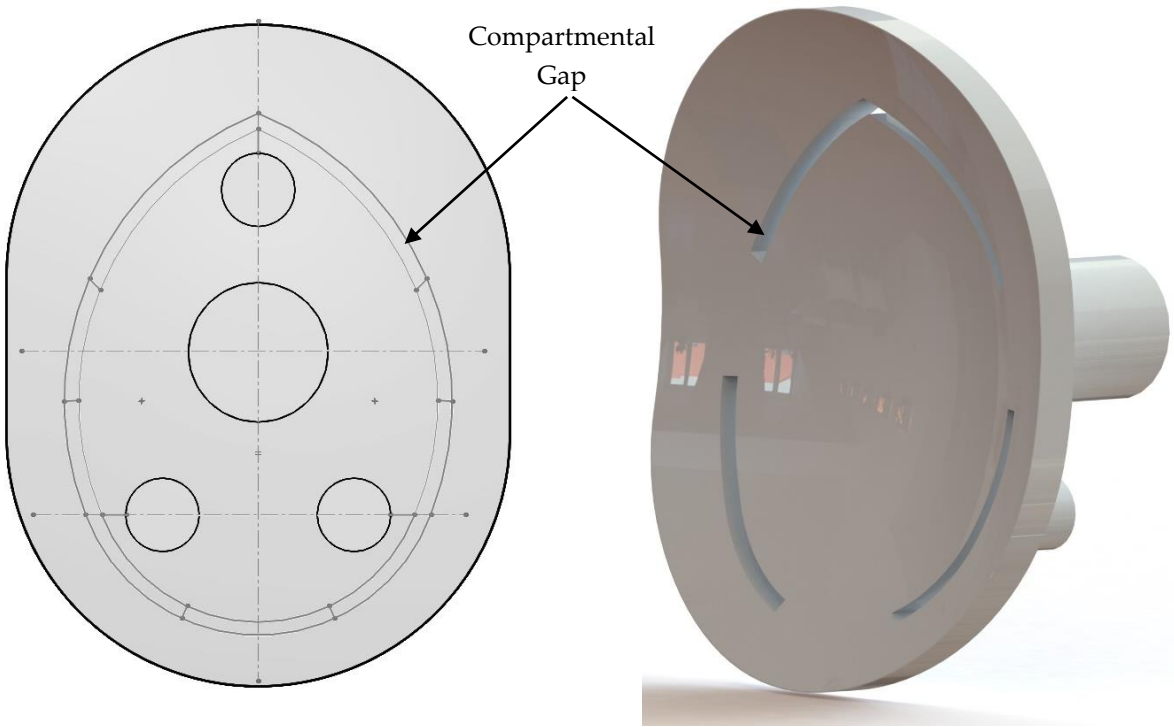

Figure 4.8 The original design of the oval glenoid was modified using (a) a pear-shaped cut around the superior and inferior pegs to create (b) the compartmental glenoid design.

4.4 An Overview of the Planned Testing Process

A schematic representation of the testing process is described in Chapter 1.5. All the designed prostheses, described in the current chapter, would be subjected to *in-silico* kinematic testing described in the following chapter. The observations made with the novel prosthesis designs would be compared to the control models of similar size. If the novel prostheses were found to significantly alter the GH kinematics, they would be redesigned. On the other hand, if no kinematic variations were observed after the introduction of the novel glenoid designs, these prosthetic cups would be subjected to a Finite Element (FE) analysis in Chapter 6. The glenoid cups are more susceptible to failure, in comparison to the humeral component, due to edge loading and hence the performance of the designed cups would only be investigated. It would have been interesting to study the effect of the force characteristics of the humeral head prosthesis with PP, but it is out of the scope of this thesis. It should also be kept in mind that the designs presented here are the first versions of the novel design concepts and appropriate recommendations would be provided after the FE analyses.

CHAPTER 5

Part of this chapter has been presented (poster) as:

Dey, R., Roche, S., Rosch, T. and Sivarasu, S. *Effect of humeral head shape on the contact radius, moment arms, and glenohumeral forces.* 8th World Congress of Biomechanics (WCB). Dublin, Ireland. (July 2018).

In-Silico Kinematic Testing of the Designed Prostheses

5.1 Introduction

Application of mechanical principles to the human body has been proven essential in understanding its functionality. Computerised musculoskeletal models enable the implementation of mechanically driven algorithms to study specific characteristics of biological joints. Muscle moment arm, joint forces, muscle moments etc. during a motion, are few of these characteristics that could be studied using in-silico biomechanical models (Holzbaur et al., 2005; Kontaxis, 2010).

Post-surgical kinematic changes are common. Investigating the extent to which these changes alter the joint biomechanics might be essential in limiting the risks of revision surgeries. Biomechanical models aid surgeons to make informed, engineering driven, changes to surgical practices and prosthetic designs. These changes are often intended to increase the mechanical advantage of the joint. There exists several shoulder and elbow musculoskeletal models, such as the Stanford VA Upper Limb Model (Holzbaur et al., 2005), the Delft Model (Nikooyan et al., 2010) etc., which allow an *in-silico* study of shoulder kinematics.

This chapter initially focuses on the development of a biomechanical model for a healthy shoulder. A previously validated upper arm model – Newcastle Shoulder Model (NSM) (Charlton & Johnson, 2006) was modified to create the patient-specific model. This chapter further describes the method to transform the healthy shoulder model into a post–TSA shoulder model. Basic overview of the normal functionality of GH joint and the roles played by various muscles is also described. This would be necessary to comprehend the pre – and post – surgical kinematics reported by this study. The current chapter reports on the muscle moment arms observed for the healthy and all the post – TSA models developed.

5.2 Movements of GH Joint

The Sagittal, Coronal, and Horizontal/Transverse planes equally divide a human body (Fig. 5.1). These static planes could also be used to describe the movements of the upper limb, originating from the GH joint.

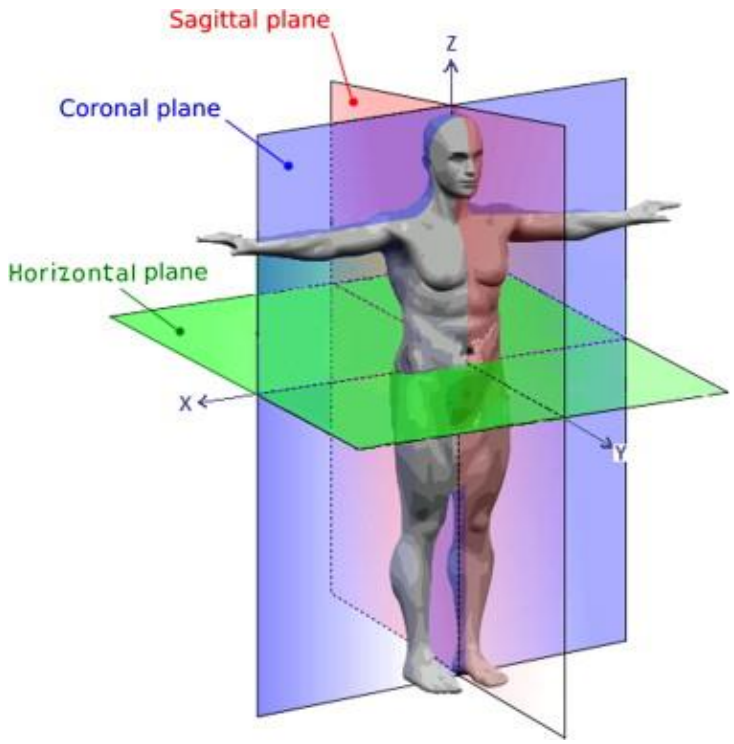

Figure 5.1 Cardinal planes of the human body. s*ourced from* (Marras et al., 2010).

The GH joint, by the virtue of its osseous geometry, is the most mobile articulation in a human body. The humeral head translates and rolls on the glenoid cavity surface. The articulating surfaces are held in position by the soft tissues surrounding the bones. Apart from this, it has been observed that the negative intra-articular pressure inside the GH joint, under loading, also contribute towards the stability of the joint (Halder et al., 2000; Kent, 1971).

In the Coronal plane, the abduction and the adduction of the arm could be observed. During this motion, the scapula moves upward and outward and the humerus elevates by an arc of 120° - 164° (Culham & Peat, 1993; Gill et al., 2006; Kent, 1971). Adduction could be

defined as the motion that is opposite to that of abduction and hence, its range depends on the arc made by the humerus during depression from the highest point of abduction to the anatomical position (Fig. 5.2).

Forward flexion and extension of the upper arm occur in the Sagittal plane. During flexion, the scapula slides anteriorly outwards and the humerus elevates within the range of 120° - 159° (Gill et al., 2006; Kent, 1971). The maximum range of extension movement (hyperextension) has been reported to be 55°. A combination of the abduction, adduction, flexion, and extension is called circumduction (Fig. 5.2). The internal and external rotation of the humerus also known as medial and lateral rotation takes place on the Transverse plane. The maximum observed range for medial rotation lies between 65° and 90° and the maximum range for lateral rotation lie within 85° and 90°.

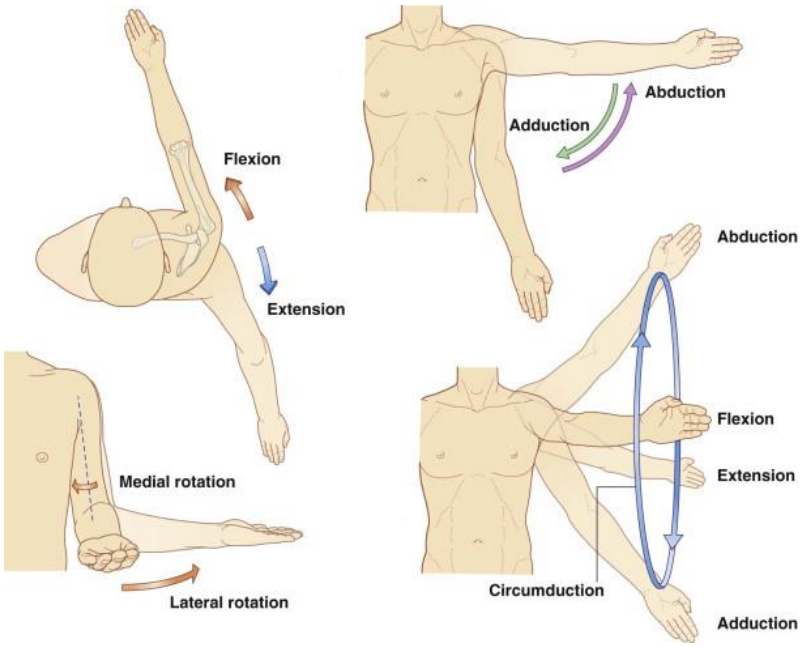

Figure 5.2 The movements allowed by the GH joint. *sourced* from (Drake et al., 2015)

5.3 Muscles of the GH joint

5.3.1 The Rotator Cuff Muscles

The rotator cuff muscles (Fig. 5.3) play a major role in the dynamic stabilization of the GH joints and appropriate loading of the humeral head, aiding it to rotate or translate on the

glenoid fossa. The rotator cuff group constitutes of the supraspinatus, the infraspinatus, the teres minor and the subscapularis (Halder et al. 2000). Among the four rotator cuff muscles, the subscapularis lies anteriorly with respect to the scapula and attach to the lesser tuberosity of the humerus while the other three muscles lie posterior to the scapula and attaches to the greater humeral tuberosity. The supraspinatus muscle runs superior to the scapular spine while the infraspinatus and the teres minor muscles run inferior to the scapular spine (Drake et al., 2015; Halder et al., 2000).

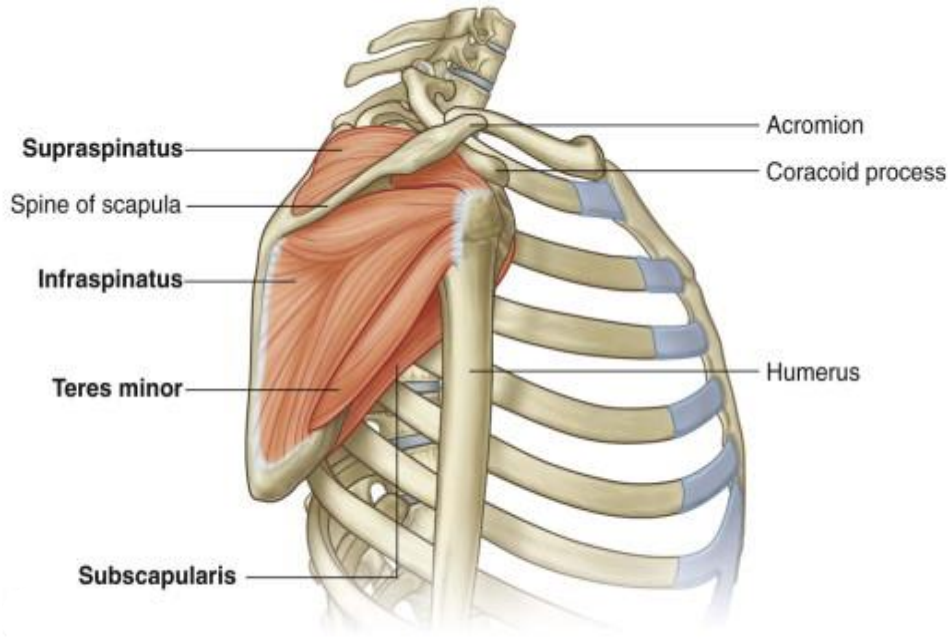

Figure 5.3 Rotator Cuff group of muscles. s*ourced from* (Drake et al., 2015)

This group of muscle enables forward flexion and abduction. The activity of the infraspinatus and the teres minor were observed to peak during the end of abduction and the early and last phases of flexion. They also prevent posterior dislocation of the humeral head. The force required to produce external rotation was found to be shared by the infraspinatus and teres minor in a ratio of 3:2. The supraspinatus works as force couple with the deltoid. It assists in initiating the forward flexion and also facilitates abduction after it has been initiated by the deltoid. It further reduces the superior translation of the humeral head. The

subscapularis muscle was found to be most active during the middle phases of forward flexion and abduction. Being anterior to the scapula, this muscle was found to produce high internal rotation forces and also played an important role in preventing inferior and anterior dislocation of the humeral head (Halder et al., 2000; Kent, 1971).

5.3.2 The Deltoid

The deltoid muscles (Fig. 5.4) could be divided into three parts; the anterior deltoid, the middle deltoid and the posterior deltoid. The middle and the posterior deltoid originate from the scapula and the anterior deltoid originate from the clavicle. All the parts converge and insert into the lateral aspect of the humeral shaft (Drake et al., 2015).

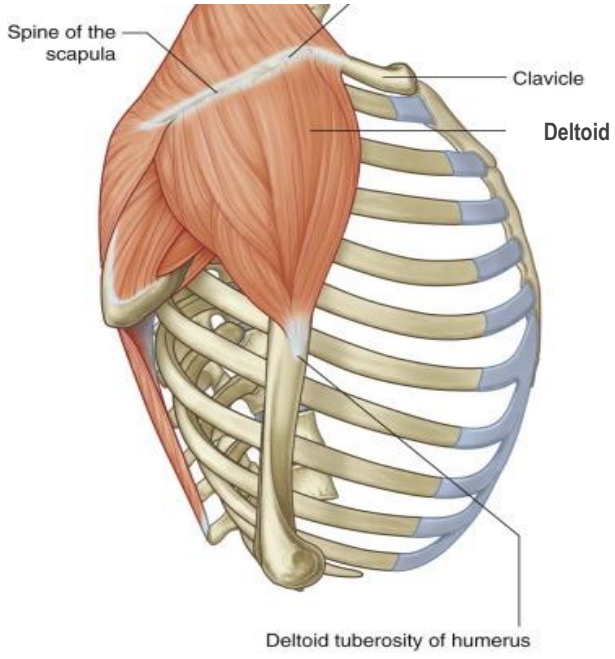

Figure 5.4 Deltoid group of muscles. s*ourced from* (Drake et al., 2015).

The line of action of the deltoid muscles is similar to that of the supraspinatus muscle. The deltoid contraction results in superior humeral head translation. To prevent the humeral head from superior impingement and to provide continuous articulation of the glenoid and the humerus, the teres minor, the subscapularis and the infraspinatus balance vertical pull of

the deltoid. The deltoid is the primary abductor of the GH joint. The middle deltoid initiates the abduction motion which is then taken over by the anterior and the posterior deltoid. The anterior and the middle deltoid also perform a majority of the adduction. The anterior deltoid and the posterior deltoid contribute to the motion of flexion and extension respectively (Culham & Peat, 1993; Halder et al., 2000).

5.3.3 Other Muscles

A synergy of muscle movements enables the GH joint to achieve its complete RoM. The scapulohumeral rhythm (SHR) is one of the examples of this synergy. The SHR could be best observed during the flexion and abduction. In these two motions, the ST joint was always observed to begin the motion and, in adults, it shared the motion with the GH joint in a ratio of 1:2 (Halder et al., 2000; Kent, 1971). Alongside the rotator cuff and the deltoid muscle groups, which are responsible for most of the GH movements, there are other muscles which are essential for GH motion and stability.

The pectoralis major and the latissimus dorsi connect the thoracic cavity to the humerus. These two muscles anchor the bone on the thoracic cavity and take part in extension, internal rotation and the adduction of the GH joint (Jeno & Bhimji, 2018; Kent, 1971).

The levator scapulae, rhomboids, serratus anterior, and trapezius join the thoracic cavity and the scapula. The serratus anterior attaches to the inferior aspect of the anterior scapula providing horizontal stability and the trapezius, rhomboids, and levator scapulae attaches to the superior and medial aspect of the medial scapular margin providing vertical stability. Collectively, these muscles prevent the winging of the scapula. The serratus anterior muscle draws the scapula anteriorly while the superficial trapezius and the deep-seated rhomboids & levator scapulae elevate the scapula (Gilroy et al., 2008; Kent, 1971).

The teres major, coracobrachialis, biceps, and triceps join the scapula and the humerus. The teres major originates from the posterior scapula and inserts near the intertubercular groove of the humerus. It facilitates adduction, internal rotation, and extension of the GH joint (Halder et al., 2000). The long head of the biceps superiorly stabilizes the GH joint as it passes

through the humeral intertubercular groove inserting into the supraglenoid tubercle (Culham & Peat, 1993; Halder et al., 2000). The coracobrachialis originates from the coracoid process while the triceps long head originates from the infraglenoid tubercle. Though both of these muscles take part in the adduction of the joint, the triceps also allows extension while the coracobrachialis muscle allows flexion of the GH joint (Halder et al., 2000).

5.3.4 Muscle Moment Arm

During any movement of the GH joint, muscles change in length by extending or shortening. This depends on the effect the muscle has on that movement. Clinically, muscle moment arm could be defined as the factor with which the efficacy of a muscle's potential to generate movement in a joint could be measured (Ingram et al., 2015; Sherman et al., 2013). The muscle moment arm is a scalar ratio measure using the tendon excursion method (An et al., 1983). This method, as implemented in OpenSim, calculates the displacement of the muscle tendon, at the point of attachment, for every degree of movement produced (Ackland et al., 2008; Sherman et al., 2013).

5.4 The Motion Testing Pipeline (MTP)

To investigate the effect of the designed implants on GH kinematics, an in-silico musculoskeletal study was designed. This involved developing an OpenSim shoulder model using 3D reconstructed bone models. This model was further used to implant the control TSP and the designed prostheses. To these models, a set of pre-defined RoM was applied and muscle moment arms were measured. The overall set-up was based on the original Newcastle Shoulder Model (NSM) (Charlton & Johnson, 2006), the access to which was facilitated by the collaboration with the Hospital for Special Surgery (HSS), New York City, New York, USA.

5.4.1 Developing the Control Musculoskeletal Model

A CT scan belonging to a healthy subject was selected to create the solid model of the upper thorax. The model consisted of 6 bone segments, i.e., the thorax, the scapula, the humerus, the radius and the ulna. The reconstruction of the bones was performed in Materialize Mimics®.

Since there are no OpenSim model that accurately represents a post-TSA GH joint, it was necessary to build a musculoskeletal model from scratch which can be later modified into a post-TSA articulation by introducing the prosthesis designs.

These bones were assigned independent coordinate systems. To assign these coordinate systems a combination of recommendations provided by the International Shoulder Group (ISG) and the ISB were used (Charlton & Johnson, 2006; Kontaxis, 2010; van der Helm, 1996; Wu et al., 2005). SolidWorks® was used to generate the coordinate systems for each section of the model. The thoracic cavity (Fig. 5.5) origin was placed on the center of the superior most arc of the manubrium, the Incisura Jugularis (IJ). The Y-axis was defined as the perpendicular line joining the centers of the lines connecting the Processus Xiphoideus (PX) to the spinal process of T8 and IJ to the spinal process of C7. The X-axis was defined as the line drawn parallel to the plane perpendicular to the plane formed by the C7, IJ and the center of T8 & PX. The common perpendicular line to the X and the Y-axis was defined as the Z-axis.

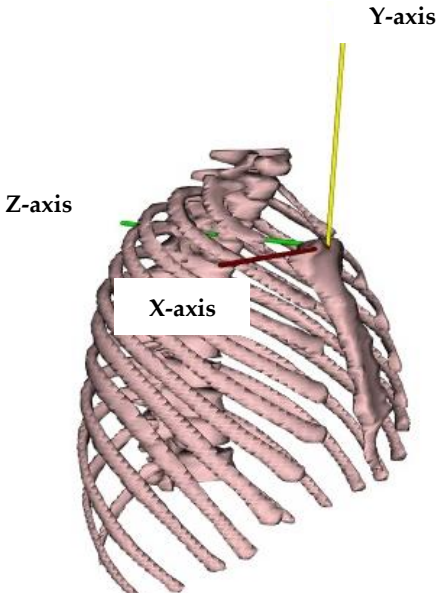

Figure 5.5 The thoracic co-ordinate system.

The origin for the clavicle was selected as the SC joint (Fig 5.6). The line connecting the SC and the AC joints was defined as the X-axis. The common perpendicular line to the clavicular X-axis and the thoracic Y-axis was defined as the clavicular Z-axis. Finally, the line perpendicular to both the Z and the X-axes was defined as the Y-axis.

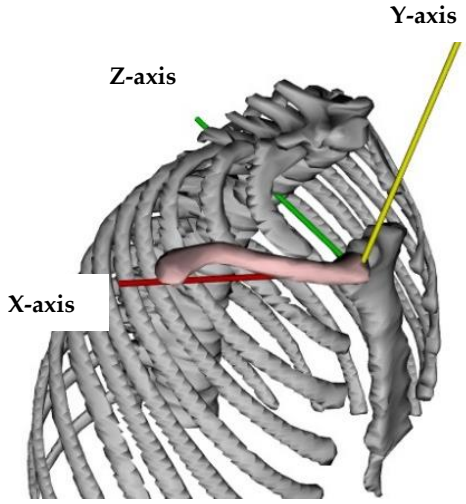

Figure 5.6 The clavicular co-ordinate system.

The origin of the scapula (Fig. 5.7) was defined as the Angulus Acromialis (AA), the most latero-posterior point of the bone. The extension of the line joining the medial point of origin of the scapular spine, Trigonum Spinae Scapulae (TSS), was defined as the X-axis. The posteriorly directed perpendicular line to the plane containing the AA, TSS, and scapular Angulus Inferior (AI) was defined as the Z-axis. The common perpendicular line to the Z and the X-axes was defined as the Y-axis.

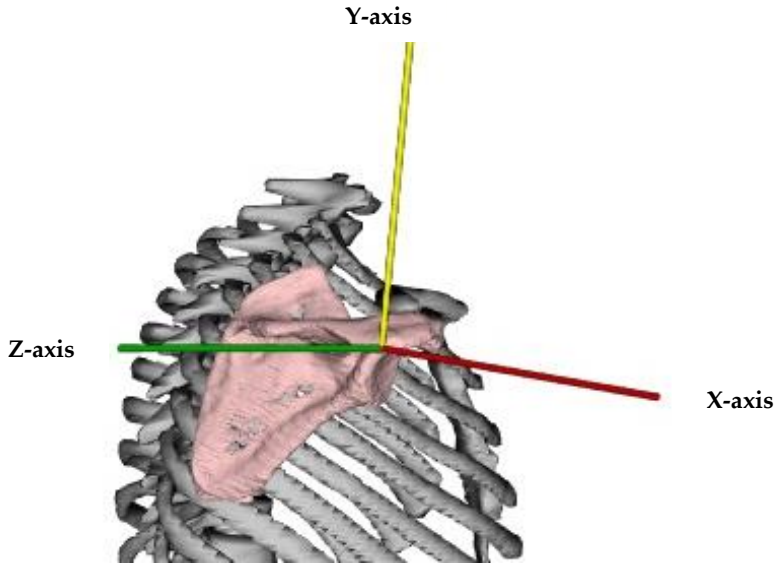

Figure 5.7 The scapular co-ordinate system.

The center of rotation (CoR) of the humeral head articular surface sphere was selected as the origin for the humerus (Fig. 5.8). The perpendicular line joining the CoR with the center of the line connecting the lateral edge (EL) and the medial edge (EM) of the humeral epicondyle was defined as the Y-axis. The perpendicular line to the plane consisting the CoR, EL, and EM was defined as the X-axis. Finally, the Z-axis was defined as the common perpendicular line to the X and Y-axes.

The center of the ulnar joint with humerus was defined as the origin for the bone (Fig. 5.9). The line joining the most medial point on the distal ulna, the Ulnar Styloid (US), to the center of the line joining the EL and EM was defined as the Y-axis. The perpendicular line to the plane consisting of US, EL, and EM was defined as Z-axis and the common perpendicular line to the Y and the Z-axes was defined as the X-axis.

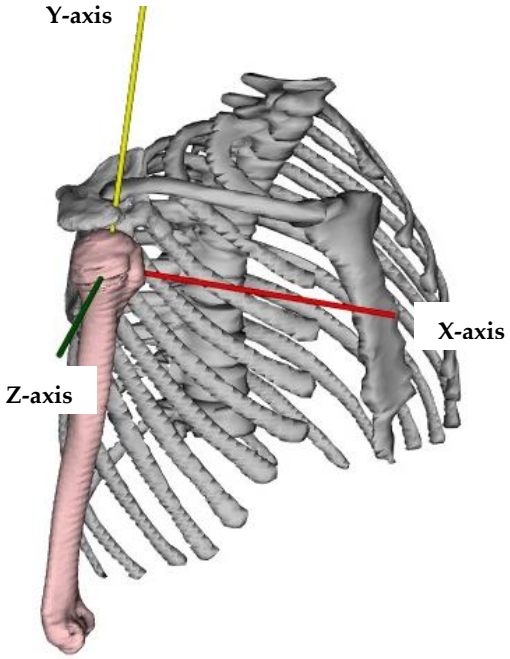

Figure 5.8 The humeral co-ordinate system.

The center of the radial head was defined as the center of the radius (Fig. 5.10). The line joining the most latero-distal point on the radial styloid (RS) to the EL was defined as the Y-axis. The X-axis was defined as the line perpendicular to the plane consisting of RS, US, and EL. Finally, the Z-axis was the common perpendicular line to the X and Y-axes.

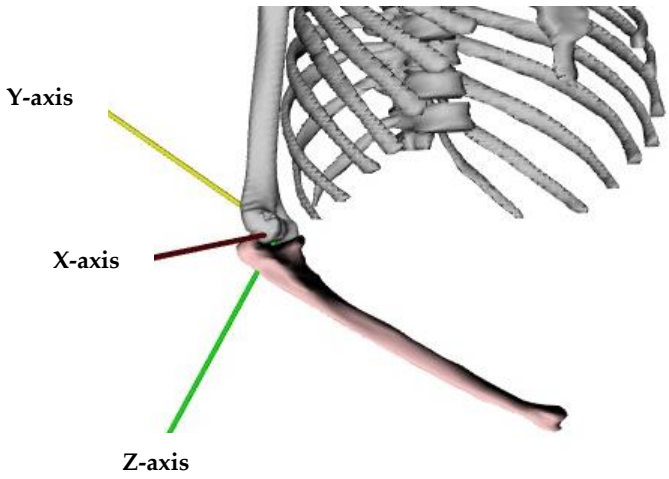

Figure 5.9 The ulnar coordinate system.

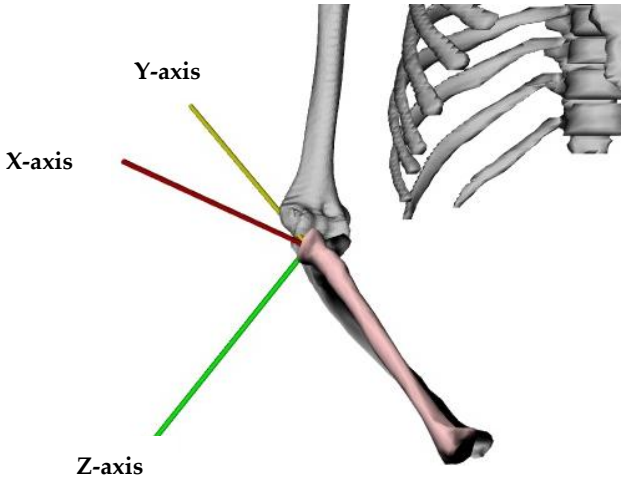

Figure 5.10 The radial coordinate system.

To create the final shoulder model (Fig. 5.11) a background OpenSim script (Appendix C) was generated. Biological joints were created using this API. A parent-child arrangement was designed, in between bones, to obtain an anatomically acceptable movement pattern. The topological view of the bone-to-bone interaction is displayed in (Fig. 5.12). The thoracic cavity was fixed to the default *"ground"* object of OpenSim platform. Further rotation and translation of the remaining bones were performed in accordance with Gilroy et al., 2008, to obtain acceptable upper body joints.

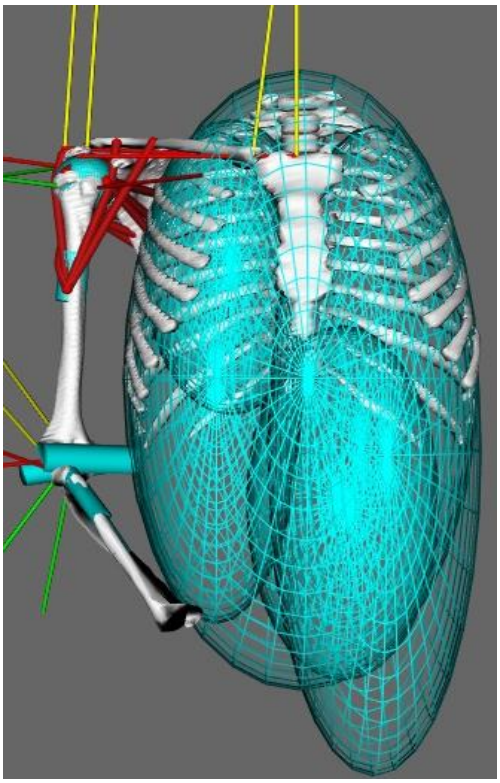

Figure 5.11 The complete healthy shoulder OpenSim model

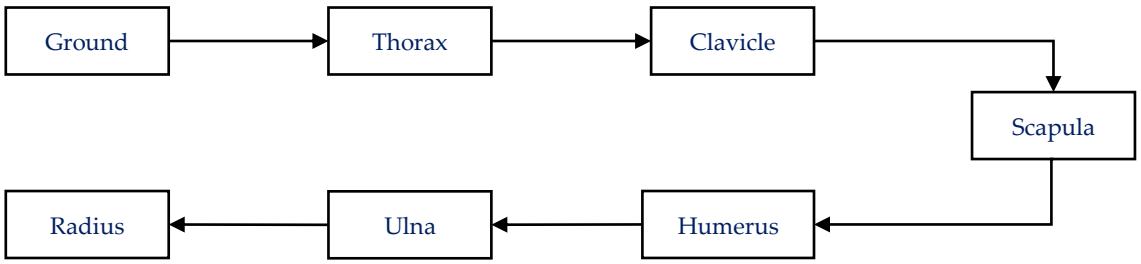

Figure 5.12 Topology of the OpenSim Shoulder model.

5.4.2 The Muscles Studied

The shoulder model (Fig. 5.11) consisted of all the muscles of the shoulder. For kinematic evaluation, the deltoid and the rotator cuff muscle groups were considered, in this study, as they are the principal contributors to the GH RoM. Although the other muscles were not deactivated, they were not considered for the study. To obtain anatomically coherent positions of the above muscles and to cover an acceptable area that the whole volume of

muscle would have otherwise covered, these elastically modeled structures were subdivided into fascicles. The division of each muscle into its fascicles was done according to Johnson et al., 1996. The anterior & posterior deltoid were divided into 2 fascicles and the middle Deltoid had a single fascicle. Among the rotator cuffs, the supraspinatus & teres minor had one fascicle each and the subscapularis & infraspinatus were divided into 3 fascicles each.

In a human body, every musculotendinous follows a certain path around bones etc., which affects its shape and functionality. To mimic this, wrapping objects (Marsden et al., 2008; Zarifi & Stavness, 2016) were introduced in the OpenSim model. Different geometrical shapes, such as cylinders, spheres, and ellipsoids, were used to mimic particular shapes of bone (Fig. 5.11).

5.4.3 Introducing the TSP to the Musculoskeletal Model

The prosthetic 3D models of the glenoid cup and the humeral head were introduced within the scapula and the humeral head models in the OpenSim setup (Fig. 5.13). The *in-silico* surgery to introduce the humeral head and glenoid prostheses were performed in a 3D modeling software, Materialise 3-matic® v 8.0.

The control prosthesis size of 56 mm (head and cup) with a height of 21 mm was found to best fit the resected healthy humerus and glenoid used to create the healthy musculoskeletal model. These bones were imported into the Materialise Mimics® environment and their coordinate systems were redefined to calculate the final rotation and translation sequences of the prostheses.

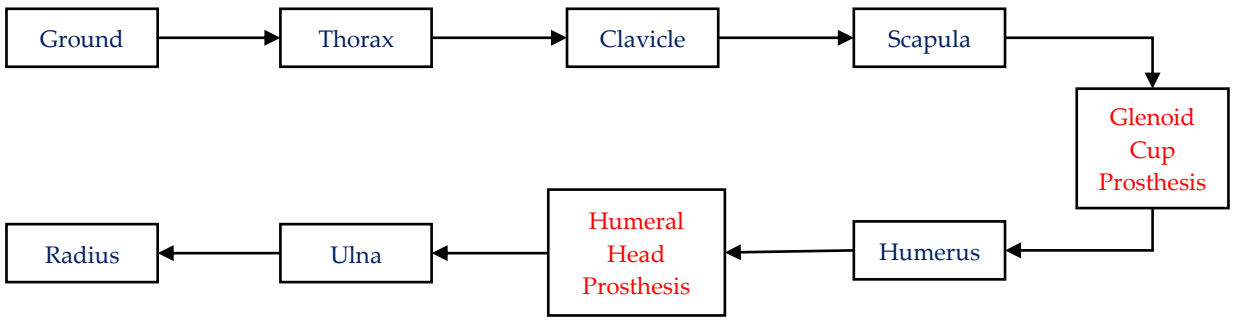

Figure 5.13 Schematic representation of the OpenSim TSP model topology.

The bones and their respective prosthesis replacements were manually superimposed in the most accurate manner. These combined structures were transferred from the Materialise Mimics® platform to the Materialise 3-matic® as a non-Manifold Assembly (NMA). Generally, the NMA feature allows Boolean operations to be performed between entities of the assembly (Gursoz et al., 1991). In both the cases, the bones were defined as the primary objects and the prostheses as the intersecting objects creating the NMA. To create the resected bones, intersecting objects were subtracted from the assembly and the remaining resected bones were re-imported into the Materialise Mimics® environment (Fig. 5.14 & Fig. 5.15 a-b).

The 3D prostheses models were re-introduced to calculate the rotation and translation required to accurately place them on the resected bones. For the glenoid prosthesis, the translation distance, in 3D, was calculated between the AA and the glenoid center (GC). The humeral head translation was the distance between the prosthetic sphere center and the humeral head articular surface center. For both the cases, the rotational matrix was calculated using a MATLAB script (Appendix D) which used the SI and AP edges of the prostheses as input.

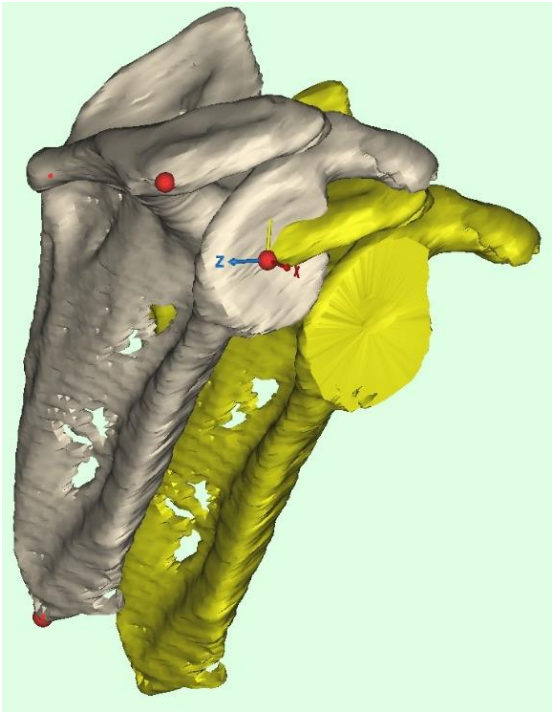

Figure 5.14 The glenoid resection process. The grey scapula represents the original scapula model while the yellow scapula represents the reamed scapula shifted according to its own coordinate system centered at AA.

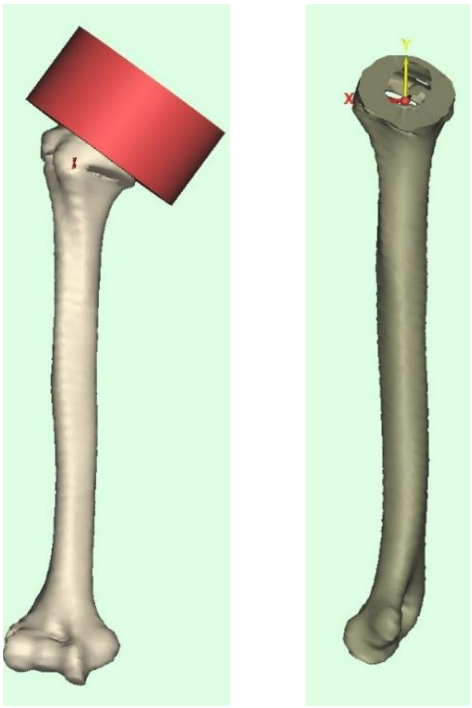

(a) (b)

Figure 5.15 The humeral resection. (a) The process of resection using a cylindrical object propagated from the prosthetic base. (b) the resected humerus with its coordinated system with its origin at the center of the humeral head sphere.

The final post–surgical OpenSim model (Fig. 5.16) was created by including the prosthetic parts. The orientation of the prostheses was edited in the background code (Appendix E). The translation was introduced in millimeters and the rotation in radians.

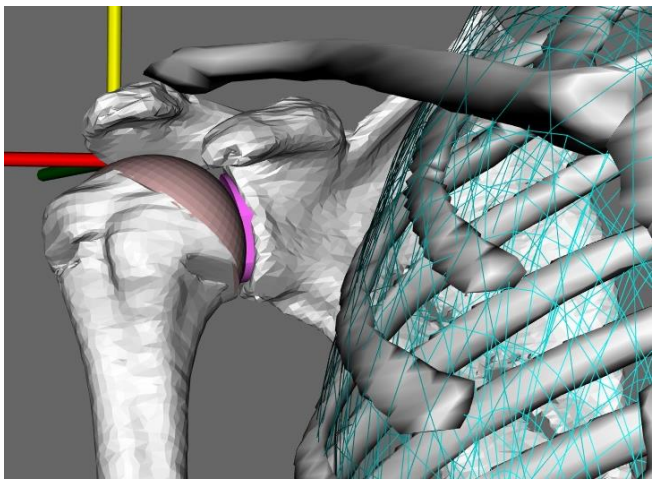

Figure 5.16 The final OpenSim TSA model with the articulating prosthetic surfaces.

5.4.4 The Induced RoM and Calculation of the Kinematic Parameters

The GH movements introduced to all the OpenSim models were generated using regression equations describing healthy scapular and clavicular RoM (Barnett et al., 1999; Marchese & Johnson, 2000). This has been previously implemented in a study by A Kontaxis & Johnson, 2009, analyzing post-RTSA kinematics. Four sets of standard GH RoM were induced this included abduction (0° to 150°), forward flexion (0° to 150°) and lateral to medial rotation (-90° to 60°) with the arm held at 20° & 90° of abduction. The kinematic parameter calculated was the muscle moment arms of the deltoid and the rotator cuff muscles.

A custom MATLAB script was generated to induce the motion and calculate the momenta arms using inverse kinematics. Appendix F provides an example of the code for a single motion (e.g. abduction) induced to calculate moment arms for middle deltoid muscle. A dummy joint was introduced in all the OpenSim models. This joint was placed in the same orientation and location as the GH CoR. This dummy joint was used as the fixed point, from where the moment arms were calculated while the humerus moved in accordance to the induced motion.

5.5 Observations from the Musculoskeletal Models

The objective for developing the anatomical shoulder OpenSim model was to investigate if any kinematic differences were induced in the joint by the population-specific prosthetic heads or the newly designed prostheses. In the real world, muscle moment arm variations are more prominent in RTSA[2] than in TSA, as the ATSP is designed to maintain the biological GH joint geometry (Ackland et al., 2012, 2010; Kontaxis, 2010). This section would, in detail, discuss the observations from all the OpenSim model created. The long-term aim of this research endeavor is to generate prosthetic models to reduce the RHE. The results from the current kinematic study could be used to validate any future cadaver testing rig in the future where one or more of the designed prostheses' kinematic performance could be investigated.

[2] Majorly in deltoid in the absence of a rotator cuff muscle group.

Table 5.1 Maximum values of the muscle moment arms observed in this study and comparable values described in the literature. The positive moment arm values indicate that the muscle had the highest effect towards the motion at that corresponding angle. Negative moment arm depicts that no effect by the muscle, on the motion, was observed. Negative angles represent external rotation

Maximum muscle moment arm in mm (GH angle)				
Muscles	**Abduction**	**Flexion**	**Internal rotation at 20° abduction[3]**	**Internal rotation at 90° abduction[4]**
Anterior Deltoid	43.72 (150°) [a]	21.01 (70°) [a]	4.95 (60°) [a]	3.48 (-90°) [a]
	30.2 (120°) [b]	40.0 (120°) [b]	0.5 (-90°) [d]	0.9 (45°) [d]
Middle Deltoid	35.01 (75°) [a]	42.1 (150°) [a]	2.59 (-90°) [a]	3.38 (-90°) [a]
	29.1 (86°) [b]; 32.0 (90°) [c]	12.2 (120°) [b]	1.0 (-90°) [d]	4.6 (-90°) [d]
Posterior Deltoid	9.80 (55°) [a]	32.37 (150°) [a]	-0.86 (60°) [a]	-1.70 (60°) [a]
	2.00 (120°) [b]	-16.3 (120°) [b]	0.0 (-90°) [d]	7.5 (-90°) [d]
Teres Minor	22.52 (150°) [a]	-1.17 (0°) [a]	-7.23 (-90°) [a]	9.98 (60°) [a]
	5.10 (120°) [b]	2.2 (120°) [b]	-10.0 (-90°) [d]; -6.0 (45°) [e]	-4.5 (-90°) [d]; -16.0 (-90°) [e]
Subscapularis	0.11 (0°) [a]	25.41 (150°) [a]	23.29 (10°) [a]	22.1 (0°) [a]
	4.25 (2.5°) [b]; 8.8 (0°) [c]	23.3 (2.5°) [b]	20 (-10°) [d]	7.12 (30°) [d]
Supraspinatus	22.85 (60°) [a]	14.78 (0°) [a]	13.17 (60°) [a]	13.17 (60°) [a]
	25.0 (6°) [b]; 30.0 (30°) [c]	42.5 (2.5°) [b]	5.0 (45°) [e]	-2.0 (45°) [e]
Infraspinatus	20.85 (150°) [a]	-1.15 (0°) [a]	-1.88 (-90°) [a]	-6.33 (-90°) [a]
	12.5 (53°) [b]; 10.0 (15°) [c]	5.65 (76.5°) [b]	-6.0 (-90°) [d]; -2.0(45°) [e]	0.01 (-90°) [d]; -9.0 (45°) [e]

[c]current study; [b](Ackland et al., 2008); [c](Liu et al., 1997); [d](Ackland & Pandy, 2011); [e](Langenderfer et al., 2006)

[3] Current study observations compared to internal to external rotation performed at [d]30° and [e]10° abduction.

[4] Current study observations compared to [e]60° abduction.

5.5.1 Model Validation

The observed healthy muscle moment arms of the rotator cuff and the deltoid groups for the four different motions were plotted (Fig. 5.18, Fig. 5.20 - 5.22) and compared to previous studies (Ackland et al., 2008; Ackland & Pandy, 2011; Langenderfer et al., 2006). As the GH joint goes through the induced motion, the instantaneous muscle moment arm changes. Table 5.1 reports the maximum moment arm observed in the current study and from previous *ins-silico* and cadaver musculoskeletal studies.

The instantaneous muscle moment arms, when plotted against the respective joint angle provides a moment arm profile for each muscle. In all the graphs, described below, a positive moment arm represents a higher influence of that muscle on the induced movement. Whereas, a negative moment arm indicates that the muscle would be more effective in reversing that motion (e.g. adducting after abduction).

5.5.1.1 Moment arms during Abduction

The middle deltoid, anterior deltoid, and the supraspinatus muscles were observed to have the largest increase in moment arm with the increase in abduction joint angle. The middle deltoid was found to have the most influence (90^{th} percentile = 34.85mm) on the motion between 65° to 85° abduction with the peak moment arm of 35mm at 75°. This observation was in-line with the middle deltoid moment arms observed in a cadaver study by Ackland et al., 2008, where they reported a maximum middle deltoid moment arm of 29mm measured at 86° abduction (Fig. 5.17).

The initial reduction of the middle deltoid moment arm, from 0° to 15° abduction, was due to the unwrapping of the muscle from its respective spherical wrapping object. Increase in the anterior deltoid moment arm was observed above 35° abduction (Fig. 5.18). The peak moment arm for anterior deltoid was 44mm at 150° with the major influence between 130° to 150° (90^{th} percentile = 40.2mm). Ackland et al., 2008, observed the anterior deltoid moment arm to be highest at 120° with a value of 30mm. In the current study, the moment arm for anterior deltoid at the identical joint angle was observed to be 33mm.

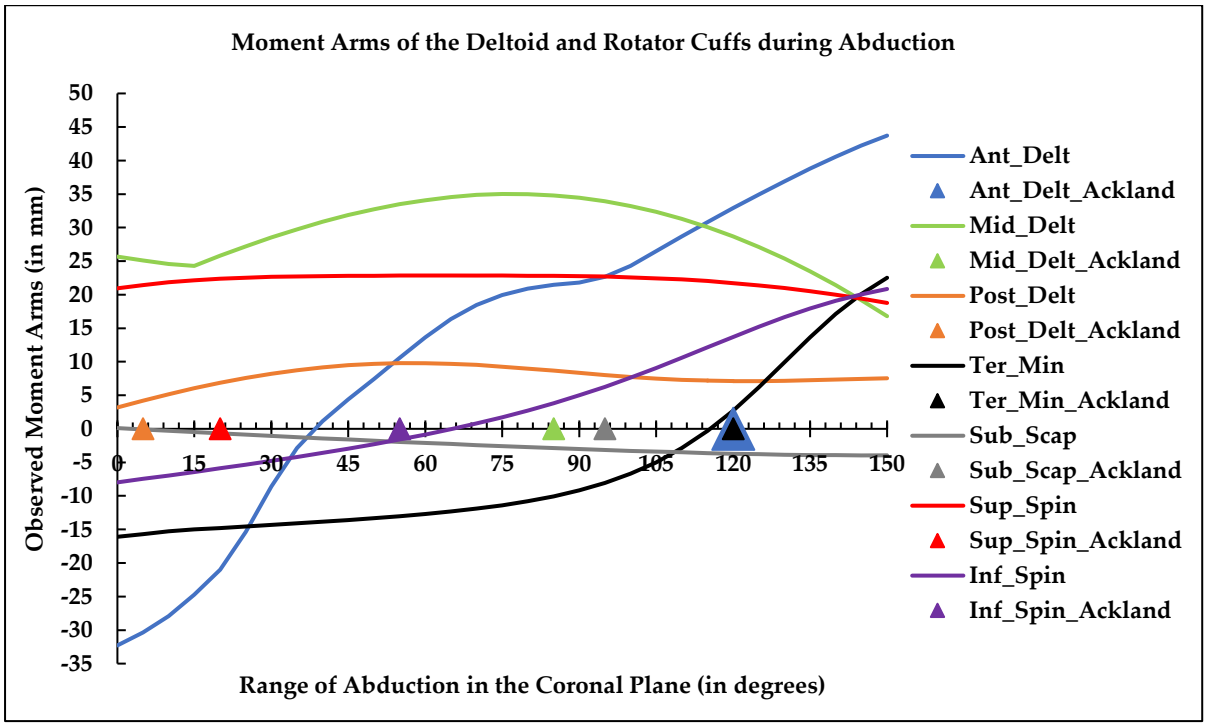

Figure 5.17 The observed moment arms of the deltoid and the rotator cuff groups during the arm elevation movement in the coronal plane represented by the solid lines. The pyramids represent the highest moment arm magnitude recorded during the same motion by Ackland et al., 2008, for a particular muscle (colour coded).

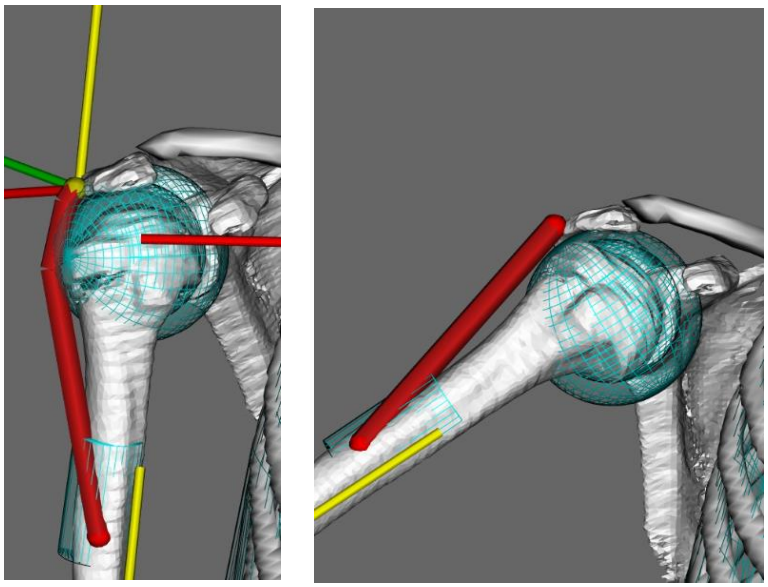

(a) (b)

Figure 5.18 Schematic representation of (a) wrapping of the middle deltoid muscle around the humeral head to resemble its anatomical shape and line of action. (b) straightening of the middle deltoid as it overcomes the influence of the wrapping object during abduction.

The differences found between the current study and literature could be, firstly, due to the fact that the earlier studies used a mechanical measurement device with freshly frozen cadaver arms while the current study aims at calculating the moment arms from the best possible representation of the GH musculoskeletal model using inverse kinematic representations from OpenSim. Secondly, the study by Ackland et al., 2008 induces a maximum of 120° abduction, hence they reported the abduction moment arm for anterior deltoid to be maximum at 120° whereas in the current study the maximum anterior deltoid moment arm was reported at 150° as it was the maximum abduction joint angle.

The supraspinatus muscle was found to have an almost constant moment arm during the motion with a difference between the highest observed moment arm and the moment arm at the start of the motion being ~2mm. The observed peak moment arm was measured to be 22.85mm at 75° abduction. This observation does not match with the reported mean maximum value of 25mm at 7° (Ackland et al., 2008). The study from the literature divides the supraspinatus muscle into its anterior and posterior aspects and reports a reduction in moment arm prior to 20° abduction. This also varies from the observations of the current study and the reason for these set of mismatching observations could be boiled down to the inaccurate SHR employed by the previous study. The previous study, did not consider the elevation of the scapula along with the humerus which could have affected the observations of the rotator cuff moment arms.

The teres minor, posterior deltoid, subscapularis and the infraspinatus muscles were observed to have relatively reduced effect on the entire abduction movement. The observations, in the current study, matches with the literature which reports minimal activation of the infraspinatus during the starting phase of the motion. While the previous studies reported an increase in infraspinatus moment arm between 15° to 25° abduction, the current study was only able to observe positive moment arm for the infraspinatus beyond 60° abduction (Ackland et al., 2008; Liu et al., 1997).

The infraspinatus moment arms were calculated, in this study, by measuring the average individual moment arms of the 3 segments (superior, middle and inferior) of the

muscle. The influence of the superior aspect of the muscle on abduction, was observed to occur earlier than the inferior aspects of the muscle as the former unwrapped from its spherical wrapping object earlier than the latter. Once unwrapped, the inferior aspect was found to have an increase moment arms at higher degrees of abduction as reported by (Ackland et al., 2008).

The moment arm profile of the teres minor was found to be identical with that reported in the literature. The muscle was observed to possess more adductive potential initially, its influence on abduction was more prominent beyond 110°. This transition was reported to occur earlier in cadaveric models and the highest moment arm was observed to be at 120° (5.1mm). The current study found the highest moment arm to be at 150° (22.5mm) and the value of moment arm at 120° (2.73mm) was found to be comparable to a previous musculoskeletal study by Ackland et al., 2008.

Posterior deltoid was observed to have an average abductive moment arm throughout the motion. The muscle was divided into 2 aspects (medial and lateral). The medial aspect was found have the least abductive moment arm compared to the lateral aspect of the muscle. No such differentiation was made in the cadaver studies. The current study observed an increase in moment arm between 20° to 40° abduction, this observation matches with the moment arm profile for the muscle reported by Ackland et al., 2008. Liu et al., 1997, reported posterior deltoid to be an adductor below 60° abduction, the study by Ackland et al., 2008, suggests that the muscle could be expected to be a contributor to the abduction motion above 70° abduction. Both the cadaver studies had more than one cadaveric specimen and the reported moment arm data was an average of all the individual moment arms. As the current study is limited to a single upper thorax model, it does not take into account the morphological variation which could affect the muscle moment arm.

The subscapularis muscle exhibited a constant reduction in moment arm and the highest ability to initiate adduction. The reported moment arms were average of 3 aspects of the subscapularis muscle (superior, middle and inferior). The superior subscapularis was observed to have the highest abduction moment arm among all the three. Literature suggests

that the subscapularis' effect on the abduction lasts for, on an average, 63° (Liu et al., 1997) and 15° (Ackland et al., 2008). The observations in this study suggest that the muscle was acting as a potential adductor between 15° and 63° of abduction with moment arms of -0.5mm and -2.3mm respectively. The overall bony geometry does play a role in determining the overall moment arm of a muscle, which might be a reason for the observed difference among the studies.

5.5.1.2 Moment arms during Forward Flexion

Apart from the infraspinatus and the teres minor muscles all the other muscles, under study, exhibited flexion moment arm either throughout the motion or during certain parts of it (Fig. 5.19). This observation is supported by a cadaveric study by Kuechle et al., 1997. Amongst the deltoid, the average anterior deltoid was observed to have the highest moment arm during the initial phase of arm elevation. The moment arm decreased post 70° of flexion. The initial observation was also reported by Ackland et al., 2008, but the subsequent reduction in moment arm was not found to be reported in the literature.

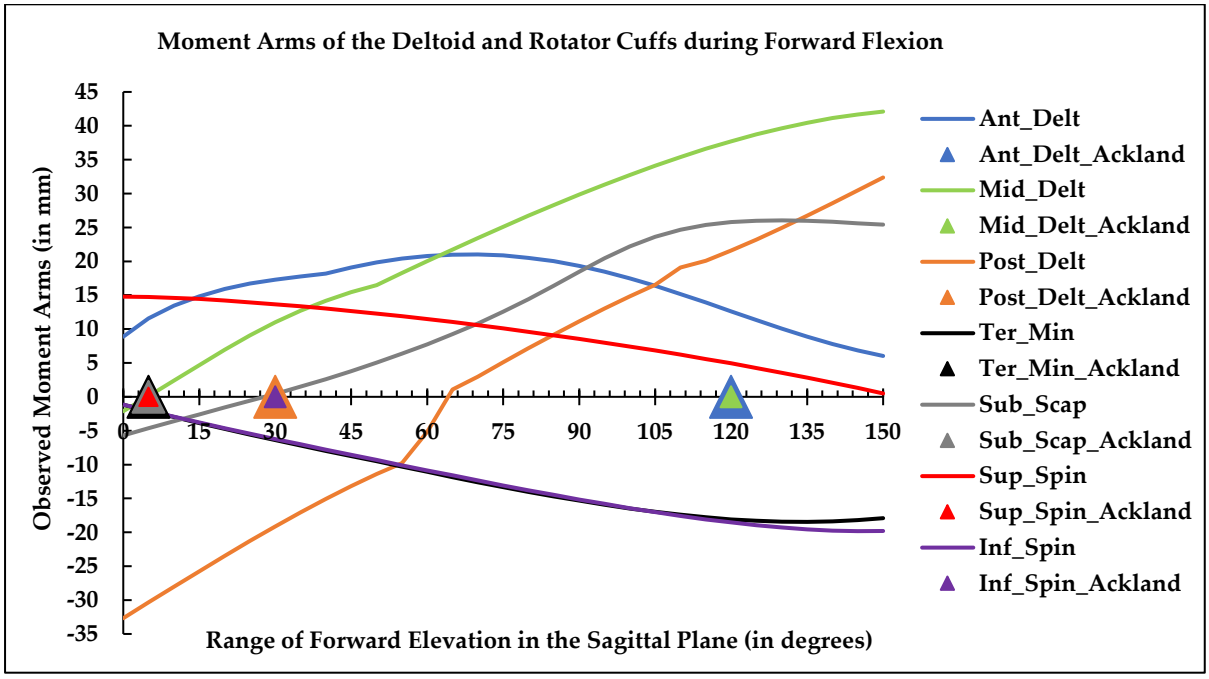

Figure 5.19 The observed moment arms of the deltoid and the rotator cuff groups during the arm elevation movement in the sagittal plane represented by the solid lines. The pyramids represent the highest moment arm magnitude recorded during the forward flexion by Ackland et al., 2008, for a particular muscle (colour coded).

In the current study, the anterior deltoid moment arm was found to be higher during the end of the abductive motion than flexion. The muscle was found to have the highest average moment arm during 60° to 80° of flexion (90th percentile = 20.84mm), with the highest value of 21mm at 70° of flexion.

Previous cadaveric studies reported the highest anterior deltoid during the end of the induced flexion movement (Ackland et al., 2008; Liu et al., 1997). In both the studies, the scapula was used only as the pathway to direct the line-of-action of the muscle force to cause the movement. No anatomically correct scapular rotation was induced mimicking the SHR. In the current study, it was observed that absence of SHR during arm elevation in the sagittal plane, the moment arm profile of the anterior deltoid (Fig. 5.20) almost exactly similar to that of the literature (Ackland et al., 2008; Liu et al., 1997).

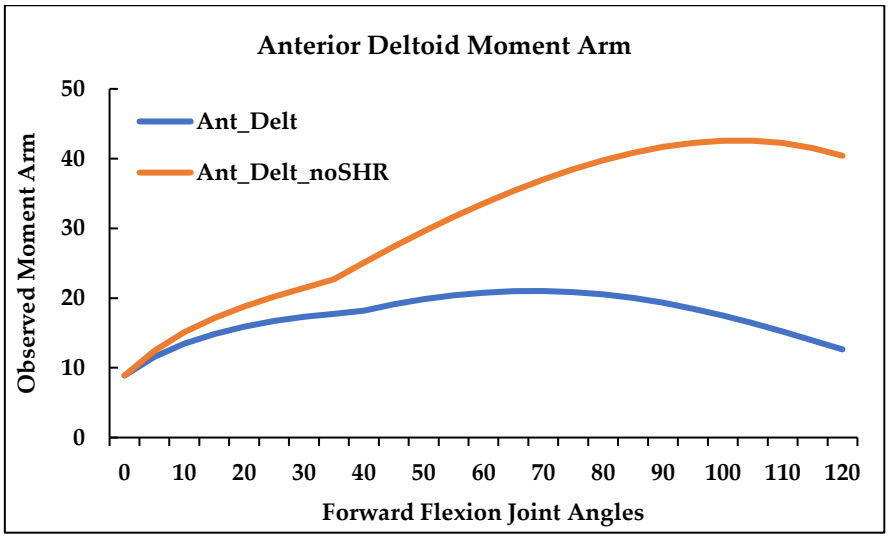

Figure 5.20 The changes in anterior deltoid moment arm observed during forward flexion with (blue solid line) and without (orange solid line) scapulohumeral rhythm (SHR).

The middle deltoid moment arm was observed to be higher moment arm than the anterior deltoid beyond 60° flexion. Liu et al., 1997, reported similar observations in their cadaveric study. The maximum moment arm of the muscle was observed to be at the end of the motion, 42 mm at 150° elevation. The middle deltoid moment arm, during flexion, was found to be higher than its abductive moment arm as was reported by the above-mentioned

cadaveric experiment. Positive moment arms were observed for the posterior deltoid above 60° flexion. This increase in moment arm occurred until the end of the motion and the highest observed moment arm value was 32.4mm at 150°. These observations are supported by the reported moment arm measurements by Liu et al., 1997, where sub-zero posterior deltoid moment arms were recorded from 0° to 60° flexion. The profile of the moment arm change also matches closely with the previous study mentioned above.

Subscapularis muscle moment arm was found to increase beyond 25° flexion with the maximum observed value of 26mm at 130°. It was found to have the maximum contribution to the movement 120° and 140° flexion (90^{th} percentile = 25.9mm). These observations were found to be in-line with the reported moment arm trend by Kontaxis, 2010. The cadaveric studies reported a reduction in moment arm for the muscle during flexion (Ackland et al., 2008; Liu et al., 1997). Consequences of neglecting the SHR was investigated for this muscle. The subscapularis moment arm during flexion without SHR was found to increase by an average of 4.9mm from 0° to 95° and decrease by an average of 7.5mm until the end of the motion. This could be a potential cause of the observed difference between the current study and the previous cadaveric ones.

The current study found that the range of inferior subscapularis moment arm was higher than the superior aspect of the muscle. The inferior aspect also had higher moment arm than its counterpart post 100° flexion. Wickham et al., 2014, found a higher volumetric contraction of the inferior supraspinatus, compared to superior, muscle during flexion. Whether this could be related to the higher moment arm demonstrated remains to be investigated. The subscapularis and posterior deltoid were the only muscles found to have both flexion and extension potential, this observation in line with past cadaveric studies (Kuechle et al., 1997).

As observed during the abduction, the supraspinatus was found to have the highest moment arm among all the muscles during the initial phase of the motion. This further suggests that the muscle plays an important role in bringing the GH joint surfaces together.

The highest value observed was 14.8mm at 0° of flexion, the moment arm value was further observed to reduce during the motion and at 150° flexion, the observed value was 0.5mm.

This trend was also observed by Ackland et al., 2008. The average infraspinatus and teres minor moment arm were found to have decreasing negative throughout the arm elevation in the sagittal plane. A similar trend was observed by Andreas Kontaxis, 2010, for infraspinatus. Ackland et al., 2008, reported increasing negative moment arm for teres minor. It is not abnormal for teres minor to have decreasing moment arm as was demonstrated by Liu et al., 1997, at certain angles of external rotation. The observations made in the current study is further supported by the cadaveric study by Kuechle et al., 1997, where the posterior rotator cuff muscles were found to have the highest depressing potential.

5.5.1.3 Moment arms during Medial Rotation

Internally rotating the humerus affected the rotator cuff moment arm more than the deltoid moment arms, irrespective of the abduction angle (Fig. 5.21 & 5.22). Among the deltoid, increasing the abduction angle from 20° to 90° increased the anterior deltoid by 9.65 mm at 90° external rotation. This observation is supported by our earlier records of increase in moment arm during abduction motion. Internally rotating the arm increased the anterior from -6.2mm to 5mm at 20° abduction, whereas at 90° abduction a decrease in moment arm was observed for the same muscle from 3.48mm to -4.7mm. This change in moment arm pattern for the anterior behavior has been reported in the literature (Ackland & Pandy, 2011).

Increasing the humeral elevation angle in the sagittal plane, during internal rotation, did not have a major effect on the middle and posterior deltoid and they were observed to decrease in both the cases. The posterior deltoid muscle was found to have the highest average moment arm, by magnitude, amongst the deltoid group. While Ackland & Pandy, 2011, reported a similar observation, Kuechle et al., 2000, reported anterior deltoid to have the highest moment arm. The variation in observation might be due to the authors of the latter study only considered deltoid moment arms during rotation at 90° abduction. At this instant, the current study was only able to observe an increase in anterior deltoid moment arm.

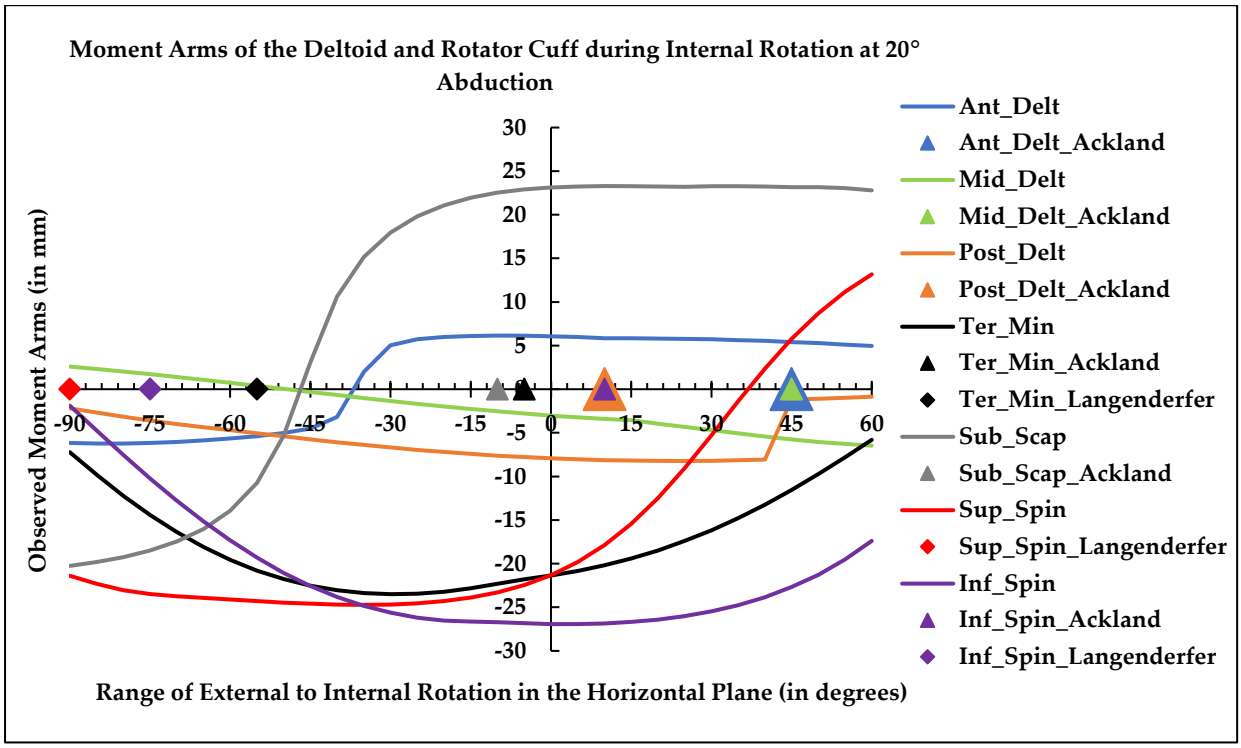

Figure 5.21 Rotator cuff and deltoid moment arms observed during maximum external rotation to maximum internal rotation motion, at 20° GH abduction, represented as coloured solid lines. The pyramids and diamonds represent the highest moment arm magnitude observed by Ackland & Pandy, 2011 and Langenderfer et al., 2006, respectively for a muscle (colour coded).

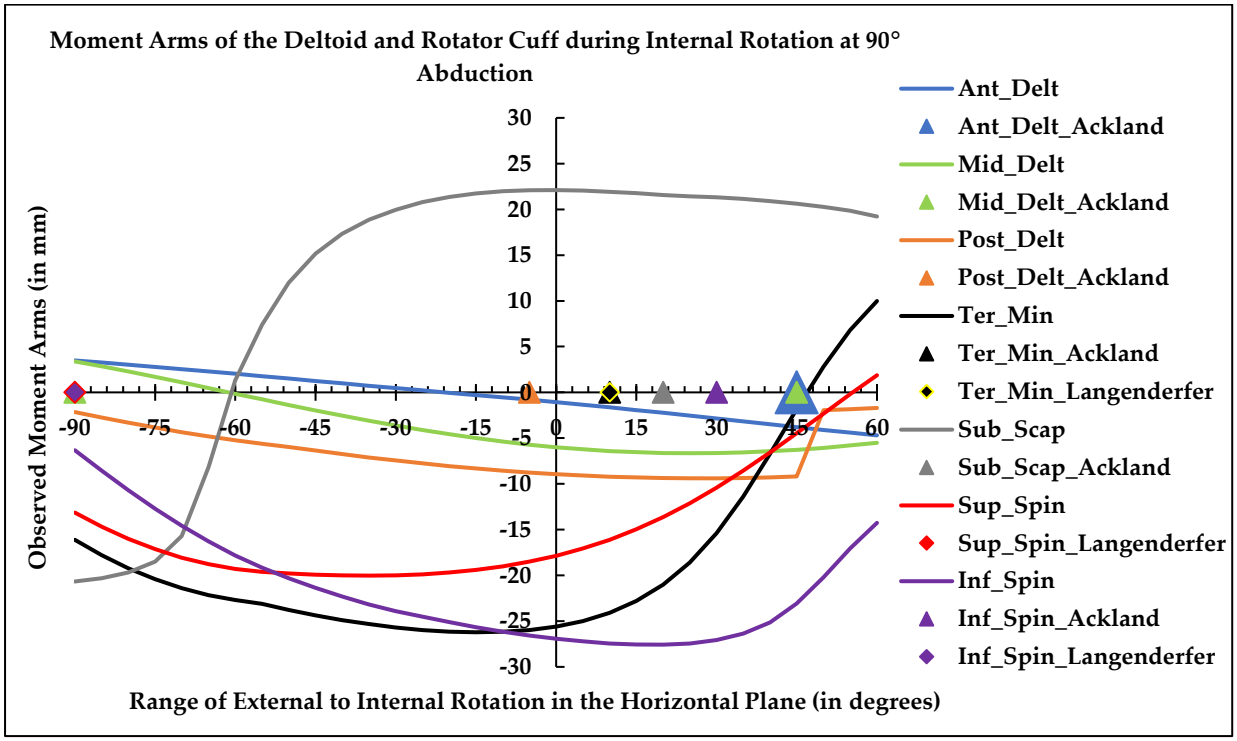

Figure 5.22 Rotator cuff and deltoid moment arms observed during maximum external rotation to maximum internal rotation motion, at 90° GH abduction, represented as coloured solid lines. The pyramids and diamonds represent the highest moment arm magnitude observed by Ackland & Pandy, 2011 and Langenderfer et al., 2006, respectively, for a muscle (colour coded).

The subscapularis muscle was observed to have the maximum internal rotation moment arm among all the rotator cuffs. During the initiation of the internal rotation movement, from the maximum external rotation, the muscle could be expected to have a very minimal effect on the motion. Its effectiveness increased post 48° and 62° of external rotation for 20° and 90° of abduction respectively. As the GH joint cross, the neutral rotation position, the muscle moment arm was observed to have minimal changes.

During the neutral to maximum internal rotation, the subscapularis muscle was observed to influence the motion mostly during the 5° to 30° internal rotation (90^{th} percentile = 22.7mm), combined for both abduction angles. Previous cadaver studies support the trend observed for subscapularis during medial rotation for an abducted arm (Ackland & Pandy, 2011; Kuechle et al., 2000). Increasing the abduction angle reduced the average moment arm, post the neutral arm position; Ackland & Pandy, 2011, reported a similar observation.

Supraspinatus, infraspinatus, and teres minor were observed to have negative moment arm for most of the internal rotation, irrespective of the GH abduction angle. This suggest that the main function of the posterior and superior rotator cuffs is to laterally rotate the humeral head. The magnitude of the infraspinatus moment arm increased, at the point of maximum external rotation, with the increase of abduction angle. A similar trend was observed for teres minor while supraspinatus moment arm magnitude was observed to drop. Kuechle et al., 2000, reported the highest negative moment arm for teres minor during internal rotation in any plane, this observation matches with the current study where the teres minor moment arm, at 90° external rotation, was found to increase in magnitude from -7.23mm to -16.11mm, at 20° and 90° abduction respectively.

With the increase in abduction angle, infraspinatus moment arm at maximum external rotation was found to increase in magnitude from -1.9mm to -6.3mm. The proof of this increase in magnitude has also been provided by further cadaveric studies (Ackland & Pandy, 2011). From these observations, it could be concluded that during the initiation of lateral rotation, infraspinatus has the highest moment arm during the conclusion of the motion, the

teres minor and the supraspinatus muscles have the highest moment arm magnitude during 20° and 90° of abduction.

The current study was not able to observe any linear change in moment arm for any muscle during any given motion as was reported by (Otis et al., 1994). During abduction and flexion motions, the middle deltoid, anterior deltoid, supraspinatus and subscapularis were found to have the most effect, while during the medial rotation the subscapularis muscle was found to have the maximum effect on the motion. Hence, going forward, only these muscles would be considered for comparison among different models.

5.5.2 Pre- and Post – TSA Kinematic Variations

Ideally, a TSA surgery replaces the glenohumeral articulating surfaces recreating the original geometry of the joint. Post, in-silico replacement of the prosthetic model of the humeral head the CoR for the biological and the TSA models were observed to be almost identical. This observation was confirmed by fitting a sphere on to the healthy and prosthetic heads and visually inspecting the CoR of the respective spheres.

The muscle moment arms for healthy and post–TSA models are represented in Fig. 5.23 for the abduction and flexion & Fig. 5.24 for internal rotation at 20° and 90° abductions. The muscles did exhibit similar moment arm profiles for each motion tested. There were differences observed in the values of instantaneous muscle moment arms, the average percentage change for all the muscles considering all the tested motions was 2.6%.

During the abduction motion, the average variation between the healthy and TSA anterior deltoid was measured to be 0.8 ± 0.05mm. This could be described as a 3.3% increase in anterior deltoid abduction moment arm in TSA OpenSim model compared to a healthy model. An overall increase in abductive moment arm of 1.8 ± 0.9mm, or 6.2%, was observed for the middle deltoid in the TSA model compared to the healthy counterpart. In the case of the supraspinatus, the TSA model exhibited an average reduction of 0.3 ± 0.01mm, or 1.33%, in abduction moment arm compared to the healthy OpenSim model.

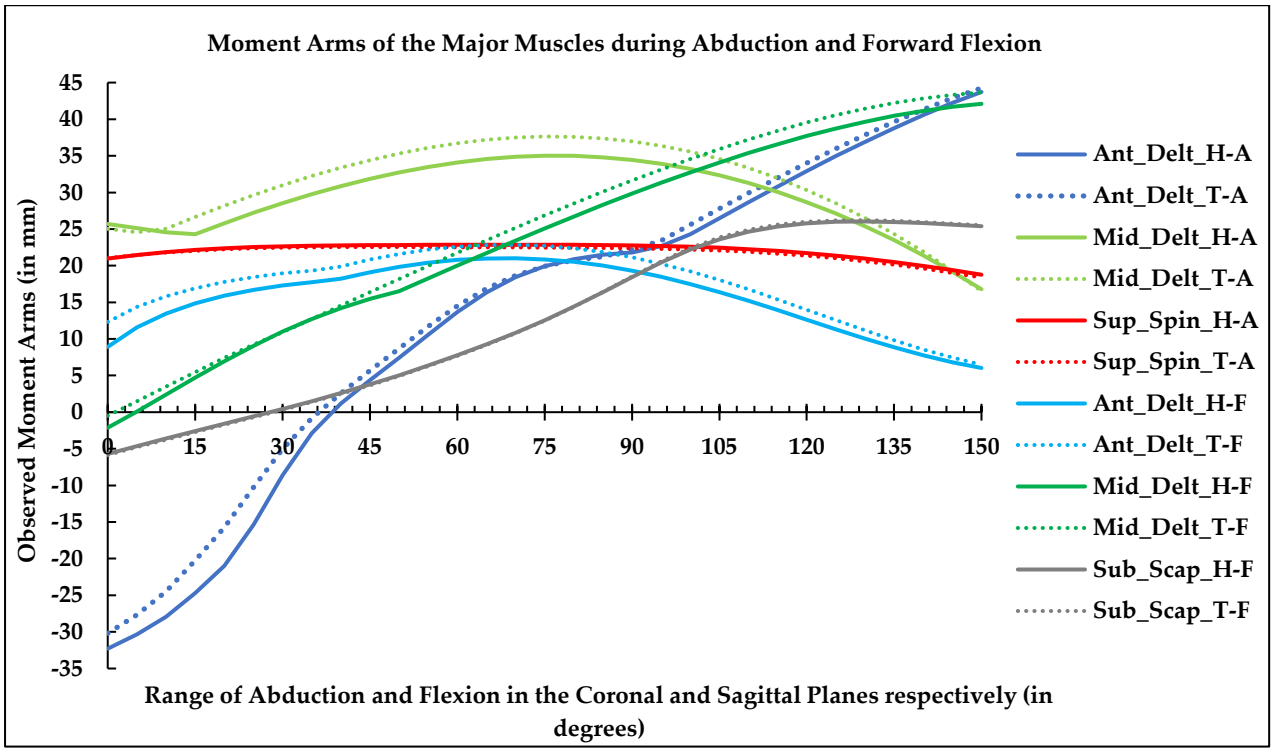

Figure 5.23 Abduction (A) and forward flexion (F) moment arms for a healthy (solid lines) shoulder model (H) and a model with its GH joint replaced (dotted lines) with control TSA prosthesis (T).

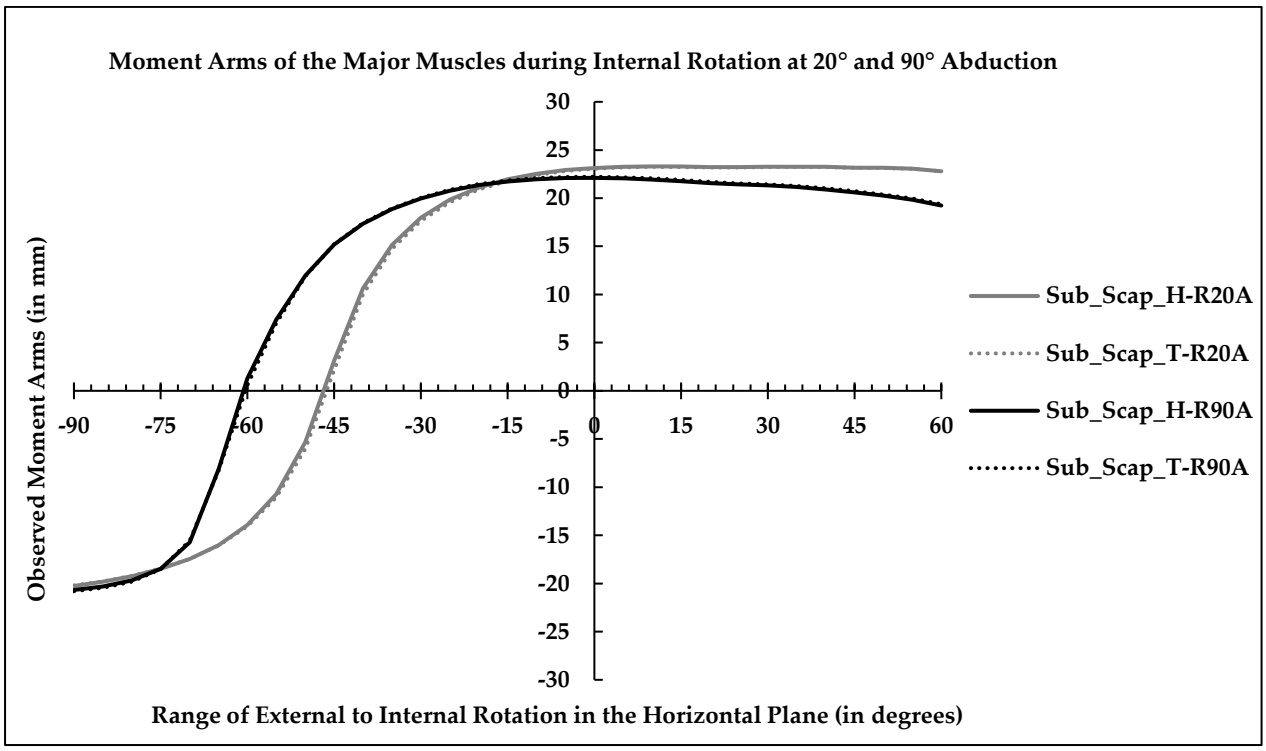

Figure 5.24 GH internal rotation with 20° abduction (R20A) and 90° abduction (R90A) moment arms for a healthy (solid lines) shoulder model (H) and a model with its GH joint replaced (dotted lines) with control TSA prosthesis(T).

Compared to the moment arm differences observed post-RTSA, the average differences observed post-TSA could be considered to be minor. During abduction in a cadaveric model, the reported average anterior and middle deltoid moment arm differences, between RTSA and healthy, were 10.4mm and 15.5mm (Ackland et al., 2010). In an OpenSim RTSA musculoskeletal model, the reported middle deltoid abduction moment variation was 20.4mm when compared to a healthy model (Kontaxis, 2010). These reported differences were, on an average, >10 times the differences that were observed in a post-TSA musculoskeletal model in the current.

Elevating the arm in the sagittal plane, during forward flexion, increased the post–TSA anterior deltoid moment arm by an average value of 1.68 ± 0.23mm or 10.8%. This was the maximum muscle moment arm percentage variation, between the healthy and TSA models, observed in this study. There was a 5.94% increase in middle deltoid elevation moment arm due to an average difference of 1.41 ± 0.38mm between the post– and pre–TSA models. The least variation in moment arms was observed for subscapularis during forward flexion. The average difference was 0.02 ± 0.1mm or 0.14% for the muscle.

Previous studies, comparing the effect of RTSA on elevating moment arm of the middle deltoid, have reported an average increase of 13.9mm (Ackland et al., 2010) and 16.7mm (Kontaxis, 2010) in the post-RTSA moment arm of the muscle. This reported middle deltoid moment arm variation was very large in comparison to the difference observed in the current study. Ackland et al., 2010, reported a reversal of the subscapularis muscle functionality, post-RTSA. In the current study the same muscle remained an active flexor pre– and post–TSA, while post-RTSA, subscapularis was observed to convert into an extensor (Ackland et al., 2010) or contribute to the flexion movement much later (in terms of GH joint angle).

Internal rotational moment arm for subscapularis was observed to decrease, post – TSA, by an average value of 0.15 ± 0.003mm, accounting for a 1.41% decrease. This observed reduction in average moment arm was at 20° abduction. During 90° abduction, the post-TSA average internal rotation moment arm of subscapularis was observed to increase by 0.02 ± 0.1mm, accounting for a 0.2% increase. A previous study reported an increase of 7.8% in the

subscapularis moment arm post-RTSA, during internal rotation at 90° abduction, when compared to a healthy shoulder (Kontaxis, 2010). Comparing healthy and post–RTSA shoulders, Ackland et al., 2012, reported significant differences in subscapularis muscle moment arm during internal rotation ranging from 1.9mm up to 4.9mm. Performing the *in-silico* TSA did not change the internal rotation moment arm as drastically as observed post-RTSA.

It could be concluded that the post-TSA muscle moment arms observed in this study during the abduction, forward flexion, and internal rotation at 20° and 90° abduction were closer to the healthy shoulder control musculoskeletal model. Though there were average differences observed, these were not as large as reported by post – RTSA models and cadaveric, which are generally considered to be significantly ($P < 0.05$) different (Ackland et al., 2012, 2010). This suggested that the *in-silico* TSA did not majorly affect the soft tissue line of action, represented by the moment arms, of the musculoskeletal model which is similar to the ideal scenario described earlier. The limitation of the current study was that only a single musculoskeletal model was used to represent the healthy and the post-TSA shoulders. This did not allow any traditional statistics tests to be performed to validate the significance of the differences observed between the models compared in this study.

5.5.3 Interpopulation Kinematic Variations

Replacing the standard TSA prostheses with the population specific anatomical shoulder implants induced population-specific changes in muscle moment arms, as described in Fig. 5.25 and Fig. 5.26. This is the first study comparing post – TSA musculoskeletal models, in OpenSim, representing three different populations. Therefore, validating the observed differences with literature was not possible. The Chinese (CHI) shoulder model had the smallest humeral head and the Swiss (CH) model had the largest humeral head. The dimension of the South African (SA) humeral head lay in between the CHI and CH models.

Average anterior deltoid, middle deltoid, and subscapularis moment arms, during forward flexion, for the SA model was lower than the CH post–TSA model by 4.0%, 2.95%,

and 1.66% respectively. When the SA and CH average anterior deltoid flexion moment arms were compared to the CHI, the former models exhibited an increase of 5.02% and 8.68% respectively. A similar increase in average subscapularis moment arm, by 8.63% and 10.12%, was observed for SA and CH models respectively when compared with the CHI average musculoskeletal model, during forward flexion. Middle deltoid moment arm during forward flexion was found to decrease by an average of 6.55% and 3.49% for the SA and CH models respectively in comparison to the CHI model.

The CHI population model, exhibited a large variation in instantaneous anterior deltoid moment arm during 0° to 40° forward flexion, compared to the SA and CH models. These instantaneous variations occurred due to the reduction in the diameter of the wrapping object used for the muscle. Closer inspections showed a sudden sliding of the lateral strand of the anterior deltoid causing the spike reduction in moment arm during the initial stages of the motion. Comparing the same strand of muscle in the other two models, it was observed that, due to the increased diameter of the wrapping object the lateral anterior deltoid muscle slid at a slower rate than the CHI model.

The average muscle moment arm for anterior deltoid and middle deltoid during abduction for the SA model was found to decrease by 4.83% and 2.3% compared to the CH shoulder model. During the same motion, an average moment arm increase of 0.4% was observed in the SA model when compared to the CH model, for supraspinatus. When the average anterior deltoid abductive moment arm for the CHI model was compared to the SA and CH models, an average increase of 5.86% and 10.2%, respectively was observed. Similar comparisons were done for average abductive moment arms for middle deltoid and supraspinatus. It was observed that the average middle deltoid moment arms decreased by 2.7% and 0.38% for SA and CH models respectively and the average supraspinatus moment arm increased by 11.17% and 10.8% for the respective models when compared to the CHI OpenSim model. This is the same trend that was observed during the forward flexion motion. The CHI model exhibited the highest middle deltoid average moment arms for forward flexion and abduction motions. This might have been due to the change in head shape, as the

middle deltoid bulge around the lateral edge of the humeral head is greatly influenced by the size of the head.

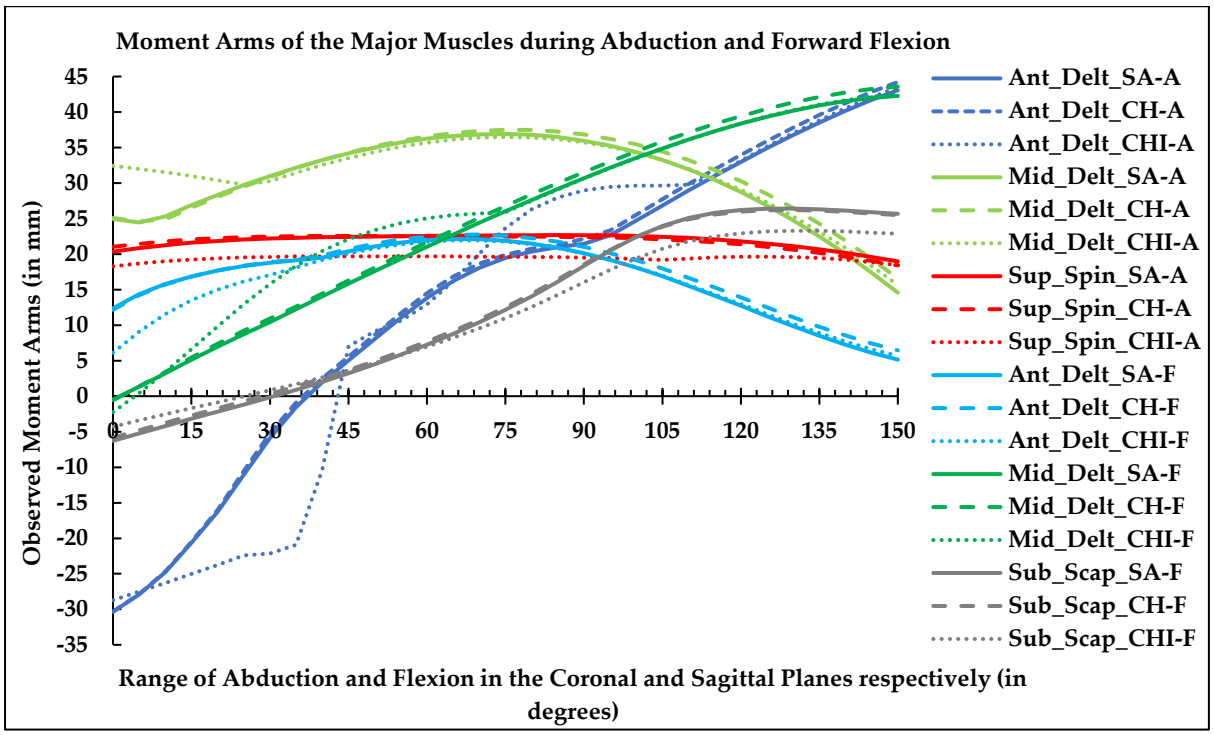

Figure 5.25. Comparing the interpopulation variation in muscle moment arms during abduction (A) and forward flexion (F) among the average South African (SA), Swiss (CH) and Chinese (CHI) prostheses.

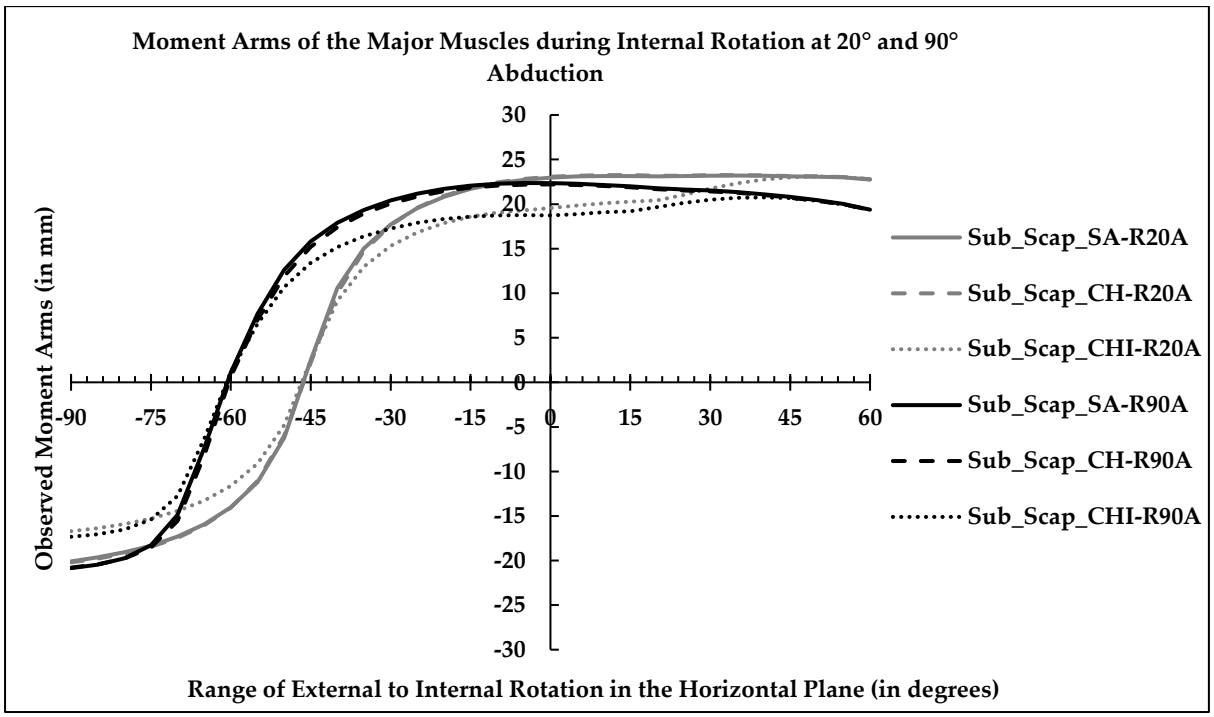

Figure 5.26. Comparing the interpopulation variation in muscle moment arms during external to an internal rotation at 20° abduction (R20A) and 90° abduction (R90A) among the average South African (SA), Swiss (CH) and Chinese (CHI) prostheses.

During the abduction motion, the average variation between the healthy and TSA anterior deltoid was measured to be 0.8 ± 0.05mm. This could be described as a 3.3% increase in anterior deltoid abduction moment arm in TSA OpenSim model compared to a healthy model. An overall increase in abductive moment arm of 1.8 ± 0.9mm, or 6.2%, was observed for the middle deltoid in the TSA model compared to the healthy counterpart. In the case of the supraspinatus, the TSA model exhibited an average reduction of 0.3 ± 0.01 mm, or 1.33%, in abduction moment arm compared to the healthy OpenSim model.

Compared to the moment arm differences observed post-RTSA, the average differences observed post-TSA could be considered to be minor. During abduction in a cadaveric model, the reported average anterior and middle deltoid moment arm differences, between RTSA and healthy, were 10.4mm and 15.5mm (Ackland et al., 2010). In an OpenSim RTSA musculoskeletal model, the reported middle deltoid abduction moment variation was 20.4mm when compared to a healthy model (Kontaxis, 2010). These reported differences were, on an average, >10 times the differences that were observed in a post-TSA musculoskeletal model in the current.

During the internal rotation of the humeral head, the CHI average post-TSA model was observed to have the lowest average subscapularis moment arm. This observation was not influenced by the GH abduction angle. At 20° of abduction, the SA and CH models exhibited an average increase of 5.51% and 5.48%, in subscapularis moment arm, compared to the CHI model. This increase was higher at 90° abduction. At this angle of elevation, the average increase was found to be 9.0% and 7.1% respectively, between the groups.

The subscapularis muscle in the CHI model was observed to peak later than the SA and the CH models. At 20° and 90° abduction, the maximum muscle moment arm for the CHI model was observed to be at 50° & 40° internal rotation respectively. In contrast to the CHI model, the SA and the CH models exhibited a maximum subscapularis internal rotation moment arm during the initial phases of the internal rotation. Between the SA and CH average post – TSA models the average increase in subscapularis moment arm, for the SA model, was found to be 0.03% and 2.1% at 20° and 90° abduction respectively. This decrease in the average

rotational moment arm of the subscapularis, with the reduction of head size, was expected. A smaller head reduces the perpendicular distance between the joint CoR and the subscapularis muscle which has a medial to lateral line-of-action.

The average percentage difference in muscle moment arms, combined for all muscles and every motion, was the highest between the CH and the CHI models, 7.03%. This might have been due to contrast in humeral head sizes used in these models. While the CH model had the largest head the CHI model was implanted with the smallest size head, representing the population. The lowest average difference was observed between the CH and the SA models, amounting to 2.27%. The difference in humeral head articular geometry was the minimum, but significant ($P < 0.05$) between the SA and CH populations. An intermediated average difference in muscle moment arms was observed between the SA and the CHI models, amounting to 6.81%.

The results in this section demonstrate that the average inter-population muscle moment arm differences could be linked to the average morphological variations of the population-specific humeral heads. Whether these, observed correlations, could be considered as significant causative factors for the moment arm differences remains to be seen. Multiple population-specific musculoskeletal models need to be analyzed in a similar manner to find the significance of the inter-population muscle moment differences observed and drive forward the quest for population-specific shoulder implants for TSA.

5.5.4 Performance of Novel Implants

A total of five new designs of TSA prostheses, introduced in Chapter 4, were tested using OpenSim. Out of the prosthetic parts tested, 3 were glenoid cups and 2 were humeral heads. The design features introduced to create the novel models of TSA prostheses did not influence the overall RoC and thickness of the glenoid and humeral components. Furthermore, the humeral head base diameter, the glenoid height, and the GH articulation were not affected by the design changes. Each of the new glenoid cups was introduced to replace the control glenoid prosthesis to create their respective post-TSA musculoskeletal model. The humeral

heads, designed with population-specific peak points, were made to replace the humeral heads in the respective population-specific musculoskeletal models.

The introduction of the novel prostheses did not change any parameters which could potentially alter the articulating CoR. The *in-silico* TSA parameters, the translation, and rotational sequences, implemented to create the musculoskeletal models were identical to their parent models. No shift in the muscle attachment points or muscle profile were induced by the implantation of the new prostheses. Therefore, the observed muscle moment arms for all the muscles in the musculoskeletal models implanted with the novel designs were identical to the control and the population-specific models. Reviewing the GH articulation during the induced RoM, no visible signs of impingement or articular dislocations were observed. Increasing the inferior width of the pear-shaped prosthesis and reducing its superior surface area did not adversely affect the GH articulation. This confirmed that the new glenoid cup implants were not going to induce any uncharacteristic post-surgical kinematics.

A study by Wang et al., 2005, it was reported that there was no significant difference between a hybrid glenoid prosthesis and the commercially available implants in post-surgical kinematics. The hybrid glenoid was structurally similar to the commercial prostheses and the *in-silico* surgical implantation followed the standardized process (Zhang et al., 2013). The glenoid designs, under study in the current chapter, did not have significant structural variance from the control glenoid cup and they were also implanted identically. Hence it could be argued that without drastically altering the glenoid prosthesis design such that the CoR of the GH articulation significantly changes, post-surgical kinematic variations might not be observed. Going forward only these implants would be undergoing further investigated using Finite Element (FE) analysis protocol explained in the next chapter.

5.6 Conclusion

This chapter explains the musculoskeletal modeling of a healthy shoulder joint and analyses the effect of replacing the articular surfaces with TSA prostheses. The observed changes in the muscle moment arms between the pre– and post–TSA models were minimum. Hence it could

be concluded that the *in-silico* shoulder biomechanical model developed in this chapter is robust in its nature and the computerized surgery was a good representation of the real-world TSA. Hence, it could be concluded that the further moment arm variations observed after introducing the population-specific humeral heads and novel glenoid cups were only due to the geometric properties of the implants.

The inter-population differences in muscle moment arms were useful in establishing the fact that the populations having bigger humeral head size variation also exhibit larger moment arm differences when compared to a population with a smaller humeral head size variation. Replacing the respective average inter-population humeral heads with another variation designed with population-specific peaks points did not alter the muscle moment arms for any muscle. This study did not take into account the muscle volume, the height or weight to create the biomechanical model. This could be a limitation in the current study.

When the novel glenoid components were made to replace the control glenoid cup absolute replication of muscle moment arms was achieved. The novel glenoid prostheses were designed to investigate their effects on *"rocking horse"* effect. Including them in the musculoskeletal study provides an *in-silico* validation that the designed implants would not alter the post-TSA muscle moment arms if implanted using the standard surgical approach and paired with a matching humeral head prosthesis. Therefore, no further design changes would be made to the glenoid prostheses before performing the FE analysis which is detailed in the next chapter.

CHAPTER 6

Performance of the Glenoid Designs under Compressive and Tangential Loading

6.1 Introduction

Radiologic evidence of radiolucent lines behind the glenoid prosthesis is the most accepted indication for aseptic glenoid loosening (Boileau et al., 2002; Matsen III et al., 2008; Strauss et al., 2009; Walch et al., 2002b). It is impossible to accurately predict from a radiograph the exact interface where the loosening occurs. This is where mechanical testing of the glenoid prosthesis is being used to better understand the glenoid loosening phenomenon. American Standard for Testing and Materials (ASTM International, 2012) provide guidelines for such mechanical studies involving anatomic glenoid prosthesis (Fig. 6.1). One such study by Junaid et al., 2010, was able to demonstrate the mechanics of glenoid implant failure for keeled and pegged cups. The separation between the UHMWPE glenoid cup and the reamed glenoid fossa was observed to occur at the PMMA (bone cement) – polyurethane (bone substitute) interface (Junaid et al., 2010).

Designing a mechanical test rig was not within the scope of this thesis and hence the investigation of glenoid loosening due to rocking horse effect was performed using Finite Element (FE) Analysis. Several FE studies on anatomic shoulder prosthesis have been performed adhering to the guidelines provided by ASTM, at various degrees. As the majority of the GH articulation occurs at the posterior-superior (PS) region of the glenoid cavity (Massimini et al., 2010), it could be expected that the inferior loosening of the glenoid cup is caused by the upward shearing force from the head. This fact was accurately predicted by Hopkins et al., 2004, using an FE study. The effect of ATSP design parameters, on its stability and cyclic wear, was provided, as an FE modeling study, in Hopkins et al., 2006a, Hopkins et al., 2006b and Hopkins et al., 2007.

Junaid et al., 2010, validated inferior loosening of the glenoid prosthesis in an FE model using a thick glenoid cup with an axial loading of 1800N. More recent studies have implemented FE approaches to evaluate novel prosthesis designs. Zhang et al., 2013, compared the von Mises and shear stresses developed on the glenoid prosthesis, cement and bone using constrained, bi-radial and unconstrained glenoid cups. Gunther et al., 2012, compared edge displacement between fully constrained and inset glenoid designs using region-based static loading FE models.

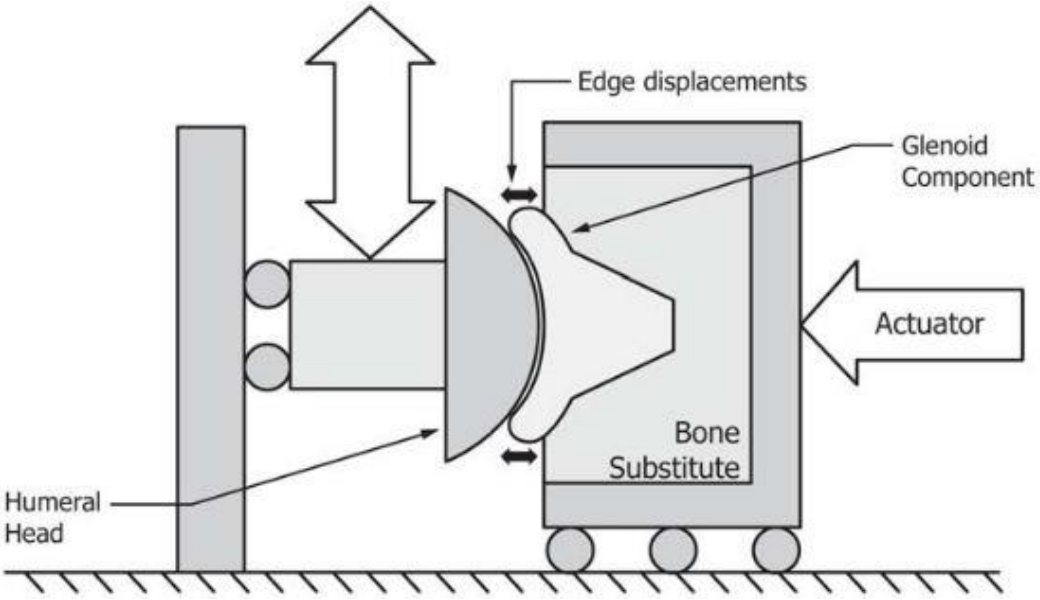

Figure 6.1 The standard ASTM glenoid testing set up. The prescribed loading is maintained constant in the axial direction, normal to the glenoid cup center, while the humeral head is displaced in one direction with a constant velocity. *sourced from* (ASTM International, 2012).

Observations from an FE model could be varied even if an identical problem scenario was simulated. The variation in the solution could be due to individual skill, the platform used to create the model, the numerical method implemented to achieve convergence, the mesh parameters, and various other factors. The results obtained from the current FE model should be viewed within the realm of the modeling approach explained in this chapter. Ideally one might expect, that the literature should provide all the required details to adapt published

models for new research study after required alterations. As this is not the case, FE model validation becomes challenging. The details of the FE model generated and the observations for the current study is reported according to the guidelines provided by Erdemir et al., 2012, and Viceconti et al., 2005.

6.2 The Finite Element Analysis Pipeline (FEAP)

The Dynamic Glenoid Loosening (DGL) test is performed in two stages. The first stage involves humeral head subluxation of a translating humeral head from the glenoid surface, in the anterior, posterior, superior or inferior direction, under compressive loading (ASTM International, 2012). Subluxation of the humeral head could be defined as the detachment of the articulating surfaces resulting into complete GH dislocation (Hopkins et al., 2006b). The second step of the DGL test involves cyclic translation of the humeral head, from the glenoid center to the 90% of the subluxation translation, in the direction of subluxation and under compressive loading.

FE studies by Zhang et al., 2013, have demonstrated that performing the first step of the ASTM DGL test was sufficient for understanding the stress characteristics of a certain glenoid design. In addition to this, if a limited movement is allowed between the bone-substitute and the prosthesis, then the effect of stress on potential loosening, for a prosthesis design, might be estimated. This chapter will be focusing on explaining the development and validation of an FE model developed to perform humeral head subluxation. It will further describe the model adaptations, performed, in order to study the stability characteristics of the novel glenoid designs. Although cyclic tests are essential in understanding all-polyethylene glenoid wear characteristics and edge displacement (Gunther et al., 2012; Hopkins, 2004), this analysis was out of the scope of this thesis.

Abaqus/Standard v6.14 (SIMULIA, Providence, RI, USA) was used to perform the FE analysis on the novel glenoid designs. Along with the FE models of the new designs, a separate model of a commercially available glenoid was generated and was treated as the control model. Post-TSA FE models employing implicit and explicit methods of solving have

been previously reported in the literature (Allred et al., 2016; Hopkins et al., 2006b). From a comparative study by Hopkins, 2004, it could be concluded from that there is no significant difference in results between the two methods of solving and hence, for the current study, a dynamic implicit method of solving was implemented. All the glenoid components under study possessed non-linear geometrical features. To account for these non-linear geometrical changes, the in-built NLGEOM feature of the software was implemented.

6.3 Generating the Control Glenoid Model

Adhering to the ASTM guidelines, the FE model consisted of following four parts: An unconstrained glenoid prosthesis, a spherical humeral head with an attached load applicator, a cement layer and a polyurethane block. Every component of the FE model, except for the humeral head, were created, using standard quadratic tetrahedral elements (C3D10) belonging to the 3D stress family.

The global size of the element was kept constant, at 1.3 mm, for each component. This element size was within the limits of most of the previously reported FE studies, using TSA prostheses (Lacroix & Prendergast, 1997; Yongpravat et al., 2013b) and enabled creating meshes comparable to the literature (Hopkins, 2004). Tetrahedral elements were utilized in this study as they were reported to perform better than hexahedral elements, such as C3D8, in models used for analyzing shear loading (Tadepalli et al., 2011). Further details of the designed parts and their interaction properties are provided below;

6.3.1 The Control Glenoid

In Chapter 4, the design process of the control glenoid, used in the current FE model, is provided. When the humeral head is sheared in any direction on the surface of the glenoid cup, the overall angle of constraint, provided by the cup geometry (43.07°) in that axis becomes an important determining factor of the subluxation load and the point of subluxation or the limit of translation for humeral head translation on the cup (Fig. 6.2 a).

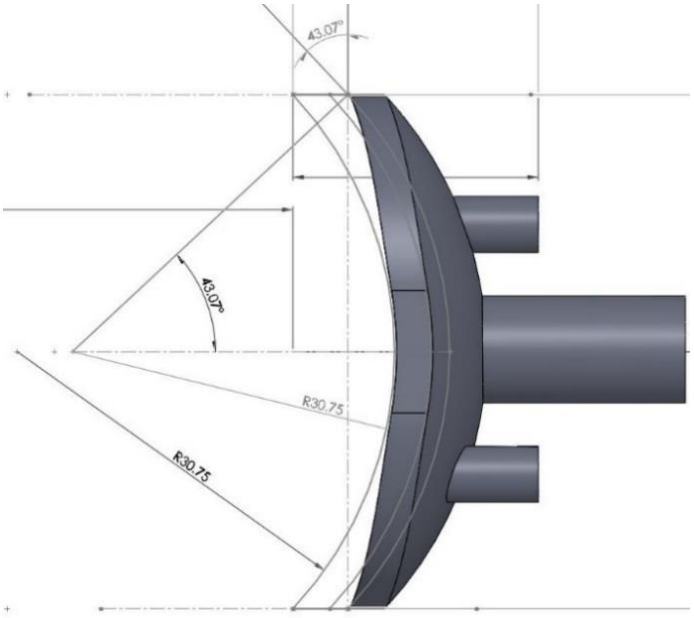

(a)

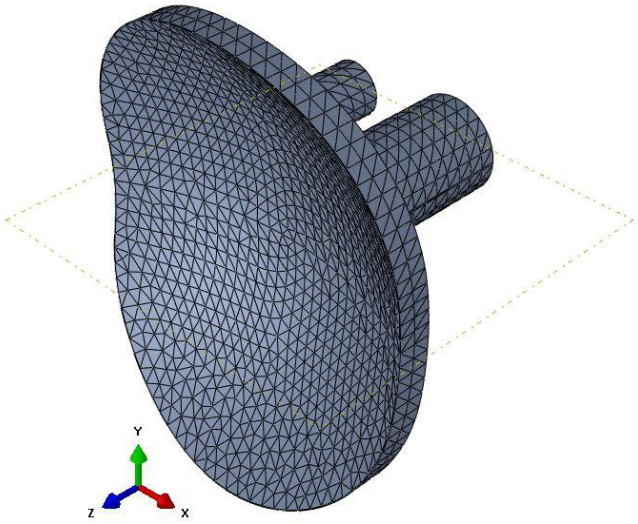

(b)

Figure 6.2 The control glenoid prosthesis created for this study (a) the geometrical features of the design as a solid model and (b) the meshed model of the glenoid cup adapted for the FE model.

The design of the control glenoid was performed in SolidWorks® Dassault Systems (Velizy-Villacoublay, France) and was exported into Abaqus platform as an ACIS (.sat) file. The glenoid cup was modeled as a deformable solid with homogeneous properties. The total number of tetrahedral elements used to form the glenoid prosthesis was 18411 resulting in the formation of 29421 nodes (Fig. 6.2 b). The number of elements was based on a similar FE study by Hopkins et al., 2006b. It was a conscious decision to make the number of elements higher

for the current study as the prostheses components were larger in comparison to the earlier study.

The material property of ultra-high molecular weight polyethylene (UHMWPE) was assigned to the control glenoid and to all the glenoid models generated ahead. The Young's modulus, density and the Poisson's ratio of the UHMWPE were set as 1260MPa, $1x10^{-11}$ tonnes/mm^3 and 0.4 respectively (Hopkins et al., 2006b; Junaid et al., 2010; Stone et al., 1999; Zhang et al., 2013).

6.3.2 The Cement Layer

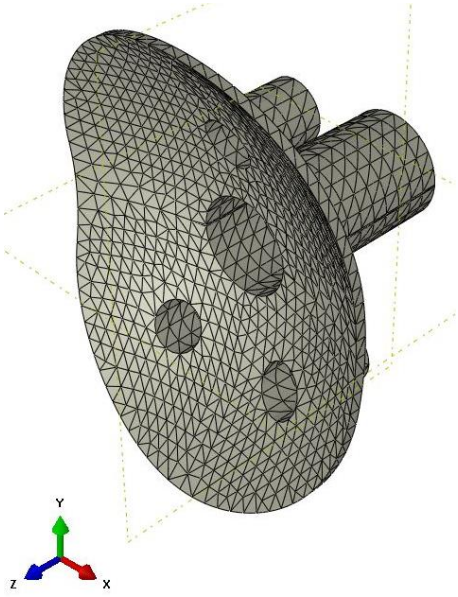

Figure 6.3 The meshed model of the PMMA bone cement component.

The cement layer (Fig. 6.3) was also designed in SolidWorks® and was imported into the FE platform as an ACIS file. Most of the design features, such as the RoC, height, and width, of the cement component were identical to the glenoid cup. Gaps were provided in the cement pegs for the insertion of the glenoid pegs (Fig. 6.4 a). The thickness of the cement was 1mm (Hopkins, 2004; Lacroix et al., 2000; Zhang et al., 2013), and was kept constant for all the future models as well. Using identical meshing parameters, 6453 tetrahedral elements were used to created cement mesh resulting into a total of 13139 nodes (Fig. 6.3). Material properties

of polymethyl methacrylate (PMMA) were assigned to the homogenous cement part. The material density, Young's modulus, and Poisson's ratio were $1.6x10^{-10}$ tonnes/mm^3, 2200MPa and 0.3 respectively (Chaplin et al., 2006; Junaid et al., 2010; Lacroix et al., 2000; Zhang et al., 2013).

6.3.3 Glenoid-Cement Constraint

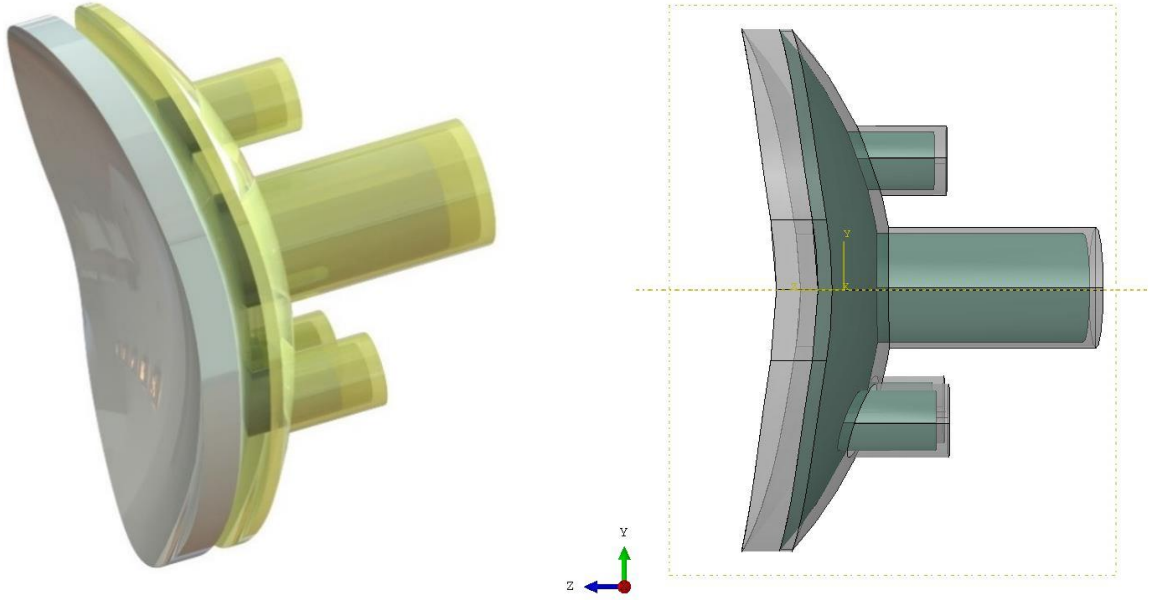

(a) (b)

Figure 6.4 (a) The bone cement (yellow) was designed to receive the glenoid (grey) pegs to form an assembly (b) with a tie constraint (green) was specified between them.

Surgeons apply the bone cement into the holes created for glenoid pegs on the reamed glenoid surface. As the glenoid gets installed into the peg holes, excess bone cement could be observed to get released from the holes and coat the glenoid – bone interface. It is also a common practice in FE modeling to fix the glenoid onto the scapula/bone substitute using PMMA (Gunther et al., 2012; Hopkins, 2004; Zhang et al., 2013). Therefore, in this study, the bone cement part was rigidly tied to the back of the glenoid after assembling the glenoid and the cement components (Fig. 6.4 a, b).

6.3.4 The Bone Substitute Block

Using a glenoid mounting object, to perform dynamic glenoid testing is a specific requirement (ASTM International, 2012). A previous FE study, comparing bone substitute and 3D scapular bone model as glenoid backing material, found no difference in the subluxation force ratio between the two cases (Hopkins, 2004). For the current study, mounting the glenoid-cement structure on a bone substitute was found essential for two reasons. Firstly, to maintain the continued adherence to the ASTM guidelines and secondly, to create a realistic FE model which could be used to observe material deformation and glenoid edge loosening under loading as observed in mechanical studies (Junaid et al., 2010).

The bone substitute was designed as a three–dimensional deformable cylindrical block, in Abaqus. The diameter of the cylindrical face was 60mm and its extruded length was 50mm (Fig. 6.5 a-b). These dimensions were selected to make sure that the mounting block accommodates for glenoids of different shapes and sizes.

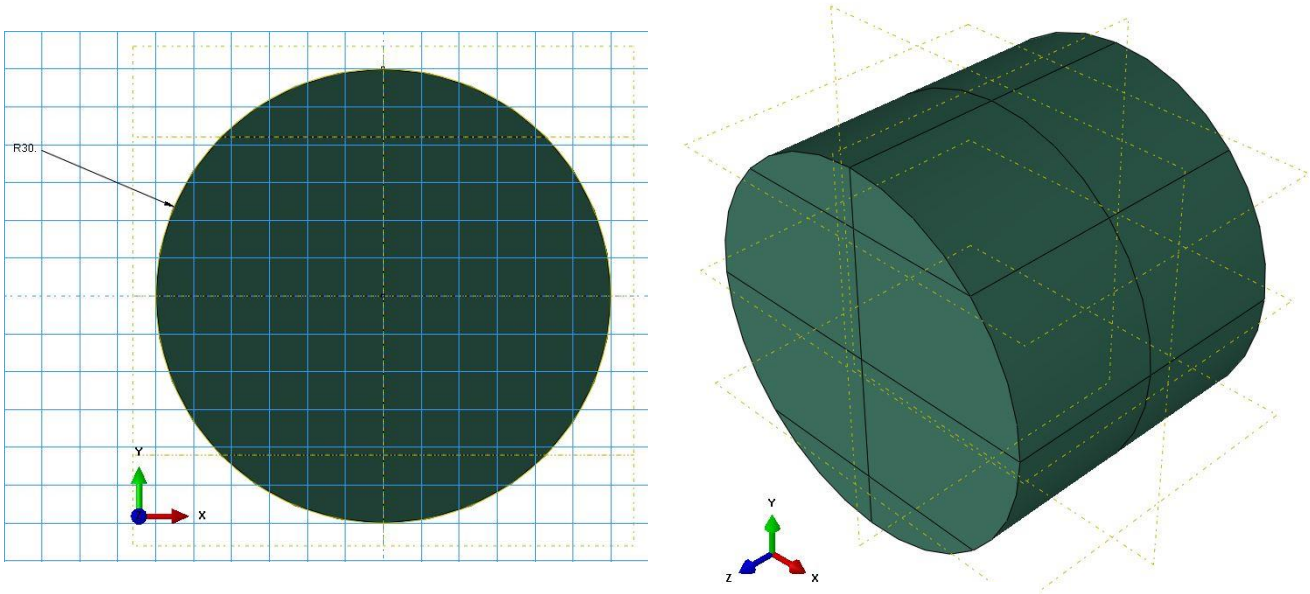

(a) (b)

Figure 6.5 The bone substitute (a) cross-sectional sketch performed in Abaqus and (b) the extruded solid model of the deformable polyurethane block.

A reaming object (Fig. 6.6 a) was designed in SolidWorks to create surgical slots, for the implant pegs, into the mounting block. The reamer was imported into Abaqus platform as described earlier and was mated with the bone substitute. The mating process inserted the curved region of the reamer into the mounting block by aligning the rectangular face of the former with the latter object. Boolean subtraction of the reaming object from the mounting block was performed to obtain the reamed bone substitute (Fig. 6.6 b).

The meshing of this object was performed with 46107 tetrahedral elements resulting into 66131 nodes. Material properties of polyurethane bone substitute foam were assigned to the glenoid mounting object. The Young's modulus, density, and Poisson's ratio were 193MPa, 1.13×10^{-3} tonnes/mm^3 and 0.3 respectively (Junaid et al., 2010; Lacroix & Prendergast, 1997; O'neill et al., 2012).

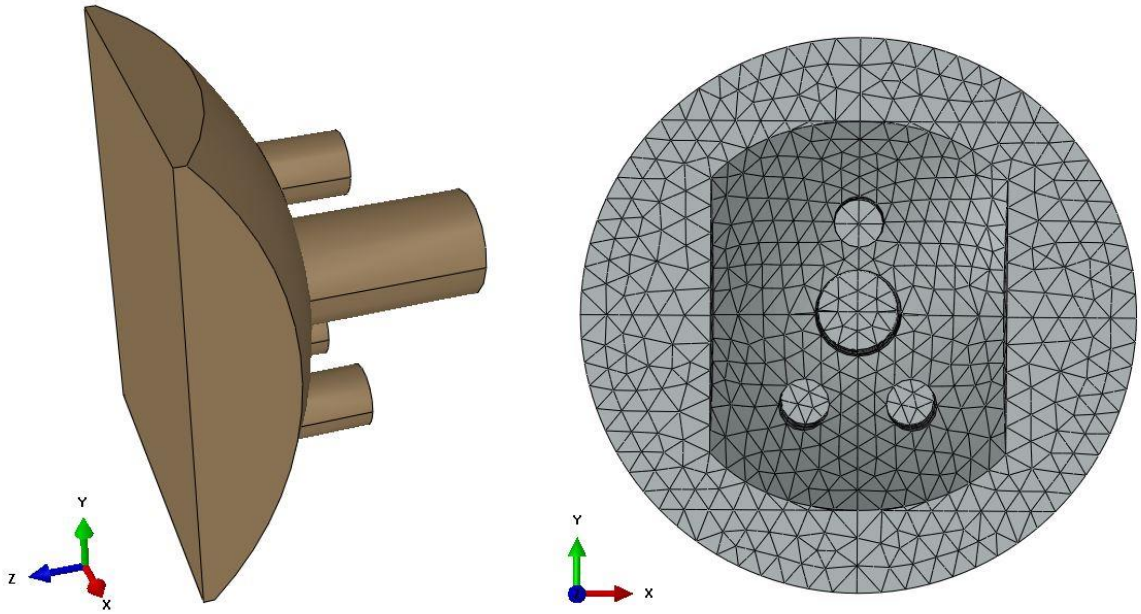

(a) (b)

Figure 6.6 (a) The reaming object designed with an identical geometry of the glenoid back and thicker pegs to create slots in the bone substitute block to mount the glenoid-cement structure; (b) the post-reaming polyurethane bone substitute object meshed with tetrahedral elements.

6.3.5 Cement-Polyurethane Interaction

Most of the shoulder FE studies in literature treat the PMMA-polyurethane bones substitute interface as a perfectly bonded surface (Hopkins, 2004; Junaid et al., 2010; Zhang et al., 2013). Although this is true for a period immediately after TSA, reports of disassociation at the same interface might suggest that certain slippage or movement in this region could be expected right before glenoid loosening.

To mimic a glenoid prosthesis close to loosening, a friction coefficient of 0.6 was applied between the posterior cement surface and the reamed surface of the polyurethane. Due to the lack of information, in the literature, regarding the exact friction coefficient between the PMMA–polyurethane, the above friction coefficient value was obtained from studies performed on cement–bone interface to understand implant characteristics in hip and shoulder (Pomwenger et al., 2015; Ramaniraka et al., 2000; Terrier et al., 2006).

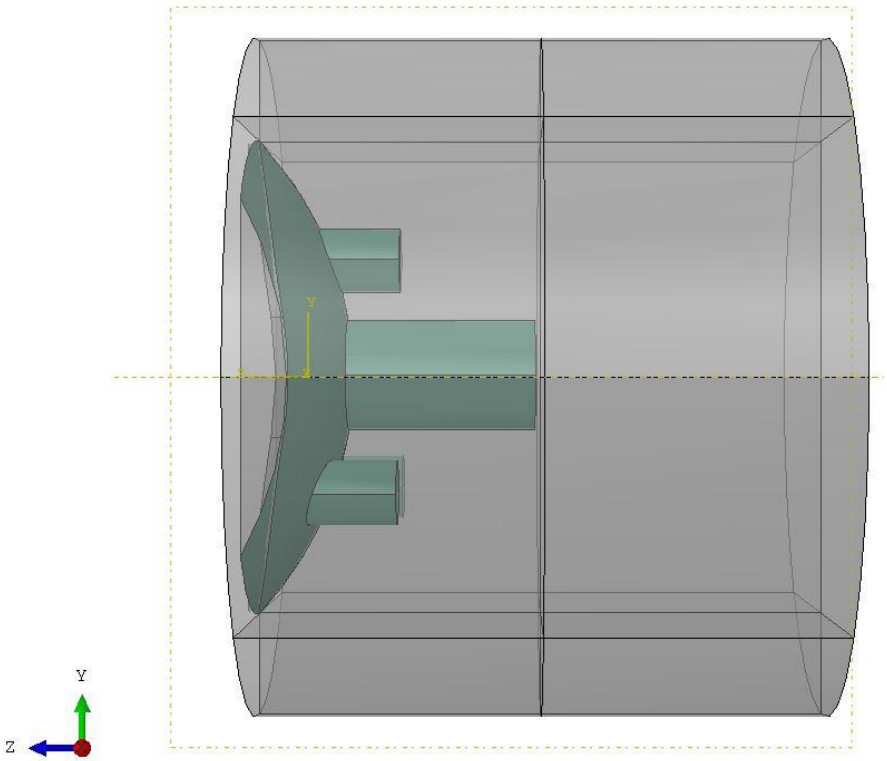

Figure 6.7 The interaction between the posterior cement and anterior surfaces of the polyurethane has been highlighted in green.

6.3.6 The Humeral Head

The humeral head was modeled as a three-dimensional discrete rigid shell in Abaqus. The shape of the head was spherical with a 28mm RoC and 21mm height. The humeral head base diameter was 52mm in diameter and was connected to a load-applicator section which was a 40mm long cylindrical structure with a 20mm wide base (Fig. 6.8 a).

The humeral head and load applicator structure were meshed using the same number of seeds as the glenoid. This resulted in a total number of 5471 R3D4 elements with 5417 nodes. There were no material properties assigned to this discrete rigid structure (6.8 b).

6.3.7 Glenohumeral Interactions

A surface to surface contact was defined between the spherical surfaces of the humeral head and the glenoid cup (Fig. 6.9). The friction coefficient of 0.07 was assigned between the contact surfaces (Anglin et al., 2000; Hopkins et al., 2006b; Pomwenger et al., 2015).

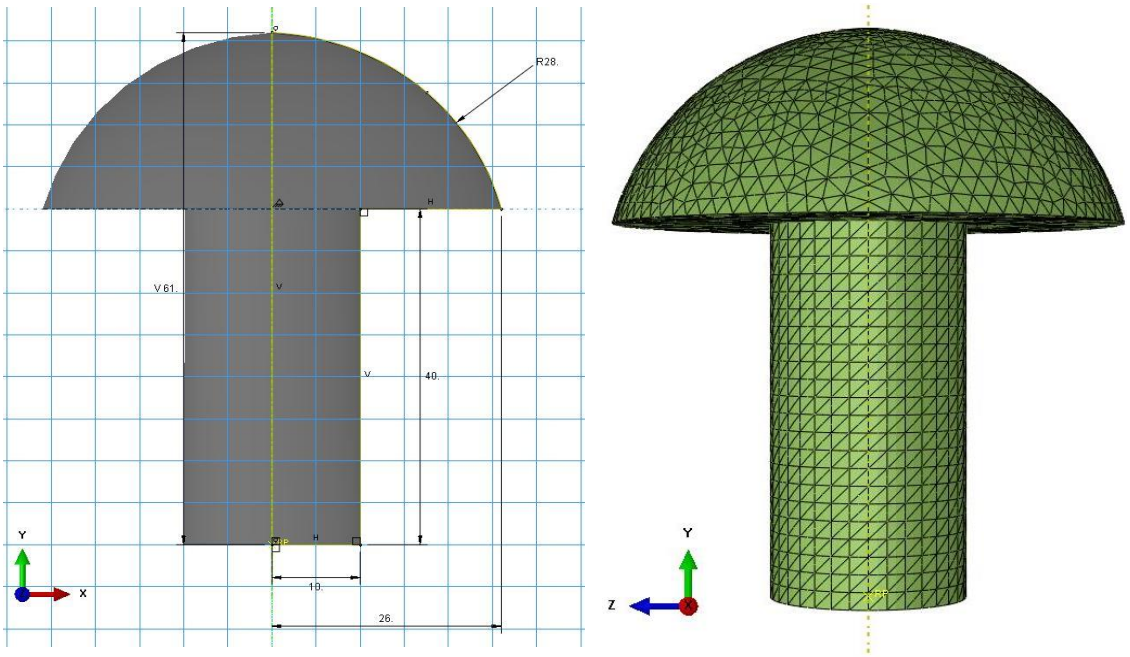

(a) (b)

Figure 6.8 (a) The cross-sectional sketch representing the revolved shell structure of the humeral head and load applicator and (b) The final meshed object with a reference point (RP) used for applying the boundary conditions.

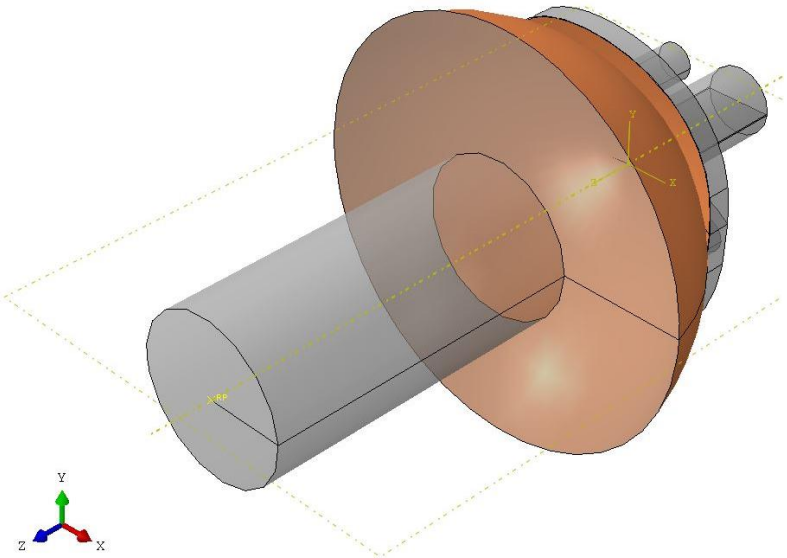

Figure 6.9 The glenohumeral surfaces selected assigned with interaction properties are highlighted in orange.

6.3.8 Assembly Loading and Boundary Conditions

To form the final assembly, shown in Fig. 6.10, the center of the humeral head surface was positioned on the center of the glenoid cup. The external midpoint of the longest glenoid cup peg was mated with the internal midpoint of the longest cement peg. Using a similar technique, the reamed polyurethane block was placed behind the cement. The boundary conditions and loads were determined from the previous experimental and FE studies.

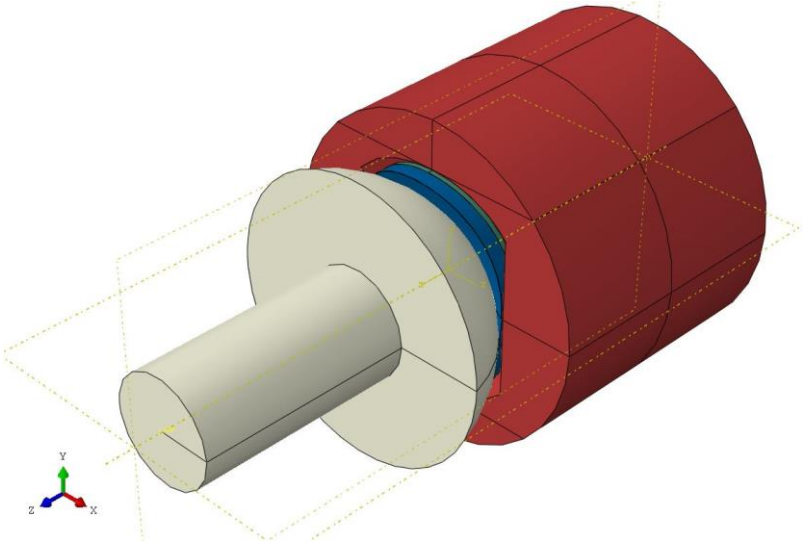

Figure 6.10 The complete assembly of the FE model consisting of the humeral head (white), glenoid cup (blue), cement backing (green) and the reamed polyurethane backing (red).

ASTM does not specify any displacement value, up to which the humeral head should be sheared in any direction. Scanning the literature carefully assisted in determining this range of displacement along with the point of subluxation for the glenoid implants under study. Unconstrained pegged glenoid prostheses studied by Hopkins et al., 2006b, observed that for a glenoid constraint angle of 43° (43.07° in the current study) and a GH conformity of 0.88 (0.91 in the current study) the maximum permitted humeral translation was about 4.5mm. Hence, a total displacement of 4.5mm was applied, to the humeral head, in the superior direction (+Y axis).

Previous work by Anglin et al., 2000, and Hopkins, 2004, suggests that if the angle of glenoid constraint or the GH mismatch is known along with the height of the prosthesis, the humeral head point of subluxation could be predicted. For the control glenoid prosthesis, the humeral head subluxation point was calculated according to the Rigid Body predictions (Anglin et al., 2000) and the, more realistic, FE predictions (Hopkins, 2004) as shown below (Fig. 6.11). The angle of constraint, GH mismatch and conformity were constant for all the glenoid designs. Hence the overall humeral displacement and the point of subluxation were kept constant for every glenoid model.

This approach was implemented to reduce the computational cost of the FE model and also as a method to overcome the challenges (Junaid et al., 2010) to accurately predict the GH subluxation point. As mentioned earlier, the glenoid length, GH conformity, and GH radial mismatch for all the glenoids, under study, were 41mm, 0.91 and 2.75mm respectively. Using Eq. 5.1 and Eq. 5.2, it was found that the maximum theoretical translation possible for the humeral head was 1.8mm and according to the literature-based FE predictions, the subluxation point was found to be 3.7mm. The displacement was applied at the back of the load applicator using a reference point. The polyurethane bone substitute was constrained at all the external points and it was only allowed to deform on the surface where the glenoid-cement object was implanted (Fig. 6.12).

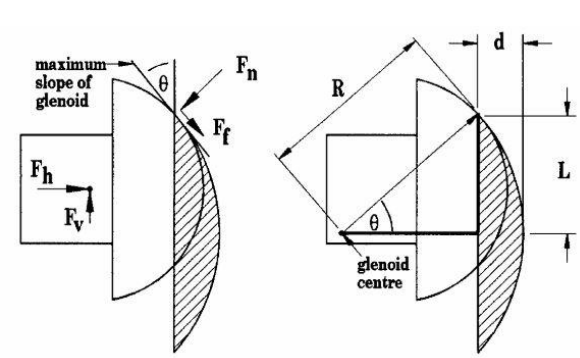

Anglin et al., 2000, based on the GH geometry, had proposed a theoretical relationship between possible humeral translation (T), glenoid length (L) and the GH conformity. This relationship is presented below;

$$T = 2 \times (1 - conformity) \qquad (6.1)$$

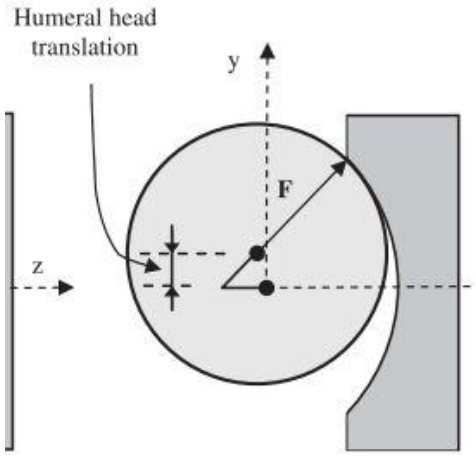

Based on FE model predictions, Hopkins, 2004, postulated a relationship between the head translation (T) and GH mismatch, given below;

$$T = (0.69 \times mismatch) + 1.84 \qquad (6.2)$$

Figure 6.11 The two models used to predict the maximum humeral head translation on the glenoid up to subluxation.

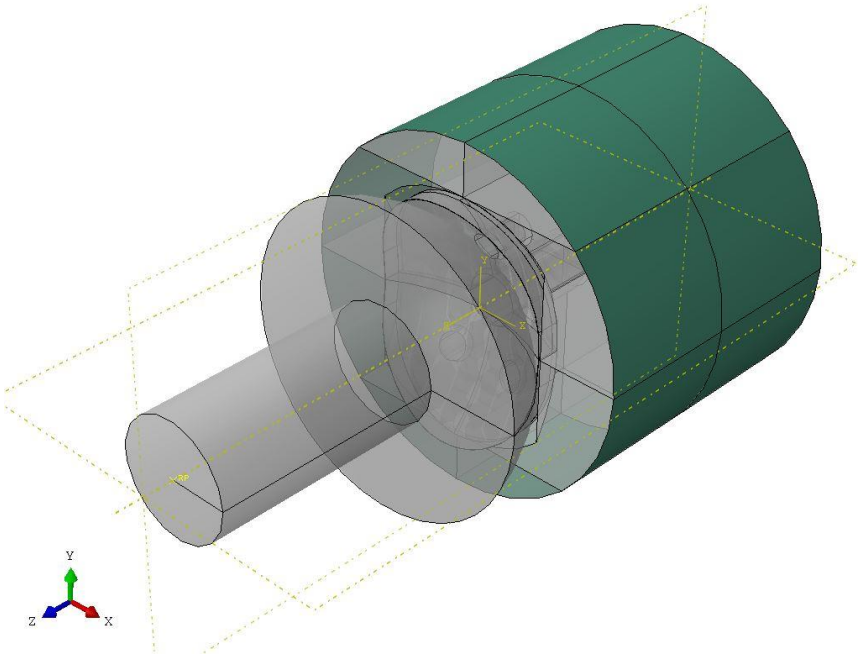

Figure 6.12 A schematic representation of the regions (green) of the assembly where boundary conditions were assigned as Encastre and Load.

Junaid et al., 2010, had implemented a different approach to calculate the vertical subluxation load of the humeral head. They had observed the subluxation load curve to transition from linear to a non-linear region and finally becoming flat until subluxation. The average load at the transition (from linear to non-linear) region of the curve was assumed to be 90% of the subluxation load, by the authors and was further used for cyclic loading. From the graphical data presented by the authors, it is quite evident that the subluxation happened when the humeral head had translated a distance >5.2mm, on the non-conforming glenoid surface. The assumed 90% load was calculated at 2.5mm of humeral displacement. It was reported in the study that this approach led to an error of 7% between the actual 90% load and the assumed load. The non-conforming glenoid cups used by Junaid et al., 2010, had a radial mismatch of 5mm.

By applying the regression formula prescribed by Hopkins, 2004, also implemented in the current study, the exact point of subluxation could be predicted to be 5.29mm which matches with the data presented by Junaid et al., 2010. This proves the accuracy of the methods used to calculate the subluxation point for the prostheses under investigation in the current study. The regression relationship (Eq. 5.2) has a limited effectiveness. Using the relationship to predict humeral head translation presented, using experimental analysis, by Anglin et al., 2000, it was observed that Eq. 5.2 failed to predict the exact subluxation point for GH mismatches >9.6mm and when smaller heads were paired appropriately sized glenoid cups (Table 6.1).

The compressive load and the shearing velocity were applied at the back of the load applicator. The whole analysis was full-Newtonian and was divided into two steps. To create stable contact between the GH surfaces, a compressive static load of 750N was applied, ramping up from 0N, for 1 second towards the glenoid surface (-Z). The second step was defined as dynamic implicit. In this step, the head was sheared towards the superior edge of the glenoid at a constant velocity of 0.1 mm/second while applying the 750N compressive load on the cup surface.

Table 6.1 Experimental translations as observed by Anglin et al. 2000, compared with the predicted translations.

Glenoid Type	Glenoid Radius (R)	Humeral Head Radius (r)	GH mismatch (R - r)	Observed Humeral Translation	Predicted Humeral Translation (Eq. 5.2)
Flat back with 2 pegs	56 mm	26 mm	30 mm	13.5 mm	22.5 mm
	40 mm	20 mm	20 mm	9.5 mm	15.6 mm
Curved back with a keel	35.6 mm	26 mm	9.6 mm	6.1 mm	8.5 mm
	26.5 mm	26 mm	0.5 mm	2.2 mm	2.2 mm
	20.5 mm	20 mm	0.5 mm	1.5 mm	2.2 mm
Flat back with 3 pegs	29.5 mm	26 mm	3.5 mm	4.4 mm	4.3 mm
Curved back with 3 pegs	29.5 mm	26 mm	3.5 mm	4.3 mm	4.3 mm

The compressive load was amplitude controlled as shown in Fig. 6.13. During the first step, the humeral head was only allowed to translate in the Z-axis and during the second step, the translation of the head was only restricted in the X-axis. The smallest step for loading was $1x10^{-6}$ seconds and the maximum permitted step size was 1 second. The software was allowed to determine the suitable step size increments between the minimum and maximum steps, in order to achieve convergence of equilibrium. The step sizes used in the current study were similar to that of previous FE analysis by Hopkins, 2004. The total force applied, displacements, principal stress, von Mises Stress, tensile stress, and reaction forces were calculated for the subluxation analysis. The calculated outputs were reported by Abaqus at an interval of 1 second or every 0.1mm of humeral head shear. The results presented for this analysis are applied vertical force (Fy), calculated at the point of compressive loading on the back of the load applicator, and its ratio with the applied compressive load (Fz) called the force ratio (Fy/Fz).

To investigate the performance of the FE model under different compressive forces and shearing velocities, ten loading conditions were simulated (Table 6.2). The values of

compressive loads and shearing velocities were within the range of the values used in previous experimental and FE studies (Anglin et al., 2000; Gunther et al., 2012; Hopkins, 2004; Junaid et al., 2010). This analysis was used for validating the control glenoid FE model.

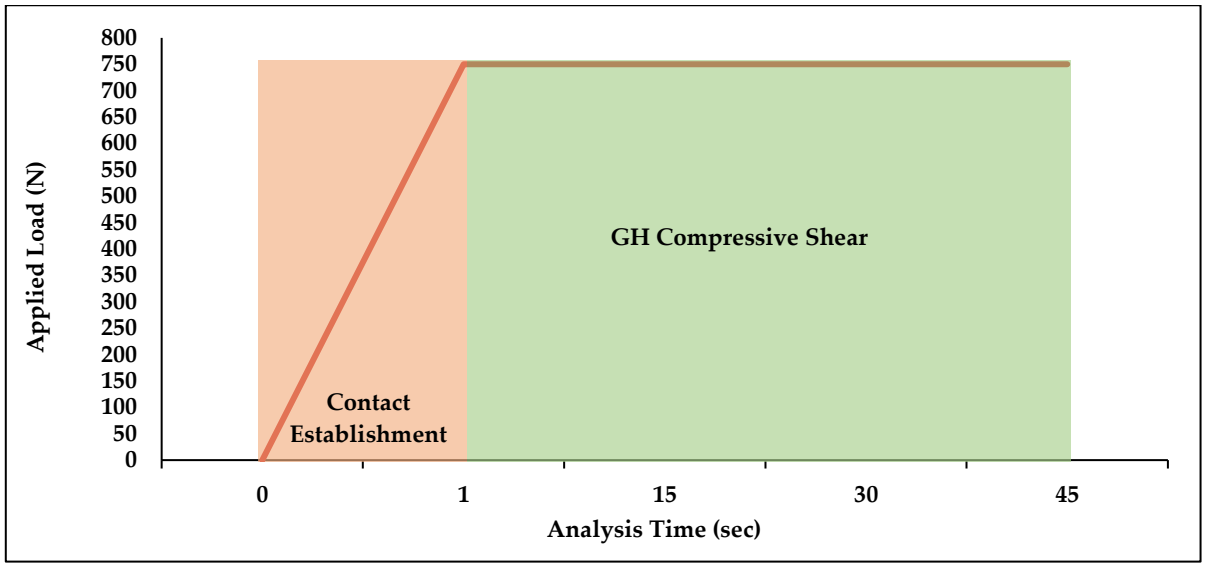

Figure 6.13 The loading amplitude applied to maintain GH contact while the head was allowed to displace a distance of 4.5mm at a rate of 0.1 mm/sec.

Table 6.2 The various loading conditions applied to the humeral head. All the applied axial loads were applied with the constant shearing velocity of 0.1mm/sec and the shearing velocities were applied under a constant axial load of 750N.

Applied Axial Load (N)	Applied Shearing Velocity (mm/sec)
250	0.05
750	0.1
500	0.25
1000	0.5
1850	0.75

6.4 Validation of the Control FE model

Establishing the GH implant contact did not damage the glenoid surface but was found to be an essential step to understand the influence of different compressive load on the produced tangential or shear forces. Under a compressive load of 750N, the shear forces were observed to increase linearly until 1.3mm of humeral translation. The shear forces increased with a

higher rate post this point until about 3mm of humeral translation. Post this point the rate of increase of the shear force decreased and almost became stagnant until the end of the translation limit. A similar pattern of change was observed between the ratio of the shear and the axial forces and the humeral head translation on the cup (Fig. 6.14).

Using the rigid body theory (based on load equilibrium Eq. 5.1) subluxation limit of 1.8mm, the force ratio and the shear force observed were 0.31 and 229.4N respectively. Higher force ratio and higher shear force values (0.71 and 528.7N) were observed at the subluxation point of 3.7mm, which was predicted using Eq. 5.2. This observation was in-line with the previous experimental and FE studies (Anglin et al., 2000; Hopkins, 2004). Using a similar glenoid prosthesis, in terms of size and constraint angle, Hopkins et al., 2006b, had reported a superior subluxation force ratio of 0.71, 0.7 and 0.73 with reconstructed scapula backing, polyurethane backing and without any backing material respectively. It further verifies that the FE based predictive method of humeral head subluxation is better than glenoid implant's geometry-based predictions.

The similarity of the above findings with the literature suggests that using a truncated translation of the humeral head, until a predicted subluxation limit and implicit method of FE solving with increased mesh density did not affect the outcome. Henceforth, the point of subluxation will be implying a humeral head translation of 3.7mm on the glenoid cup. The induced shear forces and the force ratios were observed to change with the alteration in the horizontal compressive load. Four compressive loading scenarios, apart from 750N, were simulated. Two of the compressive loads were larger than 750N while the other two loading cases were less than 750N. A decrease in the compressive load by 66% and 33% reduced the induced superior shear force at the point of subluxation by 62.8% and 30.5% respectively (Fig. 6.14). Even though the magnitude of the applied compressive load and the observed subluxation force decreased, the force ratio at subluxation increased by 11.3% (250N) and 4.2% (500N) respectively (Fig. 6.15). On the other hand, increasing the compressive load by 33% and 146.7%, raised the shear force at subluxation by 28.8% and 118.8% respectively (Fig. 6.14).

With the increase in compressive load, the force ratio was observed to decrease by 4.2% (1000N) and 12% (1850N) respectively (Fig. 6.15).

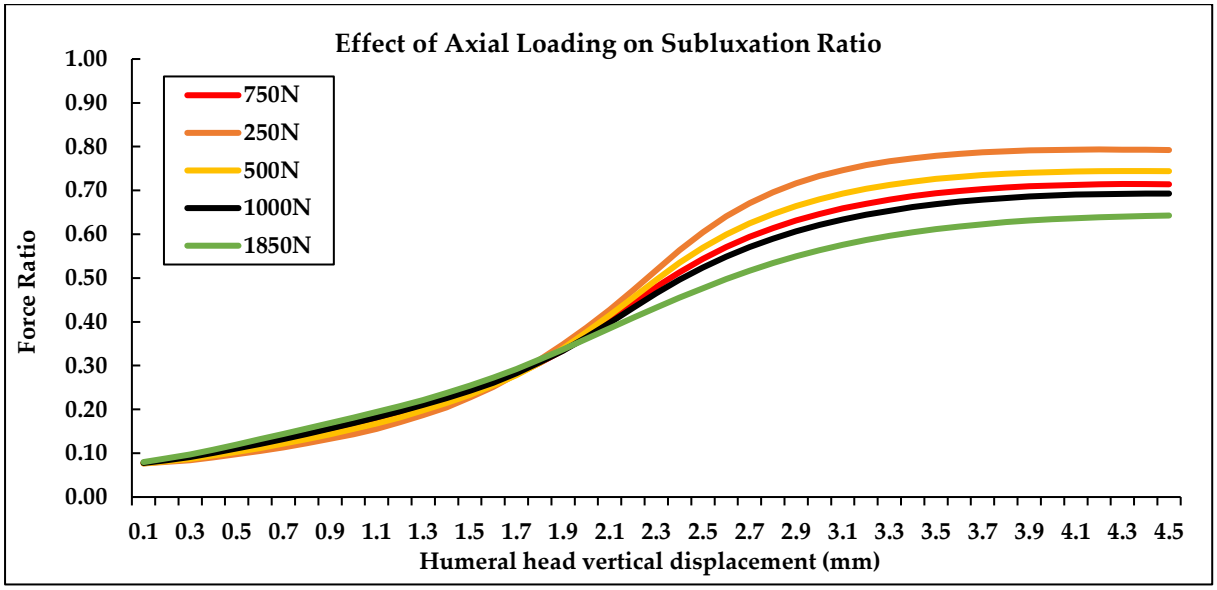

Figure 6.14 Ratio between the vertical (shear) and horizontal (compressive) force calculated for the humeral head translation under various compressive forces

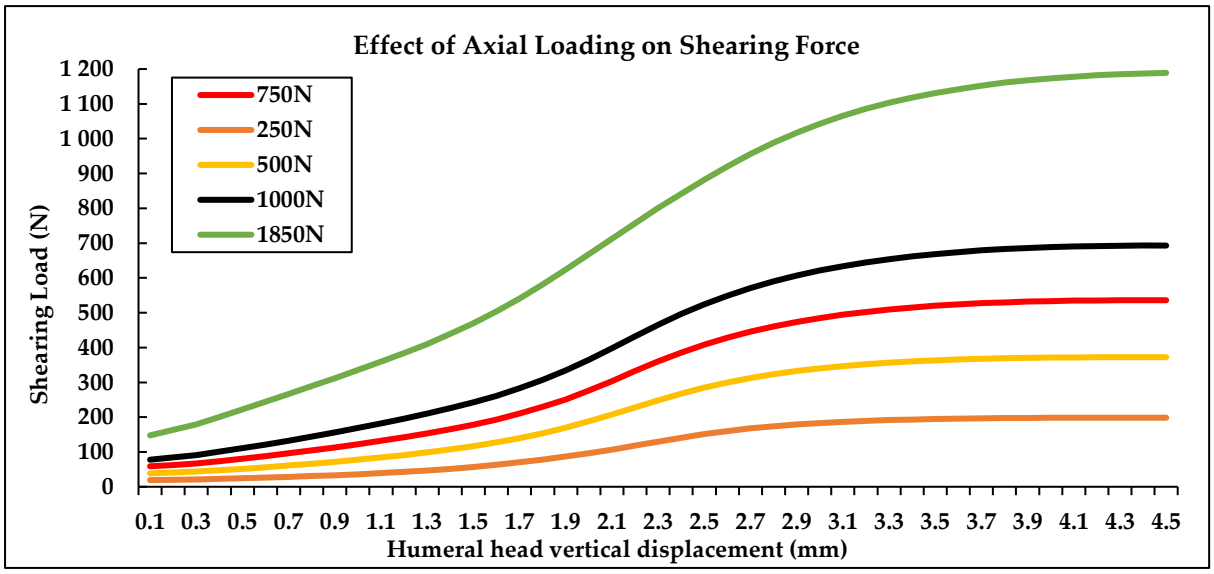

Figure 6.15 Vertical (shear) forces induced by the humeral head under the influence of various compressive loads as the head translated superiorly on the cup.

Such loading characteristics have been predicted by Anglin et al., 2000 and were experimentally observed by Lippitt et al., 1993, who induced compressive loading of 50N and 100N. Although the force ratio, at subluxation, was comparably lower in the case of a humeral

head loaded with a higher compressive force, this was not the observation throughout the humeral translation. With the increase in compressive loading, the force ratio is initially higher. This initial increase in force ratio might be occurring due to the *"deep seating"* of the humeral head on the glenoid surface under higher compression. The effect of the glenoid implant curvature or constraint on the humeral prosthesis, which is, under higher compressive load is greater than the head under lower compressive force. It is evident from Fig. 6.15 that the linear regions for the head under 1850N compressive load last longer, compared to all the other curves, as the head had to overcome higher resistance from the glenoid to reach the subluxation point.

A velocity of 0.1 mm/sec is recommended in the literature to avoid UHMWPE creep (ASTM International, 2012). Translating the humeral head with higher or lower than the prescribed shearing velocity did not affect the force ratios (Fig. 6.16) or the shearing forces. To calculate the shearing forces, the total time of the humeral translation and the point of output were altered for every simulated velocity. For instance, for 0.05mm/sec and 0.75mm/sec the total time of displacement was 90 and 6 seconds respectively and the output points were 2 and 0.13 seconds respectively. The upward velocities used in this study were comparable to Anglin et al., 2000.

In the previous study, as well, no substantial differences in the shearing load or force ratio were reported due to change in shearing velocity. In the current study, it was observed that increasing the humeral upward shearing velocity, to 2mm/sec, neither alter the subluxation force nor the force ratio at the point of subluxation. These similarities in the observations of the current model with previous experimental and FE studies might suggest that the current model is efficient and robust in predicting the effects of the design changes on the prosthesis and cement stresses and deformations. The force ratio and the superior shear force at the rigid body predicted point of subluxation was always observed to be lower than the FE predicted subluxation point (Fig. 6.14 & Fig. 6.16). At the point of GH contact, most of the force was channelled through the center of the glenoid cup, at the point of contact (Fig.

6.17 a). As the humeral head translated superiorly, the contact force between the surfaces was observed to be more distributed.

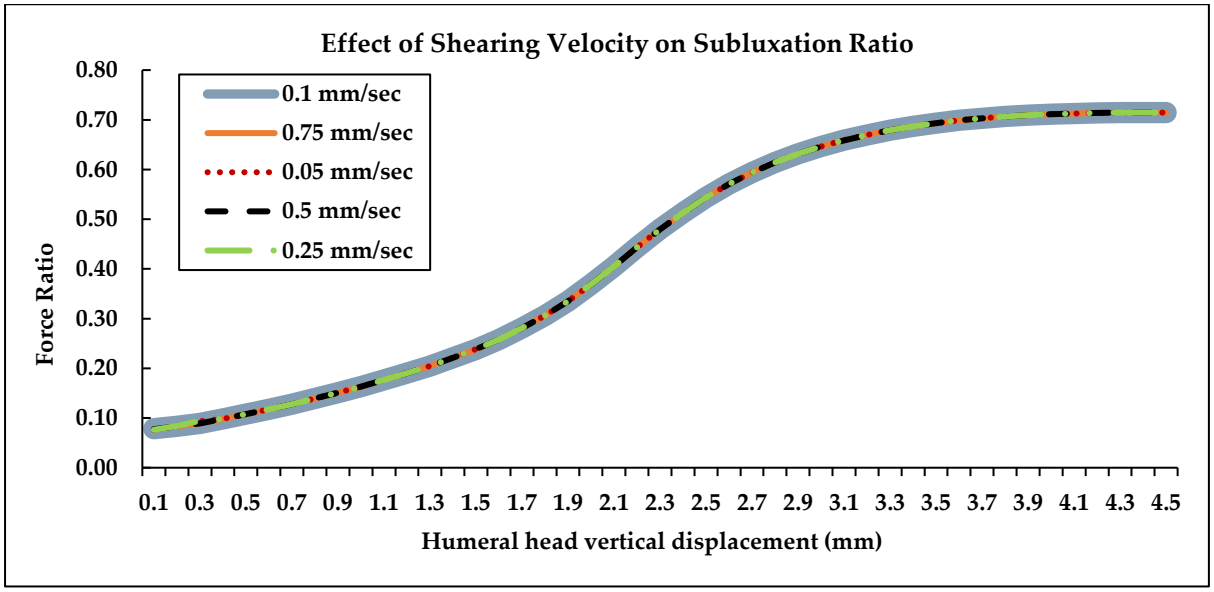

Figure 6.16 The force ratio calculated for the whole range of humeral head translation under various shearing velocities of the humeral head.

As the humeral head translated superiorly by 1.8mm, the rigid body predicted subluxation point, most of the applied load was still found to be concentric and there was no established contact between the head and the glenoid edge (Fig. 6.17 b). As the head continued its superior translation, the applied load was observed to be more evenly distributed on the glenoid surface when the head had translated an average distance of 2.5mm (Fig. 6.17 c). It was only after the head had displaced >2.7mm that the eccentric loading was observed to begin. The resultant load at the edge of the glenoid was found to reach a value of 917.6N at 3.7mm of humeral translation (Fig. 6.17 d), after which the resultant load and the shear force had minimal increase and did not affect the load ratio until the end of translation (Fig. 6.14 & Fig. 6.15). The observed resultant load, at the point of subluxation, was within the range of the reported maximum resultant loads of 787N to 1050N (Anglin et al., 2000 (1); Anglin et al., 2000), representing weight-bearing activities of daily living (ADL). The compressive deformation of the loaded edge of the glenoid cup (Fig. 6.18 b) prohibited the increase in shear

loading after the head had reached the subluxation point. At this point, maximum inferior edge distraction was observed suggesting the typical case of force imbalance (Fig. 6.18 d).

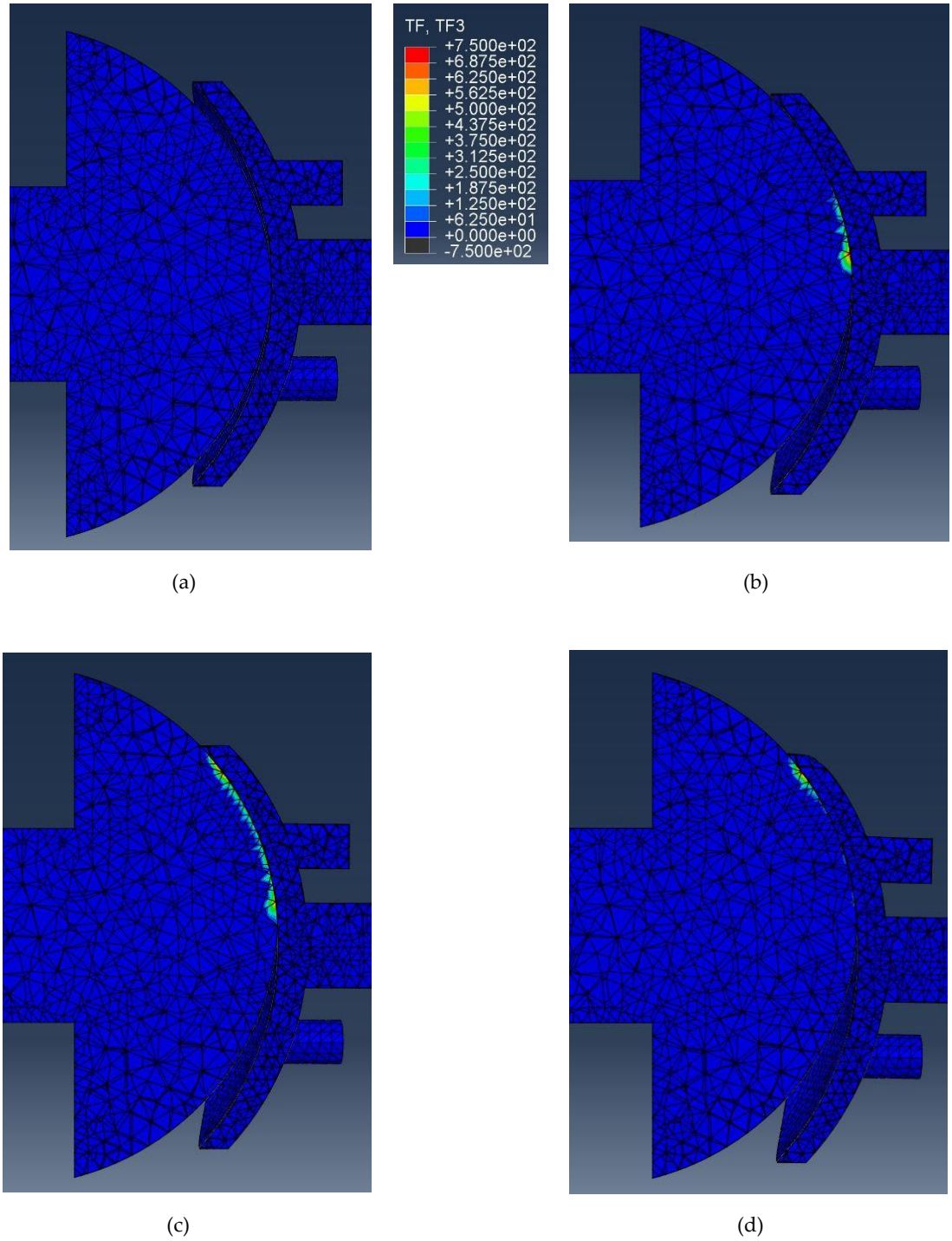

Figure 6.17 A cross-sectional view of the GH components showing the region of the applied force. (a) At the beginning of the analysis (0 mm of shear) the humeral head was in contact with the center of the glenoid cup, (b) as the head sheared up to the theoretically predicted subluxation point of 1.8mm, the force was still being applied in a region within the central and superior glenoid pegs. (c) The applied force was spread over the superior glenoid surface when the head had translated, a distance between, 2.1 to 2.7 mm. (d) The applied force was found to be only concentrated on the periphery of the glenoid cup above 3.7mm of humeral head translation, which was the predicted subluxation point calculated in this study. At this point, superior glenoid deformation is also observed.

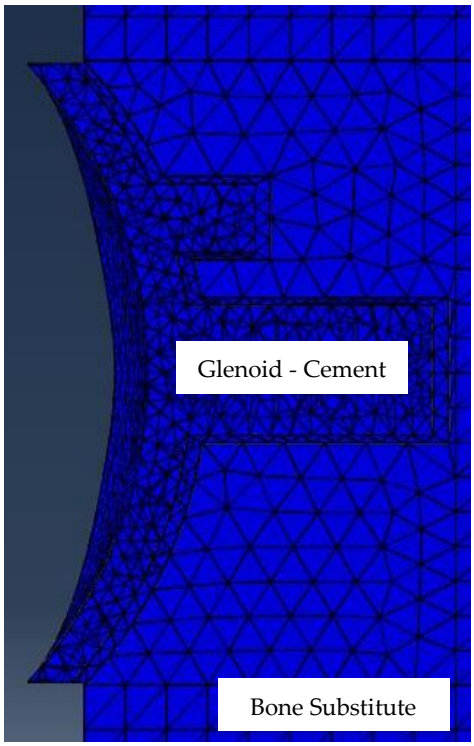

(a)

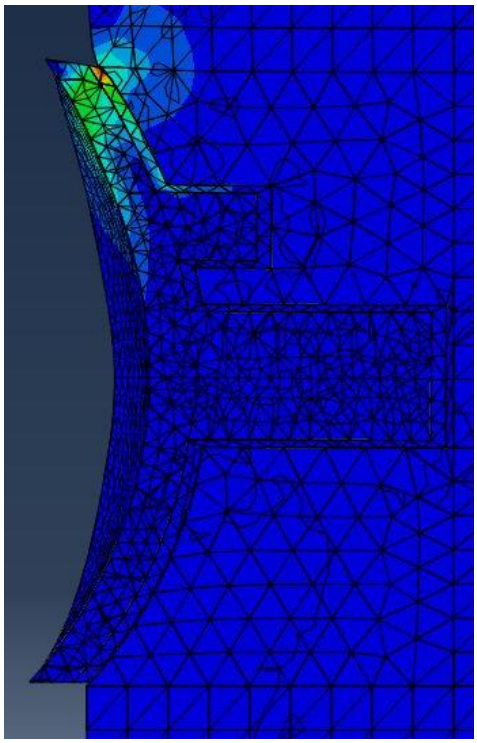

(b)

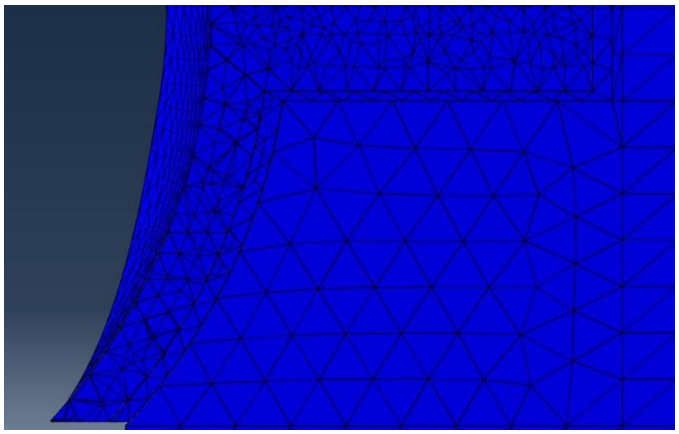

(c)

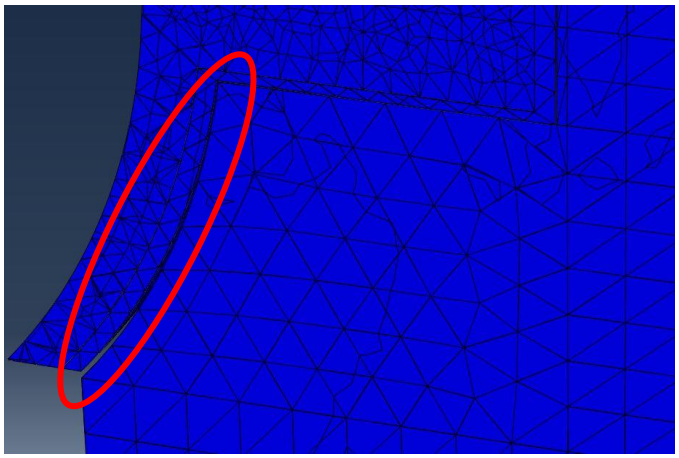

(d)

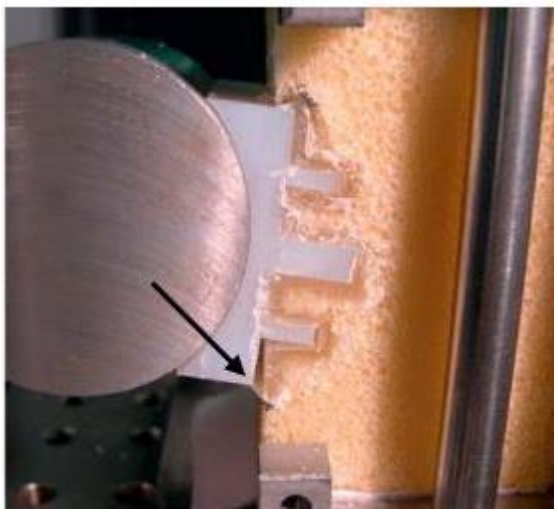

(e)

Figure 6.18 (a) The initial unloaded state of the glenoid-cement-polyurethane component set. Upon loading the glenoid component using a translating humeral head, (b) maximum deformation on the superior edge was observed at the subluxation point and the glenoid-cement component set, which (c) was in full contact with the polyurethane, was observed to (d) detach from the polyurethane surface (red circle) as was reported in (e)the literature by Junaid et al., 2010, after cyclic loading.

In a biological shoulder, the humeral head might be expected to roll after a certain amount translation on the glenoid surface, due to the actions of rotator cuffs and the GH joint capsule. As the ASTM test does not permit rotational motion of the head, physiologically accurate results might not be achieved using the process. Moreover, as explained by Hopkins et al., 2006b, the complete dislocation of the humeral head out of the glenoid cavity in physiological fashion might not be accurately replicated by an FE study. Even if the head was made to translate on the glenoid above and beyond the subluxation point, with inactive freedom of rotation, deformation of the glenoid edge was induced along with a reduction in load ratio as the resistance offered by the cup decreased.

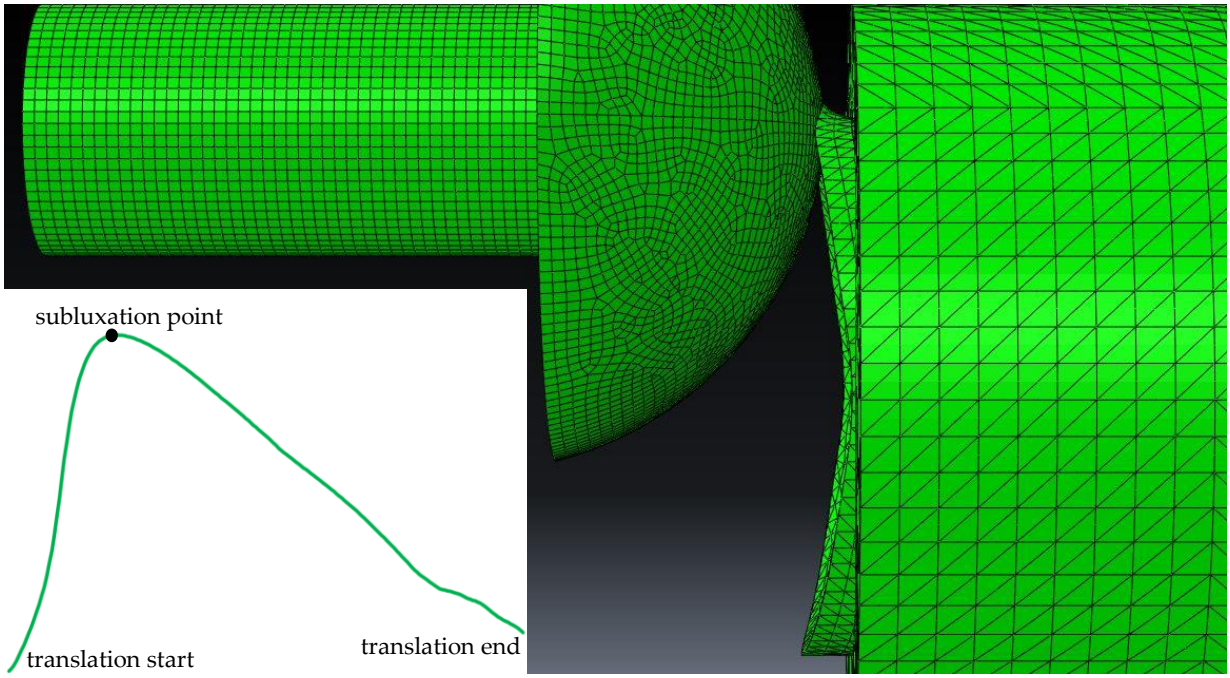

Figure 6.19 Displacing the humeral head center to the glenoid edge deforms the glenoid rim. Beyond the subluxation point the shear force and the load ratio decreases (inset).

Establishing a surface to surface interaction between the cement and polyurethane displaced the inferior edge of the cement by a value of 0.07mm, at the point of humeral subluxation. At the exact instance, the compression of the superior rim of glenoid was observed to be 0.55mm. To evaluate the inferior distraction, firstly, the distance between the most lateral edge of the glenoid cup and the edge of the polyurethane was calculated at 0mm

(Fig. 6.20 a) and 3.7mm (Fig. 6.20 b) humeral head translation. The relative difference between the two distances, i.e. Y-X, was the final reported inferior distraction.

The superior compressive deformation was evaluated as the displacement of the most superior element of the glenoid cup. This element was selected as it could be expected to undergo the maximum compression under humeral load. The average displacement of every node of this element, which was influenced by the displacement of the adjacent nodes, was presented as the final value of edge compression. The distraction measurements calculated in the current study was not found to be comparable to an FE study performed by vigorous isolated cyclic loading of similar glenoids by Gunther et al., 2012.

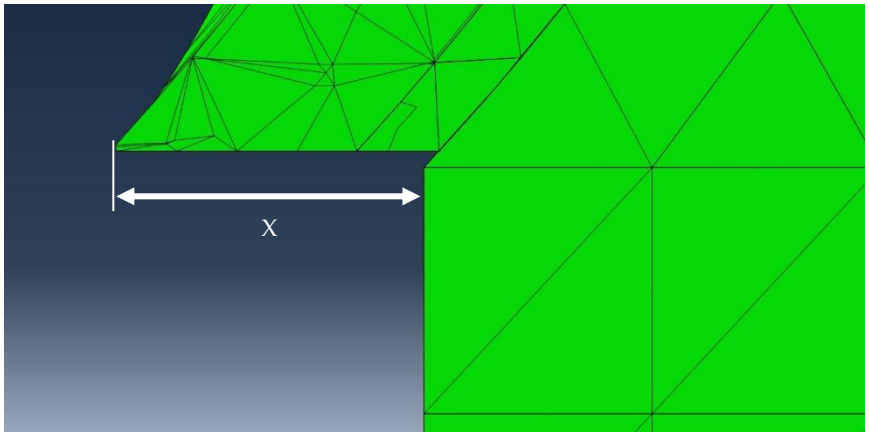

(a)

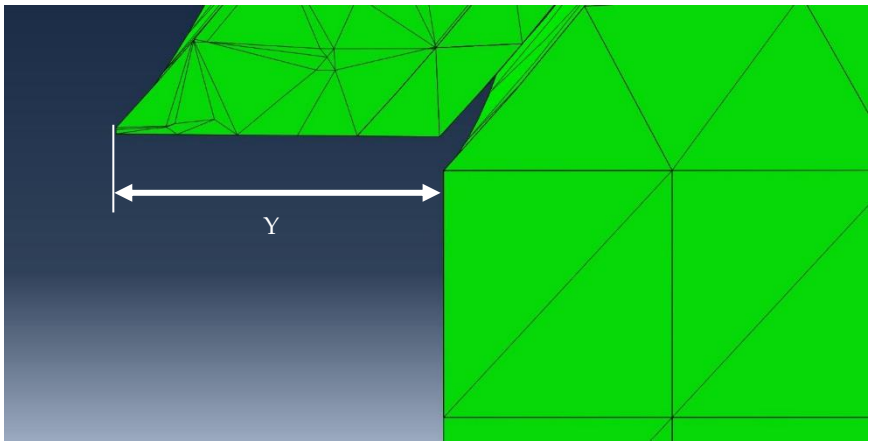

(b)

Figure 6.20 Schematic representation of the (a) glenoid-cement object attached flush on the polyurethane backing. X represents the distance between the edge of the polyurethane and glenoid cup. (b) The detachment of the cup and cement from the bone substitute surface increasing the distance between the edges, measured as Y. The inferior displacement was calculated as Y – X.

An experimental study by (Anglin et al., 2000 (1)), had reported that pegged glenoid components with curved posterior geometry demonstrated lowest inferior edge distraction after 100,000 SI loading cycles. Although it would be not appropriate to compare the distraction values of the current study, with the values obtained after cyclic tests, it is still worth mentioning that the average post-cyclic inferior distraction was about 0.08mm. In the same study, it was reported that the pre-cyclic inferior distractions were about 0.04mm which are much lower than the observed values in the current study. The authors reported a post-cyclic superior compressive distraction of 0.5mm. Hence, for a curved back glenoid with pegs, it could be hypothesised that single dynamic subluxation of the humeral, with appropriate cement-polyurethane interaction properties, could produce glenoid edge distractions comparable to cyclic tests. Testing this hypothesis using cyclic FE analysis is outside the scope of this thesis but would be performed in the future.

At the point of subluxation, the maximum von Mises stress was observed to be concentrated on the rear of the glenoid. The value of the von Mises stress at the back of the prosthesis was 25.4MPa (Fig. 6.21 a), which was above 21MPa, the yield strength of UHMWPE (Hopkins et al., 2006b). At the same instance, the maximum von Mises stress on the surface was 17.8MPa. Von Mises stress is a widely accepted indicator of material failure (Zhang et al., 2013) as it represents the combined effects of the principal stresses in all the three principal axes. The observed stresses in this study suggest that the posterior surface of the glenoid has a higher probability of failure, under compressive shear forces, than its articulating surface. The maximum principal stress was found to be 14.5MPa, concentrated on the edge of the glenoid (Fig. 6.12 b). Investigating a curved back keeled glenoid prostheses, Terrier et al., 2012, had reported von Mises stress of 28.3MPa on the surface of a 2mm thick glenoid subjected to an average abductive load of 970N. Increasing the thickness of the prosthesis by 200%, to 6mm, reduced the von Mises stresses on the glenoid surface by 50%. This suggests that the thickness chosen for the prosthesis in the current study falls within the acceptable limits and would be able to sustain physiological loading conditions.

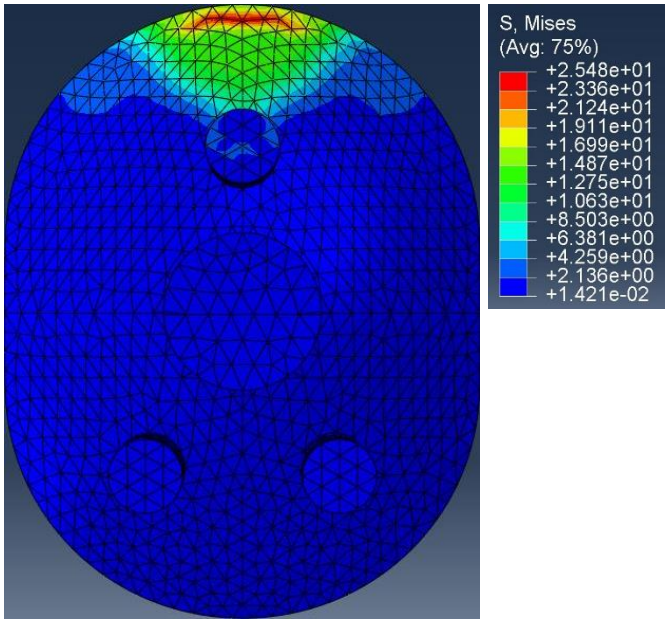

(a)

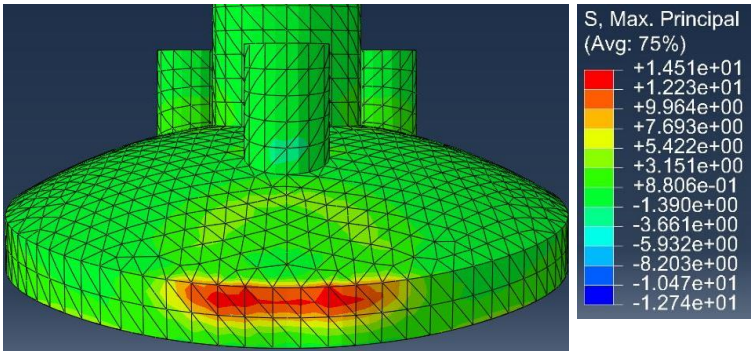

(b)

Figure 6.21 At the point of subluxation (a) maximum von Mises stress on the posterior edge of the glenoid and (b) maximum principal stress on the superior edge of the cup.

In the case of the PMMA bone cement, the maximum tensile stress at the point of subluxation was observed to be 6.19MPa. The position of this stress was concentrated around the superior edge of the cement mantle. Using Weibull distribution, a third order polynomial relationship (Eq. 5.3) between the probability of hand-mixed bone cement surviving (Ps) 10 million (10^7) cycles under uniform tensile stress (σ), which was provided by Murphy & Prendergast, 2000.

$$P_s = 1.8365 - 0.0005\sigma^3 + 0.0202\sigma^2 - 0.3304\sigma \qquad (6.3)$$

Superior translation of the humeral head prosthesis gradually increased the tensile stress on the cement layer until it reached the maximum value at the point of subluxation. The variation in Ps for the region experiencing highest tensile stress until subluxation is provided in Fig. 6.22. The cement regions that could be expected to have the maximum survival probability, under uniform tensile stress, were the areas between the central and the superior pegs. The superior edge of the cement mantle and the edges of the pegs demonstrated least survival probability and might be the regions of failure crack initiation.

The maximum cement tensile stress at the superior edge, at the point of subluxation, was found to be lower than the metal-backed and all polyethylene keeled glenoid components (Lacroix & Prendergast, 1997). If the whole cement mantle was under a uniform tensile stress of 3.3MPa, its probability of surviving 10^7 loading cycles would be 95% (Allred et al., 2016; Hopkins et al., 2004; Lacroix et al., 2000). The average percentage of the cement mantle, in the current study, having a 95% chance of surviving 10^7 cycles of subluxation loading was 99.9%. This was calculated by analyzing the tensile stress magnitude for each element in the cement layer throughout the humeral head displacement leading to subluxation. The cement mantle survival percentage is quite high and matches with previous FE studies on curved back polyethylene pegged prostheses.

Cement survivability has been reported to depend on the glenoid cup alignment and quality of the glenoid bone. A cement layer sandwiched between an all-polyethylene cup and rheumatoid bone has lower chances of surviving 10^7 cycles than a cement layer connecting the cup and normal bone (Hopkins et al., 2004; Lacroix et al., 2000). Altering the version and the inclination of the glenoid cup has also been reported to reduce the cement mantle survivability (Allred et al., 2016; Hopkins et al., 2004). A pegged glenoid prosthesis aligned centrally to a glenoid vault consisting of healthy glenoid bone would have, on average, at least 94% of the cement layer surviving 95% of the 10^7 cycles (Hopkins et al., 2004; Lacroix et al., 2000). This suggests that the control glenoid implantation process and the combined material properties assigned to the components, in this study, created an acceptable representation of the real-world post-surgical TSA model.

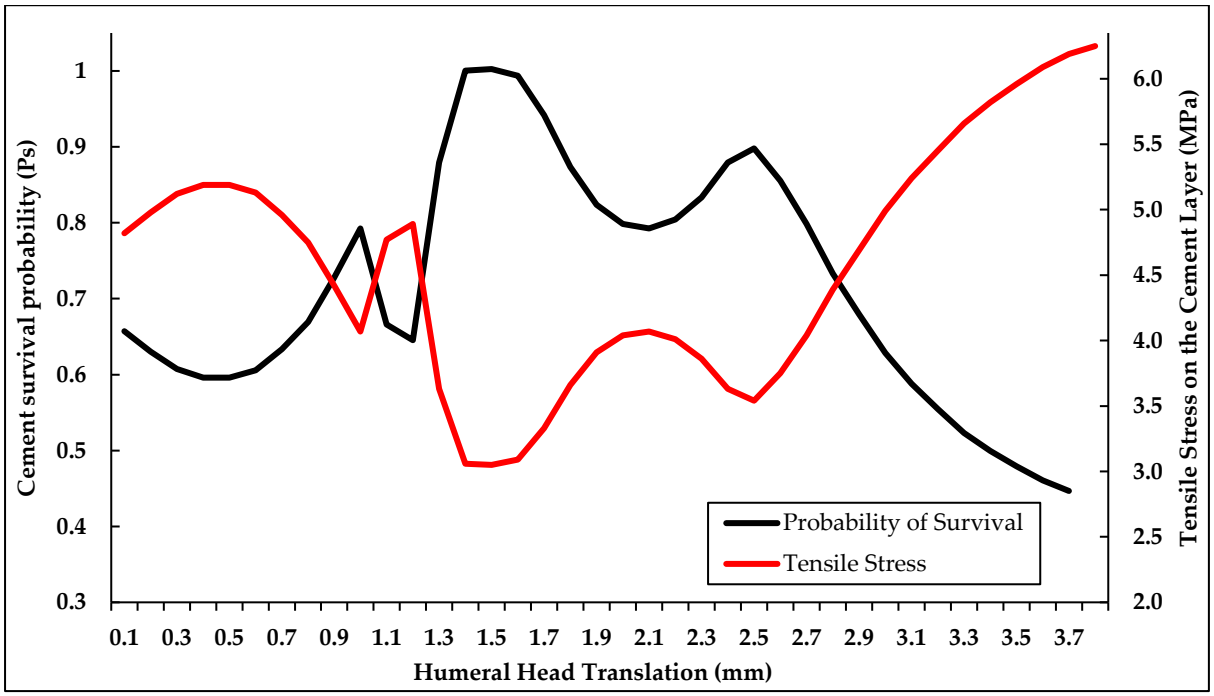

Figure 6.22 The survival probability of the cement regions (P_s), for 10 million cycles, under the direct influence of superior humeral translation.

6.5 FE models of the Novel Prostheses

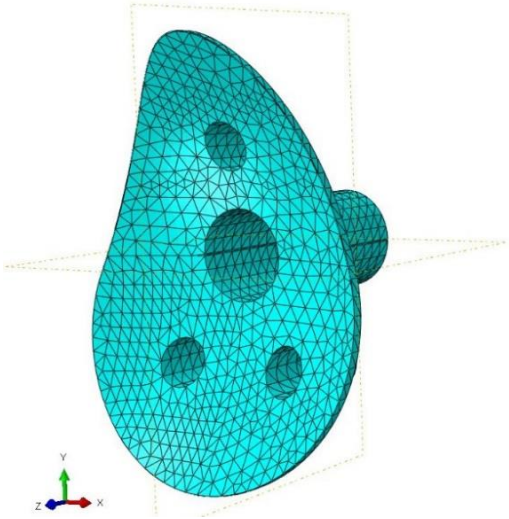

Figure 6.23 The cement backing for the pear-shaped glenoid.

The underlying designs of the bi-radial and the compartmental glenoids were similar to the control designs as far as the structural boundaries of the cup are concerned. The shape of the

pear-shaped glenoid was significantly different from the control glenoid cup. While the cement layer geometry was kept identical for the former two designs, it had to be altered for the pear-shaped glenoid (Fig. 6.23). The respective FE models for each of the glenoid designs were created as a variation of the control FE model.

In each of these models, only the glenoid component was altered except for the model for the pear glenoid, where the cement structure was also replaced. The newly introduced glenoid and cement components were re-meshed using the same global element size of 1.3, as was used to create the control FE model. Utilising similar meshing method produced minimal variations in the final number of elements and nodes as reported by Gunther et al., 2012.

Table 6.3 Mesh details of different glenoid and cement objects used in the current study.

Model Containing	Glenoid Prosthesis		Cement Backing	
	Elements	Nodes	Elements	Nodes
Control Glenoid	18411	29421	6453	13139
Bi-radial Glenoid	17874	28520	6453	13139
Compartmental Glenoid	17738	28954	6453	13139
Pear Glenoid	18874	29989	6440	13079
Average (std. dev.)	18224 (452)	29221 (546)	6450 (6)	13124 (26)

6.6 Performances of the Glenoid Designs under Humeral Loading

The shear force applied by the translating humeral head were not identical for every glenoid design. All the glenoids were observed to experience lower shear force and force ratio at the rigid body predicted subluxation point than the FE predicted subluxation point (Fig. 6.24 & 6.25). Comparing the shear to compressive force ratios of the bi-radial, compartmental and pear-shaped glenoid with the control prosthesis, the compartmental glenoid was found to have identical ratios at the point of humeral subluxation.

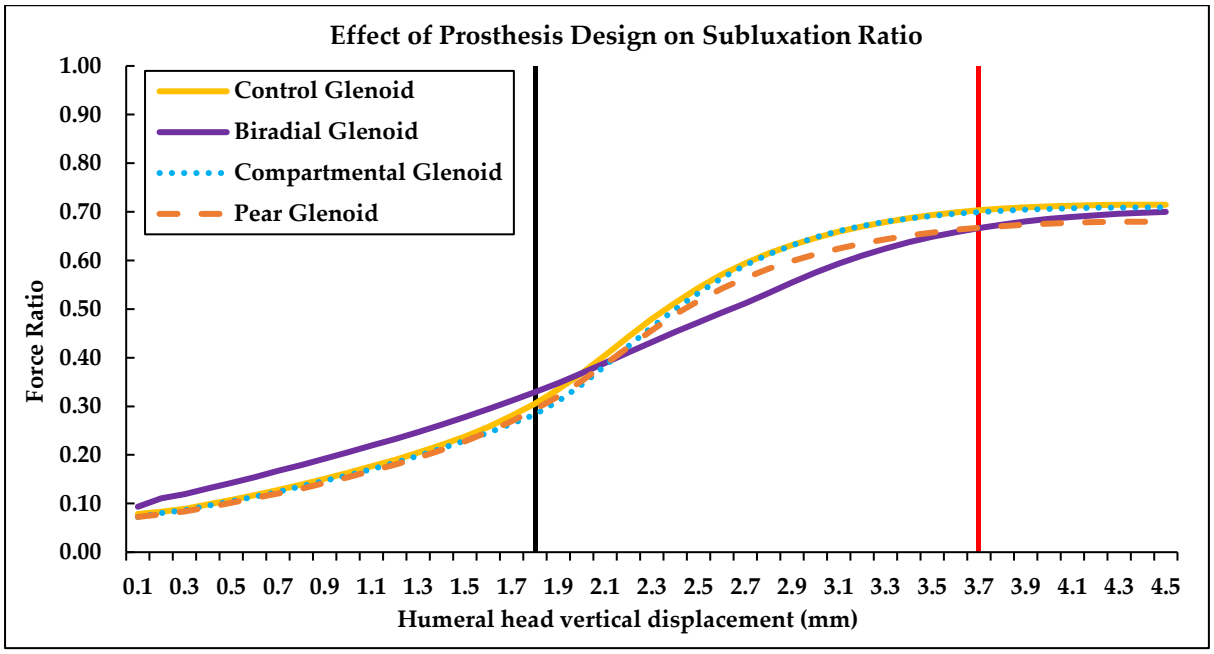

Figure 6.24 The ratio between the shear force and the applied axial loading (Fy/Fz) for all the glenoid designs. The black and red lines represent the theoretical and FE predicted humeral head translation limits respectively.

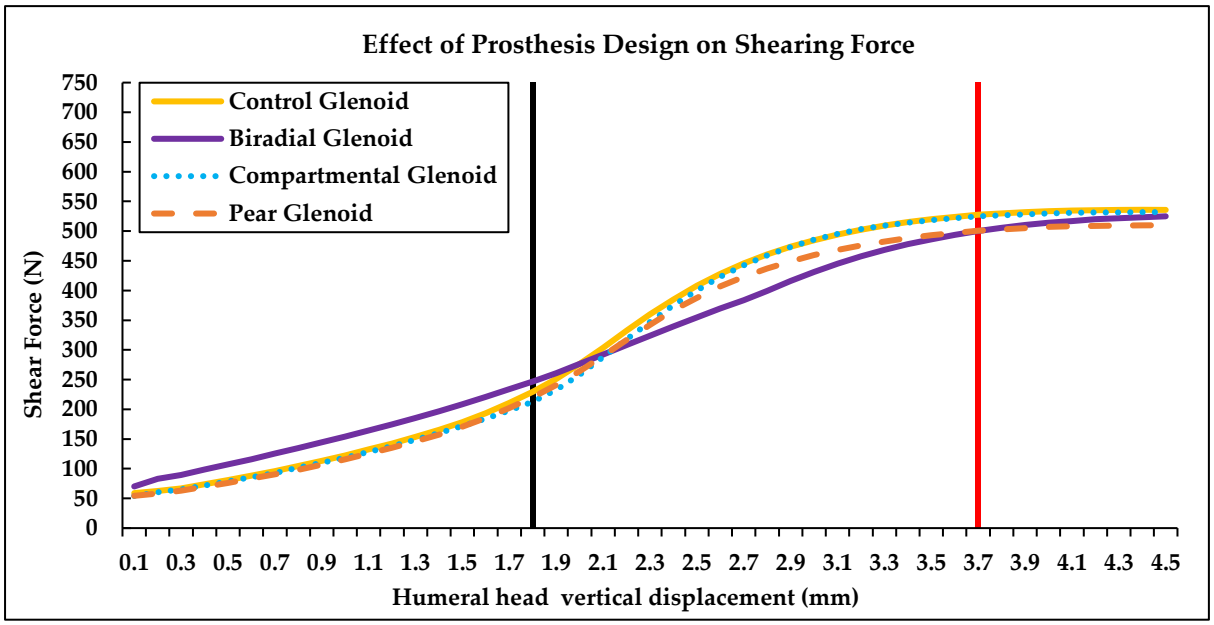

Figure 6.25 The shearing force (Fy) profile for all the glenoid designs.

The pear-shaped glenoid was found to have the lowest resistance to subluxation, as it had the lowest force ratio (Fig. 6.26). This observation corroborates one of the conclusions presented by Hopkins, 2004. The bi-radial glenoid design had the most varied force ratio profile. The probable reasons for this observation are discussed later in this section.

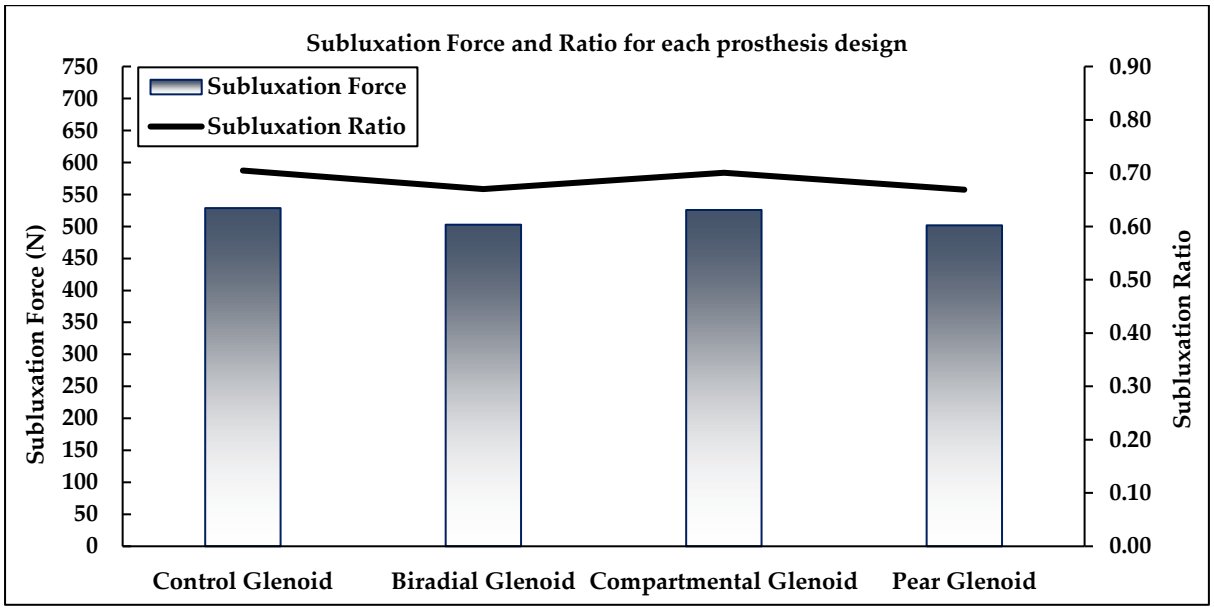

Figure 6.26 The applied shear force and the its ratio at the FE predicted subluxation point for all the glenoid designs.

The bi-radial glenoid was designed with an increased superior-posterior curvature and this might have been the primary reason behind the reduction in the implant's subluxation ratio. This glenoid could not be categorized as unstable with higher chances of superior dislocation, as the pear glenoid, because its force ratio or resistance to dislocation was observed to rise beyond the subluxation point (Fig. 6.24). Due to the change in glenoid geometry, higher loads were able to be transferred through the PS quadrant of the glenoid. This was also evident on the surface of the humeral head prosthesis. On comparing the load transfer regions on the head, it could be observed that the point humeral contact with the bi-radial glenoid was predominantly on its posterior region (Fig. 6.27 a-c), throughout the translation, while the point of contact was central to the humeral head loading the control glenoid (Fig. 6.27 d-f). Shifting majority of the applied load posteriorly did not increase the von Mises stress above the yield stress of UHMWPE until the subluxation point was reached. At this instance, the maximum von Mises stress recorded was 25.7MPa. This stress value was almost identical to that of the control glenoid and was located near the PS edge of the cup (Fig. 6.28 a). The maximum principal stress was observed to lie on the thickened PS edge of the glenoid edge (Fig. 6.28 b). The maximum principal stress (13.2MPa) at the point of subluxation was lower than the control glenoid.

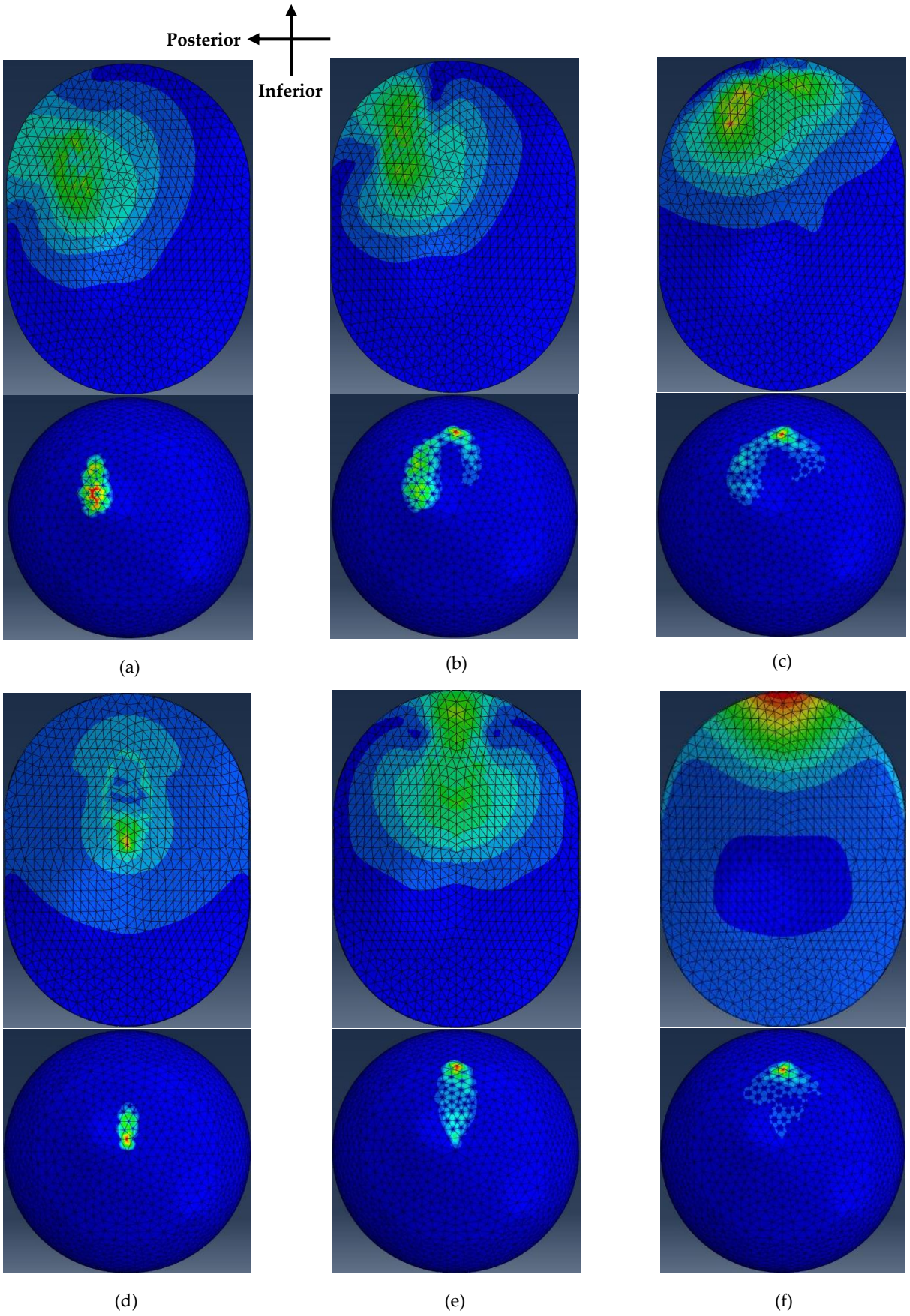

Figure 6.27 Representation of the GH contact regions for the bi-radial (a–c) and control glenoid designs (d-f). (a & d) represents the areas under contact after 1.8mm of translation. (b & e) represents the areas under contact after 2.5mm of translation and (c & f) represents the area under contact at the point of subluxation.

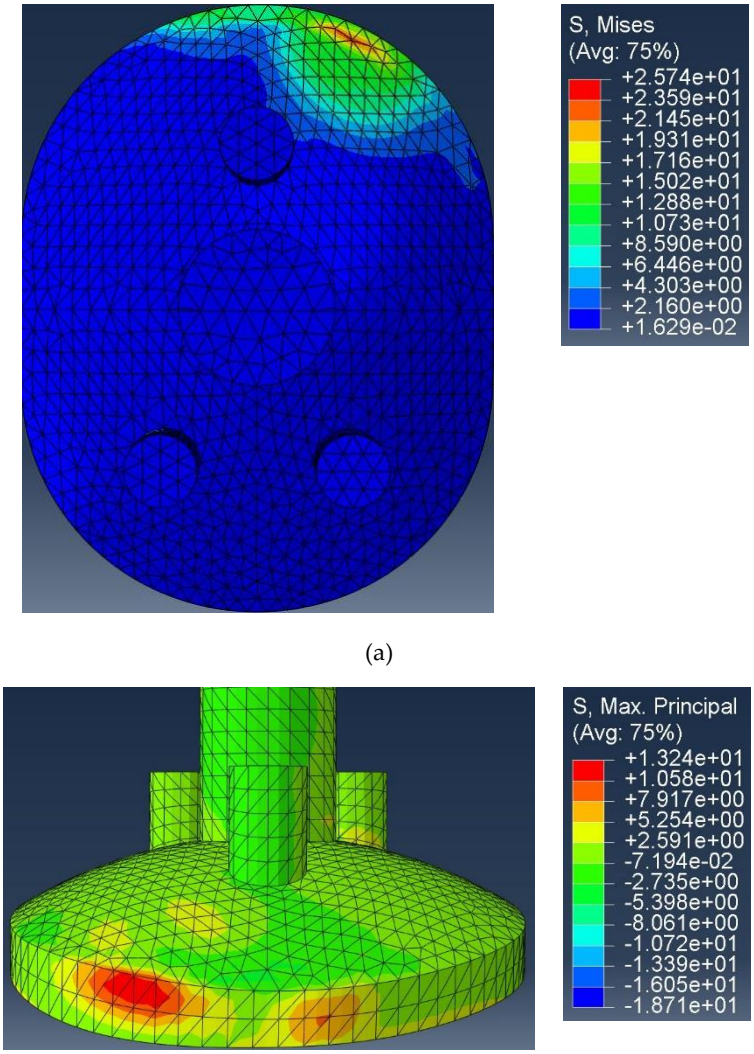

Figure 6.28 The maximum (a) von Mises stress and (b) principal stress on the bi-radial glenoid edge at the point of humeral head subluxation.

The bi-radial glenoid demonstrated reduced the edge loading compared to the control glenoid. Posterior loading of the glenoid has been reported to be the anatomic loading pattern in the healthy and post-TSA shoulder (Bergmann et al., 2007; Massimini et al., 2010; Omori et al., 2014; Westerhoff et al., 2009). Independent studies performed by Massimini et al., 2010 and Bergmann et al., 2007, on the post-TSA subjects, suggests that 61.5% of the GH contact occur on the PS quadrants of the articular surfaces (Fig. 6.29 a-b).

Moreover, the PS quadrant of the glenoid cavity has better strength characteristics and highest stress modulus compared to other quadrants of the surface (Anglin et al., 1999).

Hence, structurally it might be beneficial to channel the joint contact forces posteriorly, through the bi-radial glenoid, into the glenoid vault to possibly increase osteointegration and reduce glenoid edge loading.

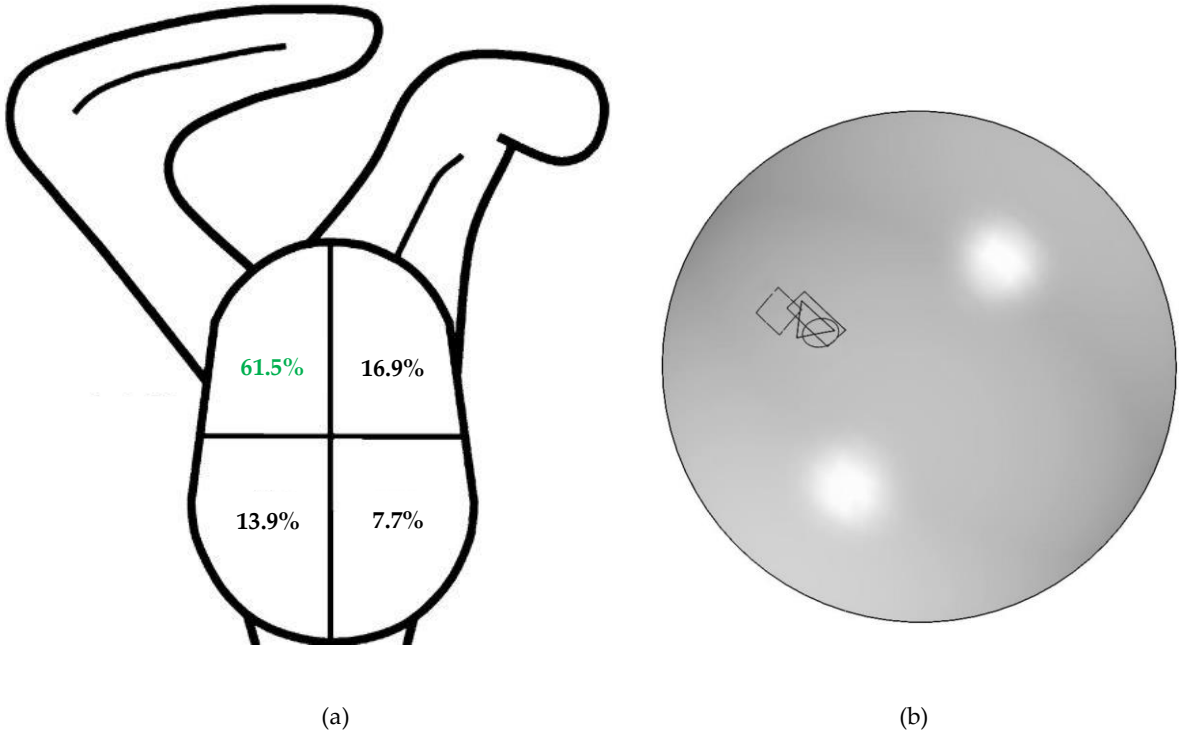

(a) (b)

Figure 6.29 (a) GH contact centroids during abduction and humeral rotation, distributed along the various quadrants of the glenoid surface. *Modified from* (Massimini et al., 2010). (b) Predicted humeral head contact points using the force vectors recorded using an instrumented humeral prosthesis (Bergmann et al., 2007). The circle, rectangle, square and triangle denotes the point of contact during the abduction, lifting a coffee mug, combing hair and forward flexion respectively.

The possible challenges of implementing the bi-radial design of the glenoid cup might arise if the patient has a posteriorly eroded, such as the B1 and B2 glenoids (Vo Ba et al., 2017). In such a scenario, a combination of bi-radial glenoid design with augmented posterior glenoid backing (Allred et al., 2016) could be the glenoid design of choice. Although the bi-radial glenoid exhibited reduced inferior edge distraction, the separation at the edge diagonally opposite to the superior thickened region of the prosthesis was 0.09mm. This value was higher than the control glenoid inferior distraction. The superior edge compression for both the glenoids was identical.

The cement under the bi-radial glenoid was found to be exposed to higher tensile stress than the control glenoid. The 95% probability for the 1mm thick cement mantle to survive 10^7 loading cycles was reduced to 99.6%. There is a further room for optimizing this bi-radial design to overcome these hurdles and future cyclic tests would be essential in predicting the wear characteristic of the thickened region of the surface. Introducing compartments throughout the superior and inferior sections of the glenoid cup were found to be beneficial. The maximum von Mises stress was concentrated at the edge of the superior compartment and not at the superior edge of the prosthesis (Fig. 6.30 a-b). Although the stress was 11.2% higher, the location of the stress was within the concentric limits of the prosthesis. Moreover, the minimum von Mises stress was observed to be concentrated at the edge of the inferior compartment of the prosthesis (Fig. 6.30 b).

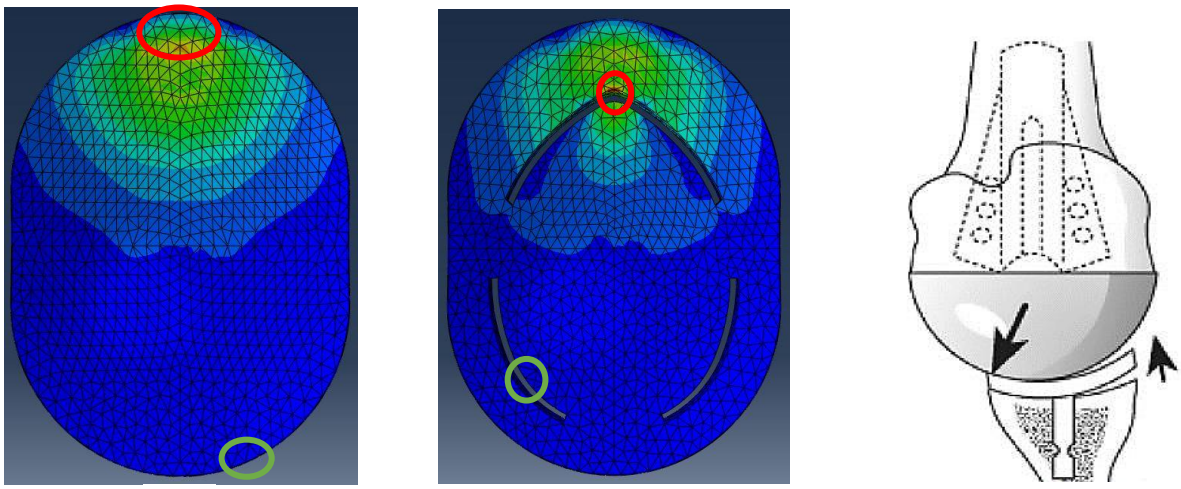

(a) (b) (c)

Figure 6.30 The locations of the maximum (red circles) and minimum (green circles) von Mises stress were found to be located on the (a) edges of the control prosthesis but within the (b) concentric zones of the compartmental prosthesis. (c) The counter-acting force couple causing the rocking horse effect *sourced from* (Matsen et al., 2008).

These observations might suggest that such a compartmental glenoid has the potential to reduce the rocking horse effects caused by the imbalance of edge loading (Fig. 6.30 c). The compartmental glenoid also design exhibits delayed edge loading (Fig. 6.31 a-c). When compared to the commercial glenoid design (Fig. 6.31 d-f), the maximum principal stress was more concentrically distributed, throughout the humeral translation. At the point of subluxation (Fig. 6.31 c), the maximum principal stress was concentrated around the superior

compartmental gap and not of the edge. The value of the stress was 9.6% higher than the control glenoid but well within the range of the UHMWPE yield limit.

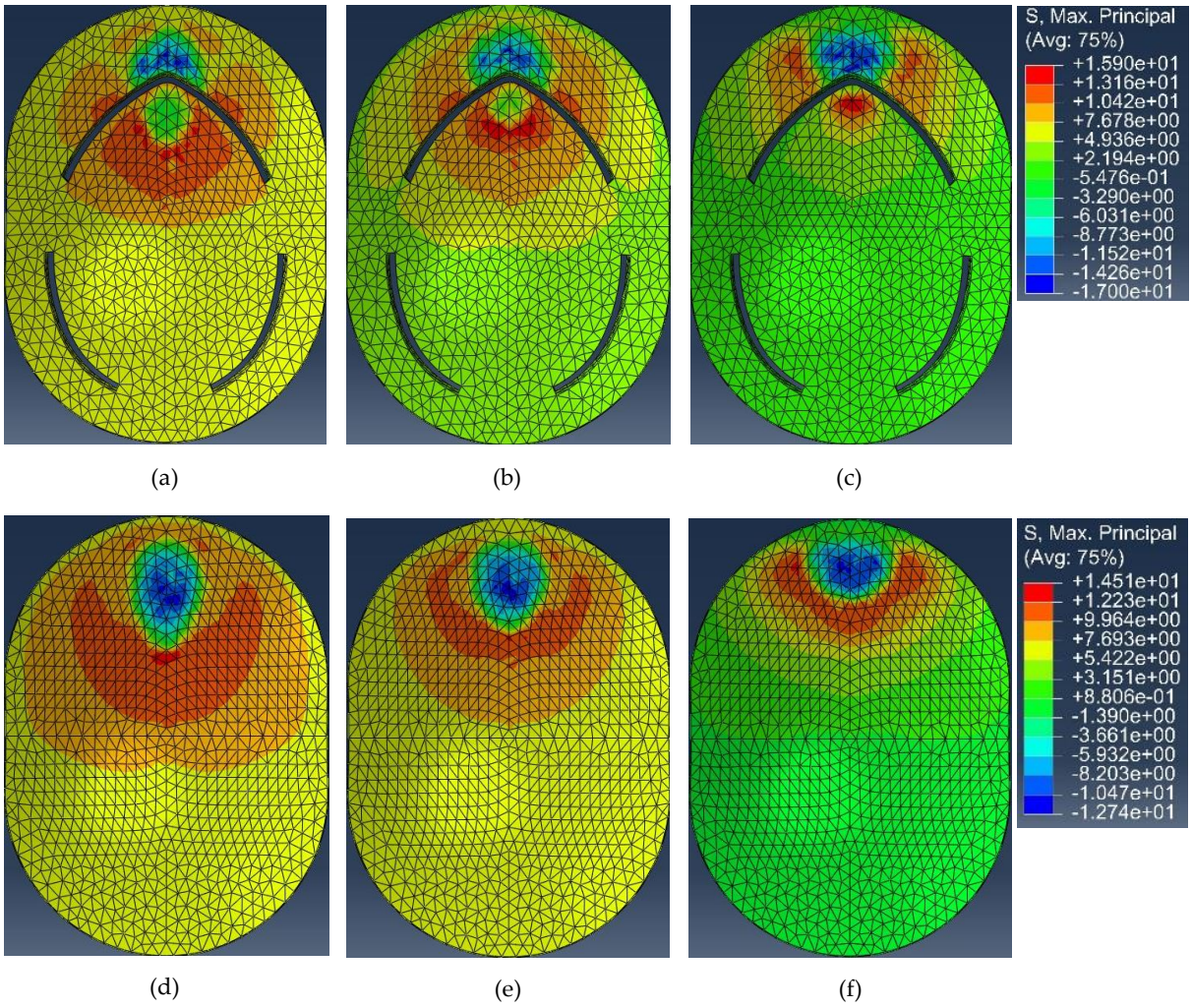

Figure 6.31 The maximum principal stress on the (a to c) compartmental glenoid and the (d to f) control glenoid after (a & d) 1.8mm, (b & e) 2.5mm and (c & f) 3.7mm of humeral head translation towards the superior edge of the respective glenoid models.

The stress on the glenoid cup was effectively transferred onto the cement layer due to the presence of the compartmental gaps (Fig. 6.32). As the head translated superiorly the tensile stress on the cement increased. The average increase in stress on the regions of the cement under the direct influence of the humeral translation was 26.3% or 1.22MPa higher in the compartmental design than the cement layer backing the control glenoid.

Higher stress induced into the cement surface might suggest an increase in the probability of that stress to be transferred to the bone. The rise in the average tensile stress

was not beyond the stress limit of the PMMA and did not reduce its theoretical probability of surviving 10 million loading cycles. Both the superior edge compression and the inferior edge distractions were reduced by 9.1% and 14.3% in comparison to the control glenoid. This might have been due to the reduced and delayed edge loading in the case of the compartmentalised design of the glenoid cup.

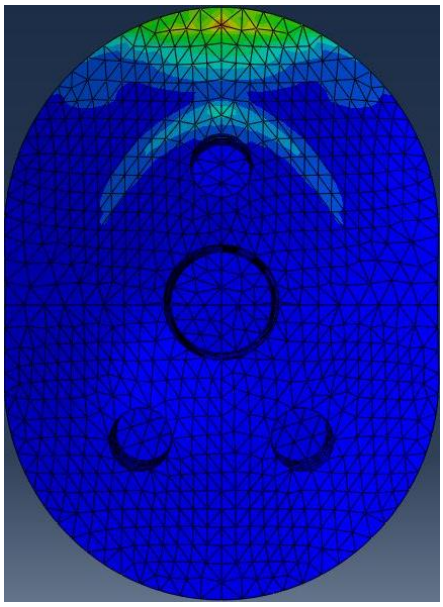

Figure 6.32 The increased cement stress on the lateral surface of the PMMA layer due to the superior gap in the compartmentalised design.

The concentration of stress on the sharp edges of the prosthesis might be detrimental for the prosthesis in the long run. A high rate of wear and tear might be expected in these regions. One of the possible solutions could be rounding or filleting the corners. The compartmental gap, between the concentric and the eccentric regions, could be further optimized to avoid overstressing the polyethylene cup. To the best of the author's knowledge, there are no glenoid designs available commercially or otherwise which could have the ability to diverge the GH joint forces concentrically and compressively towards the bone, using compartmental features on the prosthesis surface, and reduce glenoid edge loading.

Apart from exhibiting lower resistance to superior subluxation, the pear-shaped glenoid was experiencing 16.6% or 4.22MPa higher von Mises stress, at the point of humeral

subluxation. Even though compared to the control prosthesis, the compartmental glenoid experienced higher von Mises stress, the stress induced into the pear glenoid was spread over a lower surface area. The effect of higher stress on the lower area of contact near the superior edge of the cup might be an undesirable design feature for a glenoid prosthesis. Due to the testing protocol applied to the subluxation study, the effect of increasing the AP width of the glenoid could not be investigated.

Due to the insufficient area for force distribution, the pear glenoid experienced higher deformation amongst all the glenoids studied. The superior and the inferior rims of the prosthesis were compressed by 0.6mm and 0.12mm respectively, at the point of subluxation. These were respectively 20% and 71% higher than the control glenoid edge deformations.

The shape of the cement layer was modified to match the posterior profile of the pear prosthesis. The pressure on the superior cement edge was found to be 4MPa higher than the control glenoid and spread over a smaller area. This influenced the survivability of the layer of cement under the direct influence of the humeral translation. This survivability of this region was reduced by 22.5%. The pear glenoid did not show any promising characteristics of reducing the rocking of the prosthesis. The shape of the glenoid is still the most accurate representation of the glenoid cavity. Few recommended techniques that could be employed to better the performance of the pear-shaped glenoid could be; using it as an inset glenoid cup or modifying its glenoid rim design to mimic the functionality of the glenoid labrum. These alterations might take the glenoid cup design towards being more anatomic, in shape, whose functionality should be investigated and verified in future studies.

A summary of the biomechanical and finite element observations is presented in the Table 6.4. From these observations, it might be justified to propose a conclusion that the compartmental glenoid could be a beneficial cup prosthesis. The design of this prosthesis is a combination of the healthy pear-shape and the arthritic oval-shape of the glenoid fossa. The introduction of separation, in the form of gaps, between the concentric and the edges of the prosthetic glenoid cup exhibited higher load transfer towards the glenoid bone surface instead of the implant edges.

Table 6.4 A summarized interpretation of the observations from the biomechanical and finite element analysis for all the new glenoid design concepts.

	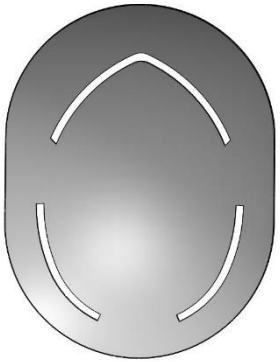 **Compartmentalised Glenoid**	 **Bi-radial Glenoid**	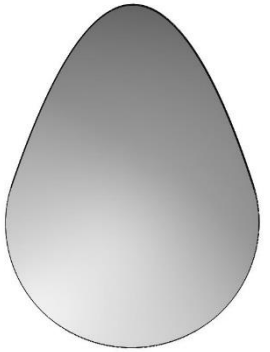 **Pear-shaped Glenoid**
Biomechanical Impact	Constructing gaps between concentric and eccentric regions did not alter muscle moment arms.	Introducing a separate radius in the PS section of the glenoid did not change the post-TSA kinematics.	As most of the motion involved humeral head rotation, reducing the superior surface area of the glenoid did not affect the kinematics.
Post-TSA Stability	Exhibited identical stabilization characteristics as the control glenoid cup, under humeral loading.	Demonstrated higher posterior loading and grater contact with the posterior region of the humerus.	The ratio between the shear and compressive forces suggest reduced superior stability in maintaining the GH articulation.
Force Imbalance on the Edges	The maximum and the minimum loads occurred at the edges of the concentric region instead of the eccentric regions of the cup.	Due to the posterior shift of the humeral forces the SI force imbalance was reduced, while a component of this imbalance was found at the diagonally opposite edges.	Force imbalance and superior edge compression was observed to be the highest amongst all the tested glenoid designs.
Characteristics of Cement Stress	Higher stresses were induced through the gaps of the cup, within the yield strength of the PMMA.	The cement stress was higher in the PS section, compared to the control model. This could be considered a challenge regarding the bi-radial model.	Even though the pear-shaped cement layer exhibited similar loading pattern as the control cement layer, its long-term survival was reduced.

6.7 Conclusion

This chapter describes a computational FE model created to investigate the stress characteristics of the glenoid designs using ASTM specifications. The FE model consisting of an accurate model of a commercially available glenoid cup was compared and validated with previous experimental and FE studies. The resulting shear force, its ratio with the axial force and the stresses on glenoid and cement were found to be comparable to the literature.

Among the new glenoid designs, the bi-radial glenoid exhibited the most anatomical GH force transfer as it shifted the articular contact posteriorly. The compartmental glenoid displayed promising characteristics of reducing the counter edge loading of the cup. The pear-shaped glenoid was found to higher chances of superior dislocation and also higher stress-induced deformations. Regarding the cement stress and survivability, the PMMA edges were found to be more susceptible to disintegration due to higher tensile stress concentration. Although this was the case for all the glenoids tested, the pear-shaped prosthesis was found to experience higher pressure on the edges due to a reduced superior surface area which compromised the cement survivability. Highest concentric stress transfer, from the implant to cement, was observed to occur for the compartmental glenoid due to the gaps separating the concentric and eccentric compartments.

The primary limitation of the study presented in this chapter was that the performance of only one instance for each design was investigated. As literature suggests that prosthesis design features such as conformity and mismatch affect the stress on the implants and its joint stability. Only one model belonging to each of the novel glenoid designs were tested using the FE model. Hence, no statistical methods could be implemented to derive any significance of the characterized differences. The second limitation of this study was that no cyclic testing was performed on the glenoid cups as it was out of the scope of this thesis. The strength of the current study was that it laid the foundation for future cyclic and mechanical studies which could be performed on similar implants further characterizing their performance under humeral loading.

CHAPTER 7

Conclusions and Future Work

The long-term success of the Total Shoulder Arthroplasty (TSA) has been reduced by several factors. This has led to post-surgical discomfort, loss in RoM and revision surgeries. One of the major causes of this failure has been the loosening of the glenoid component due to the imbalance of the glenohumeral (GH) forces on its surface. The available Anatomical Total Shoulder Prosthesis (ATSP) is modeled in accordance to the arthritic geometry of the GH joint which increases the available surface area of the glenoid component and exposing it to the *"rocking horse"* effect.

The main aim of the thesis was to develop conceptual designs of the ATSP prostheses towards reducing the *"rocking horse"* effect. In the process of achieving its overall aim, this thesis presented a study comparing morphometry of two geographically distinct populations. Using the morphometric observations, the thesis described the design process of population-specific humeral head prosthesis which was later examined for induced kinematic changes using *in-silico* musculoskeletal models.

Finally, new conceptual designs of glenoid prostheses were introduced. These designs were partly inspired by the original anatomical geometry of a healthy glenoid fossa. Finite element models were used to investigate the possible effects of these novel glenoid designs on the post-surgical survival characteristics, such as eccentric loading, implant to bone force transfer, GH stability and cement stresses.

The overall conclusion culminating from the various chapters that are presented in this thesis, could be framed as, *"Introducing anatomical features, such as a compartmentalised pear-shaped region into the current oval design of glenoid prosthesis, to restrict eccentric loading, could be a favorable strategy to reduce the rocking horse effect."* This was a goal-oriented thesis and these goals were briefly described in the section of Chapter 1.5. The final conclusions were also segregated in a similar manner and are detailed in the following sections.

7.1 Conclusion I

The initial goal of the thesis was to understand the GH morphometry of the native South African population, as a representative cohort of the sub-Sahara Africa. The native morphology was further compared to the GH joints of a European cohort. From this analysis, it could be concluded that *"The only statistically significant inter-population differences existed in the humeral head size and the GH mismatch between the studied cohorts. Moreover, there is at least 9% of biological head sizes for which no optimum size of ATSP exists."*

Humeral head size plays a major role in converting the muscular forces into joint moments and driving the GH motion. Improper sizing of the humeral head prosthesis may lead to over-stuffing or under-stuffing of the joint space. So far, the current prosthesis designs are based on studies that had not considered non-Caucasian GH morphometry. Hence, one of the novel aspects of the current research was to study a set of GH joints belonging to the non-Caucasian population and establishing morphometric variances between a different set of GH joints belonging to the Caucasian population. The results from this study also suggested that the humeral head shape is better represented by an asymmetric 3D ellipse than a sphere. This was because the observed widths of the humeral head base and the circular radius of its articular surface in the SI and AP directions were unequal.

Further investigating into this elliptical morphometry of the humeral head and its effect on GH contact forces, it was realized that *"A humeral head was thickest at an offset from its geometrical center and the central thickness of the humeral head was found to be significantly smaller than the peak thickness of the head. When the peak and the central thicknesses were adapted into modeling two sets of elliptical humeral head prostheses, the heads modeled with peak thickness were more likely to impart concentric forces than their counterparts."*

Ease of manufacturing an asymmetric elliptical humeral head implant might be one of the possible reasons for adhering to the spherical shape of the humeral head prosthesis. Altering the shape of the prosthesis base into an ellipse has been demonstrated to reduce overhang and better fit the proximal humeral surface. The second novel aspect of the thesis

was to introduce the biological asymmetric nature of the humeral head into its prosthesis design and highlight the theoretical benefits of this redesigning approach. The asymmetric heads were further subjected to only musculoskeletal testing. In-silico finite element testing of the asymmetric heads were not performed during this thesis and the focus of the kinetic investigation were the novel glenoid designs. Hence, future studies on evaluating the kinetic implications of the asymmetric nature of humeral heads on the GH forces are recommended.

7.2 Conclusion II

The surgical process of replacing the arthritic GH joint surfaces with ATSP does not involve muscle damage. Hence, pre- and post-surgical kinematics should be almost identical in the case of TSA. To achieve the second goal an *in-silico* musculoskeletal model was created. Post-validation of the model, it was modified to investigate the kinematic changes induced by the population-specific humeral prosthesis and the new glenoid implant designs. The study involving the average population-specific humeral heads from three different populations (Swiss, South African and Chinese), paired with a matching glenoid prosthesis, was used to study the population specific changes in muscle moment arms.

On comparing the kinematic outputs for abduction, forward flexion, and internal rotation, it could be concluded that *"The maximum muscle moment arm variation existed between the average Swiss and the average Chinese populations. This could be correlated to the fact that the former population had a significantly bigger humeral head than the later. Integrating this, kinematic variation, with the fact that not all head sizes in a population are catered for by the available ATSP manufacturers there exists a need for a population-specific range of prosthesis."* The overall process implemented to realize the above conclusion could be considered as the third novelty presented in this research.

The prosthetic glenoid cup is the most vulnerable component in ATSP with the highest failure rate. Majority of these failures have been associated with the *"rocking horse"* effect causing progressive loosening of the polyethylene glenoid prosthesis. Conceptually new

designs of the glenoid components were introduced with the aim to reduce the force imbalance causing the prosthesis *"rocking"*.

By performing the same set of motions using the new glenoid cups it was concluded that *"Only altering the shape of the glenoid or its surface profile is not enough to change the post-surgical muscle moment arms. Major changes in prosthetic thickness, which effectively lateralises or medialises the humeral head, and changes in surgical methods, altering the GH positions, should be avoided if identical post-surgical kinematics is to be achieved."*

7.3 Conclusion III

The final goal of the research was to study the performance of the glenoid prostheses under standardized loading conditions. ASTM recommendations were followed and a finite element (FE) was developed and validated using literature. The validated model was modified, and the modifications included the introduction of the bi-radial, the compartmental and the pear-shaped glenoid components. The cement layer was only modified for the pear prosthesis to match its posterior profile. In each of the analyses the humeral head translation on the glenoid cup, until subluxation, was performed under a constant axial load.

By comparing the performance of the control glenoid model with the new designs it could be concluded that *"The bi-radial glenoid with thickened superior-posterior aspect was able to direct the GH forces towards the posterior region of the cup, reducing the superior edge loading. The pear-shaped glenoid showed the lowest resistance to superior subluxation of the head. The compartmental glenoid was designed as a combination of the pear (healthy shape of the fossa) and oval-shaped (post-arthritic shape of the fossa) prostheses, separated by gaps. The gaps provided in the compartmentalised glenoid were observed to reduce eccentric loading of the cup by channeling the forces into the cement layer and by restricting the GH loads within the concentric regions of the prosthesis."*

Apart from the pear-shaped glenoid, the design and testing of the bi-radial and the compartmental glenoids could be considered as the fourth novelty of this thesis. The novel glenoid cups were able to reduce or delay the eccentric loading of the cup by altering the GH

stress pattern or by containing the stresses into a region of the cup which has sufficient bone backing and is supported by pegs drilled into the glenoid vault.

In summary, this thesis presents a research pipeline that was developed to transfer GH morphometric features into ATSP designs, with an overall aim to reduce glenoid cup failure, which could be tested using the standardized protocols. Before implementation, each step of the pipeline was validated using available literature. This research had set out to achieve three goals which resulted in the realization of four novel aspects. Based on the outcomes of the project, recommendations for future studies to further the research and address the limitations are detailed in the following section.

7.4 Recommendations for Future Research

The current thesis has laid the groundwork for determining population-specific variation in GH morphometry. The studied populations were sourced from two geographically distinct countries from where only ethnically different cadavers were selected. Ideally, increasing the population-specific cohorts by including cadavers from other sub-Saharan and European countries is recommended.

The overall effect of the limitations mentioned in this thesis is varied. The limitations represent two aspects about the thesis, firstly they direct towards future research studies & aid in determining their scope and secondly the limitations provide an idea of the possible investigations that could have been included in the thesis which might have added valuable information but would have steered the research in a direction different to which it had initially set-out for. The second aspect becomes an important representation of the candidate's decision-making capability which is essential for completing a doctoral thesis which is both time and resource bound. Therefore, the limitations mentioned in this thesis were essential to maintain the focus of the research on its aims & objectives and complete it within the strict doctoral thesis timeline. The initial drawback of having inadequate subjects for the morphometric analysis was highlighted by the lower statistical power value of 0.7. The following limitation of not comparing the 3D morphometric measurements using

reconstructed CT scans with 2D radiographs did not majorly affect the investigation as the former was well validated using the former studies from literature. Unavailability of the height and weight information along with the subject specific muscle volume data reduced the possibility to scale the musculoskeletal models according to the patient specific data. The only physical variation among the musculoskeletal models was the size of the humeral head which affected the motion-induced muscle moment arms. Hence it can be argued that not having all the demographic information limited the musculoskeletal models from being closer to real world, but the models were successful in predicting the kinematics variations induced by changing humeral head dimensions.

The fourth limitation was due to investigating the inter-population kinematic variations using a single average model representing each population. This limitation did not allow the investigation of statistical significance among the population. This becomes a topic of future study which is currently underway. A similar limitation existed in the Finite Element Analysis, where only one size of each glenoid design was tested during the humeral head subluxation analysis. Although, a wider size spectrum of glenoid prostheses would have provided a broader understanding of the kinetic performance of the novel glenoid designs but performing these tests would have been time intensive. Hence, the decision of performing the subluxation tests using glenoid designs with 28mm RoC was made. This ensured that the in-silico observations could be verified and validated with the existing Finite Element studies in the literature involving similar sized prosthesis. The final limitation of this thesis was not backing up the subluxation test with the cycling loading of the novel glenoid designs as specified in ASTM F2028-08 guidelines. Performing the cyclic tests would have provided a complete assessment of the novel glenoid designs but few studies in the literature have only reported observations from humeral head subluxation tests as a valid test to determine glenoid component's force characteristics. Therefore, keeping in mind the timeline of the thesis and the Finite Element approaches reported in the literature, even by not including the cyclic dynamic glenoid loosening analysis this thesis was able to provide substantial kinetic characteristics of the novel glenoid designs.

Analysing the morphometries of larger representations of ethnically different inhabitants would broaden the understanding of the variances observed between them. Future studies should also focus on the inter-population variances in the angle of inclination and version of both the glenoid fossa and the humeral head. Including these parameters would provide a comprehensive understanding of all the prosthetic design parameters for ATSP. The cohort of 3D remodelled bones obtained during the course of this morphometric investigation could be utilised in the future to create population-specific statistical shape models (SSM). Creating SSM will aid in further quantifying the specific variances that exist between the GH bones of sub-Sahara African and European cohorts. These models could also be implemented to create population-specific musculoskeletal models with emphasis on particular morphological variances.

In South Africa, there is limited knowledge regarding the exact number of shoulder surgeries taking place annually and the TSA failure rates. The commercial manufacturers often report the number of prostheses sold in this country with other developing countries. This suggests that the number TSA and RTSA surgeries in South Africa is significantly lower than the USA and UK, but the precise frequency is not well documented. It is proposed that future researchers in the Orthopaedic Biomechanics Lab, UCT should work closely with the South African Orthopaedic Association to determine the important statistics related to shoulder surgeries, such as:

a. The number of TSA and RTSA performed annually.
b. The total number of revision surgeries performed.
c. Major indicators for revisions and reasons for failure.
d. The average cost of shoulder surgery and the demographic details of the patients.

Inter-population differences in muscle moment arms were observed during unloaded ADLs. During the *deltopectoral approach*, the subscapularis muscle is detached from its insertion and retracted medially to access the GH joint. This muscle is often attached back to its original alignment using sutures after replacing the GH joint surfaces. Along with this, the

joint capsule is also removed during the surgery. Future musculoskeletal models should consider the implications of a having weak subscapularis during movements such as internal rotation and adduction. This could be achieved by introducing a dynamic fatigue component in the analysis (Ma et al., 2009). The loss of stability caused by the absence of the joint capsule should also be mimicked, under loaded conditions, in the future studies.

Multiple discussions with shoulder surgeons have shed light upon the fact that there is limited or no information regarding the most common areas of GH contact during ADLs. Current knowledge of GH contact areas are based on static studies (Massimini et al., 2010; Yamamoto et al., 2007), dynamic changes in these contact points have never been studied. As shoulder replacements are common in older individuals, it could be argued that their use of dominant and non-dominant upper are limited. Future studies are recommended to quantify the GH areas under contact during the most common activities including, but not limited to, eating, combing hair and performing desk jobs.

One of the recommended methods is implanting instrumented humeral or glenoid components in patients undergoing TSA and continuously monitor the prostheses contact points wirelessly. A non-invasive approach could be tracking bio-markers attached to the upper body using motion capture methods and replicating them in computerized musculoskeletal models to assess the contact points.

The weight of the humeral head prosthesis is very different from the resected humeral head which is mainly constituted of cartilaginous and cancellous bone tissues. This variation in weight might alter the tension on the surrounding soft tissues and has never been studied before. Future musculoskeletal studies should aim towards factoring-in the weight of the prosthesis in the analysis to achieve higher kinematic accuracy.

A study using FE models of the GH components was presented in Chapter 6. In this study, the novel glenoid cup designs were loaded using standard physiological loads. Under a constant compressive load, the humeral head was translated until subluxation. The next logical step should be to perform cyclic loading of the glenoid prostheses until 90% of the

subluxation distance. Different sizes of the novel glenoid prostheses paired with matching humeral heads should be considered for future analyses for which the described FE model could be modified.

Rigorous laboratory testing of the prostheses designs is highly recommended before commercialization attempts. These tests should make use of the kinematic and mechanical, test rigs that have been already presented in the literature (Ackland et al., 2008; Gunther et al., 2012; Junaid et al., 2010). A part of these studies should also focus on finding out the exact friction co-efficient of bone cement (PMMA) and bone substitute (Polyurethane) interface using the pin on disc methods.

Manufacturing the prostheses might be a challenge in South Africa, as there are no indigenous manufacturers in the country and using foreign commercial facilities for the same would be highly expensive. To overcome this constraint, it is recommended to set-up future collaboration with the Centre for Rapid Prototyping and Manufacturing (CRPM) which is a specialized medical implant producing research laboratory hosted by the Central University of Technology (CUT) in Free State. CRPM uses additive manufacturing to develop the implants using composite materials. Introducing novel joint prosthesis often demands surgical alterations. In order to quantify the possible alterations that might have been introduced by the implants presented in the current research, future cadaver studies should be considered.

Replacing the highly mobile GH joint with prostheses has been challenging from the onset of TSA. Over the years, ATSP designs have been modified to achieve a better post-surgical outcome. The observations presented in this thesis suggest that incorporation of certain anatomical features in the ATSP design, especially in the glenoid cup, to contain the forces within the concentric region of the glenoid cup might be essential to overcome current post-TSA complications.

7.5 Final Thesis Conclusion

In the light of the conclusions presented above, the take-home message from this thesis could be summarised as *"Biomechanical and anatomical variations exist between ethnically different populations. Providing population-specific ATSP might catering for these differences. While anatomical modeling of the humeral head prosthesis increases concentric loads, thickening the posterior glenoid cup and providing gaps between its concentric and eccentric regions might diminish eccentric loading, and aseptic glenoid loosening."*

References

Ackland, D. C., Pak, P., Richardson, M., & Pandy, M. G. (2008). Moment arms of the muscles crossing the anatomical shoulder. *J. Anat*, *213*, 383–390. https://doi.org/10.1111/j.1469-7580.2008.00965.x

Ackland, D. C., & Pandy, M. G. (2011). Moment arms of the shoulder muscles during axial rotation. *Journal of Orthopaedic Research*, *29*(5), 658–667. https://doi.org/10.1002/jor.21269

Ackland, D. C., Richardson, M., & Pandy, M. G. (2012). Axial Rotation Moment Arms of the Shoulder Musculature After Reverse Total Shoulder Arthroplasty. *The Journal of Bone & Joint Surgery*, *94*(20), 1886–1895. https://doi.org/10.2106/JBJS.J.01861

Ackland, D. C., Sasha, R.-Z., Richardson, M., & Pandy, M. G. (2010). Moment Arms of the Shoulder Musculature After Reverse Total Shoulder Arthroplasty. *The Journal of Bone & Joint Surgery*, *92*(5), 1221–1230. https://doi.org/10.2106/JBJS.I.00001

Aitchison, G. A., Hukins, D. W. L., Parry, J. J., Shepherd, D. E. T., & Trotman, S. G. (2009). A review of the design process for implantable orthopedic medical devices. *The Open Biomedical Engineering Journal*, *3*, 21–27. https://doi.org/10.2174/1874120700903010021

Akinpelu, A., Alonge, O., Adekanla, B., & Odole, A. (2010). Pattern of Osteoarthritis Seen In Physiotherapy Facilities in Ibadan and Lagos, Nigeria. *African Journal of Biomedical Research*, *10*(2), 111–115. https://doi.org/10.4314/ajbr.v10i2.50612

Allred, J. J., Flores-Hernandez, C., Hoenecke, H. R., & D 'lima, D. D. (2016). Posterior augmented glenoid implants require less bone removal and generate lower stresses: a finite element analysis. *Computer Modeling*, *25*, 823–830. https://doi.org/10.1016/j.jse.2015.10.003

An, K. N., Ueba, Y., Chao, E. Y., Cooney, W. P., & Linscheid, R. L. (1983). Tendon excursion and moment arm of index finger muscles. *Journal of Biomechanics*, *16*(6), 419–425. https://doi.org/10.1016/0021-9290(83)90074-X

Anglin, C., Tolhurst, P., Wyss, U. P., & Pichora, D. R. (1999). Glenoid cancellous bone strength and modulus. *Journal of Biomechanics*, *32*(10), 1091–1097. https://doi.org/10.1016/S0021-9290(99)00087-1

Anglin, C., Wyss, U. P., & Pichora, D. R. (2000). Mechanical testing of shoulder prostheses and recommendations for glenoid design. *Journal of Shoulder and Elbow Surgery*, *9*(4), 323–331. https://doi.org/10.1067/mse.2000.105451

Anglin, C., Wyss, U. P., & Pichora, D. R. (2000). Shoulder prosthesis subluxation: Theory and experiment. *J Shoulder Elbow Surg*, *9*(2), 104–114. https://doi.org/10.1067/mse.2000.105139

Arthritis Foundation. (2018). *Arthritis By The Numbers*. Retrieved from https://www.arthritis.org/Documents/Sections/About-Arthritis/arthritis-facts-stats-figures.pdf

ASM International®. (2009). Co-20Cr-15W-10Ni. *Materials and Coatings for Medical Devices:*

Cardiovascular ASM Materials for Medical Devices Database Committee, 69–73. Retrieved from www.asminternational.org

ASTM International. (2012). F2028-08(2012)e1 Standard Test Methods for Dynamic Evaluation of Glenoid Loosening or Disassociation, 1–15. https://doi.org/10.1520/f2028-08r12e01

Barnett, N. D., Duncan, R. D. D., & Johnson, G. R. (1999). The measurement of three dimensional scapulohumeral kinematics ± a study of reliability. *Clinical Biomechanics* , *14*, 287–290. Retrieved from http://www.clinbiomech.com/article/S0268-0033(98)00106-5/pdf

Bergmann, G., Graichen, F., Bender, A., Kaä, M., Rohlmann, A., & Westerhoff, P. (2007). In vivo glenohumeral contact forces—Measurements in the first patient 7 months postoperatively. *Journal of Biomechanics*, *40*, 2139–2149. https://doi.org/10.1016/j.jbiomech.2006.10.037

Bergmann, G., Graichen, F., Bender, A., Rohlmann, A., Halder, A., Beier, A., & Westerhoff, P. (2011). In vivo gleno-humeral joint loads during forward flexion and abduction. *Journal of Biomechanics*, *44*, 1543–1552. https://doi.org/10.1016/j.jbiomech.2011.02.142

Bishop, J. Y., & Flatow, E. L. (2005). Humeral head replacement versus total shoulder arthroplasty : Clinical outcomes — A review. *Journal of Shoulder and Elbow Surgery*, *14*(1S), 141–146. https://doi.org/10.1016/j.jse.2005.09.027

Bohsali, K. I., Wirth, M. a, & Rockwood, C. a. (2006). Complications of total shoulder arthroplasty. *The Journal of Bone and Joint Surgery. American Volume*, *88*(10), 2279–2292. https://doi.org/10.2106/JBJS.F.00125

Boileau, P., Avidor, C., Krishnan, S. G., Walch, G., Kempf, J.-F., & Molé, D. (2002). Cemented polyethylene versus uncemented metal-backed glenoid components in total shoulder arthroplasty: A prospective, double-blind, randomized study. *Journal of Shoulder and Elbow Surgery*, *11*(4), 351–359. https://doi.org/10.1067/MSE.2002.125807

Boileau, P., Moineau, G., Morin-Salvo, N., Avidor, C., Godenèche, A., Lévigne, C., … Walch, G. (2015). Metal-backed glenoid implant with polyethylene insert is not a viable long-term therapeutic option. *Journal of Shoulder and Elbow Surgery*, *24*(10), 1534–1543. https://doi.org/10.1016/J.JSE.2015.02.012

Boileau, P., Sinnerton, R. J., Chuinard, C., Walch, G., & Chuinard, C. C. (2006). Arthroplasty of the shoulder. *J Bone Joint Surg [Br]*, *88*, 562–575. https://doi.org/10.1302/0301-620X.88B5

Boileau, P., Trojani, C., Walch, G., Krishnan, S. G., Romeo, A., & Sinnerton, R. (2001). Shoulder arthroplasty for the treatment of the sequelae of fractures of the proximal humerus. *Journal of Shoulder and Elbow Surgery*, *10*(4), 299–308. https://doi.org/10.1067/mse.2001.115985

Boileau, P., & Walch, G. (1997). The three-dimensional geometry of the proximal humerus. Implications for surgical technique and prosthetic design. *The Journal of Bone and Joint Surgery. British Volume*, *79*(5), 857–865. https://doi.org/10.1302/0301-620X.79B5.7579

Bonnevialle, N., Melis, B., Neyton, L., Favard, L., Molé, D., Walch, G., & Boileau, P. (2013). Aseptic glenoid loosening or failure in total shoulder arthroplasty: Revision with glenoid reimplantation. *Journal of Shoulder and Elbow Surgery*, *22*(6), 745–751. https://doi.org/10.1016/j.jse.2012.08.009

Brand, R. A. (2011). The classic: Articular replacement for the humeral head. *Clinical Orthopaedics and Related Research*, *469*(9), 2409–2421. https://doi.org/10.1007/s11999-011-1944-5

Brand, R. A., & Bigliani, L. U. (2011). Biographical Sketch Charles S. Neer, II, MD (1917 - 2011). *Clin Orthop Relat Res*, *469*, 2407-08. https://doi.org/10.1007/s11999-011-1944-5

Bryce, C. D., Pennypacker, J. L., Kulkarni, N., Paul, E. M., Hollenbeak, C. S., Mosher, T. J., & Armstrong, A. D. (2008). Validation of three-dimensional models of in situ scapulae. *Journal of Shoulder and Elbow Surgery*, *17*(5), 825–832. https://doi.org/10.1016/j.jse.2008.01.141

Buchler, P., Ramaniraka, N. A., Rakotomanana, L. R., Iannotti, J. P., & Farron, A. (2002). A finite element model of the shoulder: application to the comparison of normal and osteoarthritic joints. *Clinical Biomechanics*, *17*(9–10), 630–639. Retrieved from http://ac.els-cdn.com/S0268003302001067/1-s2.0-S0268003302001067-main.pdf?_tid=36c4c098-77a0-11e7-a313-00000aacb360&acdnat=1501691746_7ff95537f3f2fe6ecee4b1ca07716fca

Cabezas, A. F., Krebes, K., Hussey, M. M., Santoni, B. G., Kim, H. S., Frankle, M. A., & Oh, J. H. (2016). Morphometric analysis of anatomy can be very valuable to a surgeon when assessing patient-specific implant needs prior to commencing any orthopedic procedure. *Clinics in Orthopedic Surgery*, *8*, 280–287. https://doi.org/10.4055/cios.2016.8.3.280

Chaplin, R. P. S., Lee, · A J C, Hooper, · R M, & Clarke, · M. (2006). The mechanical properties of recovered PMMA bone cement: A preliminary study. *J Mater Sci: Mater Med*, *17*, 1433–1448. https://doi.org/10.1007/s10856-006-0619-3

Charlton, I. W., & Johnson, G. R. (2006). A model for the prediction of the forces at the glenohumeral joint. *Proceedings of the Institution of Mechanical Engineers, Part H: Journal of Engineering in Medicine* , *220*(8), 801–812. https://doi.org/10.1243/09544119JEIM147

Chillemi, C., & Franceschini, V. (2013). Shoulder osteoarthritis. *Arthritis*, *2013*, 370231. https://doi.org/10.1155/2013/370231

Churchill, R. S., Brems, J. J., & Kotschi, H. (2001). Glenoid size, inclination, and version: An anatomic study. *Journal of Shoulder and Elbow Surgery*, *10*(4), 327–332. https://doi.org/10.1067/mse.2001.115269

Cignoni, P., Callieri, M., Corsini, M., Dellepiane, M., Ganovelli, F., & Ranzuglia, G. (2008). *MeshLab: an Open-Source Mesh Processing Tool*. (Vittorio Scarano and Rosario De Chiara and Ugo Erra, Ed.), *Eurographics Italian Chapter Conference*. The Eurographics Association. https://doi.org/10.2312/LocalChapterEvents/ItalChap/ItalianChapConf2008/129-136

Cofield, R. H. (1994). Uncemented Total Shoulder Arthroplasty A Review. *CLINICAL ORTHOPAEDICS AND RELATED RESEARCH Number*, *307*, 86–93. Retrieved from http://citeseerx.ist.psu.edu/viewdoc/download?doi=10.1.1.730.3119&rep=rep1&type=pdf

Cohen, J. (1992). A Power Primer. *Psychological Bulletin [PsycARTICLES*, *112*(1). Retrieved from http://www2.psych.ubc.ca/~schaller/528Readings/Cohen1992.pdf

Coigny, F., Todor, A., Rotaru, H., Schumacher, R., & Schkommodau, E. (2016). Patient-specific hip prostheses designed by surgeons. *Current Directions in Biomedical Engineering*, *2*(1),

565–567. https://doi.org/10.1515/cdbme-2016-0163

Creamer, P. (2000). Osteoarthritis pain and its treatment. *Current Opinion in Rheumatology*, *12*, 450–455. Retrieved from http://ovidsp.tx.ovid.com/sp-3.28.0a/ovidweb.cgi?WebLinkFrameset=1&S=FJDKFPPPPEDDDHFKNCFKGHLBDGMKAA00&returnUrl=ovidweb.cgi%3F%26Full%2BText%3DL%257cS.sh.22.23%257c0%257c00002281-200009000-00019%26S%3DFJDKFPPPPEDDDHFKNCFKGHLBDGMKAA00&directlink=http%3A%2F

Croop, B., & Lobo, H. (2010). MECHANICAL AND VISCO-ELASTIC PROPERTIES OF UHMWPE FOR IN-VIVO PRODUCT DEVELOPMENT. *DatapointLabs*. Retrieved from http://www.datapointlabs.com/testpaks/2010spemedical.pdf

Culham, E., & Peat, M. (1993). Functional anatomy of the shoulder complex. *J Orthop Sports Phys Ther*, *18*(1), 342–350. https://doi.org/10.2519/jospt.1993.18.1.342

Daggett, M., Werner, B., Collin, P., Gauci, M. O., Chaoui, J., & Walch, G. (2015). Correlation between glenoid inclination and critical shoulder angle: A radiographic and computed tomography study. *Journal of Shoulder and Elbow Surgery*, *24*(12), 1948–1953. https://doi.org/10.1016/j.jse.2015.07.013

Day, J. S., Lau, E., Ong, K. L., Williams, G. R., Ramsey, M. L., & Kurtz, S. M. (2010). Prevalence and projections of total shoulder and elbow arthroplasty in the United States to 2015. *Journal of Shoulder and Elbow Surgery*, *19*, 1115–1120. https://doi.org/10.1016/j.jse.2010.02.009

de Beer, J., & Bhatia, D. N. (2009). Shoulder injuries in rugby players. *International Journal of Shoulder Surgery*, *3*(1), 1–3. https://doi.org/10.4103/0973-6042.50874

De Puy. (2013). DePuy Synthes GLOBAL AP Surgical Technique.

De Wilde, L., Saartje Defoort, B., Tom G M Verstraeten, B. R., Wendy Speeckaert, B., & Philippe Debeer, B. (2012). A 3D-CT scan study of the humeral and glenoid planes in 150 normal shoulders. *Surg Radiol Anat*, *34*, 743–750. https://doi.org/10.1007/s00276-011-0836-4

Deore, V. T., Griffiths, E., & Monga, P. (2018). Shoulder arthroplasty—Past, present and future. *Journal of Arthroscopy and Joint Surgery*, *5*(1), 3–8. https://doi.org/10.1016/J.JAJS.2017.12.001

DePuy Synthes. (2013). SURGICAL TECHNIQUE GLOBAL AP ™ ADJUSTABLE PROSTHESIS. Retrieved from https://emea.depuysynthes.com/hcp/shoulder/products/qs/global-ap-shoulder-system

Dey, R., Roche, S., Rosch, T., Mutsvangwa, T., Charilaou, J., & Sivarasu, S. (2018). Anatomic variations in glenohumeral joint: an interpopulation study. *JSES Open Access*, *2*(1), 1–7. https://doi.org/10.1016/J.JSES.2017.11.007

Donlon, D. A. (2000). The value of infracranial nonmetric variation in studies of modern Homo sapiens: An Australian focus. *American Journal of Physical Anthropology*, *113*(3), 349–368. https://doi.org/10.1002/1096-8644(200011)113:3<349::AID-AJPA6>3.0.CO;2-2

Drake, R. L., Vogl, W., Mitchell, A. W. M., & Gray, H. (2015). *Gray's anatomy for students*. Philadelphia, PA : Churchill Livingstone/Elsevier. Retrieved from https://uct.primo.exlibrisgroup.com/discovery/fulldisplay?docid=alma999680698704041&context=L&vid=27UCT_INST:27UCT&lang=en&search_scope=MyInst_and_CI&adaptor=Local Search Engine&tab=Everything&query=any,contains,grays anatomy&sortby=rank&offset=0

Eichinger, J. K., & Galvin, J. W. (2015). Management of complications after total shoulder arthroplasty. *Current Reviews in Musculoskeletal Medicine*, *8*(1), 83–91. https://doi.org/10.1007/s12178-014-9251-x

Elite Surgicals. (2017). elitesurgical | Vectis Shoulder. Retrieved February 26, 2018, from https://www.elitesurgical.com/red-bear

Erdemir, A., Guess, T. M., Halloran, J., Tadepalli, S. C., & Morrison, T. M. (2012). Considerations for reporting finite element analysis studies in biomechanics. *Journal of Biomechanics*, *45*, 625–633. https://doi.org/10.1016/j.jbiomech.2011.11.038

Erdfelder, E., Faul, F., & Buchner, A. (1996). GPOWER: A general power analysis program. *Behavior Research Methods, Instruments, & Computers*, *28*(1), 1–11. https://doi.org/10.3758/BF03203630

Evolutis. (2016). Product Sheet UNIC(R). Retrieved from http://www.evolutisfrance.com/Data_Evolutis/downloads/Article/7_bi_unic-fp-e28.pdf

Exactech. (2017). Platform Shoulder System EQUINOXE ® PLATFORM SHOULDER SYSTEM.

Farng, E., Zingmond, D., Krenek, L., & SooHoo, N. F. (2011). Factors predicting complication rates after primary shoulder arthroplasty. *Journal of Shoulder and Elbow Surgery*, *20*(4), 557–563. https://doi.org/10.1016/j.jse.2010.11.005

Faul, F., Erdfelder, E., Buchner, A., & Lang, A.-G. (2007). G*Power 3:A flexible statistical power analysis program for the social, behavioral, and biomedical sciences. *Behavior Research Methods*, *39*(2), 175–191. https://doi.org/doi:10.3758/BF03193146

Faul, F., Erdfelder, E., Buchner, A., & Lang, A.-G. (2009). Statistical power analyses using G*Power 3.1: Tests for correlation and regression analyses. *Behavior Research Methods*, *41*(4), 1149–1160. https://doi.org/10.3758/BRM.41.4.1149

FH Ortho. (2017). Arrow Prime Dual Platform Shoulder System. Retrieved from http://www.fhortho.com/wp-content/uploads/Arrow-Prime-Brochure_072017.pdf

Franklin, J. L., Barrett, W. P., Jackins, S. E., & Matsen, F. A. (1988). Glenoid loosening in total shoulder arthroplasty. Association with rotator cuff deficiency. *The Journal of Arthroplasty*, *3*(1), 39–46. https://doi.org/10.1016/S0883-5403(88)80051-2

Frich, L. H., Møller, B. N., & Sneppen, O. (1988). Shoulder arthroplasty with the Neer Mark-II prosthesis. *Archives of Orthopaedic and Traumatic Surgery. Archiv Fur Orthopadische Und Unfall-Chirurgie*, *107*(2), 110–113. Retrieved from http://www.ncbi.nlm.nih.gov/pubmed/3358666

Frost, H. M. (1994). Wolff's Law and bone;s structural adaptations to mechanical usage: an

overview for clinicians. *The Angle Orthodontist*, *64*(3), 175–188. Retrieved from http://www.angle.org/doi/pdf/10.1043/0003-3219%281994%29064%3C0175%3AWLABSA%3E2.0.CO%3B2

Gill, H., Gustafsson, L., Hawcroft, L., & McKenna, K. (2006). Shoulder Joint Range of Motion in Healthy Adults Aged 20 to 49 Years. *British Journal of Occupational Therapy*, *69*(12), 556–561. https://doi.org/10.1177/030802260606901204

Gilroy, A. M., MacPherson, B. R., & Ross, L. M. (2008). *Atlas of anatomy* (II). India: Thieme. Retrieved from https://books.google.co.za/books/about/Atlas_of_Anatomy.html?id=_HHrnw_r1KIC&redir_esc=y

GLOBAL BURDEN OF DISEASES, INJURIES, AND RISK FACTORS STUDY 2010. (n.d.). Retrieved from http://www.healthdata.org/sites/default/files/files/country_profiles/GBD/ihme_gbd_country_report_south_africa.pdf

Green, A., & Norris, T. R. (2001). Shoulder arthroplasty for advanced glenohumeral arthritis after anterior instability repair. *Journal of Shoulder and Elbow Surgery*, *10*(6), 539–545. https://doi.org/10.1067/mse.2001.118007

Gregory, T., Hansen, U., Taillieu, F., Baring, T., Brassart, N., Mutchler, C., … Emery, R. (2009). Glenoid loosening after total shoulder arthroplasty: An in vitro CT-scan study. *Journal of Orthopaedic Research*, *27*(12), 1589–1595. https://doi.org/10.1002/jor.20912

Gunther, S. B., & Lynch, T. L. (2012). Total shoulder replacement surgery with custom glenoid implants for severe bone deficiency. *Journal of Shoulder and Elbow*, *21*, 675–684. https://doi.org/10.1016/j.jse.2011.03.023

Gunther, S. B., Lynch, T. L., O'Farrell, D., Calyore, C., & Rodenhouse, A. (2012). Finite element analysis and physiologic testing of a novel, inset glenoid fixation technique. *Journal of Shoulder and Elbow Surgery*, *21*(6), 795–803. https://doi.org/10.1016/j.jse.2011.08.073

Gupta, S., van der Helm, F. C. T., & van Keulen, F. (2004). Stress analysis of cemented glenoid prostheses in Total Shoulder Arthroplasty. *Journal of Biomechanics*, *37*(11), 1777–1786. https://doi.org/10.1016/J.JBIOMECH.2004.02.001

Gupta, S., Van Der Helm, F. C. T., & Van Keulen, F. (2004). Stress analysis of cemented glenoid prostheses in Total Shoulder Arthroplasty. *Journal of Biomechanics*, *37*, 1777–1786. https://doi.org/10.1016/j.jbiomech.2004.02.001

Gursoz, E. L., Choi, Y., & Prinz, F. B. (1991). Boolean set operations on non-manifold boundary representation objects. *Computer-Aided Design*, *23*(11), 33–39. https://doi.org/10.1016/0010-4485(91)90097-G

Halder, A. M., Itoi, E., & An, K.-N. (2000). Anatomy and Biomechanics of the Shoulder. *Orthopedic Clinics of North America*, *31*(2), 159–176.

Hasan, S. S., Leith, J. M., Campbell, B., Kapil, R., Smith, K. L., & Matsen, F. a. (2002). Characteristics of unsatisfactory shoulder arthroplasties. *Journal of Shoulder and Elbow Surgery*, *11*(5), 431–441. https://doi.org/10.1067/mse.2002.125806

Hertel, R., & Ballmer, F. T. (2003). Observations on retrieved glenoid components. *The Journal of Arthroplasty*, *18*(3), 361–366. https://doi.org/10.1054/arth.2003.50048

Hertel, R., Knothe, U., & Ballmer, F. T. (2002). Geometry of the proximal humerus and implications for prosthetic design. *Journal of Shoulder and Elbow Surgery*, *11*(4), 331–338. https://doi.org/10.1067/mse.2002.124429

Hertz, H. (1896). *Miscellaneous papers*. (Jones and Schoot, Ed.). London: Macmillan. Retrieved from https://archive.org/details/cu31924012500306

Hill, J. M., & Norris, T. R. (2001). Long-term results of total shoulder arthroplasty following bone-grafting of the glenoid. *The Journal of Bone and Joint Surgery. American Volume*, *83–A*(6), 877–883. Retrieved from http://jbjs.org/content/83/6/877.abstract

Holzbaur, K. R. S., Murray, W. M., & Delp, S. L. (2005). A Model of the Upper Extremity for Simulating Musculoskeletal Surgery and Analyzing Neuromuscular Control. *Annals of Biomedical Engineering*, *33*(6), 829–840. https://doi.org/10.1007/s10439-005-3320-7

Hopkins, A. R. (2004). *Total Shoulder Arthroplasty simulation using Finite Element Analysis*. Imperial College London. Retrieved from https://spiral.imperial.ac.uk/bitstream/10044/1/11770/2/Hopkins-AR-2004-PhD-Thesis.pdf

Hopkins, A. R., Hansen, U. N., Amis, A. A., & Emery, R. (2004). The effects of glenoid component alignment variations on cement mantle stresses in total shoulder arthroplasty. *Journal of Shoulder and Elbow Surgery*, *13*(6), 668–675. https://doi.org/10.1016/j.jse.2004.04.008

Hopkins, A. R., Hansen, U. N., Amis, A. A., Knight, L., Taylor, M., Levy, O., & Copeland, S. A. (2006a). Wear in the Prosthetic Shoulder: Association With Design Parameters. *Journal of Biomechanical Engineering*, *129*(2), 223. https://doi.org/10.1115/1.2486060

Hopkins, A. R., Hansen, U. N., Amis, A. A., Taylor, M., & Emery, R. J. (2007). Glenohumeral kinematics following total shoulder arthroplasty: A finite element investigation. *Journal of Orthopaedic Research*, *25*(1), 108–115. https://doi.org/10.1002/jor.20290

Hopkins, A. R., Hansen, U. N., Amis, A. a., Taylor, M., Gronau, N., & Anglin, C. (2006b). Finite element modelling of glenohumeral kinematics following total shoulder arthroplasty. *Journal of Biomechanics*, *39*(13), 2476–2483. https://doi.org/10.1016/j.jbiomech.2005.07.031

Humphrey, C. S., & Gale, A. L. (2018). Spherical versus elliptical prosthetic humeral heads: a comparison of anatomic fit. *Journal of Shoulder and Elbow Surgery*, *27*(6), S50–S57. https://doi.org/10.1016/j.jse.2018.03.002

Humphrey, C. S., Sears, B. W., & Curtin, M. J. (2016). An anthropometric analysis to derive formulae for calculating the dimensions of anatomically shaped humeral heads. *J Shoulder Elbow Surg*, *25*, 1532–1541. https://doi.org/10.1016/j.jse.2016.01.032

Iannotti, J. P., Gabriel, J. P., Schneck, S. L., Evans, B. G., & Misra, S. (1992). The normal glenohumeral relationships. An anatomical study of one hundred and forty shoulders. *The Journal of Bone and Joint Surgery. American Volume*, *74*(4), 491–500. Retrieved from http://www.ncbi.nlm.nih.gov/pubmed/1583043

Ingram, D., Engelhardt, C., Farron, A., Terrier, A., & Müllhaupt, P. (2015). Muscle moment-arms: a key element in muscle-force estimation. *Computer Methods in Biomechanics and Biomedical Engineering*, *18*(5), 506–513. https://doi.org/10.1080/10255842.2013.818666

İşcan, M. Y., Loth, S. R., King, C. A., Shihai, D., & Yoshino, M. (1998). Sexual dimorphism in the humerus: a comparative analysis of Chinese, Japanese and Thais. *Forensic Science International*, *98*(1), 17–29. https://doi.org/10.1016/S0379-0738(98)00119-4

Jeno, S. H., & Bhimji, S. S. (2018). *Anatomy, Back, Muscles, Latissimus Dorsi*. *StatPearls*. StatPearls Publishing. Retrieved from http://www.ncbi.nlm.nih.gov/pubmed/28846224

Jobe, C. M., & Iannotti, J. P. (1995). Limits imposed on glenohumeral motion by joint geometry. *Journal of Shoulder and Elbow Surgery*, *4*(4), 281–285. https://doi.org/10.1016/S1058-2746(05)80021-7

Johnson, G. R., Spalding, D., Nowitzke, A., & Bogdukt, N. (1996). MODELLING THE MUSCLES OF THE SCAPULA MORPHOMETRIC AND COORDINATE DATA AND FUNCTIONAL IMPLICATIONS. *Journal of Biomechanics*, *29*, 1039–1051. https://doi.org/10.1016/0021-9290(95)00176-X

Jun, Iannotti, J. P., McGarry, M. H., Chul Yoo, J., Quigley, R. J., & Lee, T. Q. (2013). The effects of prosthetic humeral head shape on glenohumeral joint kinematics: a comparison of non-spherical and spherical prosthetic heads to the native humeral head. *Journal of Shoulder and Elbow Surgery*, *22*, 1423–1432. https://doi.org/10.1016/j.jse.2013.01.002

Jun, Lee, T. Q., McGarry, M. H., Quigley, R. J., Shin, S. J., & Iannotti, J. P. (2016). The effects of prosthetic humeral head shape on glenohumeral joint kinematics during humeral axial rotation in total shoulder arthroplasty. *Journal of Shoulder and Elbow Surgery*, *25*(7), 1084–1093. https://doi.org/10.1016/J.JSE.2015.11.058

Jun, Y., & Choi, K. (2010). Design of patient-specific hip implants based on the 3D geometry of the human femur. *Advances in Engineering Software*, *41*(4), 537–547. https://doi.org/10.1016/J.ADVENGSOFT.2009.10.016

Junaid, S., Gupta, S., Sanghavi, S., Anglin, C., Roger, E., Amis, A., & Hansen, U. (2010). Failure mechanism of the all-polyethylene glenoid implant. *Journal of Biomechanics*, *43*(4), 714–719. https://doi.org/10.1016/j.jbiomech.2009.10.019

Kaback, L. A., Green, A., & Blaine, T. A. (2012). Glenohumeral arthritis and total shoulder replacement. *Medicine and Health, Rhode Island*, *95*(4), 120–124. Retrieved from http://www.ncbi.nlm.nih.gov/pubmed/22712191

Karduna, A. R., Williams, G. R., Williams, J. L., & Iannotti, J. P. (1997). Glenohumeral Joint Translations before and after Total Shoulder Arthroplasty. *J Bone Joint Surg Am., 79(8),* 1166-74.

Kent, B. E. (1971). Functional Anatomy of the Shoulder Complex A Review. *Physical Therapy*, *51*(8), 867–888. Retrieved from https://watermark.silverchair.com/ptj0867.pdf?token=AQECAHi208BE49Ooan9kkhW_Ercy7Dm3ZL_9Cf3qfKAc485ysgAAAbgwggG0BgkqhkiG9w0BBwagggGlMIIBoQIBADCCAZoGCSqGSIb3DQEHATAeBglghkgBZQMEAS4wEQQMml24Vo4raoFqIV5oAgEQgIIBawAyxUvrzSm8VqJ8OMrR6aoeIuxP6S3hW0XWXD-KwqXS9Hh

Kiet, T. K., Feeley, B. T., Naimark, M., Gajiu, T., Hall, S. L., Chung, T. T., & Ma, C. B. (2015). Outcomes after shoulder replacement: comparison between reverse and anatomic total shoulder arthroplasty. *Journal of Shoulder and Elbow Surgery*, *24*(2), 179–185. https://doi.org/10.1016/J.JSE.2014.06.039

Kim, S. H., Szabo, R. M., & Marder, R. A. (2012). Epidemiology of humerus fractures in the United States: nationwide emergency department sample, 2008. *Arthritis Care & Research*, *64*(3), 407–414. https://doi.org/10.1002/acr.21563

Kistler, M., Bonaretti, S., Pfahrer, M., Niklaus, R., & Büchler, P. (2013). The virtual skeleton database: an open access repository for biomedical research and collaboration. *Journal of Medical Internet Research*, *15*(11), e245. https://doi.org/10.2196/jmir.2930

Knowles, N. K., Carroll, M. J., Keener, J. D., Ferreira, L. M., & Athwal, G. S. (2016). A comparison of normal and osteoarthritic humeral head size and morphology. *Journal of Shoulder and Elbow Surgery / American Shoulder and Elbow Surgeons ... [et Al.]*, *25*(3), 502–509. https://doi.org/10.1016/j.jse.2015.08.047

Kohr, R. L., & Games, P. A. (1974). Robustness of the Analysis of Variance, the Welch Procedure and a Box Procedure to Heterogeneous Variances. *The Journal of Experimental Education*, *43*(1), 61–69. https://doi.org/10.1080/00220973.1974.10806305

Kontaxis, A. (2010). *Biomechanical analysis of reverse anatomy shoulder prosthesis*. Newcastle University. https://doi.org/http://hdl.handle.net/10443/3627

Kontaxis, A., & Johnson, G. R. (2009). The biomechanics of reverse anatomy shoulder replacement – A modelling study. *Clinical Biomechanics*, *24*, 254–260. https://doi.org/10.1016/j.clinbiomech.2008.12.004

Kranioti, E. F., & Michalodimitrakis, M. (2009). Sexual dimorphism of the humerus in contemporary cretans - A population-specific study and a review of the literature. *Journal of Forensic Sciences*, *54*(5), 996–1000. https://doi.org/10.1111/j.1556-4029.2009.01103.x

Kuechle, D. K., Newman, S. R., Itoi, E., Morrey, B. F., & An, K.-N. (1997). Shoulder muscle moment arms during horizontal flexion and elevation. *Journal of Shoulder and Elbow Surgery*, *6*(5), 429–439. https://doi.org/10.1016/S1058-2746(97)70049-1

Kuechle, D. K., Newman, S. R., Itoi, E., Niebur, G. L., Morrey, B. F., & An, K.-N. (2000). The relevance of the moment arm of shoulder muscles with respect to axial rotation of the glenohumeral joint in four positions. *Clinical Biomechanics*, *15*, 322–329. Retrieved from http://www.clinbiomech.com/article/S0268-0033(99)00081-9/pdf

Kurki, H. K. (2013). Skeletal variability in the pelvis and limb skeleton of humans: Does stabilizing selection limit female pelvic variation? *American Journal of Human Biology*, *25*(6), 795–802. https://doi.org/10.1002/ajhb.22455

Kurtz, S. M., Muratoglu, O. K., Evans, M., & Edidin, A. A. (1999). Advances in the processing, sterilization, and crosslinking of ultra-high molecular weight polyethylene for total joint arthroplasty. *Biomaterials*, *20*(18), 1659–1688. Retrieved from http://www.ncbi.nlm.nih.gov/pubmed/10503968

Lacroix, D., Murphy, L. A., & Prendergast, P. J. (2000). Three-Dimensional Finite Element Analysis of Glenoid Replacement Prostheses: A Comparison of Keeled and Pegged

Anchorage Systems. *Journal of Biomechanical Engineering*, *122*, 430–436. https://doi.org/10.1115/1.1286318

Lacroix, D., & Prendergast, P. J. (1997). Stress analysis of glenoid component designs for shoulder arthroplasty. *Proceedings of the Institution of Mechanical Engineers. Part H, Journal of Engineering in Medicine*, *211*(6), 467–474. https://doi.org/10.1243/0954411981534583

Langenderfer, J. E., Patthanacharoenphon, C., Carpenter, J. E., & Hughes, R. E. (2006). Variation in external rotation moment arms among subregions of supraspinatus, infraspinatus, and teres minor muscles. *Journal of Orthopaedic Research : Official Publication of the Orthopaedic Research Society*, *24*(8), 1737–1744. https://doi.org/10.1002/jor.20188

Lazarus, M. D., Jensen, K. L., Southworth, C., & Matsen III, F. (2002). The Radiographic Evaluation of Keeled and Pegged Glenoid Component Insertion. *THE JOURNAL OF BONE AND JOINT SURGERY*, *84*(A), 1174–1182. Retrieved from www.jbjs.org.

Lehmann, L., Magosch, P., Mauermann, E., Lichtenberg, S., & Habermeyer, P. (2010). Total shoulder arthroplasty in dislocation arthropathy. *International Orthopaedics*, *34*(8), 1219–1225. https://doi.org/10.1007/s00264-009-0928-5

Lippitt, S. B., Vanderhooft, J. E., Harris, S. L., Sidles, J. A., Harryman, D. T., & Matsen, F. A. (1993). Glenohumeral stability from concavity-compression: A quantitative analysis. *Journal of Shoulder and Elbow Surgery*, *2*(1), 27–35. https://doi.org/10.1016/S1058-2746(09)80134-1

Lippitt, S., & Matsen, F. (1993). Mechanisms of glenohumeral joint stability. *Clinical Orthopaedics and Related Research*, (291), 20–28. Retrieved from http://www.ncbi.nlm.nih.gov/pubmed/8504601

Liu, J., Hughes, R., Smutz, W., Niebur, G., & Nan-An, K. (1997). Roles of deltoid and rotator cuff muscles in shoulder elevation. *Clinical Biomechanics*, *12*(1), 32–38. https://doi.org/10.1016/S0268-0033(96)00047-2

Loth, S. R., & Henneberg, M. (1996). Mandibular ramus flexure - indicator of sexual dimorphism? *American Journal of Physical Anthropology*, *99*, 473–485.

Ma, L., Chablat, D., Bennis, F., & Zhang, W. (2009). A new simple dynamic muscle fatigue model and its validation. *International Journal of Industrial Ergonomics*, *39*(1), 211–220. https://doi.org/10.1016/J.ERGON.2008.04.004

Mackay, D. C., Hudson, B., & Williams, J. R. (2001). Which primary shoulder and elbow replacement? *Annals of the Royal College of Surgeons of England*, *83*(4), 258–265.

Mamatha, T., Pai, S. R., Murlimanju, B. V., Kalthur, S. G., Pai, M. M., & Kumar, B. (2011). Morphometry of glenoid cavity. *Online Journal of Health and Allied Sciences*, *10*(3), 1–4.

Marchese, S. ., & Johnson, G. . (2000). Measuring the kinematics of the clavicle. In *6th International Symposium of the 3D Analysis of Human motion* (pp. 37–40). Cape Town: Springer International Publishing.

Marras, W. S., Lavender, S. A., Ferguson, S. A., Splittstoesser, R. E., & Yang, G. (2010). Quantitative biomechanical workplace exposure measures: Distribution centers. *Journal of Electromyography and Kinesiology*, *20*(5), 813–822.

https://doi.org/10.1016/J.JELEKIN.2010.03.006

Marsden, S. P., Swailes, D. C., & Johnson, G. R. (2008). Algorithms for exact multi-object muscle wrapping and application to the deltoid muscle wrapping around the humerus. *Proceedings of the Institution of Mechanical Engineers, Part H: Journal of Engineering in Medicine*, *222*(7), 1081–1095. https://doi.org/10.1243/09544119JEIM378

Massimini, D. F., Li, G., & Warner, J. P. (2010). Glenohumeral contact kinematics in patients after total shoulder arthroplasty. *The Journal of Bone and Joint Surgery. American Volume*, *92*(4), 916–926. https://doi.org/10.2106/JBJS.H.01610

Matsen III, F. A., Clinton, J., Lynch, J., Bertelsen, A., & Richardson, M. L. (2008). Glenoid Component Failure in Total Shoulder Arthroplasty. *J Bone Joint Surg Am*, *90*, 885–896. https://doi.org/10.2106/JBJS.G.01263

Matsuki, K., Sugaya, H., Hosihika, S., Takahashi, N., Banks, S. A., Vanasse, T., & Digeorgio, C. (2018). Three-Dimensional Measurement of Japanese Glenoid Geometry. Retrieved from https://www.ors.org/Transactions/64/1040.pdf

Matsumura, N., Oki, S., Ogawa, K., Iwamoto, T., Ochi, K., Sato, K., & Nagura, T. (2016). Three-dimensional anthropometric analysis of the glenohumeral joint in a normal Japanese population. *J Shoulder Elbow Surg*, *25*, 493–501. https://doi.org/10.1016/j.jse.2015.08.003

Mauro, C. S. (2011). Proximal humeral fractures. *Curr Rev Musculoskelet Med*, *4*, 214–220. https://doi.org/10.1007/s12178-011-9094-7

McDonald, J. H. (2014). *Handbook of Biological Statistics* (3rd ed.). Baltimore: Sparky House Publishing. Retrieved from http://www.biostathandbook.com/power.html

Mckenna, C. (2017). IF BONES COULD TALK: Estimating sex from the glenoid cavity. Retrieved from http://library2.smu.ca/bitstream/handle/01/27018/McKenna_Chelsea_Honours_2017.pdf?sequence=1

McPherson, E. J., Friedman, R. J., An, Y. H., Chokesi, R., & Dooley, L. (1997). Anthropometric glenohumeral study of normal relationships. *Journal of Shoulder and Elbow Surgery*, *6*(2), 105–112.

Merolla, G., Nastrucci, G., & Porcellini, G. (2013). Shoulder arthroplasty in osteoarthritis: current concepts in biomechanics and surgical technique. *Translational Medicine @ UniSa*, *6*(4), 16–28. Retrieved from http://www.pubmedcentral.nih.gov/articlerender.fcgi?artid=3829793&tool=pmcentrez&rendertype=abstract

Merrill, A., Guzman, K., & Miller, S. L. (2009). Gender differences in glenoid anatomy: an anatomic study. *Surgical and Radiologic Anatomy*, *31*(3), 183–189. https://doi.org/10.1007/s00276-008-0425-3

Milner, G. R., & Boldsen, J. L. (2012). Humeral and femoral head diameters in recent white american skeletons. *Journal of Forensic Sciences*, *57*(1), 35–40. https://doi.org/10.1111/j.1556-4029.2011.01953.x

Mue, D., Salihu, M., Awonusi, F., Yongu, W., Kortor, J., & Elachi, I. (2013). The epidemiology and outcome of acute septic arthritis: a hospital based study. *Journal of the West African College of Surgeons*, *3*(1), 40–52. Retrieved from http://www.ncbi.nlm.nih.gov/pubmed/25453011%5Cnhttp://www.pubmedcentral.nih.gov/articlerender.fcgi?artid=PMC4228814

Mueller, U., Braun, S., Schroeder, S., Schroeder, M., Sonntag, R., Jaeger, S., & Kretzer, J. P. (2017). Influence of humeral head material on wear performance in anatomic shoulder joint arthroplasty. *Journal of Shoulder and Elbow Surgery*, *26*(10), 1756–1764. https://doi.org/10.1016/J.JSE.2017.05.008

Murphy, B. P., & Prendergast, P. J. (2000). On the magnitude and variability of the fatigue strength of acrylic bone cement. *International Journal of Fatigue*, *22*(10), 855–864. https://doi.org/https://doi.org/10.1016/S0142-1123(00)00055-4

Musib, M. K. (2012). A Review of the History and Role of UHMWPE as A Component in Total Joint Replacements. *International Journal of Biological Engineering*, *1*(1), 6–10. https://doi.org/10.5923/j.ijbe.20110101.02

Nagels, J., Valstar, E. R., Stokdijk, M., & Rozing, P. M. (2002). Patterns of loosening of the glenoid component. *J Bone Joint Surg [Br]*, *84–B*, 83–87. https://doi.org/10.1302/0301-620x.84b1.11951

National Collaborating Centre for Chronic Conditions. (2009). *Rheumatoid arthritis: national clinical guideline for management and treatment in adults*. London: Royal College of Physicians. Retrieved from https://www.ncbi.nlm.nih.gov/pubmedhealth/PMH0009576/pdf/PubMedHealth_PMH0009576.pdf

Neer II, C. S. (1955). The Classic: Articular replacement for the humeral head. *Clin Orthop Relat Res*, (2409), 2421. https://doi.org/DOI 10.1007/s11999-011-1944-5

Neer II, C. S. (1974). Replacement arthroplasty for glenohumeral osteoarthritis. *The Journal of Bone and Joint Surgery. American Volume*, *56*(1), 1–13. Retrieved from http://www.ncbi.nlm.nih.gov/pubmed/4812164

Neer II, C., Watson, K., & Stanton, F. (1982). Recent experience in total shoulder replacement. *J Bone and Joint Surg*, *64*(A), 319–337. Retrieved from https://sci-hub.tw/https://Insights.ovid.com/crossref?an=00004623-198264030-00001

Nikooyan, A. A., Veeger, H. E. J., Westerhoff, P., Graichen, F., Bergmann, G., & Van Der Helm, F. C. T. (2010). Validation of the Delft Shoulder and Elbow Model using in-vivo glenohumeral joint contact forces. *Journal of Biomechanics*, *43*, 3007–3014. https://doi.org/10.1016/j.jbiomech.2010.06.015

O'neill, F., Condon, F., Mcgloughlin, T., Lenehan, B., Coffey, C., & Walsh, M. (2012). Validity of synthetic bone as a substitute for osteoporotic cadaveric femoral heads in mechanical testing A BIOMECHANICAL STUDY. *Bone Joint Res*, *1*(4), 50–55. https://doi.org/10.1302/2046-3758.14.2000044

Omori, Y., Yamamoto, N., Koishi, H., Futai, K., Goto, A., Sugamoto, K., & Itoi, E. (2014). Measurement of the Glenoid Track In Vivo as Investigated by 3-Dimensional Motion

Analysis Using Open MRI. *The American Journal of Sports Medicine*, *42*(6), 1290–1295. https://doi.org/10.1177/0363546514527406

Otis, J. C., Jiang, C. C., Wickiewicz, T. L., Peterson, M. G., Warren, R. F., & Santner, T. J. (1994). Changes in the moment arms of the rotator cuff and deltoid muscles with abduction and rotation. *The Journal of Bone and Joint Surgery. American Volume*, *76*(5), 667–676. Retrieved from http://www.ncbi.nlm.nih.gov/pubmed/8175814

Ousley, S., Jantz, R., & Freid, D. (2009). Understanding race and human variation: Why forensic anthropologists are good at identifying race. *American Journal of Physical Anthropology*, *139*(1), 68–76. https://doi.org/10.1002/ajpa.21006

Owaydhah, W. H., Alobaidy, M. A., Abdulrahman, @bullet, Alraddadi, S., & Soames, R. W. (2017). Three-dimensional analysis of the proximal humeral and glenoid geometry using MicroScribe 3D digitizer. *Surgical and Radiologic Anatomy*, *39*, 767–772. https://doi.org/10.1007/s00276-016-1782-y

Padegimas, E. M., Maltenfort, M., Lazarus, M. D., Ramsey, M. L., Williams, G. R., & Namdari, S. (2015). Future Patient Demand for Shoulder Arthroplasty by Younger Patients: National Projections. *Clinical Orthopaedics and Related Research®*, *473*(6), 1860–1867. https://doi.org/10.1007/s11999-015-4231-z

Papadonikolakis, A., & Matsen, F. A. (2014). Metal-Backed Glenoid Components Have a Higher Rate of Failure and Fail by Different Modes in Comparison with All-Polyethylene Components. *The Journal of Bone and Joint Surgery-American Volume*, *96*(12), 1041–1047. https://doi.org/10.2106/JBJS.M.00674

Papaioannou, V. A., Kranioti, E. F., Joveneaux, P., Nathena, D., & Michalodimitrakis, M. (2012). Sexual dimorphism of the scapula and the clavicle in a contemporary Greek population: Applications in forensic identification. *Forensic Science International*, *217*(1–3), 231.e1-231.e7. https://doi.org/10.1016/J.FORSCIINT.2011.11.010

Parker, R., & Jelsma, J. (2010). The prevalence and functional impact of musculoskeletal conditions amongst clients of a primary health care facility in an under-resourced area of Cape Town. *BMC Musculoskeletal Disorders*, *11:2*. https://doi.org/10.1186/1471-2474-11-2

Patel, R. J., Wright, T. M., & Gao, Y. (2014). Load transfer after cemented total shoulder arthroplasty. *Journal of Shoulder and Elbow Surgery*, *23*, 1553–1562. https://doi.org/10.1016/j.jse.2014.01.038

Pearl, M. L., & Kurutz, S. (1999). Geometric Analysis of Commonly Used Prosthetic Systems for Proximal Humeral Replacement Geometric Analysis of Commonly Used Prosthetic Systems for Proximal Humeral Replacement *. *The Journal of Bone & Joint Surgery*, *81–A*(5), 660–671.

Pearl, M. L., Kurutz, S., Boileau, P., Sinnerton, R. J., Chuinard, C., Walch, G., … Antonio, S. A. N. (2001). Glenoid loosening after total shoulder arthroplasty: An in vitro CT-scan study. *Journal of Shoulder and Elbow Surgery*, *25*(4), 502–509. https://doi.org/10.1016/j.clinbiomech.2004.07.001

Peltz, C. D., Zauel, R., Ramo, N., Mehran, N., Moutzouros, V., & Bey, M. J. (2015). Differences

in glenohumeral joint morphology between patients with anterior shoulder instability and healthy, uninjured volunteers. *Journal of Shoulder and Elbow Surgery*, *24*(7), 1014–1020. https://doi.org/10.1016/j.jse.2015.03.024

Pomwenger, W., Entacher, K., Resch, H., & Schuller-götzburg, P. (2015). Multi-patient finite element simulation of keeled versus pegged glenoid implant designs in shoulder arthroplasty. *Med Biol Eng Comput*, *53*, 781–790. https://doi.org/10.1007/s11517-015-1286-7

Postacchini, R., Castagna, A., Borroni, M., Cinotti, G., Postacchini, F., & Gumina, S. (2012). Total shoulder arthroplasty for the treatment of failed hemiarthroplasty in patients with fracture of the proximal humerus. *Journal of Shoulder and Elbow Surgery*, *21*(11), 1542–1549. https://doi.org/10.1016/j.jse.2011.12.007

Puttock, M. J., & Thwaite, E. G. (1969). Elastic Compression of Spheres and Cylinders at Point and Line Contact. *Commonwealth Scientific and Industrial Research Organization*. Retrieved from http://emtoolbox.nist.gov/Publications/NationalStandardsLaboratoryTechnicalPaperNo25.pdf

Ramaniraka, N. A., Rakotomanana, L. R., & Leyvraz, P. F. (2000). The fixation of the cemented femoral component. Effects of stem stiffness, cement thickness and roughness of the cement-bone surface. *The Journal of Bone and Joint Surgery. British Volume*, *82*(2), 297–303. https://doi.org/10.1302/0301-620X.82B2.0820297

Raphael, B. S., Dines, J. S., Warren, R. F., Figgie, M., Craig, E. V., Fealy, S., & Dines, D. M. (2010). Symptomatic glenoid loosening complicating total shoulder arthroplasty. *HSS Journal*, *6*(1), 52–56. https://doi.org/10.1007/s11420-009-9148-1

Ray, B., Saxena, a., Nayak, S., Pugazhendi, B., & Gayathri, B. M. V. (2015). Morphometry and anatomical variations of flexor digitorum superficialis. *Journal of Morphological Sciences*, *32*(1), 8–11. https://doi.org/10.4322/jms.056014

Razmjou, H., Holtby, R., Christakis, M., Axelrod, T., & Richards, R. (2013). Impact of prosthetic design on clinical and radiologic outcomes of total shoulder arthroplasty: a prospective study. *Journal of Shoulder and Elbow Surgery*, *22*(2), 206–214. https://doi.org/10.1016/j.jse.2012.04.016

Robertson, D. D., Yuan, J., Bigliani, L. U., Flatow, E. L., & Yamaguchi, K. (2000). Three-Dimensional Analysis of the Proximal Part of the Humerus: Relevance to Arthroplasty *. *THE JOURNAL OF BONE AND JOINT SURGERY*, *82*(11), 1594–1602. Retrieved from https://insights.ovid.com/pubmed?pmid=11097450

Rockwood, C. A. (2009). *The shoulder* (4th ed.). Philadelphia, PA : Saunders/Elsevier.

Saini, M., Singh, Y., Arora, P., Arora, V., Jain Monika Saini, K., & Jain, K. (2015). Implant biomaterials: A comprehensive review. *World J Clin Cases*, *3*(1), 52–57. https://doi.org/10.12998/wjcc.v3.i1.52

Samed. (n.d.). The South African Medical Device Industry - Facts.

Sanchez-Sotelo, J. (2011). Total Shoulder Arthroplasty. *The Open Orthopaedics Journal*, *5*, 106–114. https://doi.org/10.2174/1874325001105010106

Schaaf, A. C., & Bell, R. H. (2008). Humeral Head Height: Getting it Right. *Seminars in Arthroplasty*, *19*(1), 74–77. https://doi.org/10.1053/J.SART.2007.12.033

Schrumpf, M., Maak, T., Hammoud, S., & Craig, E. V. (2011). The glenoid in total shoulder arthroplasty. *Current Reviews in Musculoskeletal Medicine*, *4*(4), 191–199. https://doi.org/10.1007/s12178-011-9096-5

Scibek, J. S., & Carcia, C. R. (2012). Assessment of scapulohumeral rhythm for scapular plane shoulder elevation using a modified digital inclinometer. *World J Orthop*, *3*(6), 97–94. https://doi.org/10.5312/wjo.v3.i6.87

Sherman, M. A., Seth, A., & Delp, S. L. (2013). WHAT IS A MOMENT ARM? CALCULATING MUSCLE EFFECTIVENESS IN BIOMECHANICAL MODELS USING GENERALIZED COORDINATES. *Proceedings of the ... ASME Design Engineering Technical Conferences. ASME Design Engineering Technical Conferences*, *2013*. https://doi.org/10.1115/DETC2013-13633

Sinusas, K. (2012). Osteoarthritis: Diagnosis and Treatment. *Am Fam Physician*, *86*(10), 893. Retrieved from https://www.aafp.org/afp/2012/0101/p49.pdf

Skirven, T. M. (2011). *Rehabilitation of the Hand and Upper Extremity- ClinicalKey* (6th ed.). Philadelphia, PA : Elsevier Mosby. Retrieved from https://www.clinicalkey.com/#!/browse/book/3-s2.0-C20090386845

Slamin, J., & Parsley, B. (2012). Evolution of customization design for total knee arthroplasty. https://doi.org/10.1007/s12178-012-9141-z

Smith and Nephew. (n.d.). COFIELD 2 TOTALSHOULDER SYSTEM. Retrieved from http://www.bonerepmedical.com/main_site/surgical_techniques/Colfield2.pdf

Somerson, J. S., Hsu, J. E., Neradilek, M. B., & Matsen, F. A. (2018). Analysis of 4063 complications of shoulder arthroplasty reported to the US Food and Drug Administration from 2012 to 2016. *Journal of Shoulder and Elbow Surgery*. https://doi.org/10.1016/j.jse.2018.03.025

STATS SA. (2017). New mid-year estimates reveal ageing population | Statistics South Africa. Retrieved August 8, 2018, from http://www.statssa.gov.za/?p=10277

Steyn, M., & Işcan, M. Y. (1999). Osteometric variation in the humerus: Sexual dimorphism in South Africans. *Forensic Science International*, *106*(2), 77–85. https://doi.org/10.1016/S0379-0738(99)00141-3

Stone, K. D., Grabowski, J. J., Cofield, R. H., Morrey, B. F., & An, K. N. (1999). Stress analyses of glenoid components in total shoulder arthroplasty. *Journal of Shoulder and Elbow Surgery*, *8*(2), 151–158. https://doi.org/10.1016/S1058-2746(99)90009-5

Strauss, E. J., Roche, C., Flurin, P.-H., Wright, T., & Zuckerman, J. D. (2009). The glenoid in shoulder arthroplasty. *Journal of Shoulder and Elbow Surgery*, *18*(5), 819–833. https://doi.org/10.1016/J.JSE.2009.05.008

Stryker. (2017). ReUnion ® TSA Total Shoulder Arthroplasty System. Retrieved from http://az621074.vo.msecnd.net/syk-mobile-content-cdn/global-content-system/SYKGCSDOC-2-43214/2XC3XlK8bpaUl4ARJA7dIfwdjKc7Rg/RU_ST_3.pdf

Styron, J. F., Higuera, C. A., Strnad, G., & Iannotti, J. P. (2015). Greater patient confidence yields greater functional outcomes after primary total shoulder arthroplasty. *Journal of Shoulder and Elbow Surgery*, *24*, 1263–1267. https://doi.org/10.1016/j.jse.2015.04.018

Tadepalli, S. C., Erdemir, A., & Cavanagh, P. R. (2011). Comparison of hexahedral and tetrahedral elements in finite element analysis of the foot and footwear. *Journal of Biomechanics*, *44*, 2337–2343. https://doi.org/10.1016/j.jbiomech.2011.05.006

Tanck, E., Hannink, G., Ruimerman, R., Buma, P., Burger, E. H., & Huiskes, R. (2006). Cortical bone development under the growth plate is regulated by mechanical load transfer. *J. Anat*, *208*, 73–79. Retrieved from https://www.ncbi.nlm.nih.gov/pmc/articles/PMC2100179/pdf/joa0208-0073.pdf

Terrier, A., Brighenti, V., Pioletti, D. P., & Farron, A. (2012). Importance of polyethylene thickness in total shoulder arthroplasty: A finite element analysis. *Clinical Biomechanics*, *27*(5), 443–448. https://doi.org/10.1016/j.clinbiomech.2011.12.003

Terrier, A., Büchler, P., & Farron, A. (2006). Influence of glenohumeral conformity on glenoid stresses after total shoulder arthroplasty. *Journal of Shoulder and Elbow Surgery / American Shoulder and Elbow Surgeons ... [et Al.]*, *15*(4), 515–520. https://doi.org/10.1016/j.jse.2005.09.021

Terrier, A., Obrist, R., Malfroy Camine, V., Becce, F., & Farron, A. (2018). Biomechanical comparison of glenoid implants with adaptable and fixed backside curvatures in anatomic total shoulder arthroplasty. *Journal of Shoulder and Elbow Surgery*. https://doi.org/10.1016/j.jse.2018.02.050

The International Trade Administration. (2017). South Africa - Medical Devices. Retrieved May 5, 2018, from https://www.export.gov/article?id=South-Africa-medical-devices

Ubelaker, D. H., & DeGaglia, C. M. (2017). Population variation in skeletal sexual dimorphism. *Forensic Science International*, *278*, 407.e1-407.e7. https://doi.org/10.1016/J.FORSCIINT.2017.06.012

Usenbo, A., Kramer, V., Young, T., & Musekiwa, A. (2015). Prevalence of Arthritis in Africa: A Systematic Review and Meta-Analysis. *PloS One*, *10*(8), 1–19. https://doi.org/10.1371/journal.pone.0133858

van der Helm, F. C. T. (1996). A standardized protocol for motion recordings of the shoulder. In *Proceedings of the First Conference of the ISG* (pp. 1–7). Maastricht: Shaker Publishing. Retrieved from https://www.researchgate.net/profile/Frans_Van_Der_Helm/publication/238167085_A_standardized_protocol_for_motion_recordings_of_the_shoulder/links/5445ac010cf22b3c14ddec09/A-standardized-protocol-for-motion-recordings-of-the-shoulder.pdf

Viceconti, M., Olsen, S., Nolte, L.-P., & Burton, K. (2005). Extracting clinically relevant data from finite element simulations. *Clinical Biomechanics*, *20*(5), 451–454. https://doi.org/10.1016/J.CLINBIOMECH.2005.01.010

Vioarsdottie, U. S., Higgins, P. O., & Stringer, C. (2002). A geometric morphometric study of regional differences in the ontogeny of the modern human facial skeleton †. *Journal of Anatomy*, *201*, 211–229. https://doi.org/10.1046/j.1469-7580.2002.00092.x

Vo Ba, K. V, Hackett, D. J., Gee, A. O., & Hsu, J. E. (2017). IN BRIEF Classifications in Brief: Walch Classification of Primary Glenohumeral Osteoarthritis. *Clinical Orthopaedics and Related Research*, *475*(9), 2335–2340. https://doi.org/10.1007/s11999-017-5317-6

Walch, G., Edwards, T. B., Boulahia, A., Boileau, P., Mole, D., & Adeleine, P. (2002). The Influence of Glenohumeral Prosthetic Mismatch on Glenoid Radiolucent Lines. *The Journal of Bone & Joint Surgery*, *84–A*(12), 2186–2191.

Wallace, A. L., Phillips, R. L., Macdougal, G. A., Walsh, W. R., Sonnabend, D. H., & Australia, S. (1999). Resurfacing of the Glenoid in Total Shoulder Arthroplasty A COMPARISON, AT A MEAN OF FIVE YEARS, OF PROSTHESES INSERTED WITH AND WITHOUT CEMENT*. *The Journal of Bone & Joint Surgery*, *81*(4), 510–518. Retrieved from https://insights.ovid.com/pubmed?pmid=10225796

Wang, V. M., Krishnan, R., Ugwonali, O. F. C., Flatow, E. L., Bigliani, L. U., & Ateshian, G. A. (2005). Biomechanical evaluation of a novel glenoid design in total shoulder arthroplasty. *J Shoulder Elbow Surg*, *14*(15), 129–140. https://doi.org/10.1016/j.jse.2004.09.029

Warner, J. J. P., Bowen, M. K., Deng, X., Hannafin, J. A., Arnoczky, S. P., & Warren, R. F. (1998). Articular contact patterns of the normal glenohumeral joint. *Journal of Shoulder and Elbow Surgery*, *7*(4), 381–388. https://doi.org/10.1016/S1058-2746(98)90027-1

Westerhoff, P., Graichen, F., Bender, A., Rohlmann, A., & Bergmann, G. (2009). An instrumented implant for in vivo measurement of contact forces and contact moments in the shoulder joint. *Medical Engineering & Physics*, *31*, 207–213. https://doi.org/10.1016/j.medengphy.2008.07.011

Wickham, J., Pizzari, T., Balster, S., Ganderton, C., & Watson, L. (2014). The variable roles of the upper and lower subscapularis during shoulder motion. *Clinical Biomechanics*, *29*(8), 885–891. https://doi.org/10.1016/J.CLINBIOMECH.2014.07.003

Williams, G. R., & Abboud, J. A. (2005). Total shoulder arthroplasty: Glenoid component design. *Journal of Shoulder and Elbow Surgery*, *14*(1), S122–S128. https://doi.org/10.1016/J.JSE.2004.09.028

Wirth, M. A., Klotz, C., Deffenbaugh, D. L., McNulty, D., Richards, L., & Tipper, J. L. (2009). Cross-linked glenoid prosthesis: A wear comparison to conventional glenoid prosthesis with wear particulate analysis. *Journal of Shoulder and Elbow Surgery*, *18*(1), 130–137. https://doi.org/10.1016/j.jse.2008.06.015

Wirth, M. A., Loredo, R., Garcia, G., Rockwood, C. A., Southworth, C., & Iannotti, J. P. (2012). Total shoulder arthroplasty with an all-polyethylene pegged bone-ingrowth glenoid component: a clinical and radiographic outcome study. *The Journal of Bone and Joint Surgery. American Volume*, *94*(3), 260–267. https://doi.org/10.2106/JBJS.J.01400

Wirth, & Rockwood, C. A. J. R. (1996). Current Concepts Review - Complications of Total Shoulder-Replacement Arthroplasty*. *The Journal of Bone & Joint Surgery*, *78*(4), 603–616. Retrieved from http://dx.doi.org/

Wright Medical Group Inc. (2016). Tornier AEQUALIS ASCEND ™ FLEX Offers Anatomic Progression with Options. Retrieved from http://www.wmtemedia.com/ProductFiles/Files/PDFs/CAW-7058_EN_LR_LE.pdf

Wu, G., Van Der Helm, F. C. T., Veeger, H. E. J., Makhsous, M., Van Roy, P., Anglin, C., … Buchholz, B. (2005). ISB recommendation on definitions of joint coordinate systems of various joints for the reporting of human joint motion - Part II: Shoulder, elbow, wrist and hand. *Journal of Biomechanics*, *38*(5), 981–992. https://doi.org/10.1016/j.jbiomech.2004.05.042

Yamamoto, N., Itoi, E., Abe, H., Minagawa, H., Seki, N., Shimada, Y., & Okada, K. (2007). Contact between the glenoid and the humeral head in abduction, external rotation, and horizontal extension: A new concept of glenoid track. *Journal of Shoulder and Elbow Surgery*, *16*(5), 649–656. https://doi.org/10.1016/j.jse.2006.12.012

Yongpravat, C., Lester, J. D., Saifi, C., Trubelja, A., Greiwe, R. M., Bigliani, L. U., … Ahmad, C. S. (2013a). Glenoid morphology after reaming in computer-simulated total shoulder arthroplasty. *Journal of Shoulder and Elbow Surgery*, *22*(1), 122–128. https://doi.org/10.1016/j.jse.2011.12.010

Yongpravat, C., Mike Kim, H., Gardner, T. R., Bigliani, L. U., Levine, W. N., & Ahmad, C. S. (2013b). Glenoid implant orientation and cement failure in total shoulder arthroplasty: a finite element analysis. *Journal of Shoulder and Elbow Surgery*, *22(7)*, 940–947. https://doi.org/10.1016/j.jse.2012.09.007

Zarifi, O., & Stavness, I. (2016). Computer Methods in Biomechanics and Biomedical Engineering Muscle wrapping on arbitrary meshes with the heat method Muscle wrapping on arbitrary meshes with the heat method. *COMPUTER METHODS IN BIOMECHANICS AND BIOMEDICAL ENGINEERING*, 1–11. https://doi.org/10.1080/10255842.2016.1205043

Zhang, J., Yongpravat, C., Mike Kim, H., Levine, W. N., Bigliani, L. U., Gardner, T. R., & Ahmad, C. S. (2013). Glenoid articular conformity affects stress distributions in total shoulder arthroplasty. *Journal of Shoulder and Elbow Surgery*, *22*, 350–356. https://doi.org/10.1016/j.jse.2012.08.025

Zhang, Q., Shi, L. L., Ravella, K. C., Koh, J. L., Wang, S., Liu, C., … Wang, J. (2016). Distinct Proximal Humeral Geometry in Chinese. *J Bone Joint Surg Am*, *98*(207), 2071–2081. https://doi.org/http://dx.doi.org/10.2106/JBJS.15.01232

Zimmer. (2009). Anatomical Shoulder System STM, *2*.

Zumstein, V., Kraljević, M., Hoechel, S., Conzen, A., Nowakowski, A. M., & Müller-Gerbl, M. (2014). The glenohumeral joint - a mismatching system? A morphological analysis of the cartilaginous and osseous curvature of the humeral head and the glenoid cavity. *Journal of Orthopaedic Surgery and Research*, *9*(1), 1–6. https://doi.org/10.1186/1749-799X-9-34

Appendix A – MATLAB script for measuring GH morphometry

```
clc;
clear all;
close all;

fid = fopen ('014_Left_Head_1.stl', 'r');

if fid == -1
    error('Error opening file');
end

vnum=0;       %Vertex number counter.
report_num=0; %Report the status as we go.
VColor = 0;

while feof(fid) == 0                    % test for end of file, if not then
do stuff
    tline = fgetl(fid);                 % reads a line of data from file.
    fword = sscanf(tline, '%s ');       % make the line a character string
% Check for color
    if strncmpi(fword, 'c',1) == 1;     % Checking if a "C"olor line, as "C"
is 1st char.
       VColor = sscanf(tline, '%*s %f %f %f'); % & if a C, get the RGB
color data of the face.
    end                                 % Keep this color, until the next
color is used.
    if strncmpi(fword, 'v',1) == 1;     % Checking if a "V"ertex line, as
"V" is 1st char.
       vnum = vnum + 1;                 % If a V we count the # of V's
       report_num = report_num + 1;     % Report a counter, so long files
show status
       if report_num > 249;
           disp(sprintf('Reading vertix num: %d.',vnum));
           report_num = 0;
       end
       v(:,vnum) = sscanf(tline, '%*s %f %f %f'); % & if a V, get the XYZ
data of it.
       c(:,vnum) = VColor;              % A color for each vertex, which
will color the faces.
    end                                 % we "*s" skip the name "color" and
get the data.
end
%   Build face list; The vertices are in order, so just number them.

fnum = vnum/3;      %Number of faces, vnum is number of vertices.  STL is
triangles.
flist = 1:vnum;     %Face list of vertices, all in order.
F = reshape(flist,3,fnum); %Make a "3 by fnum" matrix of face list data.

%Return the faces and vertexs.

fout = F';  %Orients the array for direct use in patch.
```

```
vout = v';
cout = c';

fclose(fid);

F = fout;
V = vout*1000;
C = cout;

p = patch('faces',F, 'vertices',V);
set(p, 'facec', 'c');                % Set the face color (force it)
set(p, 'facec', [0.1 0.5 0.9]);            % Set the face color flat
set(p, 'FaceVertexCData', C);        % Set the color (from file)
set(p, 'facealpha',0.25);               % Use for transparency
set(p, 'EdgeColor','none');          % Set the edge color
%set(p, 'EdgeColor',[0.9 0.5 0.1]);         % Use to see triangles, if
needed.
set(p, 'Edgealpha',0.3);

light;                               % add a default light
daspect([1 1 1]);                    % Setting the aspect ratio
view(3);                             % Isometric view
xlabel('A-P_axis'),ylabel('S-I_axis'),zlabel('Height_axis');
title('Humeral Head');
drawnow;                             % axis manual
axis ([-30 30 -30 30 0 25]);
grid on;
hold on;
[rows,cols] = size(V);
disp(V);

% Sampling and Segmenting the head

x = 0; y = 0; z = 0; %creating the origin
plot3 (x,y,z,'k+','linewidth',8);

antpost = max(abs(V(:,1))); %scanning through the X-values A-P
ind = find(V == antpost | V== -antpost); %selects the highest value
irrespective of the sign
row = ind(1,1);
x1 = V(row,1);
y1 = V(row,2);
z1 = V(row,3);
%plot3 (x1,y1,z1,'ko');


supinf = max(abs(V(:,2)));%scanning through the Y-values S-I
ind = find(V == supinf | V == -supinf); %selects the highest value
irrespective of the sign
row = ind(1,1)-rows;
x2 = V(row,1);
y2 = V(row,2);
z2 = V(row,3);
%plot3 (x2,y2,z2,'h');

height = max(abs(V(:,3))); %scanning through the Z-values Height
ind = find(V == height | V == -height); %selects the highest value
irrespective of the sign
```

```
row = ind(1,1)-(2*rows);
x3 = V(row,1);%center of the peak point
y3 = V(row,2);%center of the peak point
z3 = V(row,3);
plot3 (x3,y3,z3,'k*','linewidth',5);
plot (x3,y3, 'ro','linewidth',5);
stem3 (x3,y3,z3,'r-','linewidth',7);
box on;

xdiff = x3-0; %distance from the origin and peak - x-axis
ydiff = y3-0; %distance from the origin and peak - y-axis
disp(['separation from the origin = ',num2str(xdiff),',',num2str(ydiff)]);

disp(['height = ', num2str(height)]);
disp(['A-P = ', num2str(antpost)]);
disp(['S-I = ', num2str(supinf)]);

H = height;
Wap = antpost*2;
Wsi = supinf*2;

AP_RoC = [(H) + ((Wap*Wap)/(4*H))];
SI_RoC = [(H) + ((Wsi*Wsi)/(4*H))];

disp(['Anterior Posterior Circular RoC = ', num2str(AP_RoC)]);
disp(['Superior Inferior Circular RoC = ', num2str(SI_RoC)]);

% Draw an arc between AP-Peak
p1=[x1 y1 z1];
p2=[x3 y3 z3];

% Radius
R = (AP_RoC/2);

%Center
xc=x3;
yc=y3;
zc=height-R;

x=linspace(p1(1),p2(1),200);
y=linspace(p1(2),p2(2),200);
z=zc+sqrt((R^2)-((x-xc).^2)-((y-yc).^2));

%plot3(x,y,z, 'k-','linewidth',5);
%plot3(p1(1),p1(2),p1(3),'*','MarkerSize',10);
%plot3(p2(1),p2(2),p2(3),'*','MarkerSize',10);
%plot3(xc,yc,zc,'*','MarkerSize',10);

% Draw an arc between SI-Peak
p1=[x2 y2 z2];
p2=[x3 y3 z3];

% Radius
R = (SI_RoC/2);

%Center
xc=0;
```

```
yc=0;
zc=height-R;

x=linspace(p1(1),p2(1),200);
y=linspace(p1(2),p2(2),200);
z=zc+sqrt((R^2)-((x-xc).^2)-((y-yc).^2));

%plot3(x,y,z, 'c-','linewidth',5);
%plot3(x,-y,z, 'c-','linewidth',5);
%plot3(p1(1),p1(2),p1(3),'*','MarkerSize',10);
%plot3(p2(1),p2(2),p2(3),'*','MarkerSize',10);
%plot3(xc,yc,zc,'*','MarkerSize',10);

%figure;
%subplot(2,1,1);
%plot (V(:,2),V(:,3));
%xlabel('S-I axis');
%ylabel('Height');

%subplot(2,1,2);
%plot (V(:,1),V(:,3));
%xlabel('A-P axis');
%ylabel('Height');

A = V(:,1); %x values
B = V(:,2); %y values
C = V(:,3); %z values
j = 1;
D(j) = 0;
D1 = 0;
D2 = 0;

%if (rows >= 8000)
    %for i=1:2:rows
        %if (A(i)<=1 && A(i)>=-1)
            %D(j) = C(i);
            %hold on;
            %if (B(i)>y3)
                %D1 = D1+D(j);
                %stem3 (A(i),B(i),C(i), 'b-');
            %else
                %D2 = D2+D(j);
                %stem3 (A(i),B(i),C(i), 'k-');
            %end
        %j = j+1;
        %end
    %end
%else
 %      for i=1:1:rows
        %if (A(i)<=1 && A(i)>=-1)
  %          D(j) = C(i);
   %         hold on;
    %        if (B(i)>y3)
     %           D1 = D1+D(j);
      %          %stem3 (A(i),B(i),C(i), 'b-');
       %     else
        %        D2 = D2+D(j);
                %stem3 (A(i),B(i),C(i), 'k-');
         %   end
```

```
      %  j = j+1;
        %end
    %end
%end

%F = D1/D2;
%disp (F);
s = 0;
t = 0;
r = 0;
l1 = 0;
l2 = 0;
for i = 1:1:rows
    if (C(i) <= 0)
        s = supinf - Wsi/4;
        if (B(i) >= s-10 && B(i)<= s+10)
            r = r+1;
            l1(r) = 2*A(i);
            %plot3 (A(i), B(i), C(i), 'k*');
        end
    end
end

if (r>1)
    for i = 0:1:r
        t = t+l1(r);
    end
end
L = t/(r-1);
F = Wap/abs(L);
```

Appendix B – Quantile-Quantile for plots all data sets

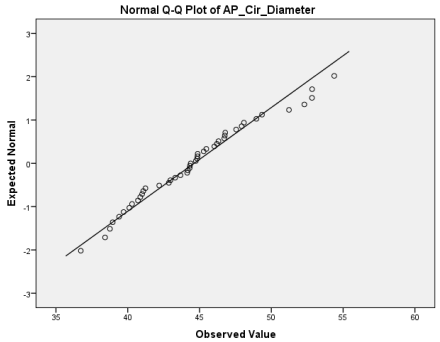

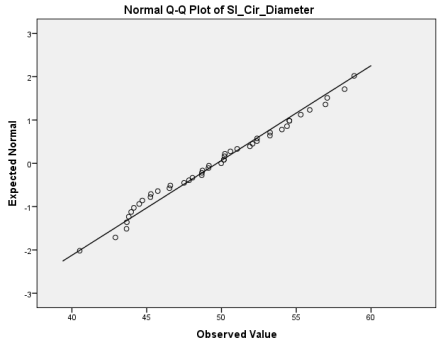

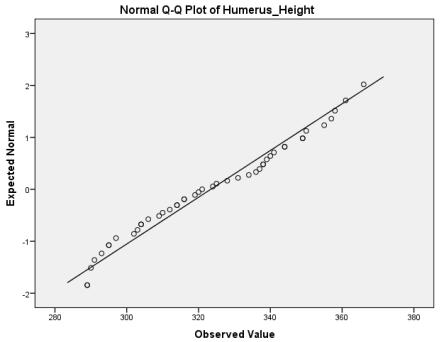

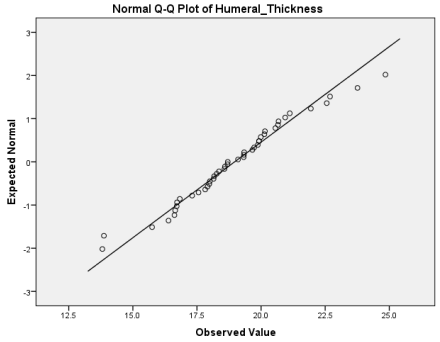

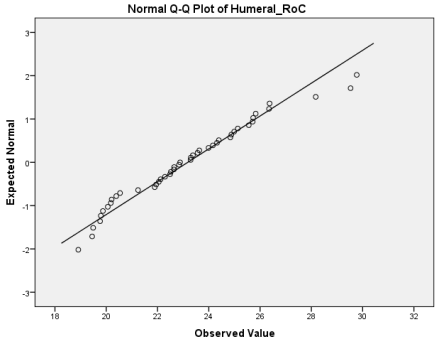

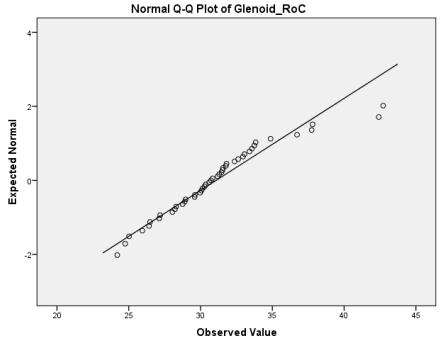

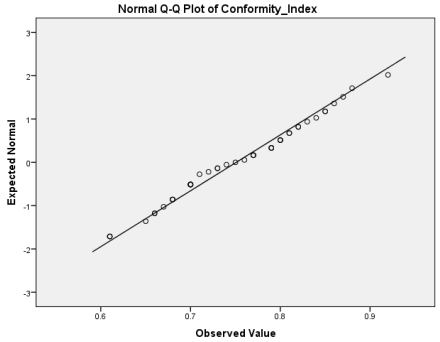

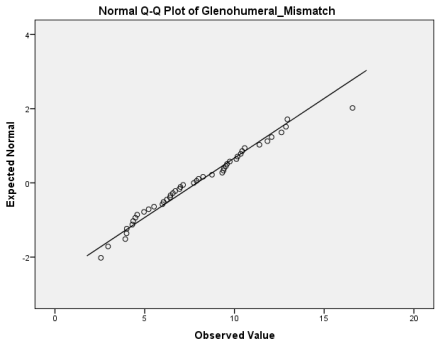

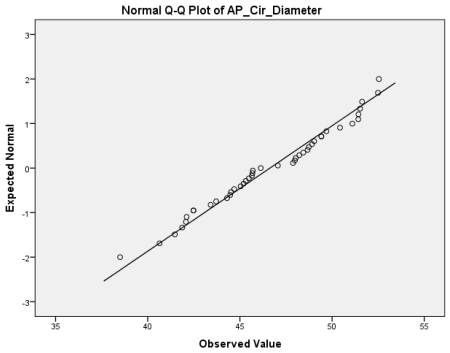
Normal Q-Q Plot of AP_Cir_Diameter
Expected Normal
Observed Value

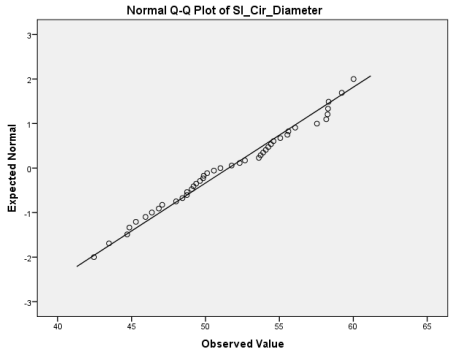
Normal Q-Q Plot of SI_Cir_Diameter
Expected Normal
Observed Value

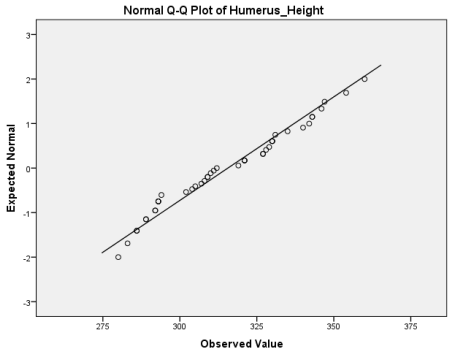
Normal Q-Q Plot of Humerus_Height
Expected Normal
Observed Value

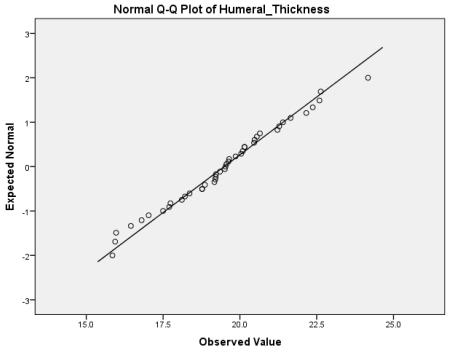
Normal Q-Q Plot of Humeral_Thickness
Expected Normal
Observed Value

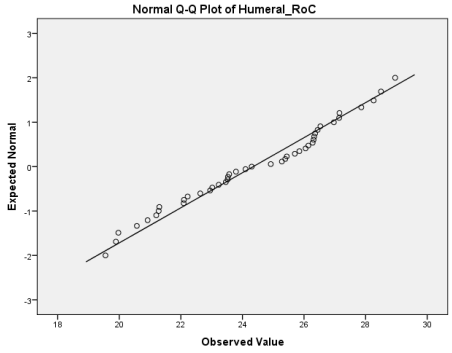
Normal Q-Q Plot of Humeral_RoC
Expected Normal
Observed Value

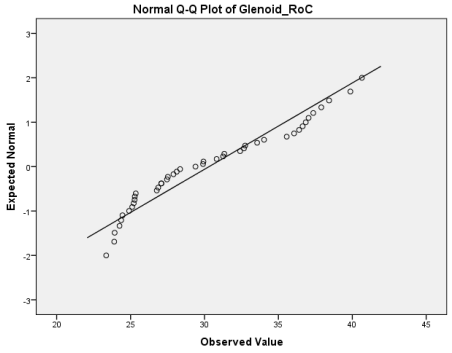
Normal Q-Q Plot of Glenoid_RoC
Expected Normal
Observed Value

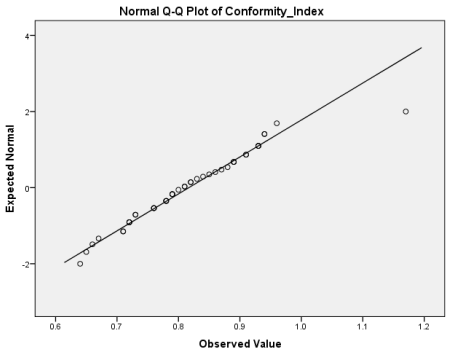
Normal Q-Q Plot of Conformity_Index
Expected Normal
Observed Value

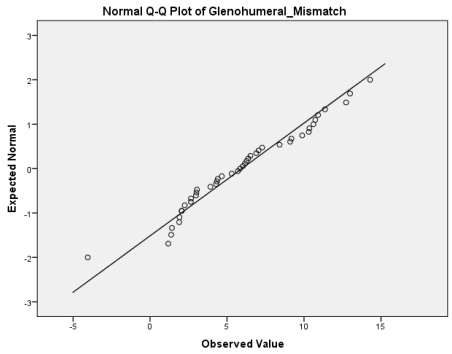
Normal Q-Q Plot of Glenohumeral_Mismatch
Expected Normal
Observed Value

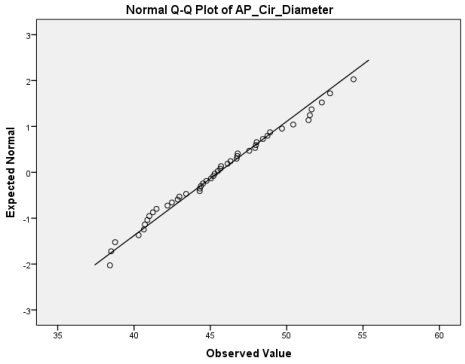
Normal Q-Q Plot of AP_Cir_Diameter
Expected Normal
Observed Value

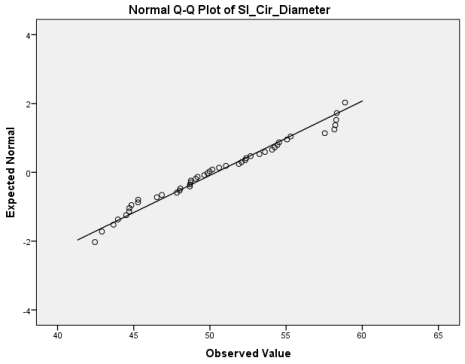
Normal Q-Q Plot of SI_Cir_Diameter
Expected Normal
Observed Value

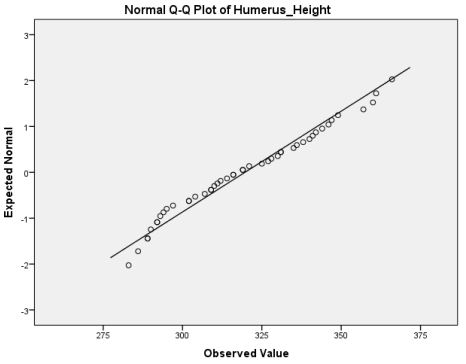
Normal Q-Q Plot of Humerus_Height
Expected Normal
Observed Value

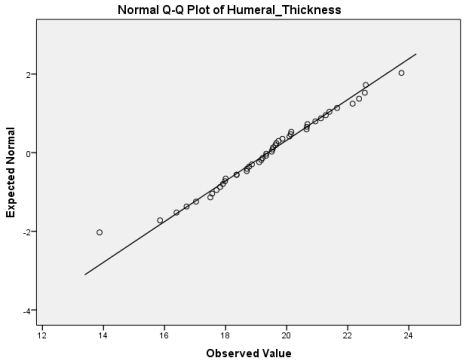
Normal Q-Q Plot of Humeral_Thickness
Expected Normal
Observed Value

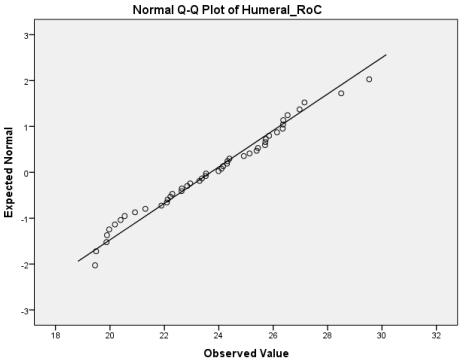
Normal Q-Q Plot of Humeral_RoC
Expected Normal
Observed Value

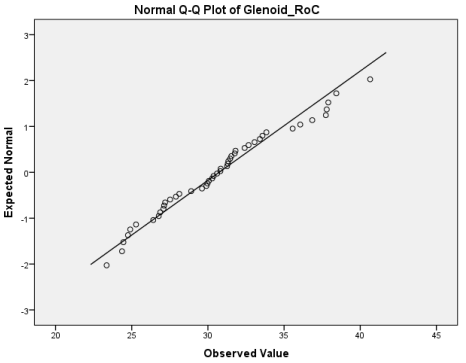
Normal Q-Q Plot of Glenoid_RoC
Expected Normal
Observed Value

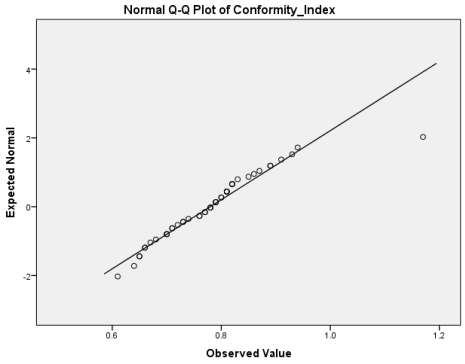
Normal Q-Q Plot of Conformity_Index
Expected Normal
Observed Value

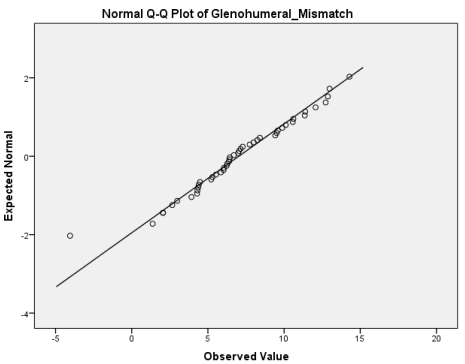
Normal Q-Q Plot of Glenohumeral_Mismatch
Expected Normal
Observed Value

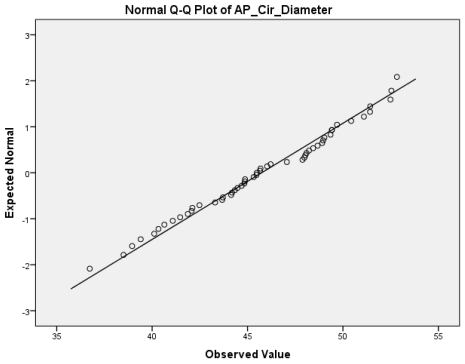
Normal Q-Q Plot of AP_Cir_Diameter
Expected Normal
Observed Value

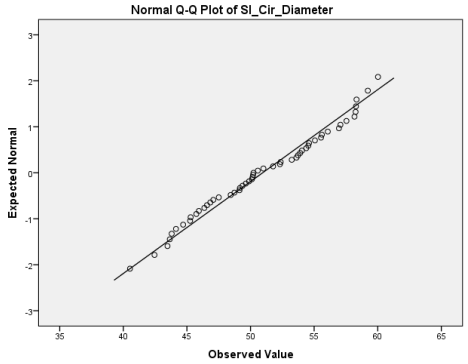
Normal Q-Q Plot of SI_Cir_Diameter
Expected Normal
Observed Value

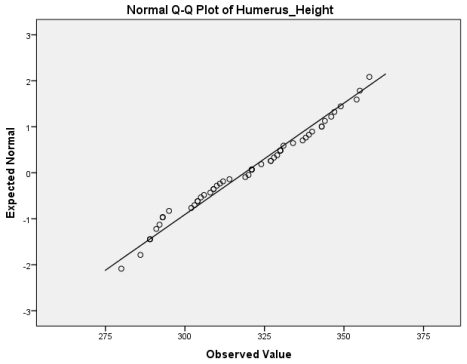
Normal Q-Q Plot of Humerus_Height
Expected Normal
Observed Value

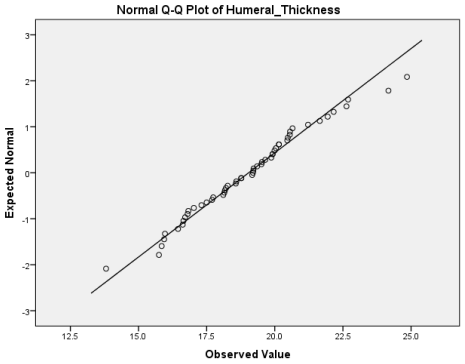
Normal Q-Q Plot of Humeral_Thickness
Expected Normal
Observed Value

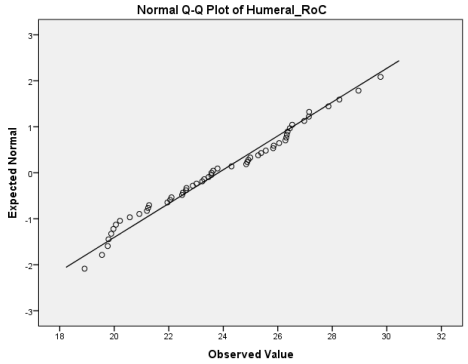
Normal Q-Q Plot of Humeral_RoC
Expected Normal
Observed Value

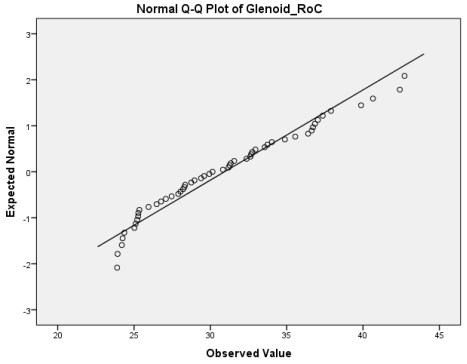
Normal Q-Q Plot of Glenoid_RoC
Expected Normal
Observed Value

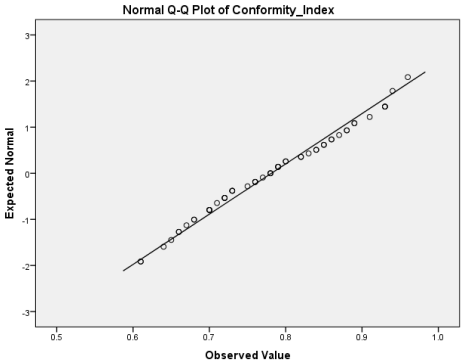
Normal Q-Q Plot of Conformity_Index
Expected Normal
Observed Value

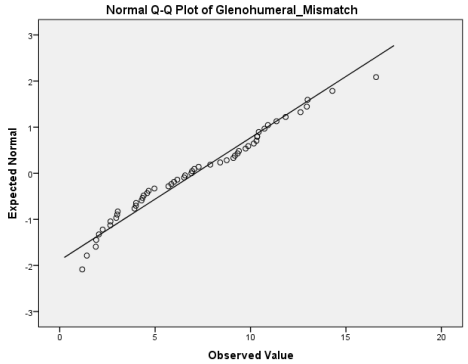
Normal Q-Q Plot of Glenohumeral_Mismatch
Expected Normal
Observed Value

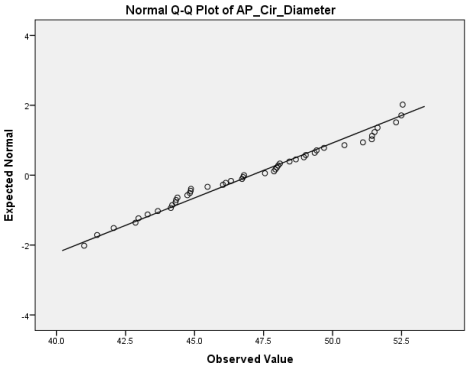
Normal Q-Q Plot of AP_Cir_Diameter
Expected Normal
Observed Value

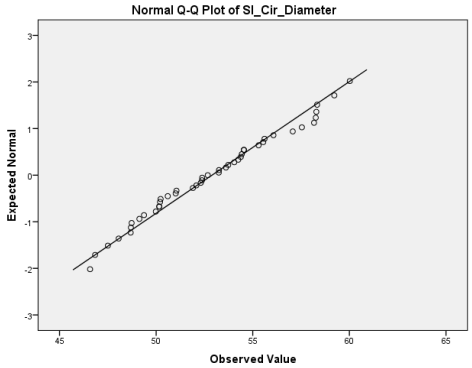
Normal Q-Q Plot of SI_Cir_Diameter
Expected Normal
Observed Value

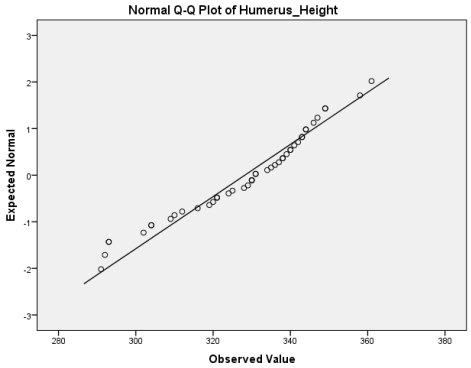
Normal Q-Q Plot of Humerus_Height
Expected Normal
Observed Value

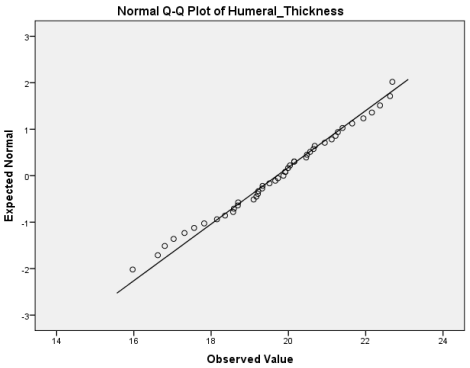
Normal Q-Q Plot of Humeral_Thickness
Expected Normal
Observed Value

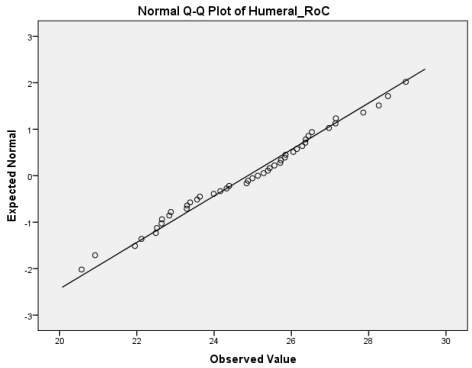
Normal Q-Q Plot of Humeral_RoC
Expected Normal
Observed Value

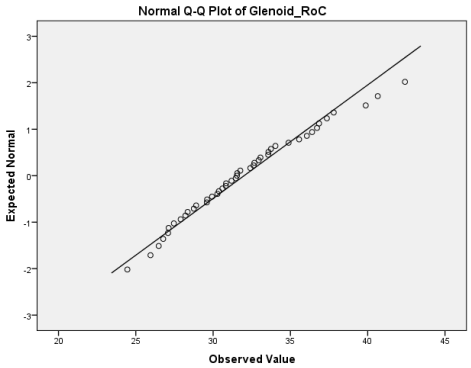
Normal Q-Q Plot of Glenoid_RoC
Expected Normal
Observed Value

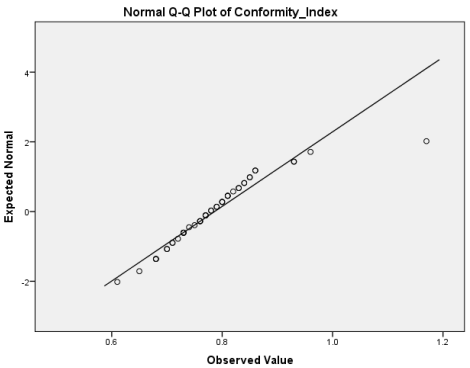
Normal Q-Q Plot of Conformity_Index
Expected Normal
Observed Value

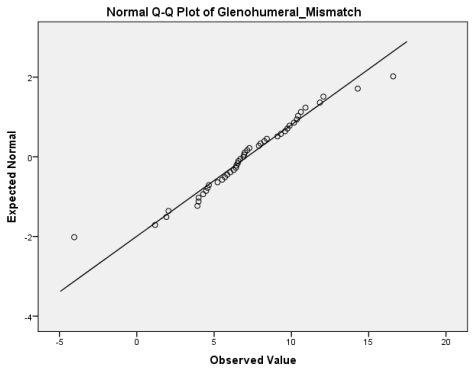
Normal Q-Q Plot of Glenohumeral_Mismatch
Expected Normal
Observed Value

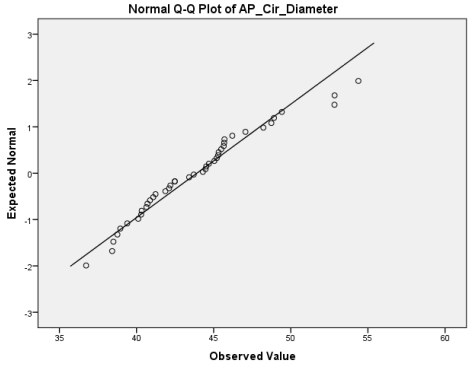
Normal Q-Q Plot of AP_Cir_Diameter
Expected Normal
Observed Value

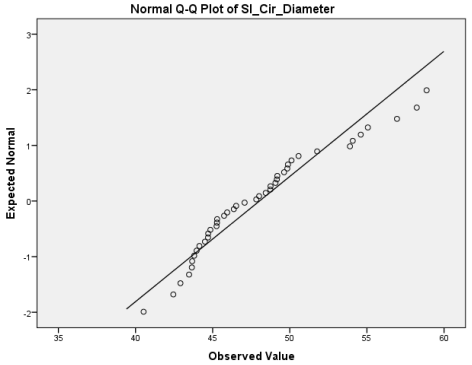
Normal Q-Q Plot of SI_Cir_Diameter
Expected Normal
Observed Value

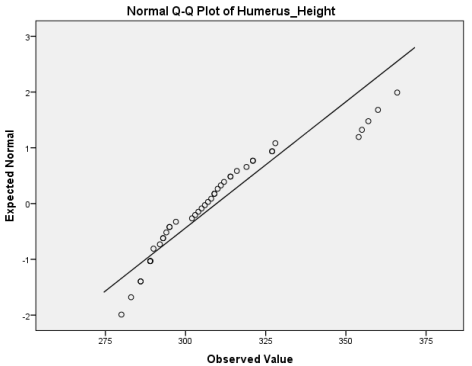
Normal Q-Q Plot of Humerus_Height
Expected Normal
Observed Value

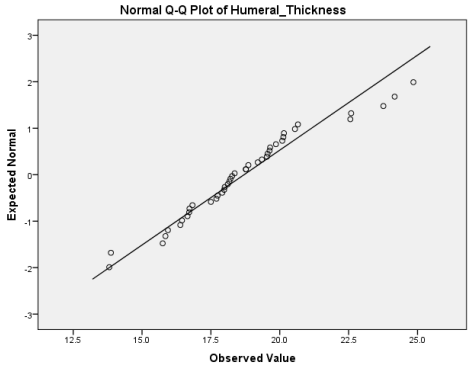
Normal Q-Q Plot of Humeral_Thickness
Expected Normal
Observed Value

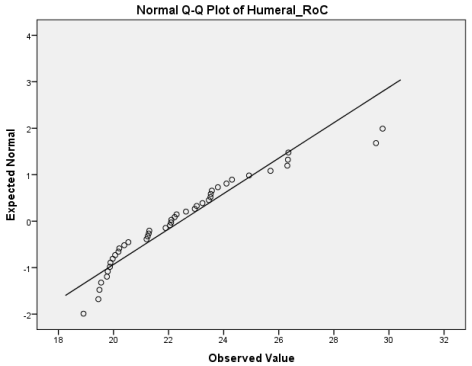
Normal Q-Q Plot of Humeral_RoC
Expected Normal
Observed Value

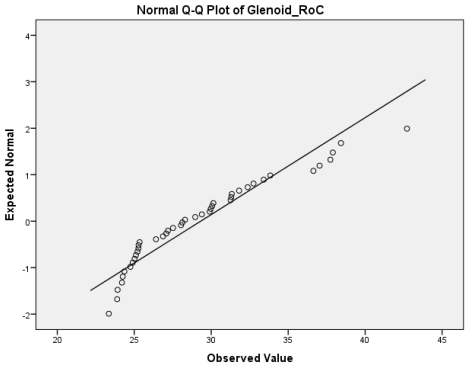
Normal Q-Q Plot of Glenoid_RoC
Expected Normal
Observed Value

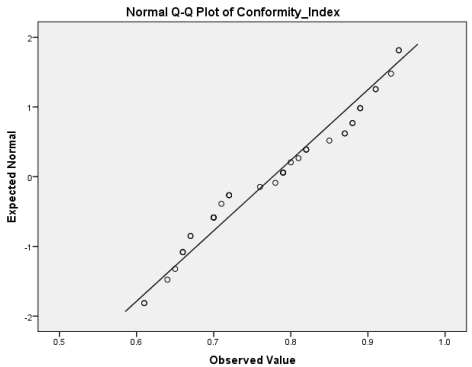
Normal Q-Q Plot of Conformity_Index
Expected Normal
Observed Value

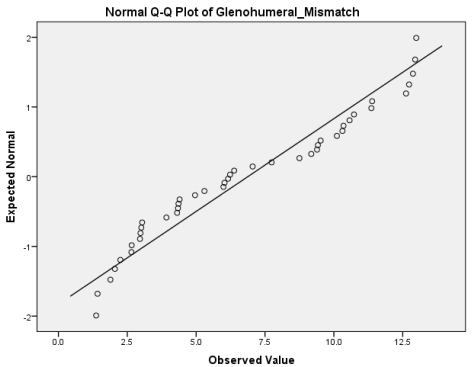
Normal Q-Q Plot of Glenohumeral_Mismatch
Expected Normal
Observed Value

Appendix C – Background code to generate the control OpenSim shoulder model

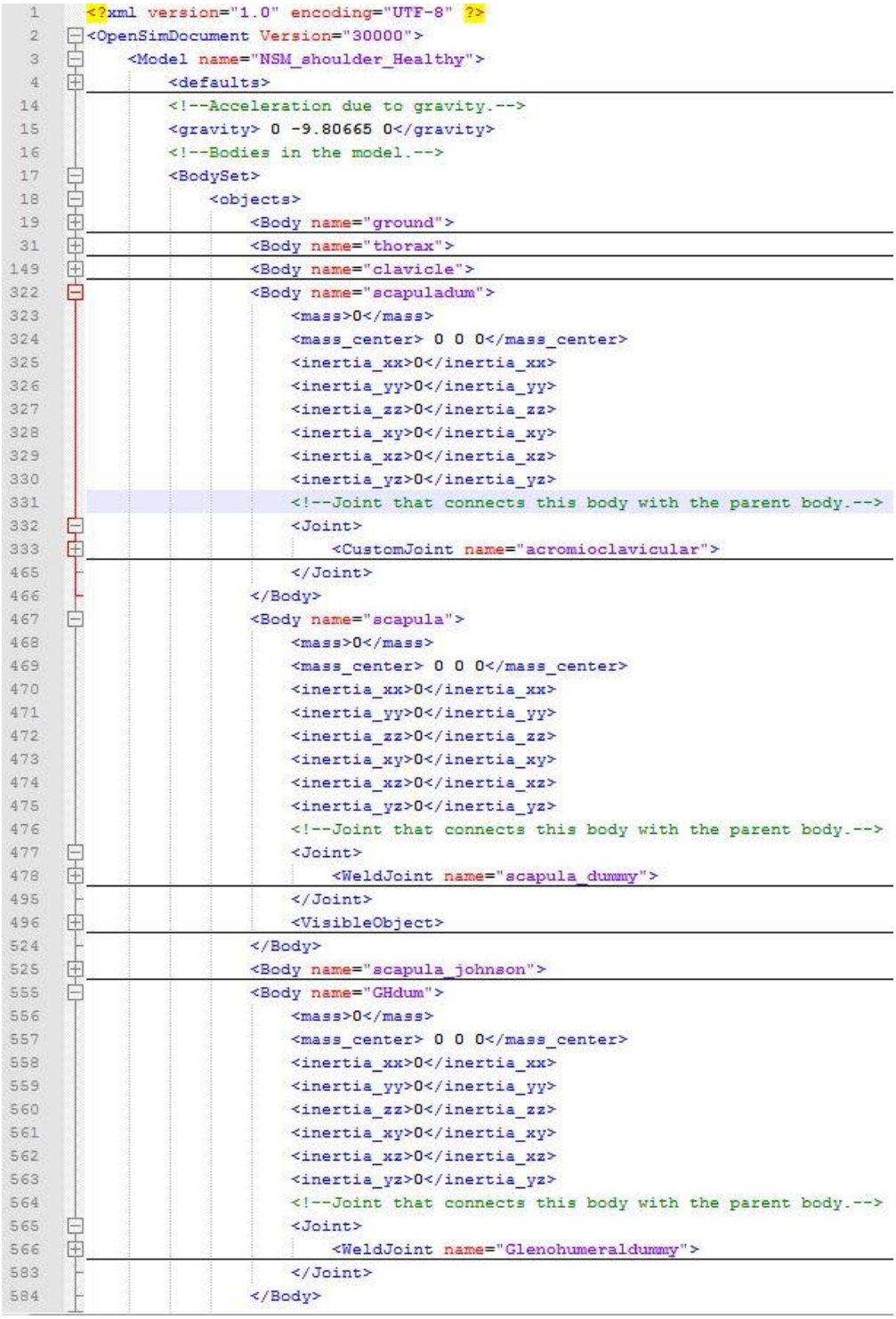

```
<?xml version="1.0" encoding="UTF-8" ?>
<OpenSimDocument Version="30000">
    <Model name="NSM_shoulder_Healthy">
        <defaults>
        <!--Acceleration due to gravity.-->
        <gravity> 0 -9.80665 0</gravity>
        <!--Bodies in the model.-->
        <BodySet>
            <objects>
                <Body name="ground">
                <Body name="thorax">
                <Body name="clavicle">
                <Body name="scapuladum">
                    <mass>0</mass>
                    <mass_center> 0 0 0</mass_center>
                    <inertia_xx>0</inertia_xx>
                    <inertia_yy>0</inertia_yy>
                    <inertia_zz>0</inertia_zz>
                    <inertia_xy>0</inertia_xy>
                    <inertia_xz>0</inertia_xz>
                    <inertia_yz>0</inertia_yz>
                    <!--Joint that connects this body with the parent body.-->
                    <Joint>
                        <CustomJoint name="acromioclavicular">
                    </Joint>
                </Body>
                <Body name="scapula">
                    <mass>0</mass>
                    <mass_center> 0 0 0</mass_center>
                    <inertia_xx>0</inertia_xx>
                    <inertia_yy>0</inertia_yy>
                    <inertia_zz>0</inertia_zz>
                    <inertia_xy>0</inertia_xy>
                    <inertia_xz>0</inertia_xz>
                    <inertia_yz>0</inertia_yz>
                    <!--Joint that connects this body with the parent body.-->
                    <Joint>
                        <WeldJoint name="scapula_dummy">
                    </Joint>
                    <VisibleObject>
                </Body>
                <Body name="scapula_johnson">
                <Body name="GHdum">
                    <mass>0</mass>
                    <mass_center> 0 0 0</mass_center>
                    <inertia_xx>0</inertia_xx>
                    <inertia_yy>0</inertia_yy>
                    <inertia_zz>0</inertia_zz>
                    <inertia_xy>0</inertia_xy>
                    <inertia_xz>0</inertia_xz>
                    <inertia_yz>0</inertia_yz>
                    <!--Joint that connects this body with the parent body.-->
                    <Joint>
                        <WeldJoint name="Glenohumeraldummy">
                    </Joint>
                </Body>
```

```
<?xml version="1.0" encoding="UTF-8" ?>
<OpenSimDocument Version="30000">
    <Model name="NSM_shoulder_Healthy">
        <defaults>
        <!--Acceleration due to gravity.-->
        <gravity> 0 -9.80665 0</gravity>
        <!--Bodies in the model.-->
        <BodySet>
            <objects>
                <Body name="ground">
                <Body name="thorax">
                <Body name="clavicle">
                <Body name="scapuladum">
                    <mass>0</mass>
                    <mass_center> 0 0 0</mass_center>
                    <inertia_xx>0</inertia_xx>
                    <inertia_yy>0</inertia_yy>
                    <inertia_zz>0</inertia_zz>
                    <inertia_xy>0</inertia_xy>
                    <inertia_xz>0</inertia_xz>
                    <inertia_yz>0</inertia_yz>
                    <!--Joint that connects this body with the parent body.-->
                    <Joint>
                        <CustomJoint name="acromioclavicular">
                    </Joint>
                </Body>
                <Body name="scapula">
                    <mass>0</mass>
                    <mass_center> 0 0 0</mass_center>
                    <inertia_xx>0</inertia_xx>
                    <inertia_yy>0</inertia_yy>
                    <inertia_zz>0</inertia_zz>
                    <inertia_xy>0</inertia_xy>
                    <inertia_xz>0</inertia_xz>
                    <inertia_yz>0</inertia_yz>
                    <!--Joint that connects this body with the parent body.-->
                    <Joint>
                        <WeldJoint name="scapula_dummy">
                    </Joint>
                    <VisibleObject>
                </Body>
                <Body name="scapula_johnson">
                <Body name="GHdum">
                    <mass>0</mass>
                    <mass_center> 0 0 0</mass_center>
                    <inertia_xx>0</inertia_xx>
                    <inertia_yy>0</inertia_yy>
                    <inertia_zz>0</inertia_zz>
                    <inertia_xy>0</inertia_xy>
                    <inertia_xz>0</inertia_xz>
                    <inertia_yz>0</inertia_yz>
                    <!--Joint that connects this body with the parent body.-->
                    <Joint>
                        <WeldJoint name="Glenohumeraldummy">
                    </Joint>
                </Body>
```

```
1241        <ForceSet>
1242            <objects>
1243                <Schutte1993Muscle_Deprecated name="Bicep_Short_Humerus">
1293                <Schutte1993Muscle_Deprecated name="Trapezius_SN">
1335                <Schutte1993Muscle_Deprecated name="Trapezius_OC_C3">
1377                <Schutte1993Muscle_Deprecated name="Trapezius_C3_C6">
1419                <Schutte1993Muscle_Deprecated name="Trapezius_C7">
1470                <Schutte1993Muscle_Deprecated name="Trapezius_T1">
1521                <Schutte1993Muscle_Deprecated name="Trapezius_T2">
1572                <Schutte1993Muscle_Deprecated name="Trapezius_T3">
1623                <Schutte1993Muscle_Deprecated name="Trapezius_T4">
1674                <Schutte1993Muscle_Deprecated name="Trapezius_T5">
1725                <Schutte1993Muscle_Deprecated name="Trapezius_T6">
1776                <Schutte1993Muscle_Deprecated name="Trapezius_T7">
1827                <Schutte1993Muscle_Deprecated name="Trapezius_T8">
1878                <Schutte1993Muscle_Deprecated name="Trapezius_T9">
1929                <Schutte1993Muscle_Deprecated name="Trapezius_T10">
1980                <Schutte1993Muscle_Deprecated name="Trapezius_T11">
2031                <Schutte1993Muscle_Deprecated name="Trapezius_T12">
2082                <Schutte1993Muscle_Deprecated name="levator_scapulae_1">
2124                <Schutte1993Muscle_Deprecated name="levator_scapulae_2">
2166                <Schutte1993Muscle_Deprecated name="levator_scapulae_3">
2208                <Schutte1993Muscle_Deprecated name="levator_scapulae_4">
2250                <Schutte1993Muscle_Deprecated name="rhomboid_minor_C6">
2292                <Schutte1993Muscle_Deprecated name="rhomboid_minor_C7">
2334                <Schutte1993Muscle_Deprecated name="rhomboid_major_T1">
2376                <Schutte1993Muscle_Deprecated name="rhomboid_major_T2">
2418                <Schutte1993Muscle_Deprecated name="rhomboid_major_T3">
2460                <Schutte1993Muscle_Deprecated name="rhomboid_major_T4">
2502                <Schutte1993Muscle_Deprecated name="rhomboid_major_T5">
2544                <Schutte1993Muscle_Deprecated name="serratus_anterior_1">
2595                <Schutte1993Muscle_Deprecated name="serratus_anterior_2">
2646                <Schutte1993Muscle_Deprecated name="serratus_anterior_3">
2697                <Schutte1993Muscle_Deprecated name="serratus_anterior_4">
2748                <Schutte1993Muscle_Deprecated name="serratus_anterior_5">
2799                <Schutte1993Muscle_Deprecated name="serratus_anterior_6">
2850                <Schutte1993Muscle_Deprecated name="serratus_anterior_7">
2901                <Schutte1993Muscle_Deprecated name="serratus_anterior_8">
2952                <Schutte1993Muscle_Deprecated name="serratus_anterior_9">
3003                <Schutte1993Muscle_Deprecated name="pectoralis_minor_1">
3045                <Schutte1993Muscle_Deprecated name="pectoralis_minor_2">
3087                <Schutte1993Muscle_Deprecated name="pectoralis_minor_3">
3129                <Schutte1993Muscle_Deprecated name="latissimus_dorsi_1">
3180                <Schutte1993Muscle_Deprecated name="latissimus_dorsi_2">
3231                <Schutte1993Muscle_Deprecated name="latissimus_dorsi_3">
3282                <Schutte1993Muscle_Deprecated name="latissimus_dorsi_4">
3333                <Schutte1993Muscle_Deprecated name="latissimus_dorsi_5">
3384                <Schutte1993Muscle_Deprecated name="pectoralis_major_clavicular_1">
3426                <Schutte1993Muscle_Deprecated name="pectoralis_major_clavicular_2">
3477                <Schutte1993Muscle_Deprecated name="pectoralis_major_clavicular_3">
3528                <Schutte1993Muscle_Deprecated name="pectoralis_major_clavicular_4">
3579                <Schutte1993Muscle_Deprecated name="pectoralis_major_clavicular_5">
3630                <Schutte1993Muscle_Deprecated name="pectoralis_major_thoracic_1">
3681                <Schutte1993Muscle_Deprecated name="pectoralis_major_thoracic_2">
3732                <Schutte1993Muscle_Deprecated name="pectoralis_major_thoracic_3">
3783                <Schutte1993Muscle_Deprecated name="pectoralis_major_thoracic_4">
```

```
3834                <Schutte1993Muscle_Deprecated name="pectoralis_major_thoracic_5">
3885                <Schutte1993Muscle_Deprecated name="deltoid_anterior_1">
3933                <Schutte1993Muscle_Deprecated name="deltoid_anterior_2">
3981                <Schutte1993Muscle_Deprecated name="deltoid_middle">
4029                <Schutte1993Muscle_Deprecated name="deltoid_posterior_1">
4077                <Schutte1993Muscle_Deprecated name="deltoid_posterior_2">
4125                <Schutte1993Muscle_Deprecated name="supraspinatus">
4175                <Schutte1993Muscle_Deprecated name="infraspinatus_1">
4225                <Schutte1993Muscle_Deprecated name="infraspinatus_2">
4275                <Schutte1993Muscle_Deprecated name="infraspinatus_3">
4325                <Schutte1993Muscle_Deprecated name="subscapularis_1">
4375                <Schutte1993Muscle_Deprecated name="subscapularis_2">
4425                <Schutte1993Muscle_Deprecated name="subscapularis_3">
4475                <Schutte1993Muscle_Deprecated name="teres_minor">
4525                <Schutte1993Muscle_Deprecated name="teres_major">
4567                <Schutte1993Muscle_Deprecated name="coracobrachialis_1">
4609                <Schutte1993Muscle_Deprecated name="coracobrachialis_2">
4651                <Schutte1993Muscle_Deprecated name="bicep_short">
4701                <Schutte1993Muscle_Deprecated name="bicep_long_2">
4763                <Schutte1993Muscle_Deprecated name="tricep_long_1">
4813                <Schutte1993Muscle_Deprecated name="tricep_long_2">
4863                <Schutte1993Muscle_Deprecated name="tricep_med_1">
4913                <Schutte1993Muscle_Deprecated name="tricep_med_2">
4963                <Schutte1993Muscle_Deprecated name="tricep_lat_1">
5013                <Schutte1993Muscle_Deprecated name="tricep_lat_2">
5063                <Schutte1993Muscle_Deprecated name="brachialis_1">
5113                <Schutte1993Muscle_Deprecated name="brachialis_2">
5163                <Schutte1993Muscle_Deprecated name="anconeus_1">
5205                <Schutte1993Muscle_Deprecated name="anconeus_2">
5247                <Schutte1993Muscle_Deprecated name="brachioradialis_1">
5297                <Schutte1993Muscle_Deprecated name="brachioradialis_2">
5347                <Schutte1993Muscle_Deprecated name="supinator_humeral_head">
5397                <Schutte1993Muscle_Deprecated name="supinator_ulnar_head_1">
5447                <Schutte1993Muscle_Deprecated name="supinator_ulnar_head_2">
5497                <Schutte1993Muscle_Deprecated name="pronator_teres_humeral_head_1">
5547                <Schutte1993Muscle_Deprecated name="pronator_teres_humeral_head_2">
5597                <Schutte1993Muscle_Deprecated name="pronator_teres_ulnar_head_1">
5647                <Schutte1993Muscle_Deprecated name="pronator_teres_ulnar_head_2">
5697                <Schutte1993Muscle_Deprecated name="pronator_quadratus_1">
5739                <Schutte1993Muscle_Deprecated name="pronator_quadratus_2">
5781                <Schutte1993Muscle_Deprecated name="l_costoclavicular">
5823                <Schutte1993Muscle_Deprecated name="l_conoid">
5865                <Schutte1993Muscle_Deprecated name="l_trapezoid">
5907            </objects>
5908            <groups>
5949        </ForceSet>
5950        <!--Markers in the model.-->
5951        <MarkerSet>
5952            <objects />
5953        </MarkerSet>
5954    </Model>
5955</OpenSimDocument>
```

Appendix D – MATLAB script to calculate the rotational matrix of the prosthesis

```
% Mimics.Output: output1
% Mimics.Input: input1, input2, input3, input4

A = input1.Points;
B = input2.Points;
C = input3.Points;
D = input4.Points;

% Calculations:

AB = (A'-B');  % Glenoid frame Y-axis
CD = (C'-D');  % Glenoid frame Z-axis

T = [0;0;0;1];

Yg = AB/norm(AB);
Xg = cross(Yg,CD/norm(CD));
Zg = cross(Xg,Yg);

Xg = [Xg;0];
Yg = [Yg;0];
Zg = [Zg;0];

R = [Xg Yg Zg T]
Ri = [Xg Yg Zg]';
Angs = (RXYZSOLV(R)); % GS Angle Solve
Angs = Angs(1,1:3);
Angs_I = (RZYXSOLV(Ri));

output1 =
struct('Type','Mimics.Medcad.Point','Name','RotationAngle','Points',Angs);
```

Appendix E – Modiefied Background code to generate OpenSim TSA model

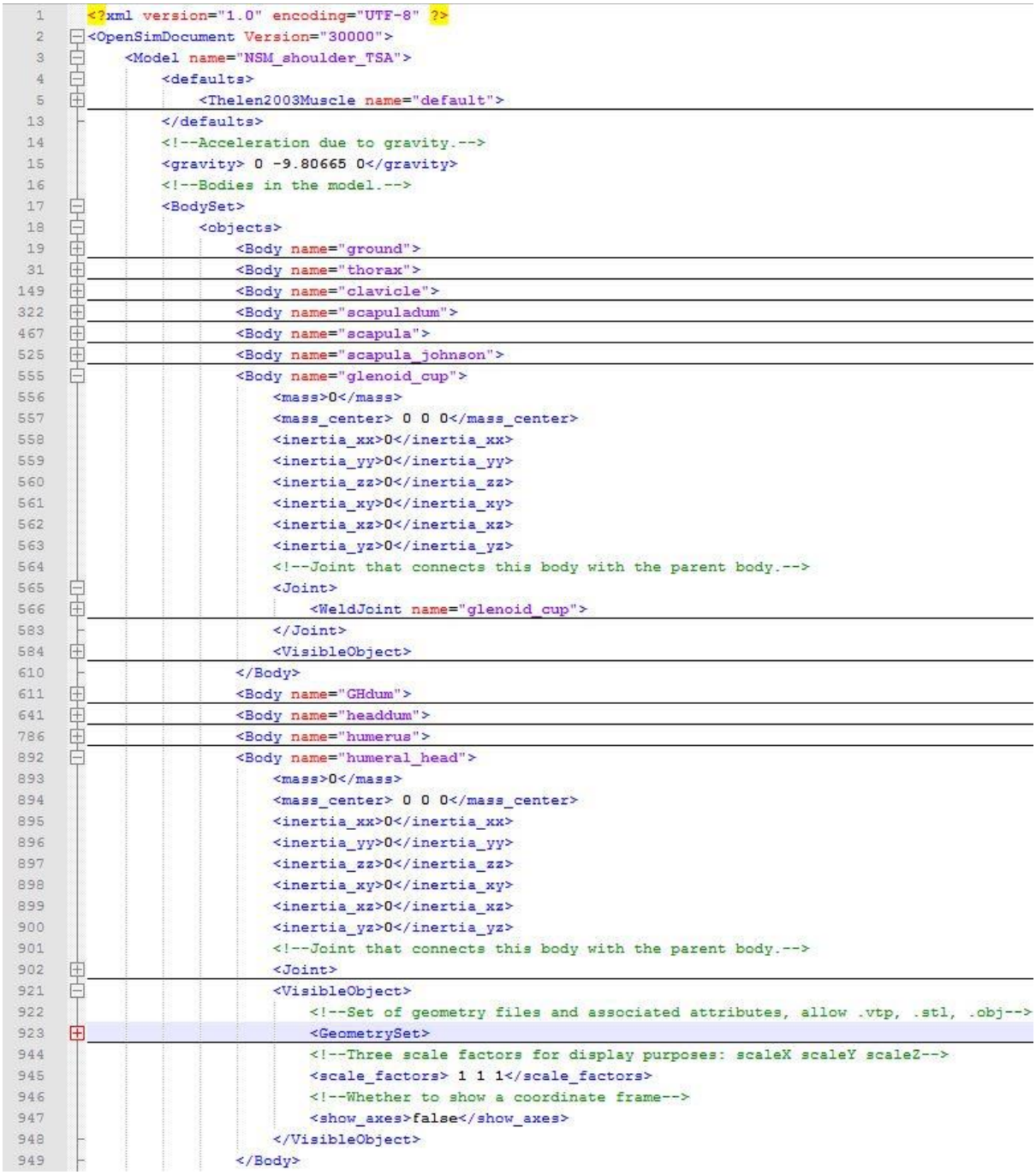

```
<?xml version="1.0" encoding="UTF-8" ?>
<OpenSimDocument Version="30000">
    <Model name="NSM_shoulder_TSA">
        <defaults>
            <Thelen2003Muscle name="default">
        </defaults>
        <!--Acceleration due to gravity.-->
        <gravity> 0 -9.80665 0</gravity>
        <!--Bodies in the model.-->
        <BodySet>
            <objects>
                <Body name="ground">
                <Body name="thorax">
                <Body name="clavicle">
                <Body name="scapuladum">
                <Body name="scapula">
                <Body name="scapula_johnson">
                <Body name="glenoid_cup">
                    <mass>0</mass>
                    <mass_center> 0 0 0</mass_center>
                    <inertia_xx>0</inertia_xx>
                    <inertia_yy>0</inertia_yy>
                    <inertia_zz>0</inertia_zz>
                    <inertia_xy>0</inertia_xy>
                    <inertia_xz>0</inertia_xz>
                    <inertia_yz>0</inertia_yz>
                    <!--Joint that connects this body with the parent body.-->
                    <Joint>
                        <WeldJoint name="glenoid_cup">
                    </Joint>
                    <VisibleObject>
                </Body>
                <Body name="GHdum">
                <Body name="headdum">
                <Body name="humerus">
                <Body name="humeral_head">
                    <mass>0</mass>
                    <mass_center> 0 0 0</mass_center>
                    <inertia_xx>0</inertia_xx>
                    <inertia_yy>0</inertia_yy>
                    <inertia_zz>0</inertia_zz>
                    <inertia_xy>0</inertia_xy>
                    <inertia_xz>0</inertia_xz>
                    <inertia_yz>0</inertia_yz>
                    <!--Joint that connects this body with the parent body.-->
                    <Joint>
                    <VisibleObject>
                        <!--Set of geometry files and associated attributes, allow .vtp, .stl, .obj-->
                        <GeometrySet>
                        <!--Three scale factors for display purposes: scaleX scaleY scaleZ-->
                        <scale_factors> 1 1 1</scale_factors>
                        <!--Whether to show a coordinate frame-->
                        <show_axes>false</show_axes>
                    </VisibleObject>
                </Body>
```

Appendix F – MATLAB script to induce motion and measure kinematic properties from OpenSim

```
clc
clear
close all
%% Initialisation:

% To 'install' the OpenSim API run the configureOpenSim.m
% Location: OpenSim installation directory (typically: C:\OpenSim
3.3\Scripts\Matlab)
% In this folder are other examples that may prove useful. Their associated
% tutorials can be found here: http://simtk-
confluence.stanford.edu:8080/display/OpenSim/Introduction+to+the+OpenSim+AP
I

import org.opensim.modeling.*
% imports all the opensim API functions into MATLAB. Required in any .m
% API functions reference:
https://simtk.org/api_docs/opensim/api_docs/index.html
    % On the side menu bar click on Classes -> Class List -> OpenSim for
    % the full list of available classes.

% Location of your OpenSim file:
modelPath = 'C:\Users\DYXROO001\Dropbox\Work\PhD\OpenS_pipelines\NSM_based
models for study\'; % laptop directory
modelFile = [modelPath,'NSM_shoulder_TSA_biradialglene.osim'];
%modelFile = [modelPath,'NSM_shoulder_TSA_biradialglene.osim'];
%modelFile = [modelPath,'NSM_shoulder_TSA_SWavg_40_15.osim'];
% < replace these strings with your own information >

osimModel = Model(modelFile); % this loads the model into MATLAB
state = osimModel.initSystem; % the current 'state' of the model

%% Basic API Utilisation:
% NB: OpenSim's API indexing start at 0, MATLAB's indexing starts at 1.
% middle deltoid

Nmusc_ant = 57;

muscles = osimModel.getMuscles(); % <show Class on website>
muscle = muscles.get(Nmusc_ant).getGeometryPath(); % get muscle geometry
path <show in Notepad++>

muscle_name = char(muscles.get(Nmusc_ant).getName()); % get muscle name

currentPath = muscle.getCurrentPath(state);
origin_M1 = currentPath.getitem(0).getLocation();
```

```
% This is equivalent to:
% origin_M2 =
osimModel.getMuscles().get(Nmusc).getGeometryPath().getCurrentPath(state).g
etitem(0).getLocation();

% Convert OpenSim vector into MATLAB vector:
origin_matlab = [origin_M1.get(0), origin_M1.get(1), origin_M1.get(2)];

% Convert MATLAB vector in OpenSim vector:
origin_osim =
ArrayDouble.createVec3(origin_matlab(1),origin_matlab(2),origin_matlab(3));

% Other variables we can extract about the muscle:
% Origin/Insertion Bodies:
BodySeg1 = muscle.getPathPointSet.get(0).getBody(); % origin body segement
BodySeg2 = muscle.getPathPointSet.get(1).getBody(); % insertion body
segment (for muscles with only 2 path points)

% Number of points along muscle path:
N = currentPath.getSize(); % For a regular muscle: 2 = no wrapping, 4 = 1
wrapping object, 6 = 2 wrapping objects

Origin = currentPath.get(0).getLocation();
MOrigin = [Origin.get(0), Origin.get(1), Origin.get(2)];
OriginBody = char(currentPath.get(0).getBodyName());

if N == 4

    WrapPt1 = currentPath.get(1).getLocation();
    MWrapPt1 = [WrapPt1.get(0), WrapPt1.get(1), WrapPt1.get(2)];
    WrapBody1 = char(currentPath.get(1).getBodyName());

    fprintf('Muscle Origin:   %son the %s\n',sprintf('%.5f
',MOrigin),OriginBody);
    fprintf('Wrap Point 1:     %son the %s\n',sprintf('%.5f
',MWrapPt1),WrapBody1);

elseif N == 6

    WrapPt1 = currentPath.get(1).getLocation();
    MWrapPt1 = [WrapPt1.get(0), WrapPt1.get(1), WrapPt1.get(2)];
    WrapBody1 = char(currentPath.get(1).getBodyName());

    WrapPt2 = currentPath.get(2).getLocation();
    MWrapPt2 = [WrapPt2.get(0), WrapPt2.get(1), WrapPt2.get(2)];
    WrapBody2 = char(currentPath.get(2).getBodyName());


    fprintf('Muscle Origin:   %son the %s\n',sprintf('%.5f
',MOrigin),OriginBody);
    fprintf('Wrap Point 1:     %son the %s\n',sprintf('%.5f
',MWrapPt1),WrapBody1);
    fprintf('Wrap Point 2:     %son the %s\n',sprintf('%.5f
',MWrapPt2),WrapBody1);

end
```

```
%% Moving through a motion:

% Import .mot file
% load('C:\Users\USER\Google
Drive\PhD\OpenSim\Z_Setup\Tasks\Abduction.txt'); % UCT directory
load('C:\Users\DYXROO001\Dropbox\Work\PhD\OpenS_pipelines\NSM_based models
for study\motion\Motions_detailed\Moment Arm Inputs\Abduction.txt');
eval('angles=Abduction;');

modelCoordSet = osimModel.getCoordinateSet(); % get the set of the model
co-ordinates (SC, AC, GH joint, etc)
nCoords = modelCoordSet.getSize(); % the number of model co-ordinates

for i = 1:length(angles) % each step of the motion

    CurrentAngle = angles(i,:); % Joint Coords for each timestep

    for j = 0:nCoords-1
        modelCoordSet.get(j).setValue(state, CurrentAngle(j+1))
    end
    muscl_lnth = double(muscles.get(Nmusc_ant).getOptimalFiberLength());
    % <Do further calculations/measurements here>

end

%% Calculating Moment Arms:

% OpenSim uses Euler angles and intrinsic rotation sequences (co-ordinate
% system changes orientation after the rotation of each element).
% e.g.: GH joint rotation: x, -z', y'' (flexion, Abduction, rotation).

% Measurement of moment arms around the humerus are clinically measured
% using an extrinsic rotation sequence (fixed co-ordinate system) relative
% to the thorax (ground). GH joint: y, z, y

% Need to convert the GH rotation using the API:

% elemental rotations of the SC and AC joints:
angles = deg2rad(angles); % convert degrees into radians for calculations
SCy = angles(:,1);
SCz = angles(:,2);
SCx = angles(:,3);
ACy = angles(:,4);
ACz = angles(:,5);
ACx = angles(:,6);

Joint = osimModel.getBodySet().get('GHdum').getJoint(); % the dummt joint
controlling GH motion in OpenSim
GSd_initial = Joint.get_orientation_in_parent; % read in the
original/default joint orientation
GSd_initial = [GSd_initial.get(0), GSd_initial.get(1), GSd_initial.get(2)];
GSd_rot_initial = rotx(GSd_initial(1))* roty(GSd_initial(2))*
rotz(GSd_initial(3)); % calculate rotation matrix

for i = 1:length(angles) % each step of the motion

    Rsc = roty(SCy(i)) * rotz(SCz(i)) * rotx(SCx(i));
```

```
    Rac = roty(ACy(i)) * rotz(ACz(i)) * rotx(ACx(i));

   % GSd_angs = deg2rad(RZYXSOLV(GSd_rot_initial*Rac'*roty(1.5)'*Rsc')); %
this 'corrects' the GH joint frame
    GSd_angs = deg2rad(RZYXSOLV(GSd_rot_initial*Rac'*Rsc')); % this
'corrects' the GH joint frame
    GSd_rot = ArrayDouble.createVec3(GSd_angs(1),GSd_angs(2),GSd_angs(3));

Joint.set_orientation_in_parent(GSd_rot);

    if i == 10
       xx = pi;
    end

    osimModel.initSystem; % update the state of the model to recognise the
change in frame

    CurrentAngle = angles(i,:); % Joint Coords for each timestep
    for j = 0:nCoords-1
        modelCoordSet.get(j).setValue(state, CurrentAngle(j+1))
    end

    GH_beta = modelCoordSet.get('GH_abd');%x-axis
    GH_gama = modelCoordSet.get('GH_flex');%z-axis
    GH_beta2 = modelCoordSet.get('GH_rot');%y axis

    % measurement moment arms relative to the three GH joint axes:
    % beta (x) / gama (z) / beta2 (y)
    MomentArm_Beta(i,1) = muscle.computeMomentArm(state,GH_beta); % in m
    MomentArm_Gama(i,1) = muscle.computeMomentArm(state,GH_gama); % in m
    MomentArm_Beta2(i,1) = muscle.computeMomentArm(state,GH_beta2); % in m
end

MomentArms_Gama = MomentArm_Gama*1000; % in mm
MomentArms_Beta = MomentArm_Beta*1000; % in mmMomentArms_Beta_2 =
MomentArm_Beta*1000;
MomentArms_Beta2 = MomentArm_Beta2*1000; % in m

fprintf('Middle Deltoid: \n');
disp (MomentArms_Beta);
steps = linspace(0,150,31)';
hold on;
plot(steps,MomentArms_Beta,'b-','linewidth', 2);
plot(steps,muscl_lnth,'b.','linewidth', 2);
axis([-1,151,-60,60]);
title('Moment Arm During Abduction');
xlabel('Abduction Range of Motion (degrees)');
ylabel('Moment Arm (mm)');
```

Research Outputs and Achievements during the Doctoral Thesis

Publications

- **R. Dey**, S. Patnaik, G. Nair, S. Steiner and S. Sivarasu. **An intra-operative device (Pat-Rig) for parallel drilling and femoral landmark estimation during MPFL reconstructive surgery.** *Under Review at South African Orthopaedic Journal.*

- **R. Dey**, S. Roche, T. Rosch, T. Mutsvangwa, J. Charilaou, and S. Sivarasu. **Anatomical variations in gleno-humeral joint: an inter population study.** *Journal of Shoulder and Elbow Surgery OA, 2(1), 1-7, March 2018.* **https://doi.org/10.1016/j.jses.2017.11.007.**

- **R. Dey**, S. Patnaik and S. Sivarasu. **Novel Device to Accurately Locate Femoral Insertion Landmark in Medial Patellofemoral Ligament (MPFL) Reconstruction.** *ASME. Frontiers in Biomedical Devices, 2017 Design of Medical Devices Conference ():V001T11A019.* **https://doi.org/10.1115/DMD2017-3500.**

- **R. Dey**, S. Patnaik, S. Steiner and S. Sivarasu. **Low-Cost Three-Dimensional Printed Surgical Drill-Guiding Device for MPFL Reconstruction (Pat-Rig)1.** *ASME. J. Med. Devices. 2016;10(2):020914-020914-3.* **https://doi.org/10.1115/1.4033205.**

Conference Presentations

- **R. Dey**, S. Roche, T. Rosch and S. Sivarasu. **Effect of humeral head shape on the contact radius, moment arms, and glenohumeral forces.** *8th World Congress of Biomechanics (WCB), Dublin, Ireland, July 2018. (Poster Presentation).*

- **R. Dey,** S. Roche, T. Mutsvangwa and S. Sivarasu. **An inter-population study between African and European glenohumeral articulating surfaces.** *8th World Congress of Biomechanics (WCB), Dublin, Ireland, July 2018. (Oral Presentation).*

- J. Charilaou, **R. Dey**, S. Roche, S. Sivarasu, F. Hansson, R. van Staden and S. Maqungo. **Quantitative fit analysis of acromion and clavicle plates using acromion fracture 3D anatomical models.** *8th World Congress of Biomechanics (WCB), Dublin, Ireland, July 2018. (Oral Presentation).*

- **R. Dey**, S. Roche, and S. Sivarasu. **Recent finding in glenohumeral contact kinetics in Total Shoulder Arthroplasty.** *3rd South African Biomedical Engineering Conference (SABEC), Stellenbosch, South Africa, April 2018. (Podium Presentation).*

- **R. Dey**, S. Roche, T. Rosch, T. Mutsvangwa, J. Charilaou, and S. Sivarasu. **Are South African shoulders different? An unique inter-population morphometric investigation.** *63rd Congress of the South African Orthopaedic Association (SAOA), Port Elizabeth, South Africa,2017. (Oral Presentation).*

- J. Charilaou, S. Roche, **R. Dey**, S. Sivarasu, F. Hansson, R. van Staden, S. Maqungo, and C. Linden. **Scapula fractures: Planning osteosynthesis using 3D printed anatomical model.** *38th International Society of Orthopaedic Surgery and Traumatology (SICOT) Orthopaedic World Congress, Cape Town, South Africa, 2017. (Oral Presentation).*

- **R. Dey**, W. Inyang, T. Mutsvangwa, J. Charilou, S. Roche and S. Sivarasu. **A Comparative Shoulder Morphometric Study towards a Novel Metric – "Peak Points".** *24th Annual Meeting of the European Orthopaedic Research Society (EORS), Bologna, Italy, September 2016. (Oral Presentation).* Published in **The Bone and Joint Journal**.

- A.O. Inyang, **R. Dey**, T. Mutsvangwa, S. Roche, S. Sivarasu. **Morphometric measurements of the South African proximal humerus.** *24th Annual Meeting of the European Orthopaedic Research Society (EORS), Bologna, Italy, September 2016. (Oral Presentation).* Published in **The Bone and Joint Journal**.

- **R. Dey**, S. Patnaik, G. Nair, S. Steiner and S. Sivarasu**, Performance evaluation of a low cost 3D-printed drill-guiding device (Pat-Rig).** *MEIBIOENG '16, Oxford, United Kingdom, September 2016. (Poster Presentation).*

- A.O. Inyang, **R. Dey**, T. Mutsvangwa, S. Roche and S. Sivarasu. **Investigating the Three-Dimensional Geometry of the South African Proximal Humerus.** *11th Conference of the International Shoulder Group (ISG), Winterthur, Switzerland, July 2016. (Oral Presentation).*

- **R. Dey**, T. Mutsvangwa, J. Charilou, S. Roche and S. Sivarasu. **Determination of morphological parameters of humeral articulating surfaces using Matlab**. *2nd SU Biomedical Engineering Conference, Stellenbosch, South Africa, February 2016. (Oral Presentation).*

Achievements

- **Travel Grant** – Awarded 25000 ZAR (~ $2000) to attend and present research at the 8th World Congress of Biomechanics 2018, Dublin, Ireland.
- **Innovation Most Likely to Find Markets** by The Department of Science and Technology (DST) Republic of South Africa. Representing the Additive Manufacturing Team from The University of Cape Town (UCT) and the Innovation Bridge Award 2017.
- **3rd Best Overall Free Paper Presentation** by The South African Orthopaedic Association (SAOA) for the paper **Quantitative fit analysis of a scapula plating system,** which highlighted the current limitations of the current scapula fracture fixation plates. (September 2017).
- **Best Clinical Study done in Laboratory Setting** by Department of Surgery, Groote Schuur Hospital, Cape Town, South Africa. (Nov. 2016).

- **Innovation Doctoral Scholarship 2016 and 2017** by National Research Foundation, South Africa.
- **Grant-holders Linked Scholarship 2015** by National Research Foundation, South Africa.
- **Best Student Award** by CARDEA Biomedical Technologies during a 3day workshop on Biomedical Signal Processing using Matlab (VIT, 2010).

"Imagination is more important than knowledge.

For knowledge is limited.

Imagination encircles the world."

- *Albert Einstein.*